Probes on the Lower Charge Density Wave State of $NbSe_3$: Magnetic Field, Temperature Gradient, and Pulsed Electric Field Effects

By

Philip Anthony Parilla

A.B. (University of Chicago) 1979
M.A. (University of California) 1983

DISSERTATION

Submitted in partial satisfaction of the requirements for the degree of

DOCTOR OF PHILOSOPHY

in

PHYSICS

in the

GRADUATE DIVISION

of the

UNIVERSITY OF CALIFORNIA at BERKELEY

Approved:

Chair ..... Date 11/21/89

..... 11/21/89

L.M. FALICOV 11/22/89

Probes on the Lower Charge Density-Wave State of $NbSe_3$: Magnetic Field, Temperature Gradient, and Pulsed Electric Field Effects

Philip Anthony Parilla

Probes on the Lower Charge Density Wave State of $NbSe_3$: Magnetic Field, Temperature Gradient, and Pulsed Electric Field Effects

Philip Anthony Parilla

Department of Physics
University of California, Berkeley

ABSTRACT

An investigation of the lower-temperature charge-density-wave [CDW] state of $NbSe_3$ was performed using three different techniques.

An investigation of the anomalous magnetoresistance seen in $NbSe_3$ was performed. Specifically, measurements were made to detect possible magnetic-field-induced conversion between normal and CDW carriers. To this end, the frequency-dependent conductivity was measured as a function of the magnetic field. Also examined was the proportionality constant between the narrow-band-noise [NBN] frequency and the CDW current; this constant is expected to depend on the CDW carrier concentration. In a separate experiment, the resistance increase caused by application of uniaxial stress, which has characteristics similar to the magnetic field effects, was examined in conjunction with a magnetic field for possible interactions between the two phenomena.

In crystals with a temperature difference ΔT across the sample, a detailed investigation was performed on the splitting of a sliding CDW into velocity "sub-domains". Phase slip centers [PSC] are expected to occur between these sub-domains. A theory is developed based on the minimization of CDW phase strain and PSC energies. It predicts scaling behavior between the number of sub-domains and ΔT and that the dynamic properties of the CDW are sensitive to the relative directions of the heat and electrical currents. Experiments testing this model were performed and the results show very good agreement with the model.

The transient voltage response to current pulses was measured. In isothermal samples, the transient response consists of a ringing at the NBN frequency. The ringing amplitude was measured as a function of the initial bias level and shows a sharp peak centered slightly above zero initial bias. In another experiment, the ringing amplitude was measured as a function of zero bias duration. The results indicate that the CDW repins in approximately 80 nanoseconds.

The transient response also was measured in samples with a temperature gradient in order to examine the formation of sub-domains and PSC's. Detailed analysis is performed in both the time and frequency domains and shows that sub-domains form extremely fast or already "pre-exist" prior to the application of the pulse.

Alex Zettl

for my parents,

Ralph Michael and Marie Louise Parilla

and for my loving wife,

Susan

Acknowledgments

It is a difficult task to comprehend the tremendous support that has made this thesis possible. This support has been continuous over a lifetime and has come in many forms: from help in finding the right screw for equipment to a reassuring hug when weeks worth of work has been ruined by an unfortunate mishap. Trying to acknowledge this support is very much like taking a photograph of majestic scenery. When you stand before the panoramic view, you are filled with awe and are humbled; and yet, when you show the snapshots to friends and neighbors, the image is there but the awe is not. As you read this acknowledgement, keep in mind that it is but a snapshot of the support that has been given to me.

I thank my thesis adviser, Professor Alex Zettl, for his direction and guidance, tips on experimental techniques, help in strengthening my skills, and financial support. My gratitude goes to Professor Leo Falicov and Professor Eugene Haller for their critical reading of this thesis and for being on my thesis committee.

There have been many comrades who have fought along beside me in the trenches of the laboratory. They have provided me with insight and assistance flavored with companionship and amusement. I thank Dr. L. C. Bourne, Gabriel Briceno, Brian Burk, Norman Carey, Bill Creager, Mike Crommie, Dr. R. P. Hall, Storrs Hoen, Professor Mark Sherwin and Dr. Ulrich Walter. A special thanks goes to Dr. Angelika

Behrooz for her assistance with the temperature gradient experiments discussed in Part 2. Deep gratitude is also extended to Dr. Steve Jordan and Gary Kelderhouse, my good friends who introduced me to the laboratory and help me develop many of the skills I now possess.

Dr. Mike Hundley deserves a special mention. Most of the work mentioned in this thesis has been performed with some degree of collaboration with Mike. He has provided helpful assistance in the laboratory and has been very instrumental in developing ideas. We have engaged in many hours of fruitful and stimulating discussions interspersed with pleasant conversation and humorous anecdotes. His warm friendship has made graduate school a much more pleasant experience.

My acknowledgment would not be complete without thanking the support staff of the Physics Department at Berkeley. This includes the people in the machine and electronic shops, the purchasing department, and the departmental office especially John Davis, Ken Grove, Frank Lopez, Ivo Michelli, Ken Miller, and Lynn Pelosi.

As a relatively new parent, I am just beginning to comprehend the incredible support that my own parents have given me. Their love and assistance have no bounds. They have planted in me a love and a curiosity of life that has led me here. It is impossible to fully express my love and gratitude for them. It is only fitting that I dedicate this thesis, in part, to my father and to the memory of my mother.

I thank all my friends and family whose companionship and love make such an endeavor as this worthwhile. To my son Tony whose energy and joyfulness can rejuvenate me even on my worst days, I thank for making me feel like a kid again. Finally and most of all I thank my wife, Sue, for being there whenever I needed her, constantly giving of herself, skillfully managing with my absence, supporting our household, caring for our son, proofreading, and being a friend, a soul mate, and a lover.

The research comprising this thesis was supported in part by NSF Grants DMR 84-00041 and 83-51678 with additional contributions from the Alfred P. Sloan Foundation, General Motors Research Corporation, IBM Corporation, and the E.I. DuPont De Nemours and Co.

Vita

February 15, 1957	Born in Elmhurst, Illinois
June, 1979	A. B. Honors in Physics University of Chicago
December, 1983	M. A. in Physics University of California, Berkeley, CA
December, 1978 to July, 1981	Associate Electronics Engineer and Technician, Laboratory for Astrophysics and Space Research, Chicago, IL
September, 1981 to December, 1989	Teaching and Research Assistant, Department of Physics, University of California, Berkeley, CA

Publications

1. P. Parilla and A. Zettl. Transient charge density wave dynamics in $NbSe_3$. Phys. Rev. B**32**, 8427 (1985).

2. P. Parilla, M. F. Hundley, and A. Zettl. Magnetic-field-induced carrier conversion in a charge density wave conductor. Phys. Rev. Lett. **57**, 619 (1986).

3. M. F. Hundley, P. Parilla, and A. Zettl. Charge density wave magnetodynamics in $NbSe_3$. Phys. Rev. B**34**, 5970 (1986).

4. A. Zettl, M. F. Hundley, and P. Parilla. Magneto-transport studies in charge density wave conductors. Syn. Met. **19**, 807 (1987).

5. P. Parilla, N. Carey, and A. Zettl. Stress-dependent magnetoresistance in $NbSe_3$. Solid State Commun. **64**, 417 (1987).

6. M. F. Crommie, Amy Y. Liu, A. Zettl, Marvin L. Cohen, P. Parilla, M. F. Hundley, W. N. Creager, S. Hoen, and M. S. Sherwin. c-axis Pressure Dependence of Normal and Superconducting State Properties of $YBa_2Cu_3O_7$. Phys. Rev. B**39**, 4231 (1989)

7. P. A. Parilla, A. Behrooz, and A. Zettl. Sub-domain Scaling and Asymmetry in $NbSe_3$. Submitted to Phys. Rev. Lett.

8. P. A. Parilla, M. F. Hundley, and A. Zettl. Charge Density Wave Sub-domain Formation in an Applied Temperature Gradient. Submitted to Phys. Rev. Lett.

9. P. A. Parilla, A. Behrooz, and A. Zettl. Charge Density Waves in an Applied Temperature Gradient: Experiment. To be published.

10. P. A. Parilla, M. F. Hundley, and A. Zettl. Charge Density Waves in an Applied Temperature Gradient: Theory. To be published.

11. P. A. Parilla, M. F. Hundley, and A. Zettl. Formation Time of Charge-Density-Wave Sub-domains in $NbSe_3$ Crystals. To be published.

12. P. A. Parilla and A. Zettl. Observation of Fast Narrow-Band-Noise Fluctuations in $NbSe_3$ Crystals. To be published.

Table of Contents

Chapter

Chapter

Chapter

List of Figures

Figure

Figure

Chapter 1

Introduction and Motivation

Introduction

Over the past 15 years, there has been considerable effort applied toward understanding the transport properties of quasi-one-dimensional and quasi-two-dimensional conductors[1]. A common feature of low dimensional metals is the formation of an insulating density-wave ground state (either charge-density-wave [CDW] or spin-density-wave [SDW]). The metal-insulator transition often occurs at temperatures below room temperature. The formation of the density wave is associated with the nesting ability of the Fermi surface: electronic states with $\Delta k = 2k_F$ mix and form an energy gap in the electronic spectrum. If the nesting is complete, then the material will undergo a full metal-insulator (or rather metal-semiconductor) transition; for example, this is the case for $(TMTSF)_2PF_6$[(2)], NbS_3, TaS_3, $(TaSe_4)_2I$, and $K_{0.3}MoO_3$.

When the nesting is substantial but incomplete, the transition may still occur but excess normal carriers can remain in metallic bands to give metallic or semimetallic behavior; this is the case for niobium triselenide ($NbSe_3$) which undergoes two CDW transitions (T_{P1}=144 K, T_{P2}=59 K) and both result from an incompletely nested Fermi surface. The

transitions are marked by resistance anomalies below T_{P1} and T_{P2}, but metallic behavior is recovered as $T \rightarrow 0$[3].

In many of the CDW materials, including $NbSe_3$, TaS_3, $K_{0.3}MoO_3$, and $(TaSe_4)_2I$, an electric field greater than a threshold field E_T will cause the CDW to depin from the impurities present in the crystal and move through the crystal carrying current as it does. The most striking feature associated with the sliding of a CDW is the presence of a periodic current (or voltage) oscillation commonly referred to as narrow-band noise [NBN]. The spectrum of the NBN signal consist of narrow peaks at a fundamental frequency and its harmonics[4]; the magnitude of the NBN frequency is directly proportional to the CDW current[5] (and hence its velocity as well). The existence of the NBN along with the many interesting effects associated with it[6] provide important diagnostic tools useful in investigating the dynamical nature of CDW systems. For example, the overall quality of the NBN spectrum is believed to directly reflect the coherence of the dynamical CDW state.[7] Interestingly, $NbSe_3$ was the first material to display CDW conduction[8], and has been the most widely studied in terms of CDW dynamics. One reason for its popularity stems from the exceptional quality of the NBN signal displayed by $NbSe_3$ crystals in general.

Motivation

This thesis examines three aspects of the charge density wave in $NbSe_3$: magnetic field effects, temperature gradient

effects, and pulsed electric field effects. Brief descriptions and background information on these effects are listed below.

Magnetic Field Effects

Recently, a great deal of theoretical and experimental work has been done on the effect of a magnetic field on incompletely nested systems in organic and inorganic low-dimensional materials. In the organics, the Bechgaard salts ($(TMTSF)_2X$; X = ClO_4, PF_6) show unusual magnetoresistance reminiscent of the quantum Hall effect; the magnetoresistance is the signature of *magnetic-field-induced* phase transitions from the metallic state through a cascade of SDW states[9]. The very low temperatures ($T < 2K$) and moderate to high magnetic fields ($6 \rightarrow 30$ T) needed to observe this phenomenon point to the quantization of orbital motion as being of primary importance in these quasi-two-dimensional systems. Indeed, the leading theoretical explanations contain the essential idea of a competition between the quantized orbital motion and the nesting properties of the Fermi surface.[10]

In the inorganics, $NbSe_3$ shows an anomalously large magnetoresistance in the lower CDW state ($T < T_{P2}$).[11] The initial evidence suggested that the magnetic field decreased either the number or the mobility of the normal electrons thereby enhancing the resistance.[11] Theoretical work by Balseiro and Falicov[12] showed that, in systems with a stable density-wave ground state, a magnetic field can enhance the

energy gap through destruction of electron-hole pockets of the imperfectly nested Fermi surface. The theory implies that the *magnetic field can induce a direct conversion of normal carriers to CDW carriers.* The magnetic-field experiments discussed in this thesis are the author's and coworkers' attempt to detect this magnetic-field-induced carrier conversion in the lower CDW state of $NbSe_3$.

Temperature Gradient Effects

In a given material, the CDW parameters are in general very temperature dependent. For example, the CDW amplitude Δ, the depinning field E_T, and the ohmic (normal carrier) resistivity ρ_n are all sensitive functions of temperature. These parameters also determine the CDW phase velocity and hence the NBN spectrum in the non-linear region. A useful technique to explore CDW coherence is thus to measure CDW dynamics, including the NBN spectrum, in the presence of an applied temperature gradient.

Original studies[13] of the NBN spectrum in relatively short samples (< 0.4 mm) of $NbSe_3$ in a temperature gradient demonstrated that the quality and amplitude of the noise are not degraded by the gradient, but instead the spectrum reflects only the average sample temperature. Subsequent experiments on longer $NbSe_3$ samples have indicated that the application of a temperature gradient can result in single[14,15,16] or multiple[17,18] splittings of the NBN fundamental. These results provide strong evidence that a

temperature gradient forces the CDW to break up into a number of serially arranged velocity-coherent regions called *sub-domains*, with the CDW velocity of a given sub-domain determined by the values of the temperature-dependent CDW parameters within it. A phase-slip process must occur at the interface between neighboring sub-domains due to the CDW velocity discontinuity that exists there.[14,18] The temperature gradient experiments and theory described in this thesis are the efforts of the author and co-workers designed to improve our understanding of temperature gradient effects on the CDW in $NbSe_3$ and other CDW conductors.

Pulsed Electric Field Effects

The motion of a CDW can be described, in the simplest sense, by taking the CDW as a rigid object and allowing it to move with respect to the lattice. At T = 0 K, an incommensurate CDW in a perfect lattice has translational invariance and could carry current without dissipation;[19] however, impurities and defects in the lattice can act to pin the CDW to the lattice and provide mechanisms for dissipation to occur. The motion of the CDW in this picture can be described by a single degree of freedom: the phase of the CDW with respect to the lattice. The classical model of Grüner, Zawadowski, and Chaikin[20] is such a model and incorporates the CDW inertia, damping and the assumption that the CDW is in a periodic potential (since translating the CDW by one wavelength results in an equivalent position). This

phenomenological model has given good qualitative results when compared to some of the experimental data; but owing to its simplicity, cannot explain all the phenomena associated with CDW dynamics.

There is a whole class of phenomena observed in CDW systems which cannot be described with only one degree of freedom; for instance, polarization of the sample, hysteresis in dV/dI curves, the existence of CDW velocity sub-domains, and memory effects fall into this category. Models developed to explain these have many degrees of freedom. The experimental evidence suggests two possibilities:

1) The CDW is not a rigid object but rather a deformable one which can adjust itself to minimize the energy of interaction with the impurities. This corresponds to the internal phase modes of the CDW.

2) The CDW amplitude can vary and, in particular, there are circumstances where the CDW amplitude can vanish. For a sliding CDW, this allows for the possibility of discontinuities in the CDW velocity accompanied by phase-slip processes.

Information about these two processes can be obtained by studying the response of the CDW to pulsed electric fields.

The internal phase modes can be investigated by studying transient "ringing" in this overdamped system. (CDW systems

appear to be overdamped from the results of frequency-dependent conductivity studies[21].) Transient ringing occurs, for example, when the bias to a sample suddenly changes from zero bias to one above threshold. The frequency of the ringing equals that of the NBN frequency[22] and the amplitude of the transient decays to the steady-state NBN amplitude. The results of these studies can be used to check the predictions of models which explicitly consider the importance of the internal phase modes.

In the motivation for the temperature gradient effects, it was described how a temperature gradient could cause the introduction of phase-slip processes and drastically change the velocity profile of the CDW by breaking the sample into multiple velocity sub-domains. Information on sub-domain formation can be obtained by applying a pulsed electric field across a sample which is predisposed to form sub-domains and observing how the CDW evolves from the pinned state where there are no phase-slip processes occurring to the sliding state where phase slip is necessary in the steady state. As might be expected, temperature gradients can be applied across a sample to predispose it to form sub-domains.

Both of the above experiments involve looking at the response of the CDW on short time scales. In the course of these experiments, many interesting features of the narrow-band noise [NBN] have become apparent; these features were not associated with the pulsed electric fields per se, but rather with the nature of the NBN as observed with fine time

resolution (<< NBN period which is ~ 0.1 → 1 μS in typical experiments). These observations are mainly concerned with the fluctuations seen in the NBN and are also reported in this thesis.

Organization of Thesis

There are three chapters which discuss magnetic field effects. Chapter 2 describes the unusual magnetic effects previously seen in $NbSe_3$ and provides the relevant background for this investigation. Work performed by the author and coworkers are detailed in chapters 3 and 4. The experiments designed to detect the magnetic-field-induced carrier conversion are reported and discussed in chapter 3. Additionally, the effects of uniaxial stress on $NbSe_3$, (which show similarities to the magnetic field effects), have been investigated in conjunction with an applied magnetic field in order to see if the two effects are interrelated; this is reported in chapter 4.

The next two chapters describe the work performed by the author and coworkers on temperature gradient effects in CDW systems. Chapter 5 reports the experimental investigation on the phenomena associated with a sliding CDW in an applied temperature gradient. Chapter 6 presents a model of the temperature gradient effects on a sliding phase-dynamical CDW.

The last three chapters discuss aspects of CDW dynamics on short time scales. Chapter 7 details the author's and co-

workers' investigation into transient ringing which is thought to occur because of the internal phase degrees of freedom. Chapter 8 reports the attempts to observe the formation time of CDW velocity sub-domains when the sample has an applied temperature gradient. This involves phase-slip processes and thus represents CDW amplitude processes. Chapter 9 looks at fluctuations of the narrow-band noise which occur on fast time scales.

---

[1]See, for example these reviews, *Low-Dimensional Cooperative Phenomena--The Possibility of High-Temperature Superconductivity*, H. J. Keller, ed. (Plenum Press, New York, 1974);

Highly Conducting One-Dimensional Solids, eds. J. T. Devreese, R. P. Evrard and V. E. Doren (Plenum Press, New York, 1975);

Physics in One-Dimension, eds. J. Bernasconi and T. Schneider (Springer-Verlag, New York, 1981);

G. Grüner and A. Zettl, *Phys. Rep.* **119**, 117 (1985);

Electronic Properties of Quasi-One-Dimensional Materials, P. Monceau, ed. (Reidel, Dordrecht, the Ne herlands, 1985);

Low-Dimensional Conductors and Superconductors, D. Jérome and L. G. Caron, eds. (Plenum Press, New York, 1987).

[2]TMTSF is the abbreviation for tetramethyltetraselenafulvalene which is an organic cation; for more information, see the reviews in the previous reference.

[3]R. M. Fleming, D. E. Moncton, and D. B. McWhan, Phys. Rev. B **18**, 5560 (1978).

[4]R. M. Fleming and C. C. Grimes, Phys. Rev. Lett. **42**, 1423 (1979).

[5]P. Monceau, J. Richard, and M. Renard, Phys. Rev. Lett. **45**, 43 (1980).

[6]see Gruner and Zettl and *Electronic Properties of Quasi-One-Dimensional Materials*, ref. 1.

[7]S.E. Brown, G. Mozurkewich, and G. Grüner, in *Lecture notes in Physics*, Vol. 217, Gy. Hutiray and J. Solyom, eds. (Springer-Verlag, New York, 1985) p. 318;
S. Bhattacharya, J.P. Stokes, M.J. Higgins, and R.A. Klemm, *Phys. Rev. Lett.* **59**, 1849 (1987).

[8]P. Monceau, N. P. Ong, A. M. Portis, A. Meerschaut, and J. Rouxel, Phys. Rev. Lett. **37**, 602 (1976).

[9]M. Ribault, J. Cooper, D. Jérome, D. Mailly, A. Moradpour, and K. Bechgaard, *J. Physique Lett.* **45** (1984) L93;
M. J. Naughton, J. S. Brooks, L. Y. Chiang, R. Chamberlin and P.M. Chaikin, *Phys. Rev. Lett.* **55**, 969 (1985).

[10]G. Montambaux, Proc. NATO ASI, Magog, Canada 1986.

[11]R. V. Coleman, G. Eiserman, M. P. Everson, A. Johnson, and L. M. Falicov, *Phys. Rev. Lett.* **55**, 863 (1985).

[12]C. A. Balseiro and L. M. Falicov, *Phys. Rev. Lett.* **55**, 2336 (1985);
C. A. Balseiro and L. M. Falicov, *Phys. Rev. B* **34**, 863 (1986).

[13]A. Zettl, M. Kaiser, and G. Grüner, *Solid State Commun.* **53**, 649 (1985).

[14]N.P. Ong, G. Verma, and K. Maki, *Phys. Rev. Lett.* **52**, 663 (1984);
G. Verma and N.P. Ong, *Phys. Rev.* B **30**, 2928 (1984).

[15]X.J. Zhang and N.P. Ong, *Phys. Rev.* B **30**, 7343 (1984).

[16]M.F. Hundley and A. Zettl, *Phys. Rev.* B **33**, 2883 (1986).

[17]S.E. Brown, A. Janossy, and G. Grüner, *Phys. Rev.* B **31**, 6869 (1985).

[18]J.W. Lyding, J.S. Hubacek, G. Gammie, and R.F. Thorne, *Phys. Rev.* B **33**, 4341 (1986).

[19]H. Fröhlich, *Proc. Roy. Soc. London* A**223**, 296 (1954).

[20]G. Grüner, A. Zawadowski, and P.M. Chaikin, *Phys. Rev. Lett.* **46**, 511 (1981).

[21]A. Zettl and G. Grüner, *Phys. Rev.* B **29**, 755 (1984); D. Reagor, S. Sridhar, and G. Grüner, *Phys. Rev.* B **34**, 2212 (1986).

[22]A. Zettl, Proceedings of International Symposium on Nonlinear Transport and Related Phenomena in Inorganic Quasi-One-Dimensional Conductors, Sapporo, 1983, p. 41.

Magnetic Field Effects

Chapter 2

Background to Magnetic Field Effects

Introduction

There is a long history of the usefulness of magnetic fields in determining and understanding the properties of materials. One of the first experiments performed on any new conducting material is the measurement of the Hall effect to determine the sign and concentration of the electrical carriers. Furthermore, at low temperatures, moderately large magnetic fields are indispensable in determining the shape of the Fermi surface as manifested in the de Hass-van Alphen and Schubnikov-de Hass effects.[1] With all the interest in $NbSe_3$ due to the CDW, there have been many investigations into its magnetic properties. This chapter reviews some of these studies. In particular, we will be concerned with the measurements throughout the temperature range where the second CDW is present ($T \leq 59$ K) since our main concern is with the possibility of magnetic-field-induced carrier conversion [MFICC].

Magnetoresistance

The impetus to search for MFICC came from an experimental study by Coleman et al.[2] and subsequent theoretical work by Balseiro and Falicov.[3] Coleman et al. reported unusual (transverse) magnetoresistance effects in

the lower CDW state ($T < 59$ K) of $NbSe_3$. At the relatively high temperature of 25 K, for example, a relative increase in the resistivity, $[\rho(H) - \rho(0)]/\rho(0)$, on the order of 5 was observed at $H = 227$ kG. The resistance versus temperature curves with and without a magnetic field is reproduced in Fig. 2-1; the corresponding relative magnetoresistance is shown in Fig. 2-2. Note that the magnitude of the lower CDW resistive anomaly is enhanced by the magnetic field and that the resistance maximum is shifted to lower temperatures. There is little if any change in the transition temperature of the lower CDW. Coleman *et al.* concluded that the large enhancement of the resistance anomaly was not caused by the dynamics of the CDW, but rather by the effect of the magnetic field on either the number or the mobility of the normal electrons.

Evidence consistent with this can be found in Fig. 2-3 which shows the effect of increasing the electric field on the dc resistance ($H = 0$ and $H = 227$ kG; $T = 30$ K; Ref. 2). At low electric fields, the CDW is pinned and does not contribute to the dc conductivity; only the normal electrons carry current. Above a threshold field E_T, CDW electrons also carry current and thus contribute to the conductivity; this leads to a reduction in the resistance as shown in the figure. At large electric fields, the conductivity of the CDW saturates. The interesting aspect of the data in Fig. 2-3 is that the saturation value is independent of magnetic field. This is in agreement with Gor'kov and Dolgov[4] who

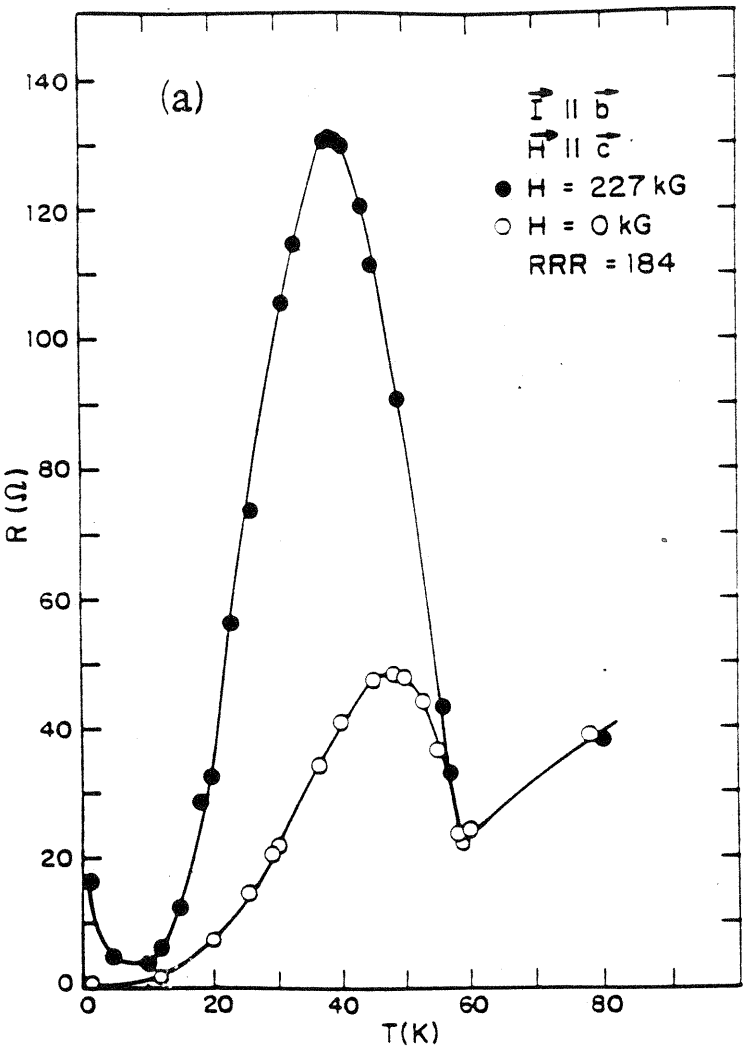

Fig. 2-1 The resistance of $NbSe_3$ as a function of temperature with and without a magnetic field (H = 0, open circles; H = 227 kG, solid circles; I_{bias} = 10 μA). From Coleman et al.

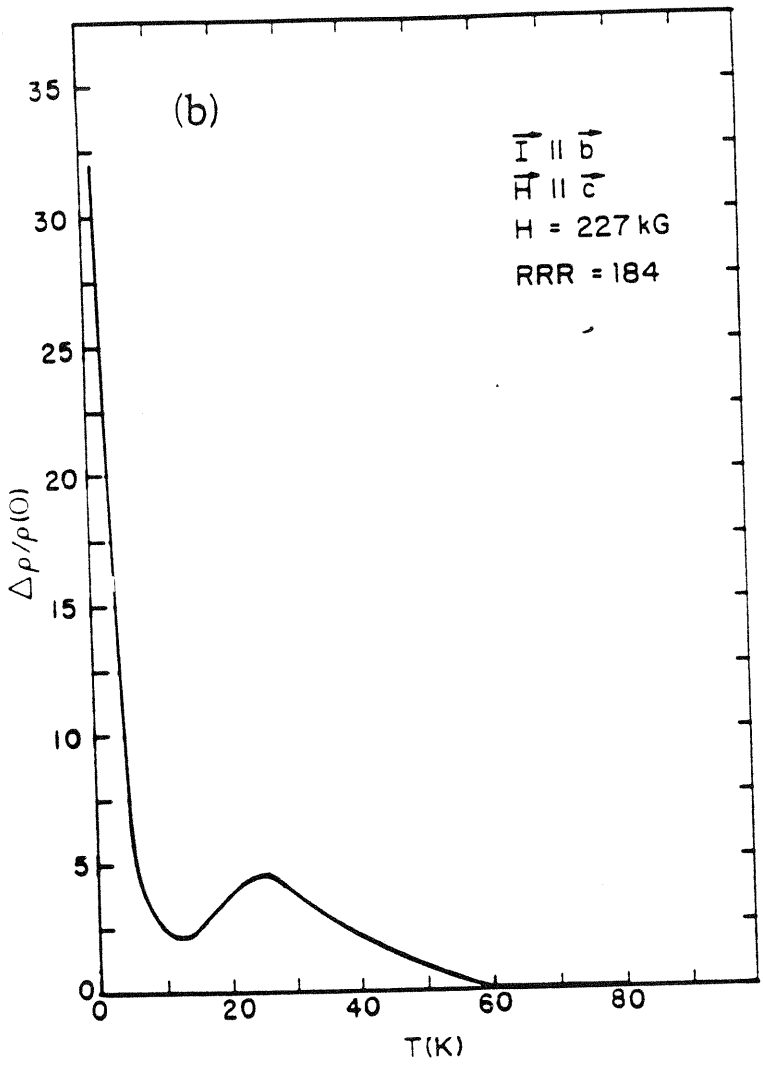

Fig. 2-2 The magnetoresistance $\Delta\rho/\rho$ calculated from the data of Fig. 2-1. Note the peak at the relatively high temperature of 25 K and that the magnetoresistance goes to zero at T_{P2}. From Coleman et al.

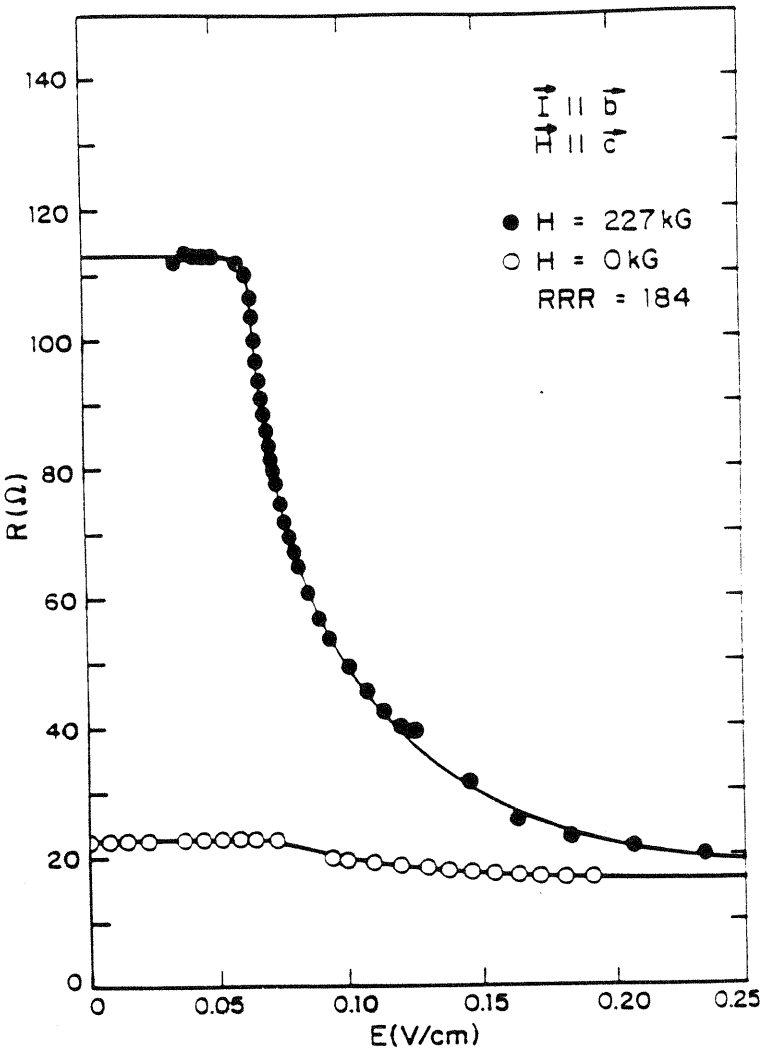

Fig. 2-3 The resistance of $NbSe_3$ as a function of electric field with and without a magnetic field (H = 0, open circles; H = 227 kG, solid circles; T = 30 K). Note that at high electric fields the resistances converge irrespective of the magnetic field. From Coleman et al.

showed that a decrease in normal electron conductivity is compensated for by an increase in the Fröhlich mode's contribution to the conductivity.

The data of Fig. 2-3 are also consistent with the magnetic field converting normal electrons to CDW electrons only, with the mobilities independent of magnetic field. The low-field resistance would reflect the (magnetic-field-dependent) concentration of normal electrons, while the high-field resistance would be magnetic-field-independent because it depends on the total concentration of electrons (a constant). An additional condition, which is sufficient to make the hypothesis of carrier conversion consistent with the data of Fig. 2-3, is that the saturated CDW mobility equals the mobility of the normal electrons:

$$\mu_{CDW}(E \rightarrow \infty) = \mu_{normal}.$$

This condition has been verified experimentally for $H = 0$.[5]

An applied magnetic field also affects the threshold field for the CDW to slide, especially at low temperatures.[6] As the magnetic field increases, E_T decreases. The decrease is small at 30 K and amounts to about -7% change in Fig 2-3 (~5 mV); however, at 20 K the change is large: a 50% reduction. This indicates that the magnetic field interacts with the pinning mechanism of the CDW. The exact nature of this pinning is not understood well enough to say how the magnetic field couples to the pinning.

The work by Balseiro and Falicov[3] demonstrated that strong magnetic fields may lead to a destruction of electron-hole pockets in imperfectly nested anisotropic conductors, leading to an H-enhanced gap at the Fermi level for a system with an intrinsically stable density-wave ground state (either CDW or SDW). The mechanism of Balseiro and Falicov (which includes the effects of band broadening and tunneling between bands) would imply that, in $NbSe_3$, the H field induces a direct conversion of normal carriers to CDW (condensed) carriers, thus effectively modifying the CDW order parameter Δ.

Hall effect

If the normal electrons in $NbSe_3$ were described well by a single-band model, then the Hall effect would easily map out any change in the concentration of the normal electrons due to the formation of the CDW's or from the conversion induced by a magnetic field. The situation in $NbSe_3$ is more complicated: even if the normal carriers consist of multiple bands, one still needs to worry about contributions from the CDW to the Hall effect. The empirical evidence suggests that the CDW only contributes to the Hall coefficient when the CDW slides and this is primarily due to the change in the longitudinal conductivity.[7] There is also the possibility that a moving CDW can directly contribute to the Hall effect.[8] This discussion will concentrate on the Ohmic Hall effect,

i.e. the CDW is pinned and does not contribute to the Hall voltage.

Ong and Monceau[9] measured the (Ohmic) Hall effect in $NbSe_3$; they found that a single-band model was not appropriate since the Hall coefficient changed sign at low temperatures (see Fig. 2-4). Ong[10] proposed a 2-band model and the available data[9,11,12] were fit to the model. He assumed the existence of two ellipsoidal closed Fermi surface pockets with one hole-like and one electron-like. At low magnetic fields where the model fit the data well, he concluded that: 1) the sign reversal of the Hall constant was dominated by changes in the mobility, and 2) the lower CDW was formed from hole-like states, i.e. near T_{P2}, the hole concentration decreases rapidly with decreasing temperature. (Because of a lack of high-temperature high-magnetic-field data, the second conclusion was reached with the additional assumption of the concentration of electron-like states being temperature independent.)

At large magnetic fields, the model does not fit the data well. It is not clear that adding a magnetic-field-dependent carrier concentration to the two-band model would rectify this discrepancy. However, a simple argument would seem to disagree with such a model: as the H-field increases, the Hall coefficient becomes more positive; this is in contradiction to the reasoning that given that the CDW is formed from hole-like states and given that a magnetic field converts additional states, one would expect the Hall

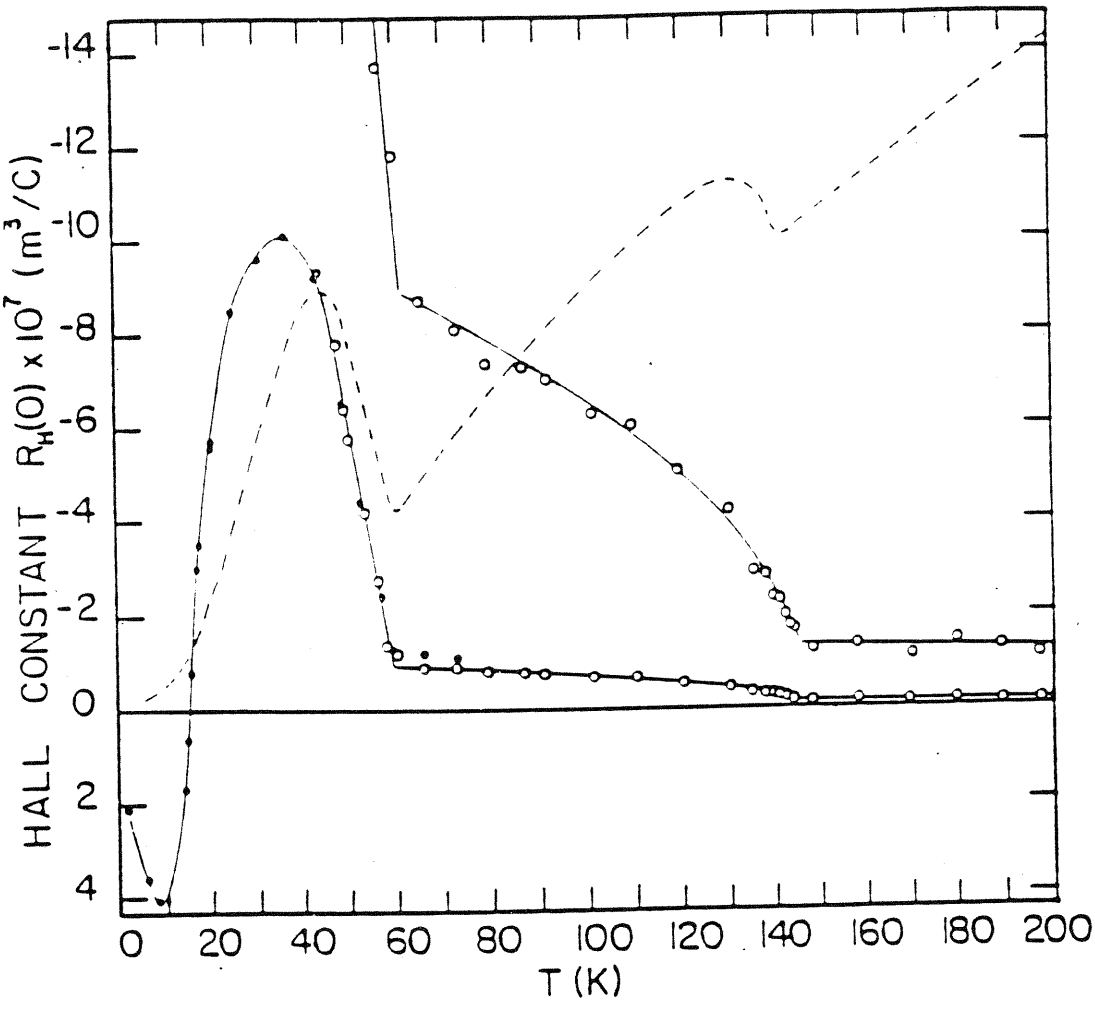

Fig. 2-4 The low-H-field Hall coefficient $R_H(H \rightarrow 0)$ versus temperature for $NbSe_3$. The open and solid circles refer to different samples. The data above 50 K are also shown with 10x magnification. Note the abrupt changes at the transition temperatures and the change of sign at 15 K. The broken line is the longitudinal resistivity; the solid lines are guides to the eye. From Ref. 9.

constant to become more negative as additional hole states were converted to the CDW. Clearly, the Hall data need a more detailed interpretation.

Thermoelectric Power

Another approach to investigate the electron transport properties of a material is the thermoelectric power [TEP]. Hundley and Zettl[13] measured the magnetothermopower of $NbSe_3$ in the temperature range 10-100 K with magnetic fields up to 75 kG. The magnetic field was perpendicular to the chain (b) axis. Figure 2-5 shows the thermopower of $NbSe_3$ at temperatures below 100 K, for selected values of applied magnetic field. Above T_{P2} = 59 K, the TEP is independent of H. On the other hand, below T_{P2} application of H results in a positive increase in the TEP, with the effect becoming larger with decreasing temperature. At T = 25 K, for example, a 75 kG magnetic field changes the TEP from zero to +60 μV/K. Below 15 K, the TEP in the high magnetic field limit appears to saturate at a maximum value of roughly +80 μV/K.

Hundley and Zettl ruled out phonon drag or conventional charge carrier diffusion as being responsible for the magnetic effects on the TEP. Instead they assumed a two-band model similar to the one used by Ong[10] (one hole-like, one electron-like). The thermopower in such a model is given by a weighted average:[14]

$$S = \frac{\sigma_e S_e + \sigma_h S_h}{\sigma_e + \sigma_h}$$

where S is the total thermopower, $\sigma_{e(h)}$ is the electron (hole) contribution to the dc electrical conductivity, and $S_{e(h)}$ is the electron (hole) contribution to the diffusion thermopower. They further assumed that the dominant effect of H is to change σ_e (in particular, n_e the concentration of electrons); σ_h, S_h, and S_e are to first order taken as independent of H. This led to a prediction on how the normal electron concentration varies with temperature and magnetic field based on the TEP data. The resulting calculation overestimated the carrier conversion when compared to any other estimate from other transport measurements and so the specifics of the model appear inconsistent with those other models. However, qualitatively the model proposed that the positive enhancement of the TEP by a magnetic field is caused by the magnetic-field-induced conversion of the electron-like states into the CDW state. As the electrons are converted, they are no longer available to compensate for the hole states and so the transport properties become more hole dominated. The electrons in the CDW state do not contribute to the thermopower.[15]

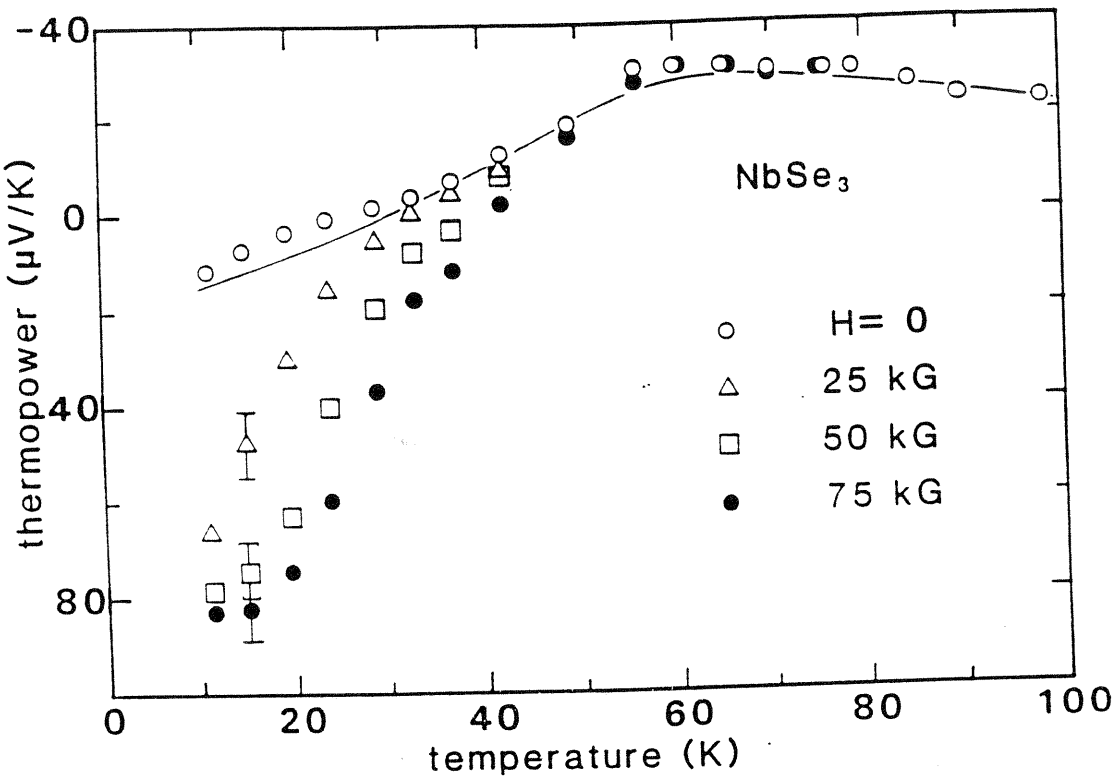

Fig. 2-5 Magnetothermopower vs temperature in $NbSe_3$. The lower CDW state is for T < 59 K. The solid line is H = 0 data from Ref. 16. From Ref. 13.

This concludes the brief introduction to the magnetic field effects in the lower CDW state of $NbSe_3$. The experiments described in the next chapter provide additional clues to the underlying mechanism of these magnetic field effects. The results of those experiments and the results of the experiments described above will be considered together in a discussion also in the next chapter.

[1]W. J. de Hass and P. M. van Alphen, *Leiden Comm.* 208d, 212a (1930), and 220d (1932);

D. Shoenberg, 'The de-Hass-van Alphen Effect', *Prog. Low Temp. Phys.* **2** (1957);

A. M. Kahn and H. P. R. Frederikse, 'Oscillatory Behavior of Magnetic Susceptibility and Electronic Conductivity', *Solid State Phys.* **9** (1959).

[2]R. V. Coleman, G. Eiserman, M. P. Everson, A. Johnson, and L. M. Falicov, *Phys. Rev. Lett.* **55**, 863 (1985).

[3]C. A. Balseiro and L. M. Falicov, *Phys. Rev. Lett.* **55**, 2336 (1985);

C. A. Balseiro and L. M. Falicov, *Phys. Rev. B* **34**, 863 (1986).

[4]L. P. Gor'kov and E. N. Dolgov, *J. Low Temp. Phys.* **42**, 101 (1981).

[5]P. Monceau, N. P. Ong, A. M. Portis, A. Meerschaut, and J. Rouxel, *Phys. Rev. Lett.* **37**, 602 (1976).

[6]Reference 2 and references within.

[7]G. X. Tessema and N. P. Ong, *Phys. Rev. B* **23**, 5607 (1981).

[8]S. N. Artemenko, E. N. Dolgov, A. N. Kruglov, Yu. I. Latyshev, Ya. S. Savitskaya, and V. V. Frolov, *JETP Lett.* **39** 308 (1984);

E. N. Dolgov, *Solid State Comm.* **50**, 405 (1984).

[9]N. P. Ong and P. Monceau, *Solid State Comm.* **26**, 487 (1978).

[10]N. P. Ong, *Phys. Rev. B* **18**, 5272 (1978).

[11]N. P. Ong and J. W. Brill, *Phys. Rev. B* **18**, 5265 (1978).

[12]R. M. Fleming, J. A. Polo, Jr., and R. V. Coleman, *Phys. Rev. B* **17**, 1634 (1978).

[13]M. F. Hundley and A. Zettl, *Solid State Commun.* **61**, 587 (1987).

[14]See, for example, F.J. Blatt, P.A. Schroeder, C.L. Foiles, and D. Greig, in Thermoelectric Power of Metals (Plenum Press, New York 1976) p. 27.

[15]J. P. Stokes, A. N. Bloch, A. Janossy, and G. Grüner, *Phys. Rev. Lett.* **52**, 372 (1984).

[16]P. M. Chaikin, W. W. Fuller, R. Lacoe, J. F. Kwak, R. L. Greene, J. C. Eckert;

N. P. Ong, *Solid State Commun.* **39**, 553 (1981).

Chapter 3

Magnetic Field Experiments

Introduction

There are basically two approaches to detect a possible conversion of normal electrons to CDW electrons with increasing magnetic field: one is to detect a decrease in the concentration of normal electrons; the other is to detect an increase in the CDW electron concentration. Examples of measurements of the former are the (low-electric-field) magnetoresistance, the Hall effect, and the thermoelectric power. Information on the CDW electron concentration can be obtained by measurement of the X-ray intensity of the CDW superlattice spots, the ac conductivity, the (high-electric-field) magnetoresistance, and the characteristics of the narrow-band noise [NBN]. The X-ray measurement would give the most direct evidence of any carrier conversion; however, due to the specialized equipment needed for an X-ray study (an X-ray probe capable of high magnetic fields and low temperatures), this measurement has not yet been done. This leaves the measurements of the transport properties as the most convenient means to obtain information on the respective electron concentrations. Unfortunately, the result of any given single measurement does not yield unambiguous information about these concentrations since other factors such as carrier mobility, band structure, and Fermi surface

characteristics come into play. Instead, one must make a number of different measurements and look for a consistent signature.

This chapter describes two experiments on $NbSe_3$ designed to detect carrier conversion. The first is a study of the characteristics of the narrow-band noise in a magnetic field (specifically how the NBN scales with the current carried by the CDW) and the second is a measurement of the ac conductivity as a function of magnetic field. The results of these experiments are then discussed taking into account the results from other experiments.

Narrow-Band Noise

In a simple model[1,2], the narrow-band noise frequency is related to the excess CDW current I_{CDW} through

$$I_{CDW} = n_c e v_c A = n_c e f \lambda A \qquad (3\text{-}1)$$

where $I_{CDW} = I_{tot} - V_s/R_o$ with I_{tot} the total sample current, V_s the time-averaged sample voltage, and R_o the low field (Ohmic) sample resistance. Also n_c is the CDW electron concentration, v_c the CDW drift velocity, A the sample cross sectional area, and λ a constant, usually taken to be the CDW wavelength. Hence for fixed n_c, I_{CDW} is directly proportional to f, and the ratio I_{CDW}/f reflects directly n_c. Measuring this ratio as a function of magnetic field yields $n_c(H)$.

Single crystals of $NbSe_3$ were mounted in a two probe configuration with the chain (b) axis of the crystal perpendicular to the field H (see Appendix B). A dc current was applied through the sample, and the voltage across the sample was amplified and detected with either a dc voltmeter or high frequency spectrum analyzer. For applied electric fields E exceeding the threshold E_T for the onset of CDW conduction, and with H = 0, a clear narrow band noise spectrum was observed, with a dominant fundamental frequency peak and numerous higher harmonics. Application of magnetic fields up to 75 kG were found to have no marked effect on the amplitude or the quality of the narrow band noise spectrum. The fundamental noise frequency f, however, was highly magnetic field dependent. (The quality of the NBN refers to the overall coherence of the NBN signal which can be gaged by the widths of the NBN peaks in the spectrum, by the degree of fluctuations in these peaks, and by the number of fundamental frequencies in the spectrum. There was a single NBN fundamental frequency present in the samples used for this experiment. During the ramping of the magnetic field, the sample had a fixed dc current bias.)

Figure 3-1 shows I_{CDW} vs f for $NbSe_3$ at T = 37.4 K, for H = 0 and for an applied field H = 75 kG. For H = 0, the linear relationship is in accord with Eqn. (3-1) and consistent with previous narrow band noise studies in $NbSe_3$[2,3,4]. With H = 75 kG, a linear dependence of f on I_{CDW} is again observed, but with a different slope. Fig. 3-1

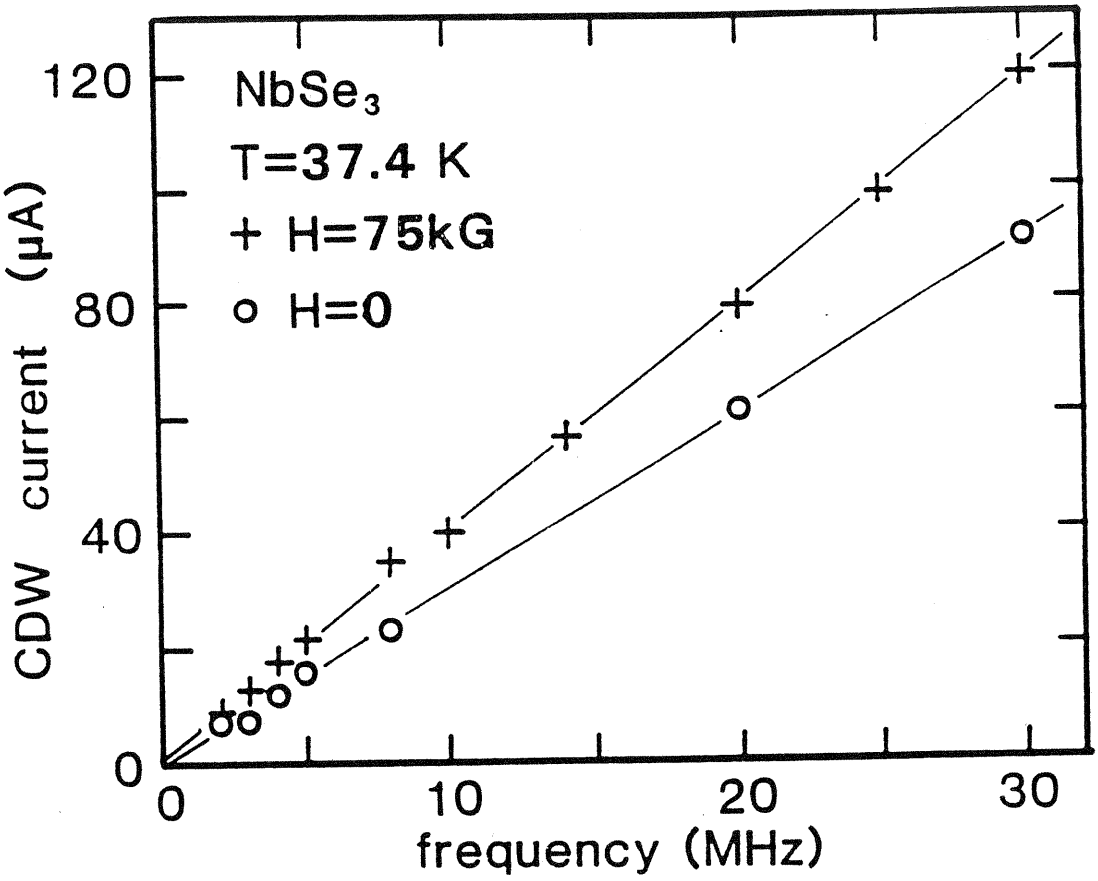

Fig. 3-1 I_{CDW} vs narrow-band noise frequency in $NbSe_3$ with and without an applied magnetic field.

demonstrates clearly that the ratio I_{CDW}/f is *increased* in the presence of an applied magnetic field. With e, λ, and A independent of H in Eqn. (3-1), Fig. 3-1 demonstrates that *the effect of a magnetic field in $NbSe_3$ is consistent with the enhancement of the CDW carrier concentration.* At 37 K, the effect of an H = 75 kG field is to increase the CDW carrier concentration by approximately 30% over the H = 0 value, a fairly dramatic change.

Data such as that shown in Fig. 3-1 were taken at various values of magnetic field strength and temperature in the lower CDW state. Figure 3-2 shows the slope I_{CDW}/f vs H for T fixed at 37.4 K. Up to H = 75 kG, a virtually linear dependence of I_{CDW}/f (and hence n_c) on H is obtained, with $d[I_{CDW}/f]/dH = 1.8 \times 10^{-3}$ $\mu A/MHz \cdot kG$. With λ = 14 Å, this corresponds to a magnetic-field-induced carrier conversion rate $dn_c(H)/dH = 3.6 \times 10^{18}$ carriers/kG·cm^3.

Figure 3-3 shows the relative increase in CDW carrier concentration, induced by an H = 75 kG field, as a function of temperature in the lower CDW state of $NbSe_3$. Near the CDW transition temperature T_P = 59 K, no increase in n_c is observed, while $n_c(H=75kG)/n_c(H=0)$ increases dramatically with decreasing temperature. Fig. 3-3 effectively defines the new CDW order parameter $\Delta(H,T)$. Previous studies[3,4] have shown that the temperature dependence of $\Delta(H=0,T)$ is borne out directly in measurements of $I_{CDW}/f \approx n_c$. The CDW carrier concentration is related to the order parameter by[5]

$$n_c(T)/n_c(T=0) \approx \Delta(T) \qquad (3\text{-}2)$$

valid for T close to T_p. For $T \ll T_p$, $\Delta(T)$ may again be related to $n_c(T)$[5], and, as in superconductors at T = 0, $n_c(T)$ equals unity, i.e. all carriers are condensed in the CDW state, *if* the system displays perfect Fermi surface nesting.

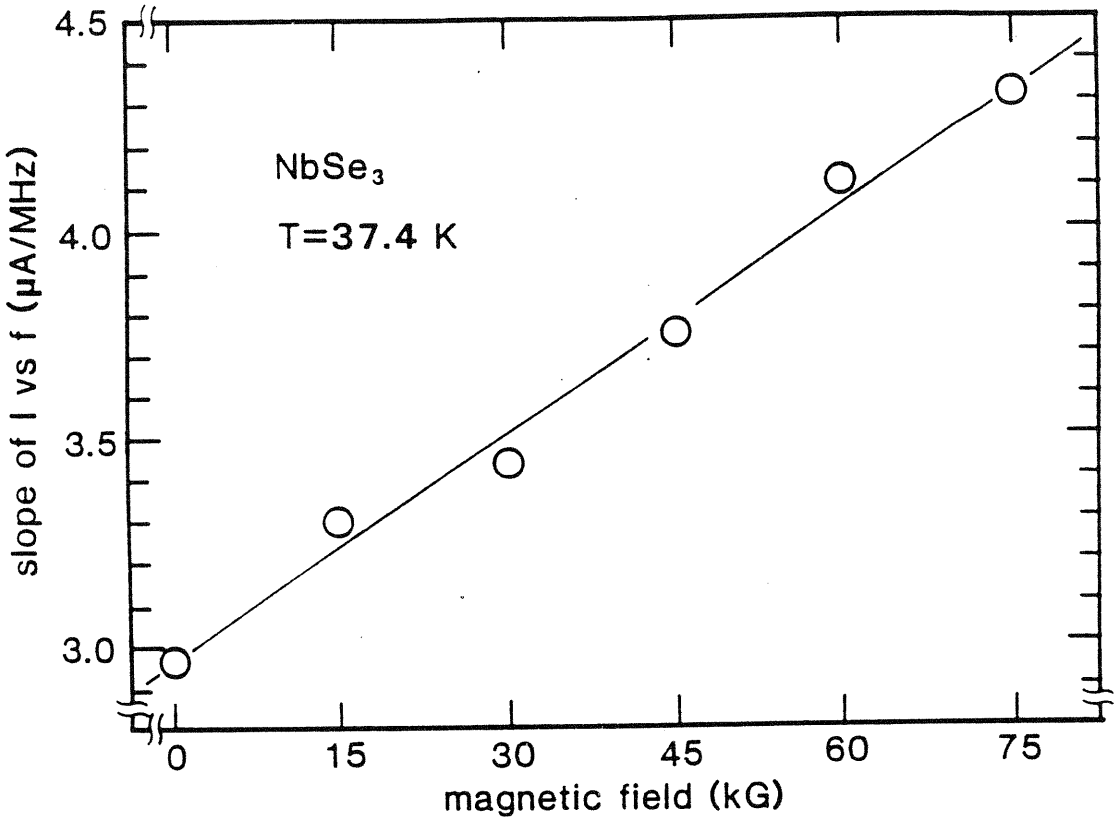

Fig. 3-2 $I_{CDW}/f \approx n_c$ vs H in $NbSe_3$. An increasing magnetic field results in an apparent increase in CDW carrier concentration. Up to H = 75 kG, the carrier conversion rate is linear in H.

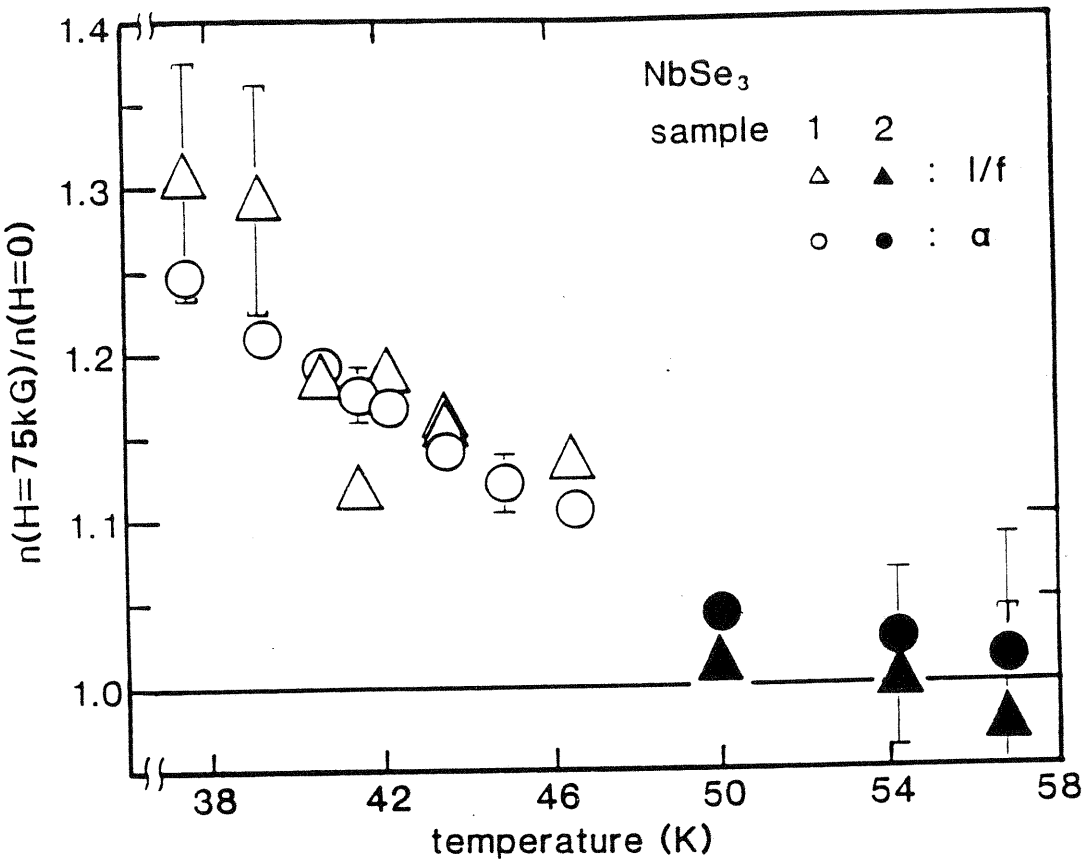

Fig. 3-3 Relative apparent increase in CDW carrier concentration due to a 75-kG field in $NbSe_3$, as a function of temperature (2-probe). The triangles refer to n_c determined directly from noise spectra, while the circles refer to the fraction of the Fermi surface destroyed (see text).

The magnetic field enhancement of n_c (and hence the enhancement of the CDW order parameter) shown in Fig. 3-3 for the narrow-band noise study, may be compared to the percentage of Fermi surface removed by the CDW transition and the applied field H. In addition to measurements of the narrow-band noise just described, we have performed pulsed low- and high-electric-field I-V studies on $NbSe_3$ in the presence and absence of magnetic fields. Consistent with the results of Coleman et al.[6], we find that although the low-field (Ohmic) resistance R_o of the crystal is strongly influenced by H, the high-electric-field (saturated) resistance R_{sat} is independent of H. In a simple approximation, the fraction of Fermi surface removed by the CDW transition and magnetic field may be expressed as[7]

$$\alpha(H,T) = \sigma_c(H,T)/[\sigma_o(H,T) + \sigma_c(H,T)] \qquad (3\text{-}3)$$

with

$$\sigma_o(H,T) = 1/R_o(H,T),$$

$$\sigma_c(H,T) = [R_{sat}(H,T)]^{-1} - \sigma_o(H,T).$$

With H = 0, approximately 60% of the remaining Fermi surface is destroyed by CDW formation at T_p = 59 K; with H = 75 kG this percentage is significantly greater, and temperature

dependent. The circles in Fig. 3-3 represent the fractional increase in α due to application of a 75 kG magnetic field. The ratio $\alpha(H=75\ kG,T)/\alpha(H=0,T)$ is seen to be in good agreement with carrier concentration increases deduced from these narrow-band noise studies. It should, however, be noted that Eqn. (3-3) represents only a crude approximation to the fraction of Fermi surface removed; a quantitative evaluation of α would require more detailed information.

The NBN investigation described above was performed on $NbSe_3$ crystals in a 2-probe configuration. The 2-probe configuration has the advantage of minimum perturbation on the coherence of the NBN signal, but has the disadvantage of contact resistance. On the other hand, a 4-probe configuration has the opposite problem: the inner voltage contacts compensate for any contact resistance, but they also severely perturb the coherence of the NBN spectrum[8] and thus make studies of the NBN difficult. Preliminary data from a 4-probe measurement disagreed with the above results and showed a much smaller effect, if any.[9] With an improved technique utilizing both 2- and 4-probe methods, Tritt et al.[10] later demonstrated that the effects of contact resistance cannot be ignored and that the effect of the magnetic field on the I_{CDW}/f ratio was a 5% increase over the zero-field ratio (T = 30 K; H = 96 kG).

Contact resistance influences the apparent value of the CDW current I_{CDW} measured in a 2-probe configuration because of the extra voltage drop across the contacts. The measured

2-probe CDW current is related to the CDW current measured 4-probe by[10]

$$I_{CDW}^{2P} = \frac{I_{CDW}^{4P}}{\left\{1 + \frac{R_c}{R_o(H,T)}\right\}} \qquad (3\text{-}4)$$

where the 2P and 4P superscripts refer to 2-probe and 4-probe respectively, R_c is the contact resistance and $R_o(H,T)$ refers to the Ohmic sample resistance. Eqn. (3-4) shows that a positive magnetoresistance will result in an apparent increase in the CDW current measured 2-probe as the magnetic field increases.

When the contact resistance is compensated for by using a 4-probe technique, the normalized values of α and I_{CDW}/f no longer track each other as they do in Fig. (3-3).[10] This forces the re-examination of the physical meaning behind the parameters α and I_{CDW}/f because they are expected to track each other. It is easily plausible that the parameter α has been misinterpreted since it is directly related to the conductivity which in turn depends on the intricacies of the Fermi surface (and not just the concentration of electrons). On the other hand, the ratio I_{CDW}/f as interpreted through Eqn. (3-1) comes from a simple and perhaps overly naive

model. Recently, strong evidence has emerged which shows that this ratio, may in fact, not accurately track n_c.

Tessema et al.[11,12] have extended the measurements of Tritt et al. to lower temperatures and have found that the ratio I_{CDW}/f decreases below ~ 35 K. This is in stark contrast to the behavior of n_c obtained from X-ray measurements[13] which show that the order parameter Δ (and hence n_c) monotonically increases and levels off as the temperature decreases. Although I_{CDW}/f and Δ track each other at temperatures near the transition[3,4], it is quite apparent they do not at low T. At these low temperatures, and when a magnetic field is applied, the ratio increases dramatically similar to the 2-probe data presented above. A possible key to understanding the decrease in the I/f ratio and its subsequent increase with magnetic field lies with the pinning of the CDW.[12]

The pinning of the CDW is directly reflected by the threshold field E_T and the pinning frequency ω_o (which are related to each other in various models). The threshold field is highly temperature dependent and magnetic field dependent (at low T), especially in the temperature ranges where the ratio I_{CDW}/f is similarly dependent. In fact, roughly speaking, the two appear to be inversely related:

$$I_{CDW}/f \propto 1/E_T(H,T)$$

or perhaps

$$I_{CDW}/f \propto C - E_T(H,T)$$

where C is some constant. We emphasize that this relationship might be purely coincidental, i.e., there is no physical relationship between the two. At this time, the exact nature of the ratio I_{CDW} remains unknown; we only mention this possibility in the spirit of conjecture. The importance of pinning in magnetic field effects also is evident in data from experiments on ac conductivity which we now present.

AC Conductivity

Here we report complex ac conductivity $\sigma(\omega)$ measurements of $NbSe_3$ in the lower CDW state, in the frequency range 4 MHz to 1 GHz, and for applied magnetic fields 0 - 75 kG. The results indicate that, in the presence of magnetic field, $\sigma(\omega)$ remains overdamped, and the conductivity lost at low frequency due to the magnetoresistance is fully recovered in the high frequency limit. At both low and high frequencies, *the dielectric response is consistent with a magnetic-field-induced conversion of normal to CDW carriers*. Furthermore, the characteristic ac "crossover frequency" ω_{CO} increases with increasing H, whereas the dc threshold field E_T decreases with increasing H; *this suggests a possible breakdown in the conventional impurity pinning mechanism* which dictates the dc and ac responses.

Our experiments were performed on single crystals of $NbSe_3$ grown by conventional vapor-transport methods, with typical minimum threshold fields E_T = 30 mV/cm at 48 K. The crystals were mounted in a 2-probe configuration with silver paint contacts, and formed the termination of a micro-coaxial cable.[8] $\sigma(\omega)$ was measured parallel to the chain (b) axis, and the magnetic field H was applied perpendicular to b. Both the real and imaginary parts of $\sigma(\omega)$, $Re\sigma(\omega)$ and $Im\sigma(\omega)$, were determined by a computer-controlled network analyzer (HP 87454A), using an ac sinusoidal excitation amplitude more than two orders of magnitude smaller than E_T. Our experimental set-up allowed simultaneous measurement of the electric-field-dependent dc conductivity $\sigma_{dc}(E)$, and observation of the narrow band noise spectrum for $E > E_T$.

Fig. 3-4 shows $\sigma(\omega)$ for $NbSe_3$ at 25 K, both with and without an applied magnetic field. From the general behavior of $\sigma(\omega)$, it is apparent that the CDW continues to behave overdamped in the presence of a magnetic field. Important features of the data are found at the frequency extremes. In the low frequency limit there is a large magnetic-field-induced reduction in $Re\sigma$, consistent with the Ohmic dc magnetoresistance. In the high frequency limit, $Re\sigma$ becomes magnetic-field-independent, and both $Re\sigma(\omega,H=0)$ and $Re\sigma(\omega,H=75kG)$ appear to approach the same saturation value.[14] Simultaneous (pulsed) measurements of $\sigma_{dc}(E)$ confirmed that this saturation value corresponds to $\sigma_{dc}(E \rightarrow \infty)$, independent of H. The crossover frequency, ω_{co}, may be defined as that

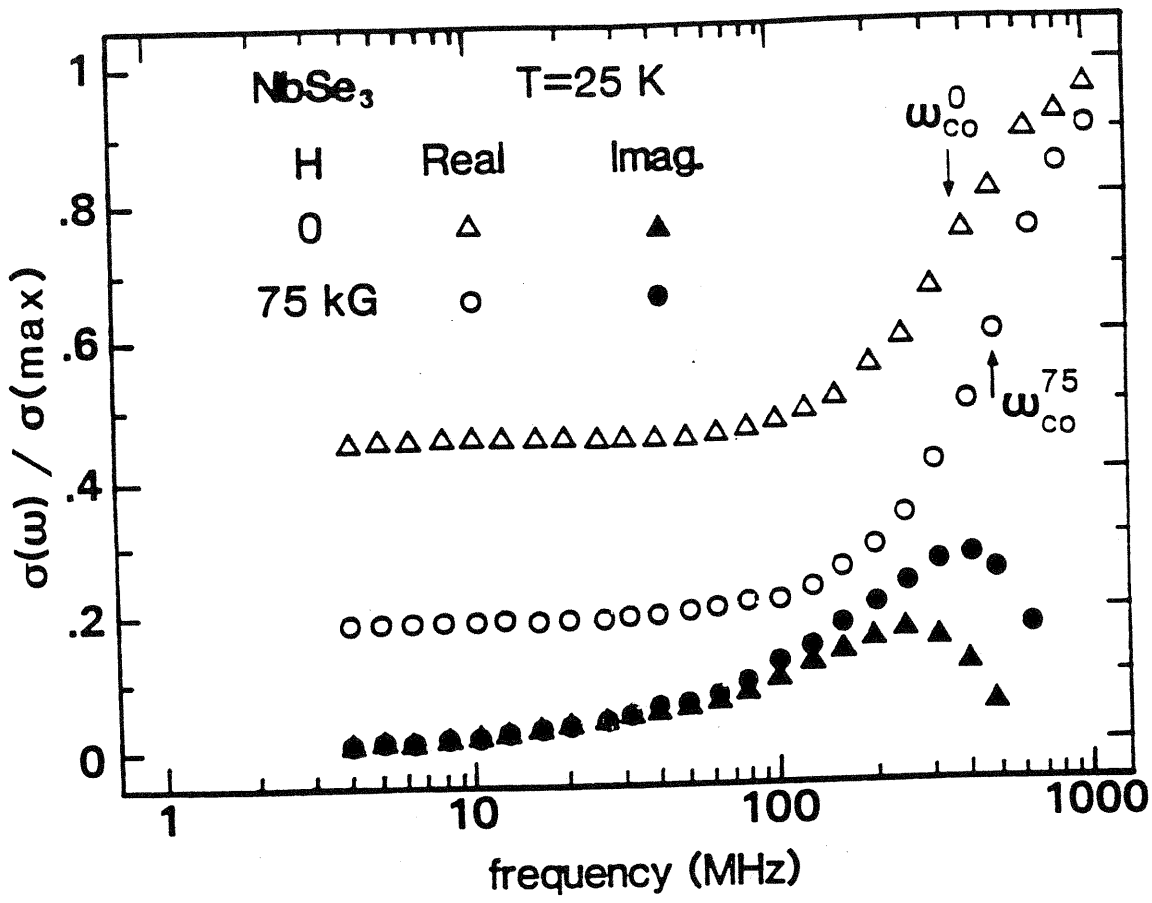

Fig. 3-4 Complex ac conductivity of $NbSe_3$ with and without a 75 kG magnetic field. The crossover frequencies are indicated by vertical arrows.

frequency for which $Re\sigma(\omega)$ has attained one half its maximum value. ω_{CO} is identified for the two data sets in Fig. 3-4. At 25 K, $\omega_{CO}(H=0)/2\pi$ = 350 MHz, while $\omega_{CO}(H=75kG)/2\pi$ = 480 MHz, an increase over the H = 0 value of approximately 37%. Fig. 3-4 shows that $Im\sigma(\omega)$ is also affected by application of a magnetic field. At low frequency no magnetic-field-induced change was detected (within our experimental resolution of $Im\sigma(\omega)/\omega = \pm$ 1pF) in $Im\sigma$, while at high frequency $Im\sigma(\omega, H=75kG)$ clearly exceeds $Im\sigma(\omega, H=0)$. At $\omega/2\pi$ = 300 MHz, for example, application of the H = 75 kG field increases $Im\sigma$ by a factor of 1.7. In addition, the peak in $Im\sigma$, which corresponds roughly to the crossover frequency in $Re\sigma$, increases with increasing H.

Experimental data such as that presented in Fig. 3-4 were obtained for the same $NbSe_3$ crystal at other temperatures in the lower CDW state. The same basic features described above were observed. Fig. 3-5 shows the characteristic crossover frequency extracted from such data, as a function of temperature. It is apparent that $\omega_{CO}(H=75kG)$ always exceeds $\omega_{CO}(H=0)$, with the relative increase becoming larger at lower temperature where the Ohmic magnetoresistance increases. Just below the transition temperature T_P = 59 K, no appreciable difference was found in ω_{CO} for H = 0 and H = 75 kG.

The main features of our experimental results appear consistent with a magnetic field induced conversion of normal to CDW carriers. At low frequencies, only the normal

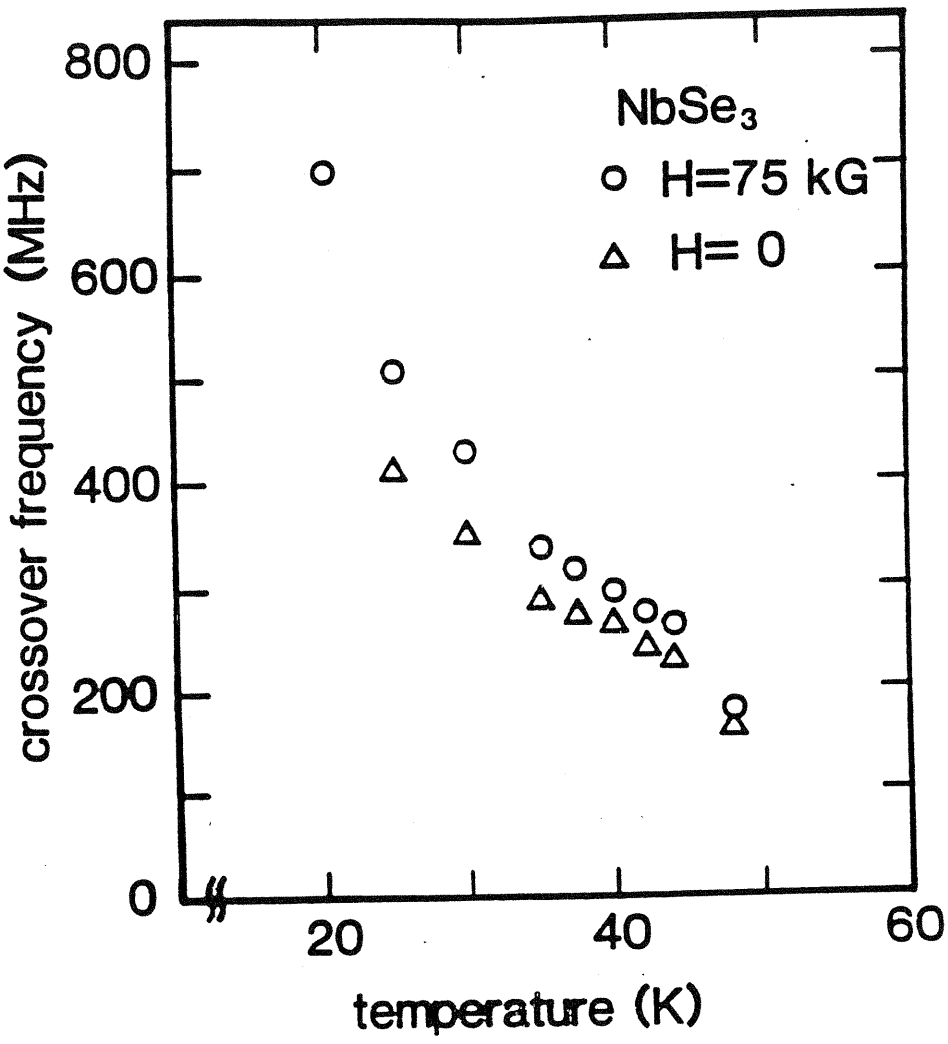

Fig. 3-5 Crossover frequency ω_{co} versus temperature in the lower CDW state of $NbSe_3$. At fixed temperature, a magnetic field increases ω_{co}

carriers contribute to Reσ, and, as observed in Fig. 3-4, Reσ is significantly reduced by application of a magnetic field. At high frequencies, Reσ has significant contributions from both CDW and normal carriers. Previous microwave and radio frequency studies[7,15] have shown that in $NbSe_3$ the high frequency conductivity attains a saturation maximum which corresponds to the (normal) conductivity expected in the absence of CDW formation. This indicates that, with H = 0, the CDW carriers have the same high frequency ac response as do the normal carriers, and the high frequency conductivity thus depends only on the total carrier concentration $n = n_n + n_c$, with n_n the normal carrier concentration and n_c the CDW carrier concentration. In Fig. 3-4, the high frequency conductivity Re$\sigma(\omega)$ is again observed to be equal to that expected in the absence of CDW formation (determined equivalently by extrapolating the Ohmic temperature dependent resistance from high temperature to low, or by direct measurement of the dc conductivity $\sigma_{dc}(E \rightarrow \infty)$), indicating a conserved total carrier concentration in the presence of H, and an insensitivity to H of the high frequency behavior of normal and CDW conduction states. For example, if the Ohmic dc magnetoresistance were strictly due to a normal carrier mobility effect (assumed frequency independent), then Re$\sigma(\omega,H=0)$ and Re$\sigma(\omega,H=75kG)$ in Fig. 3-4 would differ only by a frequency independent constant, in sharp contrast to the experimentally observed convergence in the data at high frequency.

A shift in carriers between normal and CDW states can also be inferred from $Im\sigma(\omega)$ in Fig.3-4. Normal electrons do not contribute to $Im\sigma$ in the frequency range here being considered (well below the metallic plasma frequency), and hence $Im\sigma$ is dominated by the contribution from CDW carriers. As seen in Fig. 3-4, $Im\sigma$ increases with increasing H, in particular near the ac crossover frequency. As discussed below, the low frequency behavior of $Im\sigma$ is also consistent with CDW carrier enhancement.

The increase in ω_{CO} with increasing H, as shown in Fig. 3-5, is in striking contrast to the observed decrease in E_T. We have carefully measured $E_T(H)$, for the same $NbSe_3$ crystal as was used for the data of Figs. 3-4 and 3-5, by applying a pulsed dc conductivity technique, and by observation of the onset of narrow band noise for applied steady state dc fields. For any given magnetic field, the two methods yielded identical values of E_T. The open circles in Fig. 3-6 show the ratio $E_T(H)/E_T(H=0)$ for $NbSe_3$ at selected magnetic field values and temperatures. For a given field H, the relative reduction in E_T becomes greater at lower temperature, consistent with previous studies.[6] Fig. 3-6 also contrasts the $E_T(H)$ behavior to that of $\omega_{CO}(H)$; the two parameters have dramatically opposite magnetic field dependences.

A number of models of CDW transport have been advanced, including rigid particle classical motion[1], quantum tunneling[16], and deformable medium theories based on the

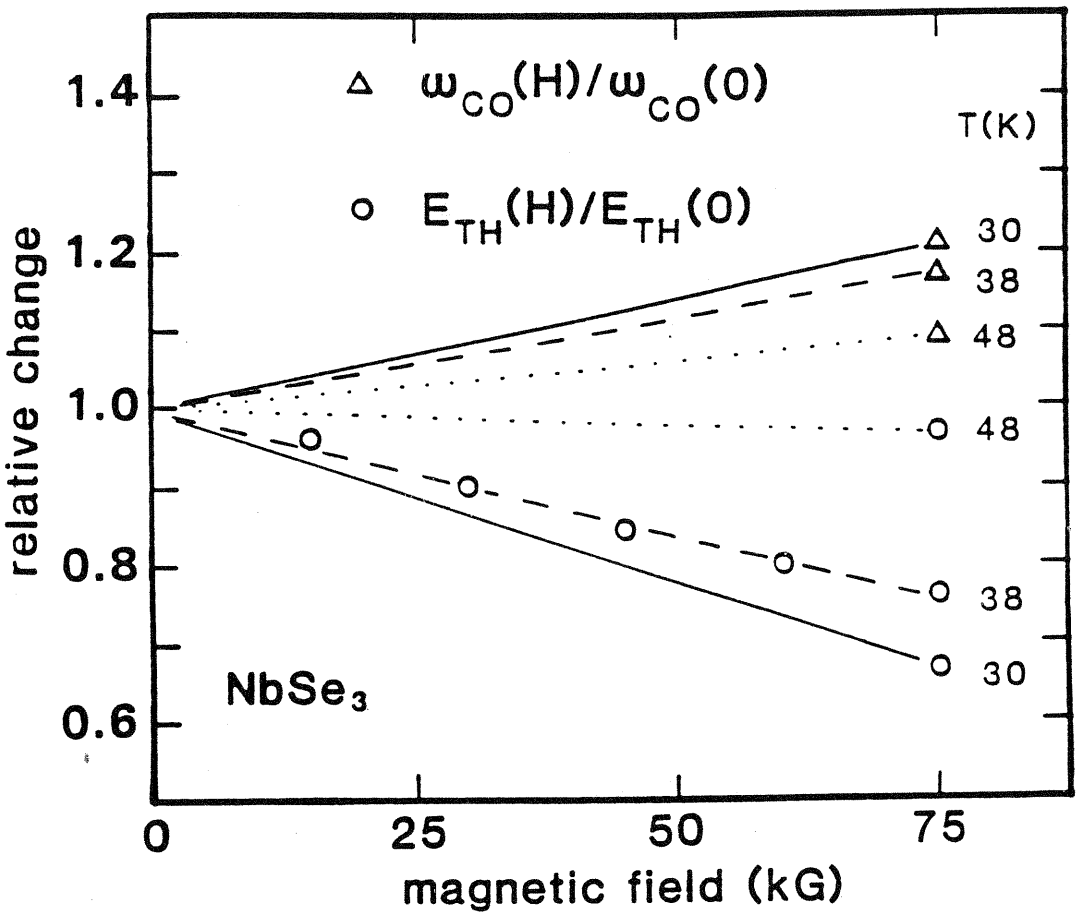

Fig. 3-6 Normalized crossover frequency and threshold electric field versus H in $NbSe_3$.

Fukuyama-Lee-Rice Hamiltonian[17]. In a very simple classical description set forth by Grüner, Zawadowski, and Chaikin[1], the CDW is treated as a charged rigid object in a periodic pinning potential. Although this model has some severe deficiencies, it allows us to readily identify important magnetic-field-dependent CDW parameters. In the model, the limiting dc conductivity of the CDW condensate is given by $\sigma_{dc,CDW}(E \rightarrow \infty) = n_c e^2 \tau_c / m^*$, while the ac conductivity is

$$Re\sigma_{CDW}(\omega) = (n_c e^2 \tau_c / m^*)[1 + (\omega_o^2 \tau_c / \omega)^2]^{-1} \qquad (3\text{-}5)$$

$$Im\sigma_{CDW}(\omega) = (n_c e^2 \tau_c / m^*)(\omega_o^2 \tau_c / \omega)[1 + (\omega_o^2 \tau_c / \omega)^2]^{-1} \qquad (3\text{-}6)$$

where τ_c is the CDW characteristic scattering time, m^* is the effective mass of electrons condensed in the CDW state, and ω_o is the CDW pinning frequency. $\omega_o^2 \tau_c$ is identified with the ac crossover frequency. We assume the total sample conductivity to be given by $\sigma_{tot} = \sigma_{CDW} + \sigma_{normal}$, where σ_{normal} represents the contribution of the normal carriers. Allowing for normal to condensed carrier conversion, the independence of σ_{tot} on H in the high frequency or high electric field limit implies

$$[n_c e^2 \tau_c / m^*] + [n_n e^2 \tau_n / m] = n e^2 \tau_n / m = \text{constant},$$

where "constant" here means a magnetic-field-independent quantity. With τ_n/m and n independent of H, we find

$$\tau_c/m^* = \tau_n/m = \text{constant},$$

independent of H.

In the low frequency limit, Eqn. (3-6) yields a dielectric constant

$$\varepsilon = 4\pi \mathrm{Im}\sigma(\omega)/\omega = 4\pi n_c e^2/m^*\omega_o^2. \qquad (3\text{-}7)$$

Experimentally, we find no magnetic field effect on the very low frequency dielectric constant, hence $\omega_o^2 m^* \propto n_c$, or, equivalently, $m^*/\tau_c \propto n_c/\omega_o^2\tau_c$. With constant m^*/τ_c, and the experimentally determined ratio

$$\omega_o^2\tau_c(H=75kG)/\omega_o^2\tau_c(H=0) = 1.2$$

(measured at T = 30K), we find

$$n_c(H=75kG)/n_c(H=0) = 1.2$$

at T = 30 K. This magnetic-field-induced increase in CDW carrier concentration is in agreement with that determined from previous magnetoresistance studies[10,18] but is in disagreement with narrow-band noise studies.[10]

The above analysis unfortunately does not allow independent determination of $m^*(H)$, $\tau_c(H)$, and $\omega_o(H)$. In Bardeen's tunneling theory[16], the dc and ac conductivities scale over a wide range of electric field and frequency, such that $\omega = 2\pi e^*\Lambda E/h$, with $e^*/e \approx m/m^*$ and Λ a CDW correlation length. Although the ac and dc conductivities for the $NbSe_3$ sample used for Fig. 3-4 did not show excellent scaling between $\sigma_{dc}(E)$ and $Re\sigma(\omega)$ at all temperatures investigated in the lower CDW state (although proper scaling was observed at selected temperatures), a rough correspondence between E and ω could always be established by matching $Re\sigma(\omega)$ at the crossover frequency to $\sigma_{dc}(E \rightarrow \infty)/2$, both with and without applied magnetic field. At T = 30K, ω/E was found to correspond to 3.0 MHz/mV (H = 0), and ω/E = 3.1 MHz/mV (H = 75 kG). Assuming Λ to be magnetic-field-independent, this leads to $m^*(H=75kG)/m^*(H=0) = 0.97$. This implies that a magnetic field does not appreciably change m^* (or τ_c), and hence the magnetic-field-induced increase in $\omega_{co} = \omega_o^2\tau_c$ is primarily due to to an effective increase in ω_o, the CDW pinning frequency.

The increase in ω_o with increasing H is in sharp contrast to the observed decrease in E_T with increasing H. Rigid particle, tunneling, and elastic medium models based on impurity pinning all predict that the ac and dc behaviors go hand in hand. For example, increases in impurity concentration generated by chemical doping or sample irradiation are predicted[19] to increase both ω_o and E_T, and

indeed this is observed experimentally in $NbSe_3$ and TaS_3[19,20]. In the context of impurity pinning (which clearly dominates at H = 0), our results would suggest that application of a magnetic field effectively reduces "dc impurity pinning" but enhances "ac impurity pinning". We therefore conclude that important magnetic-field-sensitive interactions, previously ignored by CDW theories, come into play when a magnetic field is present in $NbSe_3$. Such an effect could have its origin in interactions between CDW carriers and normal electrons, or unusual CDW-phonon scattering at intermediate frequencies. Indeed, recent work on $NbSe_3$, TaS_3, and $K_{0.3}MoO_3$ have shown important couplings between the limiting CDW and normal carrier conductivities[21]. Whether these effects are related to the magnetic field phenomena reported here remains to be seen.

Finally, we remark that the only theory which discusses the anomalous magnetoresistance effects in $NbSe_3$, that of Balseiro and Falicov[22], does not address the dynamics of the CDW condensate. An extension of this theory, which incorporates condensate magnetodynamics, may help clarify the role of impurity pinning in the presence of applied magnetic fields.

Discussion

The original intention of investigating the transport properties of $NbSe_3$ in a magnetic field was to discover a common cause of the unusual effects seen in this material.

Having presented the results of the various experiments, it is now appropriate to discuss and compare these results with respect to the current theories. In particular, we were looking for evidence of a magnetic-field-induced carrier conversion being responsible for the changes in the transport properties with magnetic field. The overall picture does not reveal unambiguous evidence that MFICC occurs although many of the experiments are consistent with MFICC and so it can not be ruled out. Furthermore, some of the experiments show an effect of the magnetic field on the pinning of the CDW and so raises the questions: 1) Through what mechanism does the magnetic field act on the CDW pinning? and 2) Can this mechanism also affect the transport properties? We will first discuss the various evidence for MFICC.

The most straightforward evidence comes from the conductivity versus electric field and conductivity versus frequency data. In both cases, the low frequency or low electric field conductivities decrease with increasing magnetic field, while the high frequency or high electric field conductivities are independent of magnetic field. Since the former is sensitive to the concentration of normal carriers and the latter is sensitive to the total concentration of carriers, this is consistent with the number of normal carriers decreasing with increasing magnetic field.

The Hall effect and the thermoelectric power do not provide as neat a picture. In the high-magnetic-field limit, they both agree that an increasing magnetic field cause the

material to appear more hole-like, i.e., the TEP and Hall resistance become more positive. Taken by itself, this fact might suggest that the electron-like states are being converted to the CDW and thus leave the hole-like states less compensated. However, this scenario is not consistent with the low-magnetic-field limit of the Hall effect which shows rapid decreases in the Hall constant at both CDW transitions implying that the CDW's are formed from hole-like states and not the electron-like states.

In the attempt to study the CDW concentration n_c through the narrow-band noise characteristics [Eqn. (3-1)], it was discovered that the measured NBN characteristics I_{CDW}/f did not accurately track n_c and so this method cannot be used unambiguously to study n_c until it is better understood. There are two possibilities; either Eqn. (3-1) is not the correct relationship between I_{CDW} and f, or the experimental technique used to measure and calculate I_{CDW} is flawed.

A possible flaw is in the measurement of the sample voltage when the CDW is moving. The technique used by Tritt et al.[10] and Tessema et al.[11] involves painting 4 silver contacts on the sample; the 2 current contacts are located at the ends of the sample while the 2 voltage contacts are located slightly in from the ends. The inner contacts would short out the electric fields in the $NbSe_3$ beneath these contacts and the CDW would very likely be pinned there. Other parts of the CDW would be sliding and an interface between sliding and pinned CDW's would form to handle the

conversion between CDW current and normal current. This region is known as a phase-slip center [PSC]. There is evidence suggesting that across PSC's there is a voltage drop associated with the current conversion process. The evidence includes measurements of the threshold field E_T as a function of sample length.[4,23] E_T diverges as the length goes to zero; this is consistent with the threshold field consisting of two parts:

$$E_T = E_{TB} + V_C/L \tag{3-8}$$

where L is the sample length, E_T (= V_S/L; V_S = sample voltage) is the experimentally measured threshold field, E_{TB} is the threshold field due to the bulk of the material, and V_C is the voltage needed to convert carriers at the contacts. This extra voltage drop would cause the measurement of I_{CDW} to be underestimated:

$$I^M_{CDW} = I_{tot} - \frac{V_s}{R_o(H,T)} = I_{CDW} - \frac{V_c}{R_o(H,T)} \tag{3-9}$$

where the M superscript refers to the measured CDW current. As the temperature decreases, R_o decreases and the error increases; furthermore, as the magnetic field increases, R_o increases, the error decreases, and an enhanced I/f ratio is observed. If V_C is constant, then the above description of

the measured I_{CDW} would qualitatively fit the results of Tessema et al. However, the temperature and magnetic field dependence of V_c is not known and could be a significant factor in Eqn. (3-9). The experimental technique could be improved by using non-perturbative voltage contacts instead of silver paint (see Appendix B).

The other possibility to explain the results of the I_{CDW}/f studies is that Eqn (3-1) is not correct (at least in the low temperature regime). Only with the results of Tessema et al.[11] has this relationship been brought into question and further investigation has been initiated. As mentioned earlier, the initial approach will be to focus on the possible role of the CDW pinning in the relationship between I_{CDW} and the NBN frequency f as a function of temperature and magnetic field.[12]

The importance of CDW pinning in the H-field effects in $NbSe_3$ is demonstrated in the ac and dc conductivity experiments as well. In the dc experiments, the threshold field is reduced at low temperatures as H increases[24] while the ac experiments show an increase in pinning frequency ω_o.[25] In the CDW theories, these two quantities are expected to track each other; this is in direct contrast to the empirical reality which shows they diverge as H increases. Understanding this 'breakdown' in the theories might be crucial to the understanding of the magnetic field effects in this system. Unfortunately, there has been very little theoretical guidance in understanding the magnetic

interaction with the dynamics of the CDW. More experiments are needed to give a detailed account of this effect so that a theory can be developed.

Conclusion

In conclusion, we find that while there are indications that magnetic-field-induced carrier conversion is occurring, there is no overwhelming proof. The question can best be answered by an experiment to measure the X-ray intensity of the superlattice spots as a function of magnetic field. Additionally, the above experiments show that there are large magnetic effects on the CDW pinning. These effects are not well understood and additional theoretical and experimental work is needed to rectify this. Only then will a clear picture emerge on the magnetic field interactions in $NbSe_3$.

[1]G. Grüner, A. Zawadowski, and P.M. Chaikin, *Phys. Rev. Lett.* **46**, 511 (1981).

[2]P. Monceau, J. Richard, and M. Renard, *Phys. Rev. Lett.* **45**, 43 (1980).

[3]J. Bardeen, E. Ben-Jacob, A. Zettl, and G. Grüner, *Phys. Rev. Lett.* **49**, 493 (1982).

[4]A. Zettl and G. Grüner, *Phys. Rev. B* **29**, 755 (1984).

[5]P. A. Lee and T. M. Rice, *Phys. Rev. B* **19**, 3970 (1979). This result supersedes earlier derivations which show $n_c \approx \Delta^2$ near T_P [see, for example, D. Allender, J. W. Bray, and J. Bardeen, *Phys. Rev. B* **9**, 119 (1974), and M. J. Rice, in *Low-Dimensional Cooperative Phenomena*, edited by H. J. Keller (Plenum, New York, 1974), p.23]. The discrepancy is discussed by Lee and Rice.

[6]R.V. Coleman, G. Eiserman, M.P. Everson, A. Johnson, and L.M. Falicov, *Phys. Rev. Lett.* **55**, 863 (1985).

[7]N. P. Ong and P. Monceau, *Phys. Rev. B* **16**, 3443 (1977).

[8]See Appendix B.

[9]P. Monceau, J. Richard, and O. Laborde, *Synth. Met.* **19**, 801 (1987);

J. Richard, P. Monceau, and M. Renard, *Phys. Rev.* B **35**, 4533 (1987).

[10]T. M. Tritt, D. J. Gillespie, A. C. Ehrlich, and G. X. Tessema, *Phys. Rev. Lett.* **61**, 1776 (1988).

[11]G. X. Tessema, J. Richard, Chen, and P. Monceau, *Bull. Amer. Phys. Soc.* **34**, 884 (1989).

[12]G. X. Tessema private communication.

[13]R. M. Fleming, D. E. Moncton, and D. B. McWhan, *Phys. Rev. B* **18**, 5560 (1978).

[14]Strictly speaking, the ac conductivity does not saturate at high (1-10 GHz) frequency, but rather reaches a broad maximum corresponding to $\sigma_{dc}(E\text{--}> \infty)$. At higher (30-100 GHz) frequency, inertial effects lead to a decreasing $Re\sigma(\omega)$ with increasing w. See S. Shridar, D. Reagor, and G. Grüner, *Phys. Rev. Lett.* **55**, 1196 (1985).

[15]G. Grüner, L.C. Tippie, J. Sanny, W.G. Clark, and N.P. Ong, *Phys. Rev. Lett.* **45**, 935 (1980).

[16]J. Bardeen, *Phys. Rev. Lett.* **45**, 1978 (1980);
see also G. Grüner, A. Zettl, W. G. Clark, and J. Bardeen, *Phys. Rev. B* **24**, 7274 (1981).

[17]H. Fukuyama and P.A. Lee, *Phys. Rev. B* **17**, 545 (1978);
P.A. Lee and T.M. Rice, *Phys. Rev. B* **19**, 3970 (1979);
L. Sneddon, M.C. Cross, and D.S. Fisher, *Phys. Rev. Lett.* **49**, 292 (1982).

[18]P. Parilla, M.F. Hundley, and A. Zettl, *Phys. Rev. Lett.* **57**, 619 (1986).

[19]Wei-yu Wu, A. Jánossy, and G. Grüner, *Solid State Commun.* **49**, 1013 (1984).

[20]W.W. Fuller, G. Grüner, P.M. Chaikin, and N.P. Ong, *Phys. Rev. B* **23**, 6259 (1981);
G. Mihály, L. Mihály, and H. Mutka, *Solid State Commun.* **49**, 1009 (1984).

[21]X.J. Zhang and N.P. Ong, *Phys. Rev. Lett.* **55**, 2919 (1986);
N.P. Ong and X.J. Zhang (to be published);
R.M. Fleming, R.J. Cava, L.F. Schneemeyer, E.A. Rietman, and R.G. Dunn, (to be published).

[22]C. A. Balseiro and L. M. Falicov, *Phys. Rev. Lett.* **55**, 2336 (1985);
C. A. Balseiro and L. M. Falicov, *Phys. Rev. B* **34**, 863 (1986).

[23]J. C. Gill, *Solid State Commun.* **44**, 1041 (1982).

[24]R. V. Coleman, M. P. Everson, G. Eiserman, and A. Johnson, *Phys. Rev.* B **32**, 537 (1985).

[25]M. F. Hundley, P. Parilla, and A. Zettl, *Phys. Rev. B* **34**, 5970 (1986).

Chapter 4

Magnetoresistance and Piezoresistance

Introduction

Similar to the anomalous magnetoresistance discussed above, there is another anomaly in the resistance in the lower CDW state of $NbSe_3$ if the crystal is longitudinally stressed along the chain axis. In a very careful and complete set of stress and resistance measurements, Lear et al.[1] showed that applied stress greatly enhances the magnitude of only the lower CDW state resistance anomaly. Stress was also found to decrease the temperature of both CDW transitions. The data from Lear et al. are reproduced in figure 4-1. Notice the similarity between the effect of a magnetic field and uniaxial stress on the lower CDW resistive anomaly (compare with figure 2-1). Although it is clear that the effects of stress and magnetic field are not equivalent in $NbSe_3$ (Stress changes the transition temperature while the magnetic field gives little or no change.), one can ask if they affect the CDW system in similar ways. This question is addressed in this series of experiments.

We have performed magnetoresistance measurements on $NbSe_3$ under uniaxial stress and find that a large stress greatly reduces the magnetoresistance. Similarly, a large magnetic field reduces the effect of stress on the

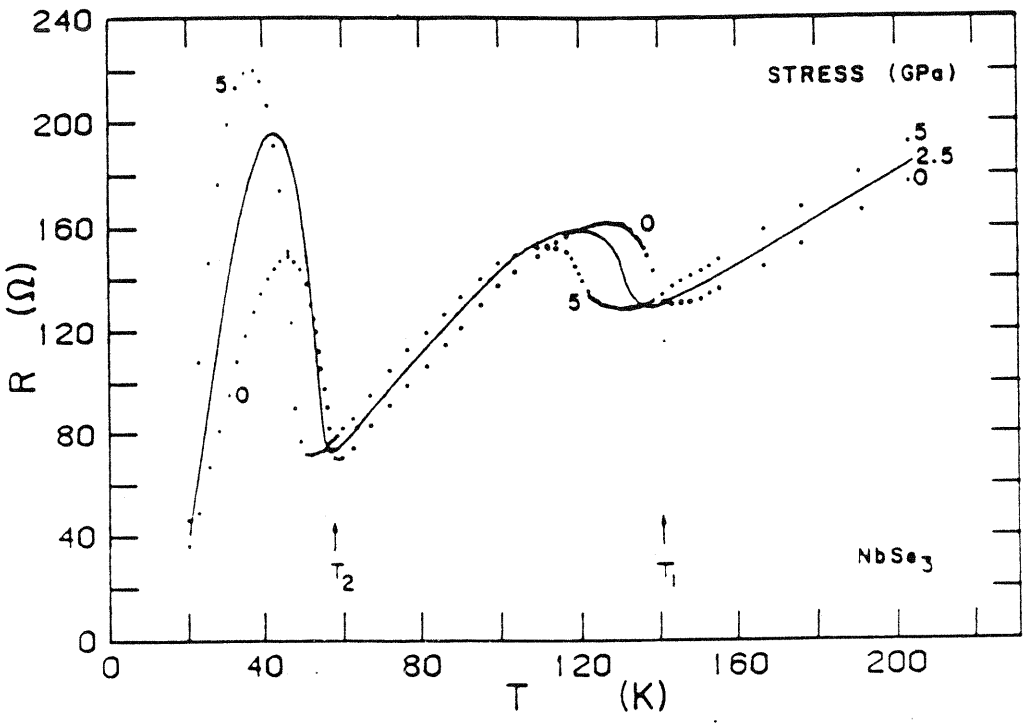

Fig. 4-1 Resistance of a $NbSe_3$ sample as a function of temperature with stress as a parameter. Note the enhancement of the resistive anomaly in the lower CDW state with stress and the shift of the transitions temperatures of both CDW's. (From Lear et al.)

resistance. The results are consistent with the magnetic field and uniaxial stress acting on similar portions of the Fermi surface.

Experimental set-up

Single crystals of $NbSe_3$ were mounted in a four-probe contact configuration using silver paint and one mil gold wires. In addition, a cyanoacrylate glue was applied over all the contacts to prevent the sample from breaking free under stress; thus the portion of the sample under stress was between the voltage contacts. The experimental setup allowed stress to be applied while the sample was in a magnetic field oriented perpendicular to the chain (b) axis of the crystal. A 200 Hz low-level AC current was applied to the sample and the resistance was measured using a lock-in with a resistance bridge. The stretching apparatus consists of a differential-screw micrometer connecting a stainless-steel rod to a sapphire block via a lever arm. Another sapphire block is fixed in close proximity to the first and the sample is mounted between the two blocks. The lever arm is needed to translate the motion of the micrometer into a motion perpendicular to the magnetic field which then gives the desired orientation of the crystal to the field (see Fig. 4-2). When the temperature of the apparatus was changed, the samples were bowed with the stretcher in order to prevent damage to the crystal due to thermal contraction. At the temperature where measurements were made, the zero of strain

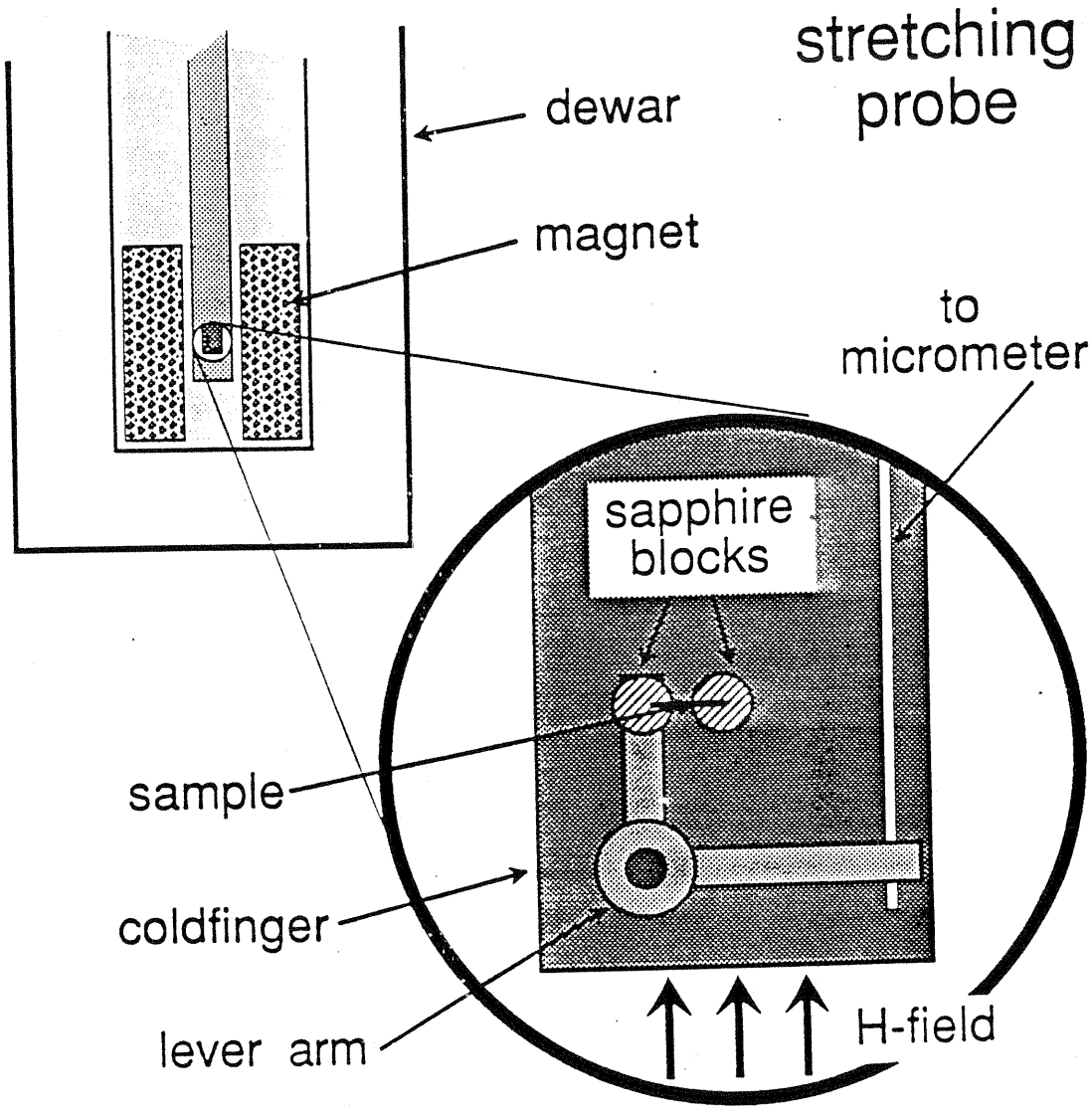

Fig. 4-2 shows the basic operating configuration of the stretching probe which allowed simultaneous application of stress along the chain direction and a magnetic field perpendicular to the chain direction.

was taken to be at the micrometer reading where a resistance change was first detected. Thus, the apparatus allowed a given strain to be applied and the stress was calculated from the previously measured Young's modulus[2] and resistance studies[1].

Results

Figure 4-3 shows typical resistance versus stress curves at various magnetic fields for sample #1. The lower curve was made with no magnetic field applied while the upper two curves had fields of 37.5 kG and 75 kG respectively. The curves have not been shifted with respect to one another; their displacement results solely from the magnetoresistance. The data here clearly demonstrate that as the magnetic field increases, the change of the resistance due to stress decreases; there is little stress dependence on the resistance in the presence of a large magnetic field.

Similarly, figure 4-4 shows resistance versus magnetic field at various stress for sample #2. Again, the curves have not been shifted with respect to each other; the displacement is caused by the resistance change due to the applied stress. As the field increases, the slope of the curves also increase; however, at a given strength of the magnetic field, the slope of curves with less stress is always greater than or equal to the slope of curves with more applied stress. As a result, the net change in the resistance due to magnetic field is less when stress is

applied compared to that of no stress: Stress eliminates additional magnetoresistance.

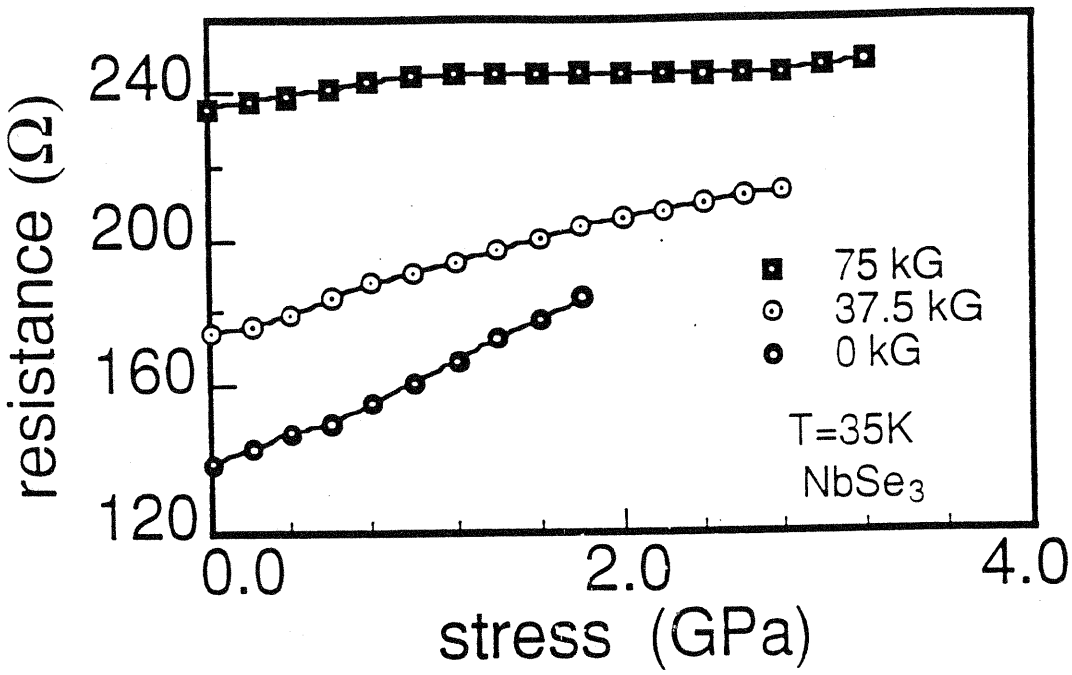

Fig. 4-3 Resistance versus the applied stress at various magnetic fields. As the field increases, the resistance change due to stress decreases. The curves have not been shifted with respect to one another.

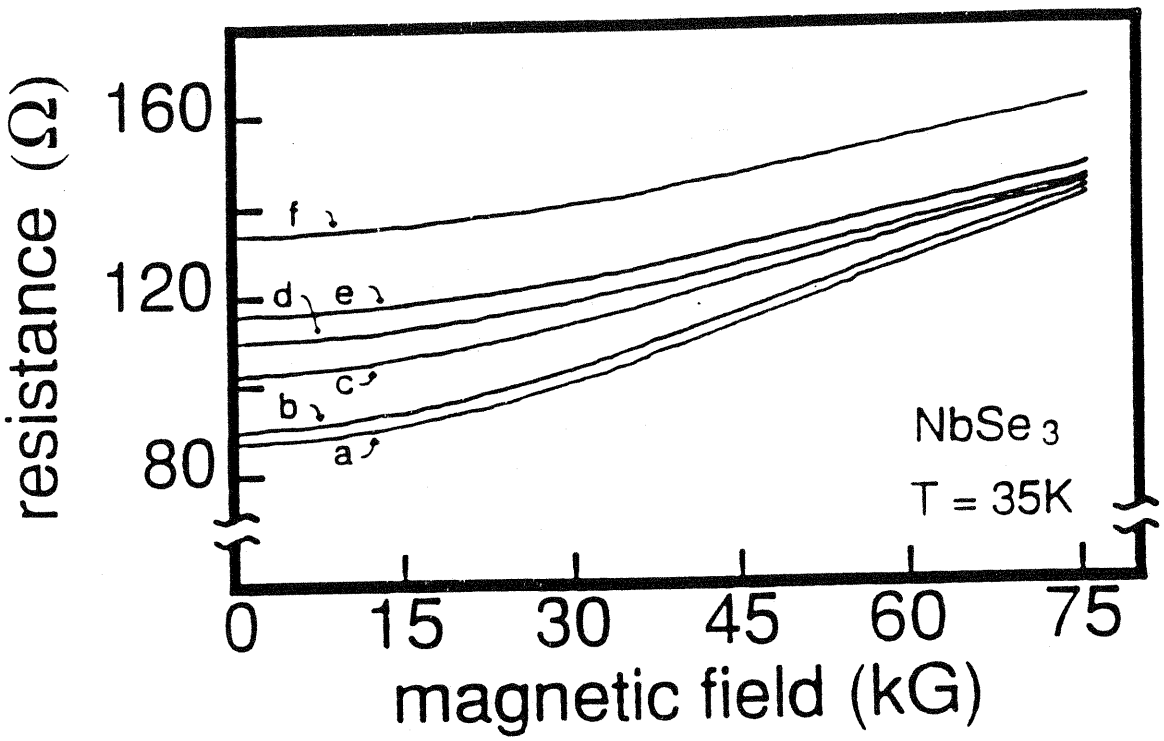

Fig. 4-4 Resistance versus magnetic field at various stresses: a) 0 GPa, b) 0.2 GPa, c) 1.1 GPa, d) 1.6 GPa, e) 2.0 GPa, and f) 3.1 GPa. The magneto-resistive increase is less when stress is applied. The curves have not been shifted with respect to one another.

Discussion

Longitudinal stress causes two actions: elongation along the chain direction and contraction transverse to the chains. Lear et al.[1] have estimated the Poisson ratio and found there to be significant transverse contraction. As mentioned previously, uniaxial stress lowers both the CDW transition temperatures in $NbSe_3$, while enhancing the lower CDW resistive anomaly. In comparison, hydrostatic pressure also lowers the transition temperatures, but inhibits the lower CDW resistive anomaly[3]. Eventually with increasing hydrostatic pressure, the CDW transition is suppressed at $\approx$ 6 kbar; under this pressure the specimen becomes superconducting at $\approx$ 3 K[(4)]. Pressure decreases the amplitude of the CDW gap and the number of condensed carriers[5]. Apparently, the interchain coupling dominates in affecting the transition temperature and the intrachain coupling affects the resistive anomaly.

The above data show that the effects of magnetic field and stress on $NbSe_3$ in the lower CDW state are interrelated. The exact nature of this interrelationship still remains unclear. As was mentioned in the previous chapter, there exists evidence suggesting that the magnetic field induces a carrier conversion from the normal to the CDW state. If stress caused a similar action, then the application of stress would give a smaller magnetoresistance since there would be less normal carriers available for conversion. By

assuming that stress and the magnetic field do indeed convert carriers, one can estimate the magnitude of CDW carrier concentration (n_c) conversion by the change in the Ohmic resistance.[6] Data shown in figure 4-3 were used to calculate the effect that the magnetic field (H) has on stress-induced conversion while data illustrated in Fig. 4-4 give the effect stress (σ) has on magnetic field carrier conversion. The unperturbed CDW carrier concentration will be estimated as $n_c \approx 10^{21}$ carriers/cm^3. The value for magnetic field carrier conversion at zero stress is then $dn_c/dH = 3.5 \times 10^{18}$ carriers/cm^3-kG and is in good agreement with previous studies[7,8]. With application of stress, this value is reduced by 40% at σ = 1.6 GPa and by 66% at σ = 3.1 GPa. Similarly, the zero magnetic field value for $dn_c/d\sigma$ ($\approx 9 \times 10^{19}$ carriers/cm^3-GPa) is reduced by 66% at 37.5 kG and by 89% at 75 kG.

It would be extremely interesting if, by the action of stress or magnetic field on $NbSe_3$, the sample became completely insulating due to complete destruction of the Fermi surface. A study could then be made on the importance of the degree of nesting of the Fermi surface on the properties of the CDW and the effect the presence of free carriers has on the CDW system. From the above estimates, it would seem that the application of a magnetic field is the more appropriate method in attempting to induce a metal-insulator transition. This is not surprising since stress lowers the CDW transition temperature (T_{P2}) and the resulting

increase in the normalized temperature (T/T_{P2}) inhibits the effectiveness of stress on the CDW system; furthermore, the maximum stress allowed is limited by the mechanical strength of the sample. The effect of the magnetic field is not limited in these ways. In fact, it could be speculated that the increased normalized temperature caused by stress is partly responsible for the effect on the magnetic field carrier conversion which is highly temperature dependent[7,8,9].

Conclusion

Previous resistance versus temperature data suggested that uniaxial stress and magnetic field affect the lower CDW state in $NbSe_3$ in similar ways. This suggestion is strengthened by the resistance studies presented here which show that the effects of uniaxial stress and magnetic fields are interrelated. The nature of this relationship remains unknown. Similar experiments to those proposed for the magnetic field investigation could be useful in determining the interrelationship between the two. However, the additional complication of applying strain (as well as high magnetic field and at low temperatures) makes these experiments difficult. As was the case for the magnetic field effects alone, the definitive experiment is the measurement of the X-ray superlattice spot intensity as a function of stress and magnetic field.

[1]R. S. Lear, M.J. Skove, E.P. Stillwell, and J. W. Brill, *Phys. Rev. B* **29**, 5656 (1984).

[2]J. W. Brill, *Mol. Cryst. Liq. Cryst.* **81**, 107 (1982).

[3]J. Chaussy, P. Haen, J. C. Lasjaunias, P. Monceau, G. Waysand, A. Waintal, A. Meerschaut, P. Molinié, and J. Rouxel, *Solid State Comm.* **20**, 759 (1976).

[4]A. Briggs, P. Monceau, M. Nunez-Regueiro, J. Peyrard, M. Ribault, and J. Richard, *J. Phys. C* **13**, 2117 (1980).

[5]J. Richard and P. Monceau, *Solid State Comm.* **33**, 635 (1980).

[6]Using the technique outlined by Eqn. (3-3).

[7]P. Parilla, M. F. Hundley, and A. Zettl, *Phys. Rev. Lett.* **57**, 619 (1986).

[8]M. F. Hundley, P. Parilla, and A. Zettl, *Phys. Rev. B* **34**, 5970 (1986).

[9]M. F. Hundley and A. Zettl, *Solid State Comm.* **61**, 587 (1987).

The Effect of a Temperature Gradient on a Sliding CDW

Chapter 5

Experiments on Sliding CDW's in an Applied Temperature Gradient

Introduction

By far the most dramatic and obvious effect that a temperature gradient induces in a crystal with a sliding CDW is the splitting of the narrow-band noise (NBN) peaks.[1,2] Given that the NBN frequency is proportional to the CDW velocity[3], this implies that the crystal divides into sections each with a CDW moving at a distinct velocity. We refer to these sections as *CDW velocity sub-domains*. Initially, the focus of temperature gradient studies by others concerned the origin of the NBN; subsequently, as the evidence became more clear, the investigations focused on how the moving CDW can break into multiple sub-domains. The evidence shows that the sub-domains tend to be arranged serially along the chain axis and that each sub-domain acts, in many respects, independently of the other sub-domains.[2,4,5] The purpose of this series of experiments is to investigate, in detail, the behavior of a sliding CDW in the presence of a temperature gradient.

It is first appropriate to define and illustrate the concepts which we use in this investigation. We use the term *sub-domain configuration* to refer to the CDW velocity profile

of the entire sample. The characteristics of primary concern are the number of sub-domains and the values of the average velocities of these sub-domains; for a more complete description, the location and size of the sub-domains need to be specified also. These characteristics can all be time-dependent and, of course, depend on the externally-controlled parameters (temperature, temperature gradient, bias current, etc.). CDW phase slip processes must occur between the sub-domains to handle the CDW velocity discontinuity there and we refer to these as phase slip centers (PSC). The concept of a sub-domain configuration at a given instant in time is illustrated in Fig. 5-1.

A similar concept is the *NBN configuration* which is defined here to be the total NBN spectrum at a given instant in time. The concept of a spectrum varying with time is not compatible with a strict Fourier representation of the signal. Instead, one must use the concept of instantaneous frequency and instantaneous amplitude of an oscillator.[6] During an experiment, this instantaneous spectrum is approximated by taking a truncated Fourier transform (by analog or digital means). The sample consists of a small number of sub-domains, each of which is viewed as having an oscillator with instantaneous frequency and amplitude. The NBN configuration is expected to parallel the sub-domain configuration closely but the relationship is <u>not</u> one-to-one.

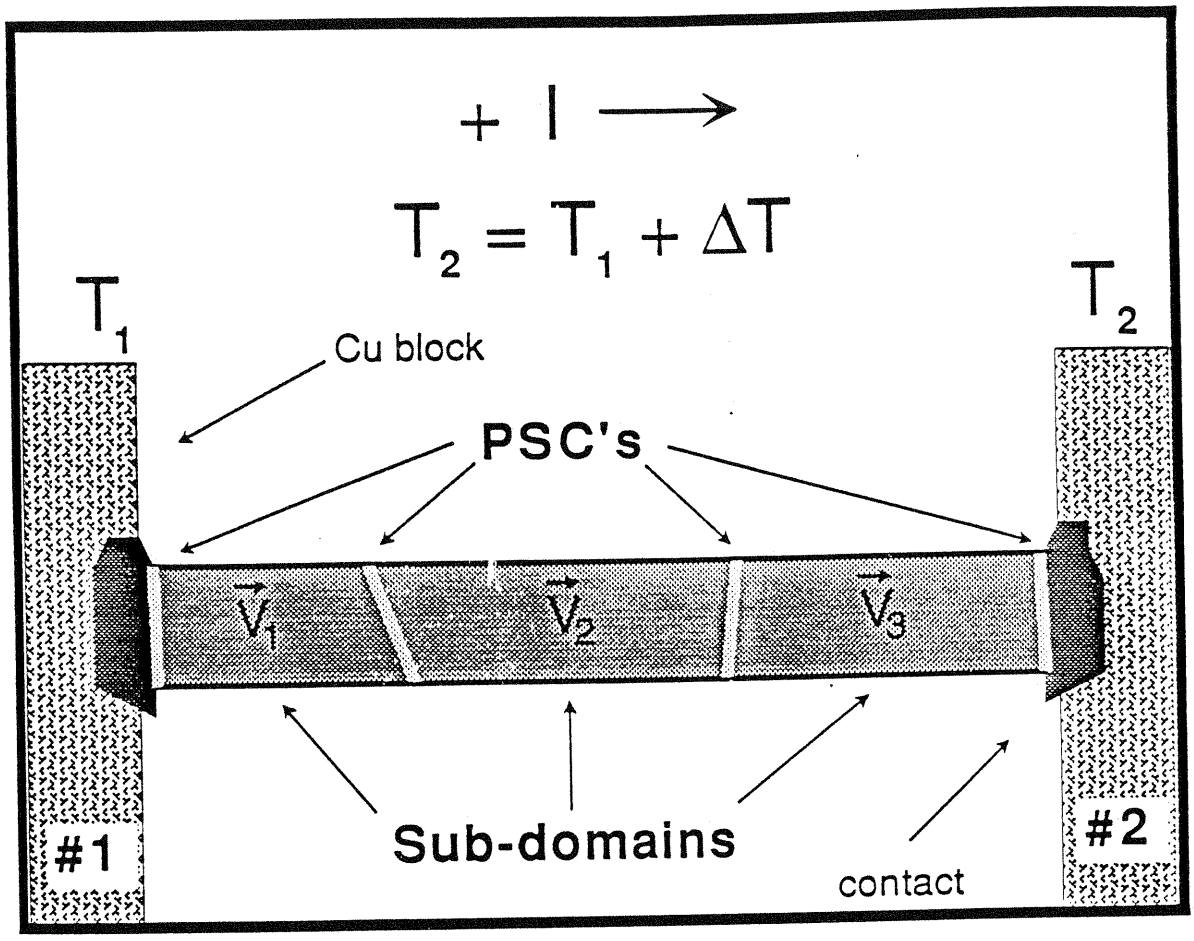

Fig. 5-1 illustrates an idealized sample with a sliding CDW whose sub-domain configuration consists of four phase slip centers (PSC). Two PSC's occur at the contacts while two occur within the sample and divide the CDW into three sub-domains. The CDW in each of the sub-domains move at unique velocities. The convention for the signs of the current I and the temperature difference across the sample ΔT are shown at the top of the figure.

There are also practical problems in detecting the NBN configuration which can lead to misinterpreting the sub-domain configuration. Two examples of misinterpretation are as follows. The first is the case where the NBN amplitude of a sub-domain falls below the background noise; the sub-domain is then not detectable even though it exists. The second concerns the case where two sub-domains have a frequency difference smaller than the frequency resolution of the experimental apparatus; the two domains are then misinterpreted as one. This latter case does not cause any serious difficulties in these experiments since as the temperature gradient increases, the difference between the NBN frequencies also increases and there will always come a point where the two frequencies are resolvable. The former case also appears not to pose much of a problem. Experience has shown that the NBN signal only falls below the background noise over relatively short time periods (< 1 msec).[7] While it is very important to consider such effects in experiments on short time scales, the time scale of the the experiments described in this chapter is several seconds, if not minutes. However, samples with no detectable NBN, but with evidence of CDW motion, have been seen.[8] The lack of NBN in these cases can be attributed to the large volume of the sample, inhomogeneous current distribution, or poor sample quality. None of these conditions apply here and all samples showed good quality NBN under isothermal conditions. Therefore, we will assume that the NBN configuration accurately represents

the sub-domain configuration in that it provides the number and velocities of the sub-domains.

The experiments reveal that sub-domains have a rich and complicated behavior. Some of these characteristics can be easily described in a quantitative manner, while others can not. This chapter is divided into three parts. The first part describes the experimental set-up and method. We report the qualitative observations in the second part; this is necessary in order to appreciate the full behavior associated with this phenomenon. The third part discusses the analysis of those characteristics which lend themselves to be quantified.

I. Experimental Set-up and Method

Our experiments employed single $NbSe_3$ crystals grown by traditional vapor transport methods. Quantitative measurements were made on three different samples whose lengths were 0.9, 1.6, and 1.3 mm (corresponding to samples #1, #2, and #3 respectively). For these measurements, only samples displaying a single clean NBN peak (and its harmonics) under isothermal conditions and split NBN peaks in a temperature gradient are used; others are rejected.[9] Qualitative observations are made on these samples as well as others. Samples are mounted with silver paint in a two-probe configuration between two copper blocks which served as both electrical contacts and thermal anchors. The copper blocks are thermally isolated from the coldfinger and each has a

heater to vary its temperature. The sample chamber is evacuated and the probe cooled using a He gas-flow system. All measurements are made on the lower CDW state ($T < 60$ K). Differential thermocouples measure the temperature gradient across the sample as well as the temperature difference between the copper blocks and the cold finger. The temperature of the cold finger is measured using a calibrated diode temperature sensor.

It is important to distinguish among the different experimental configurations defined by the directions of the temperature gradient and the electrical current. In general, there are four configurations: $+I,+\Delta T$; $-I,+\Delta T$; $+I,-\Delta T$; and $-I,-\Delta T$. These directions are defined in Fig. 5-1 and ΔT is the temperature difference across the entire sample (positive current implies that electrons flow in the negative direction). For a symmetrical sample, i.e. one that shows mirror symmetry through its center with the mirror plane perpendicular to the chain axis, the number of non-equivalent configurations is reduced to two, since $+I,+\Delta T$ and $-I,-\Delta T$ are physically equivalent and so are $+I,-\Delta T$ and $-I,+\Delta T$. However, this symmetry can easily be broken by, for instance, a non-uniform distribution in the location or strength of the impurities. Another possibility is the occurrence of non-equivalent electrical contacts. In order to compile a complete description of the temperature-gradient effects, all four configurations are measured for each of the samples in these experiments.

The temperature behavior of the CDW velocity is characterized by measuring the NBN frequency versus temperature (30 K $\leq$ T $\leq$ 60 K) at a fixed set of bias currents under isothermal conditions. The data for sample #2 are shown in Fig. 5-2. In this way, a bias can be chosen which is appropriate for the entire temperature range and provided an estimate of the range for which increasing ΔT would cause further NBN splittings ($\Delta T_{MAX} \approx 25$ K with the temperature of the cold end at 30 K).

A typical experimental run starts with the temperature of the sample above the transition temperature of the second CDW (T > 59 K). The sample is then slowly cooled to approximately 30 K with zero bias current. This initial procedure erases all metastable configurations of the CDW and ensures that the CDW starts off in a "virgin" state for all the runs. The sample is then current biased above threshold so that the CDW slides. The magnitude of the bias current is roughly twice the threshold field at the lowest temperature and many times threshold at higher temperatures. Ideally, it would have been appropriate to bias the sample in the high field limit at all temperatures, since later a model is introduced which assumes such a limit. However, practical considerations[10] mandated this compromise. Throughout the entire run, the bias magnitude and direction is kept constant; this is to ensure that no spurious metastable

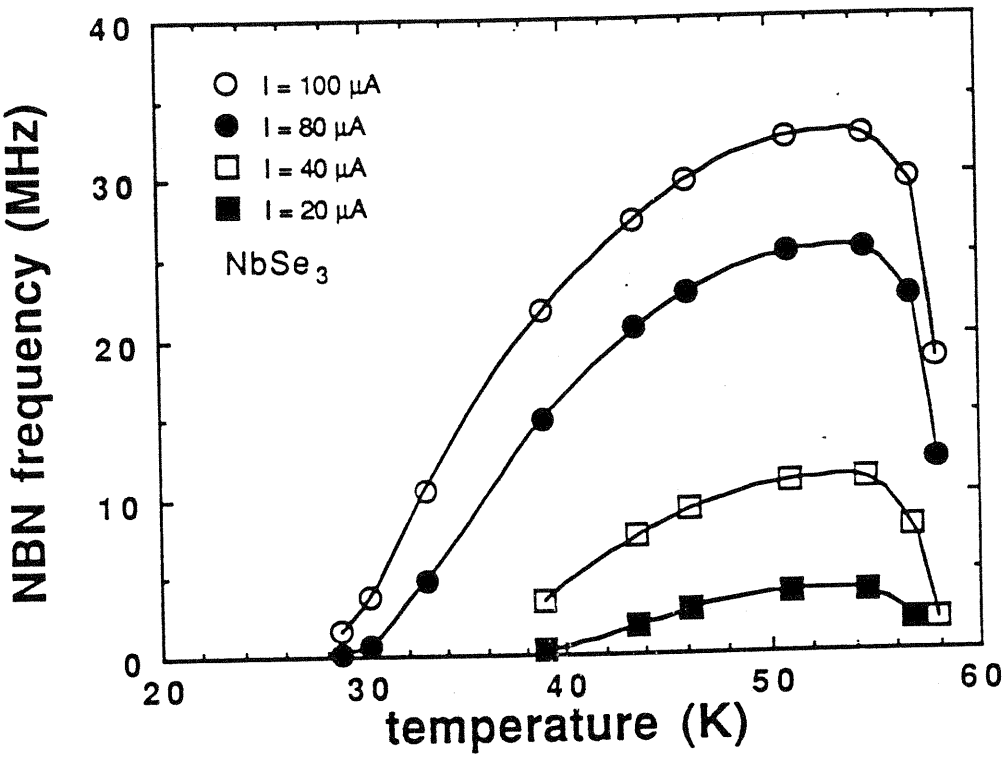

Fig. 5-2 Narrow-band-noise frequency as a function of temperature for various bias currents in an isothermal $NbSe_3$ crystal. Since $f_{NBN} \propto v_c$, the plots represent the highly temperature-dependent nature of the CDW velocity.

states are introduced which might effect comparisons among the different runs.

A temperature gradient is then slowly applied to the sample by turning on one of the copper-block heaters. The temperature gradient is increased monotonically in small increments. After each increment, there is a waiting period of about a minute to ensure that the temperature profile of the probe has reached its steady state. The NBN frequencies and the temperature information are then recorded. Particular care is taken to record the points where the NBN split. Data are taken until increasing the temperature gradient produced no more NBN splittings or until the NBN spectrum degrades in quality to the point where an accurate recording of the NBN configuration is no longer possible.

II. General Observations

There are many parameters which affect the splitting. The most critical parameter is, of course, the temperature difference across the sample ΔT. The average temperature and length of the sample also affect the splitting (longer samples have a greater tendency to split). In a few samples, increasing the bias current alone can cause the NBN to split (under isothermal conditions) although this tended to occur in samples with multiple NBN peaks. In high quality samples with only a single NBN peak under isothermal conditions, the tendency is for the splitting to be independent of the bias magnitude even with an applied temperature gradient. An

exception to this occurs at low biases where the NBN frequencies are close together. Finally, the splitting depends on the particular sample. Included in this sample dependency are impurities and defects which can vary in size, strength, and distribution. Impurities and defects must play a crucial role, especially when one considers crystals which show splitting even in the absence of any temperature gradient.

Of particular interest are the dynamics of the NBN peaks which occur in the splitting process. The phenomenon is easily observed in $NbSe_3$ with a spectrum analyzer while slowly increasing ΔT. A typical spectrum analyzer provides "snapshots" of the NBN spectrum at a fixed rate (approximately 35 Hz for a HP8558B[11]) which sets the time resolution of the experiment. Observations taken via spectrum analyzer show a variety of rich and complex behavior associated with domain splitting. There are two characteristics which are particularly noticeable in the splitting behavior. The first is the smoothness versus the abruptness of the splitting, and the second is the general stability of the NBN spectrum.

A smooth split is characterized as having the NBN peak split apart smoothly into two with the separation of the two peaks dependent on the magnitude of ΔT. In this case, the frequency difference of the peaks can be made arbitrarily small. For an abrupt split, the single peak suddenly splits into two peaks separated by a finite frequency difference

(Δf). The experimental parameters can be adjusted so that neither the split state nor the unsplit state is entirely stable and the sample seems to randomly oscillate between the two states. Depending on the sample, the time scale of these oscillations can be fast, often on the same order as the scan rate of the spectrum analyzer. The time scale of the actual splitting or merging is faster than the scan rate of the analyzer; if one scan shows a single peak, the very next one can show the split peaks. The abruptness of the change makes it appear as though the peaks "snap" together or "snap" apart and we refer to this abrupt splitting as "snapping" behavior. When this snapping occurs, the frequencies of the split peaks bracket the frequency of the unsplit peak; this is very suggestive that the unsplit peak represents a compromise CDW velocity when the sample is of one domain. The finite frequency difference that separates the peaks after they snap apart represents the minimum frequency difference for the two peaks ($\Delta f = \Delta f_{min}$); any attempt to reduce this difference results in the peaks merging into one.

An example of snapping behavior is given in Fig. 5-3 which shows two unaveraged NBN spectra obtained by capturing single traces on the spectrum analyzer. ΔT was set so that neither the split state nor the unsplit state was stable. One trace was captured (the unsplit one), and then traces were captured by trial and error until an example of the split state was recorded. The top trace shows the single unsplit peak and the lower trace shows the two peaks that

resulted from the single peak splitting. In this particular sample under the given circumstances, Δf_{min} = 0.4 MHz; also note that the split peaks bracket the unsplit peak. The two traces are vertically offset for clarity.

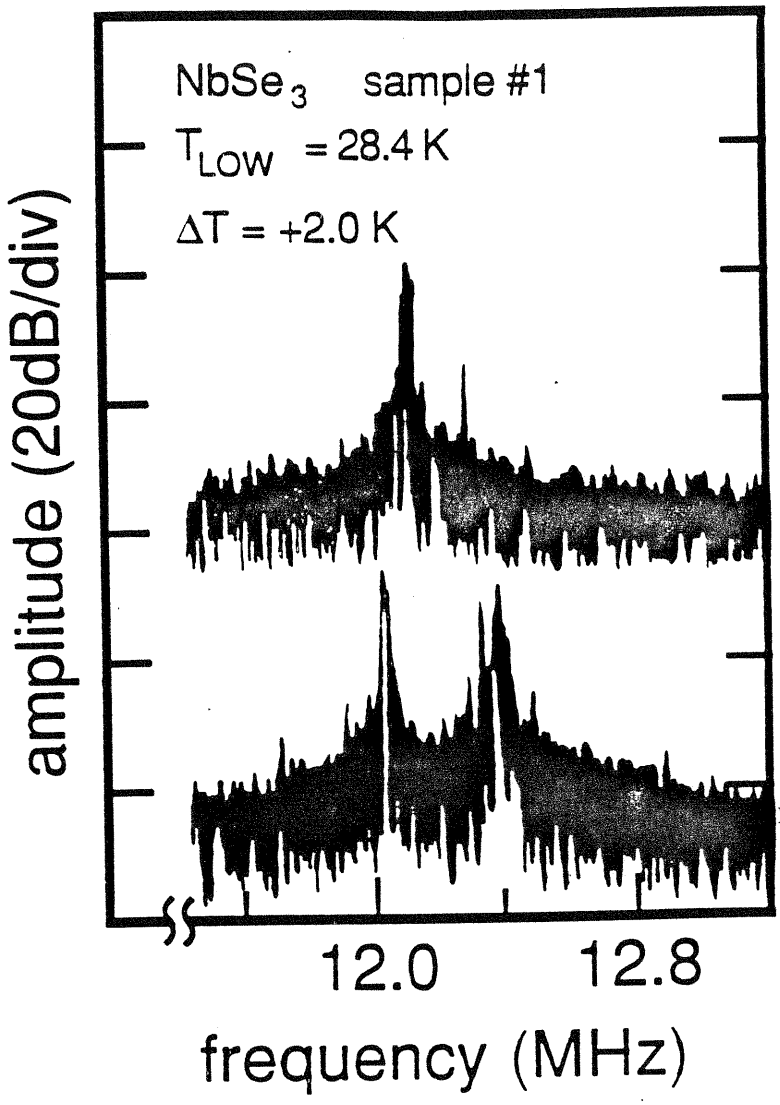

Fig. 5-3 shows two unaveraged NBN spectra obtained by capturing single traces on the spectrum analyzer. The top trace shows the single unsplit peak and the lower trace shows the split state. In this example, Δf_{min} = 0.4 MHz; also note that the split peaks bracket the unsplit peak. The two traces have been vertically offset for clarity.

The stability of the NBN splitting is reflected in the fluctuations of the NBN. Here, the term "fluctuations" refers to spontaneous variations in the amplitude, frequency, or number of the NBN peaks. There is a wide range in the degree of fluctuations present in these systems: a peak may approach the stability of an unsplit peak under isothermal conditions or it may be so chaotic that it is barely discernible. It is sample dependent and the stability of the peak changes as the experimental parameters change. All NBN peaks show fluctuations in their amplitude and frequency[5,12]; however, in this case, the fluctuations can be quite large and almost certainly reflect an instability in the sub-domains.

In general, the fluctuations present in samples with multiple NBN peaks appear to be greater than those in single peak samples. Furthermore, there often is an increase in the fluctuations just before the critical value of ΔT where a NBN peak is observed to split and the fluctuations mainly involve this splitting peak, although other peaks can be affected too. As observed on the spectrum analyzer, these fluctuations can cause the width of the NBN peak to increase, rapid variation of the position of the NBN peak from trace to trace, or a combination of the two. Fluctuations on a time scale shorter than the sweep rate of the spectrum analyzer contribute to the width of the NBN peaks as seen on the spectrum analyzer, while fluctuations on a time scale longer

than the sweep rate cause variations in the NBN spectrum as seen from trace to trace of the spectrum analyzer.

If it is a snapping-type split, a slight increase in ΔT above where the fluctuations increase causes the situation where neither the split state nor the unsplit state is stable. A further increase in ΔT causes the peaks to predominantly remain split with an occasional merging occurring. There are still strong fluctuations present at this point in both peaks especially those of a long time scale (i.e. as seen from trace to trace) and these might represent incomplete mergings. As the temperature difference ΔT is increased still further, the long-time-scale fluctuations are significantly reduced and can even disappear altogether. The short-time-scale fluctuations can be reduced also (as reflected in the NBN width), but not nearly as much. The description of a smooth type splitting is very similar except that it is much more difficult to tell exactly when the peak has split. Another difference is that there appears to be a tendency for the peaks to be wider in a smooth split over a snapping type split.

An example is provided by sample #1. The first split occurred near $\Delta T = 2.0$ K and was of the snapping type (see Fig. 5-3). Increasing ΔT reduced the long-time-scale fluctuations drastically while the widths of the peaks did not noticeably change. At a slightly higher ΔT, the widths of the peaks dramatically changed: the lower-frequency peak's width broadened considerably while the higher

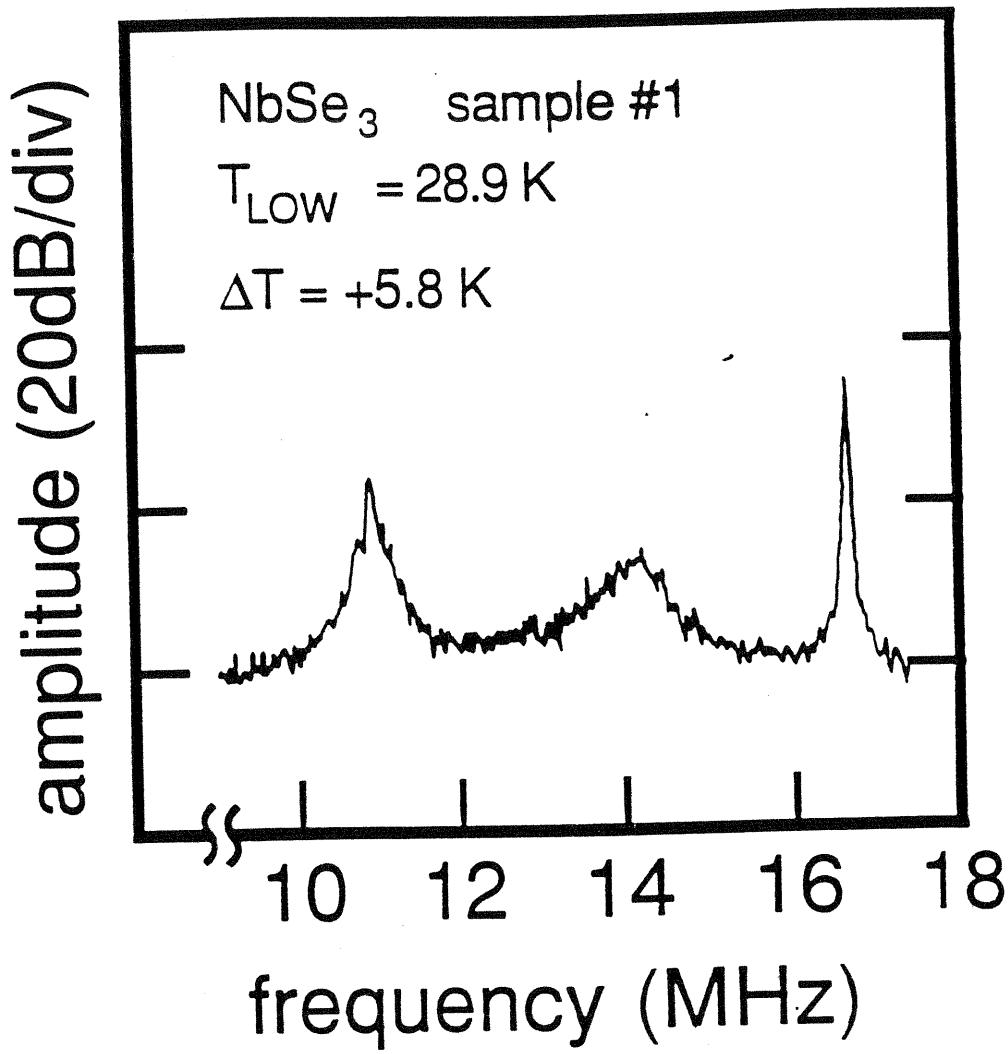

Fig. 5-4 shows the averaged NBN spectrum for sample #1 with I = -80 μA, ΔT = +5.8 K and T_{LOW} = 28.9 K. There are three NBN peaks present in the data corresponding to three sub-domains. At the point where this spectrum was taken, there were very little fluctuations in the positions of the peaks from trace to trace and so the widths of the peaks do not result from the averaging process. Note that the lower-frequency peaks' widths are much wider than the highest frequency peak.

frequency one's decreased in width and became very stable. With a still higher ΔT, it was observed that the lower peak had split into two. During and just after this split ($\Delta T \approx +4.4$ K), the two lower NBN frequencies were fluctuating wildly and it was difficult to clearly see the middle peak. By increasing ΔT, the distance between the peaks increased and the fluctuations from trace to trace decreased, but the widths of the NBN peaks did not. Now the middle peak was clearly visible. This situation is shown in the averaged spectrum of Fig. 5-4. At the point where this spectrum was taken, there were very little fluctuations in the positions of the peaks from trace to trace and so the widths of the peaks do not result from the averaging process.

The overall impression that one gets from observing the NBN splittings is that the wild fluctuations are a result of an instability between two sub-domains (or a "single" sub-domain undergoing the splitting process). This could be due to an unstable PSC, for instance. Indeed, it is observed that wildly fluctuating NBN signals often occur in adjacent pairs. This was particularly evident in sample #1. On occasion, under the same conditions as Fig. 5-4, the highest frequency peak's width would spontaneously broadened followed by the two higher frequency peaks having increased long-time-scale fluctuations. Just as quickly, the increased fluctuations would decrease and the width of the highest frequency peak would revert to its normal thin state. Fig. 5-4 shows the more prevalent condition for this sample where

the two lower peaks tended to "interact" with each other and the highest frequency peak was stable and isolated. Note that the relative widths of the peaks reflect this condition.

In summary, a typical CDW sample often shows a range of behaviors depending on the parameters; this range can be quite large. Most splitting events tend to show smooth behavior with moderate NBN fluctuations present. It is common to see occasional snapping behavior in a sample that might otherwise be classified as smooth and vice versa. It is also common to observe both stable and unstable splittings in the same sample; and occasionally, it is possible to observe an extremely stable split NBN peak. There is strong evidence to suggest that the instabilities seen in the NBN spectrum results from an "interaction" between two sub-domains. Which behavior a particular sample displays at any given time depends on the dc bias, temperature, temperature gradient, and the past history of the sample and shows that the underlying dynamics behind the splittings are complicated.

III. Quantitative Analysis

Before beginning the quantitative analysis in detail, we mention the observation that many of the CDW phenomena examined in these experiments depend on the directions of the temperature gradient and the electrical current. As previously mentioned, the general situation has four possibilities: $+I,+\Delta T$; $-I,+\Delta T$; $+I,-\Delta T$; and $-I,-\Delta T$. It is

also expected for a symmetrical sample that $+I,+\Delta T$ be equivalent to $-I,-\Delta T$ and $+I,-\Delta T$ be equivalent to $-I,+\Delta T$. Although the data show significant differences between the so-called equivalent experimental configurations (EEC), these are very sample dependent and are small compared to the differences seen between the unequivalent experimental configurations which show universal behavior across all the samples. This leads to the conclusion that the primary effect only depends on the relative directions of the current and the temperature gradient; we refer to these as the parallel ($+I,+\Delta T$ and $-I,-\Delta T$) and anti-parallel ($+I,-\Delta T$ and $-I,+\Delta T$) configurations. Accordingly, our main focus will be on the differences between these two configurations.

- **Scaling of Sub-domain Number with ΔT**

The purpose of this phase of the experiment is to determine whether the number of sub-domains as a function of ΔT can be described in a quantitative manner. In particular, these experiments were performed in conjunction with the development of a model to describe the splitting behavior (see Chapter 6), and so, the data were analyzed to discover its consistency with the predictions of the model. The model predicts that the number of sub-domains N should scale roughly with some power of ΔT in the large-N limit. However, the experiments are always performed in the low-N limit. Furthermore, in analyzing the data from the experiments, it is convenient and useful to be able to use standard fitting

procedures (such as least-squares) to determine the best estimate for the scaling coefficient. The scaling data, however, are in the form of a series of discrete step functions which are not a proper form for utilizing such procedures. The solution to these difficulties comes from the model's prediction that the center of the step closely follows a pure scaling behavior and suggests that the data can be fit to the equation

$$N = \Omega \langle \Delta T_N^2 \rangle^{\mu} \tag{5-1a}$$

or the equation

$$N' \equiv N \left(1 - \frac{1}{4N^2} \right)^{-\frac{1}{3}} = \Omega' \langle \Delta T_N^2 \rangle^{\mu'} \tag{5-1b}$$

$$\langle \Delta T_N^2 \rangle \equiv \frac{1}{2} \left[(\Delta T_{N-1,N})^2 + (\Delta T_{N,N+1})^2 \right] \tag{5-1c}$$

where $\Delta T_{N,N+1}$ is the temperature difference applied across the sample at which the number of sub-domains goes from N to N+1. Note that $\langle \Delta T_N^2 \rangle$ defines the center of the step in ΔT^2-space. A fit using Eqn. (5-1a) will give a good estimate of the scaling coefficient μ independent of the parameters in the model. A fit to this equation, though, will have a bias associated with it because the data consist of values of N

which are small; fitting the data to Eqn. (5-1b) removes this small-N bias.[13]

In the process of actually recording the data, it is sometimes difficult to tell exactly how many sub-domains are present in the sample at any given time. This is especially true at the critical ΔT where a splitting event is thought to occur and the NBN spectrum tends to be unstable. When this happens, the event is tentatively identified as a new sub-domain formation; ΔT is then further increased in the hope that the spectrum will stabilize. Often it does and the number of sub-domains can then be accurately counted. If the number of sub-domains has increased, then the tentative identification is recorded as being confirmed; otherwise, it is marked as a "false alarm".

The reproducibility of the data is checked by repeating the measurements of identical experimental configurations. It is found that the positions $\Delta T_{N,N+1}$ of the splitting events are reproducible within $\pm$ 10%; although, many events show tighter tolerances in the reproducibility. As was related above, it is sometimes difficult to ascertain when the splitting event has occurred. Splitting events which are difficult to see tend to be less reproducible. Of course, some of this increased irreproducibility is probably due to the increased uncertainty in determining the occurrence of the splitting event. There is also the possibility that these "messy" splitting events are intrinsically more

irreproducible and reflects the metastability often seen in these systems.

On a few occasions, the number of sub-domains is observed to decrease with increasing ΔT. This is always a "temporary" event in that one of the following occurred:

1) After waiting a period of time with no change in the experimental parameters, the number of sub-domains will spontaneously increase back to its original value.

2) Increasing ΔT slightly causes the number of sub-domains to increase back to its original value.

3) A large increase in ΔT is needed to cause the number of sub-domains to increase back to its original value. In this case, the *original* increase has only been present for a short range of ΔT.

We view these events as again reflecting the highly metastable nature of these systems and that each of these can be interpreted as an anomalous deviation of the sub-domain number N. In the first two cases, it is the decrease in N which is the anomalous event; while in the last case, it is the original increase which is the anomalous event. The last case is the most prevalent; and in all the cases, these

anomalous deviations are not figured into the N versus ΔT data.

The scaling of the sub-domains with ΔT strongly depends on the relative directions of the temperature gradient and the electrical current. There is also the smaller sample-dependent effect where the EEC actually show slight differences. Examples of both of these are plotted in Figs. 5-5 which show the raw data, i.e., the number of sub-domains versus ΔT, of two samples with two runs each. Fig. 5-5a shows the drastic change in the sub-domain splitting when going between the parallel and anti-parallel configurations. When in the anti-parallel configuration, the sample tends to divide into many more sub-domains than the parallel configuration. This effect is seen in all the samples.

Fig. 5-5b demonstrates how the EEC deviate from the expected behavior of a symmetrical sample. The figure shows the data obtained from sample #3 for the two different runs in the parallel configuration. The data suggest that the deviation manifests itself as a shift in the scaling behavior around $\Delta T = 0$. The dotted line marks the approximate center of symmetry for the sub-domain scaling and the distance from the dotted line to the origin denotes the magnitude of this shift (~ 1 K in Fig. 5-5b). By measuring this shift in the anti-parallel configuration, another estimate for the shift is obtained. The two estimates usually agree to within 0.2 K.

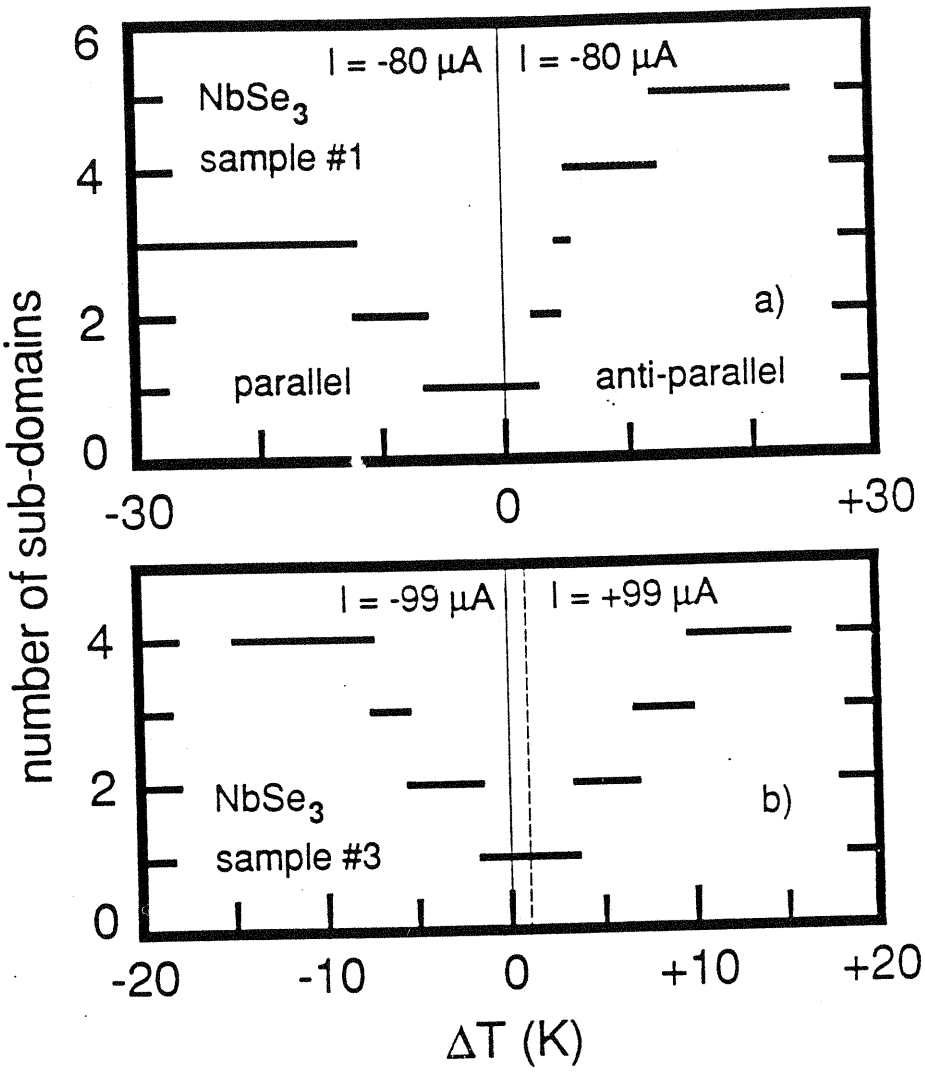

Fig. 5-5 gives examples of the raw data (number of sub-domains versus ΔT). a) contrasts the different splitting abilities of the parallel and anti-parallel configurations. b) demonstrates how the sample can deviate from the expected behavior of a symmetrical sample by showing how the center of symmetry (dotted line) does not coincide with $\Delta T = 0$.

The data are fit to Eqns. (5-1) as prescribed using the standard least-squares method. As is well known with this method, the influence of a particular datum point on the fit depends on its distance from the mean of the data points. This makes the extreme data points important in influencing the fits; and in particular, our concern is with the datum point associated with the N = 1 step for two reasons. First, there is the low-N bias which was already mentioned above; this can be compensated for by using Eqn. (5-1b) for the fit instead of Eqn. (5-1a). Second, there is the shift in ΔT of the raw data as represented in Fig. 5-5b. This shift can be significant enough compared to the first step location that one needs to consider how it influences the fit. To test this, we compared the fits between the raw data and data that had been reshifted so that the EEC were symmetrical around $\Delta T = 0$. The fit is indeed drastically altered. Because the main effect seen in these experiments is associated with the differences between the parallel and anti-parallel configurations and because the shift in the EEC is sample dependent, the raw data are reshifted so that the EEC are symmetrical around $\Delta T = 0$ before the data are fit to the equations. The shifts for the samples are #1:$\Delta T_s \approx 0.0$ K, #2:$\Delta T_s \approx -0.5$ K, and #3:$\Delta T_s \approx +1.0$ K (ΔT_s marks the distance from the origin to the approximate line of symmetry; the data are shifted by adding $-\Delta T_s$ to the original ΔT).

An example of the fits for a parallel and an anti-parallel configuration is shown in the log-log plots of Fig.

5-6. The hatched lines show the step widths and the circles show the locations of the ΔT^2-centers of the steps. The solid lines are the least-squares fit to these centers using Eqn. (5-1a). Note that the slopes of the two lines are approximately equal and that the difference between the anti-parallel (upper line) and the parallel (lower line) configurations are different y-axis intercepts. This means that the scaling coefficient μ is <u>independent</u> of the experimental configuration while the proportionality constant Ω depends on whether the sample is in the parallel or anti-parallel configuration.

The results for the scaling coefficient μ from all the runs and all three samples are displayed in the histogram of Fig. 5-7a. Although there is scatter in the data especially with larger values of μ, the bulk of the data produce a peak which has a median of $\mu \approx 0.35$. The model predicts that the value of μ depends on the parameters of the model. In particular, there are two limits which exist and cover most of the parameter space. These limits correspond to the magnitude of the parameter ν of the model and are referred to as the small-$|\nu|$ and large-$|\nu|$ limits which predict $\mu = \frac{1}{5}$ and $\mu = \frac{1}{3}$ respectively. Obviously, the scaling data are in good agreement with the large-$|\nu|$ limit of the model.

As mentioned earlier, the model also predicts that there is a small bias in the estimate of μ when fitting Eqn. (5-1a) to data where the number of sub-domains is small. This can be corrected in the large-$|\nu|$ limit by fitting to Eqn. (5-1b)

instead. When this is done, it produces the histogram shown in Fig. 5-7b. The median of this histogram is $\mu' \approx 0.33$ which is in excellent agreement with the large-$|v|$ limit prediction of the model.

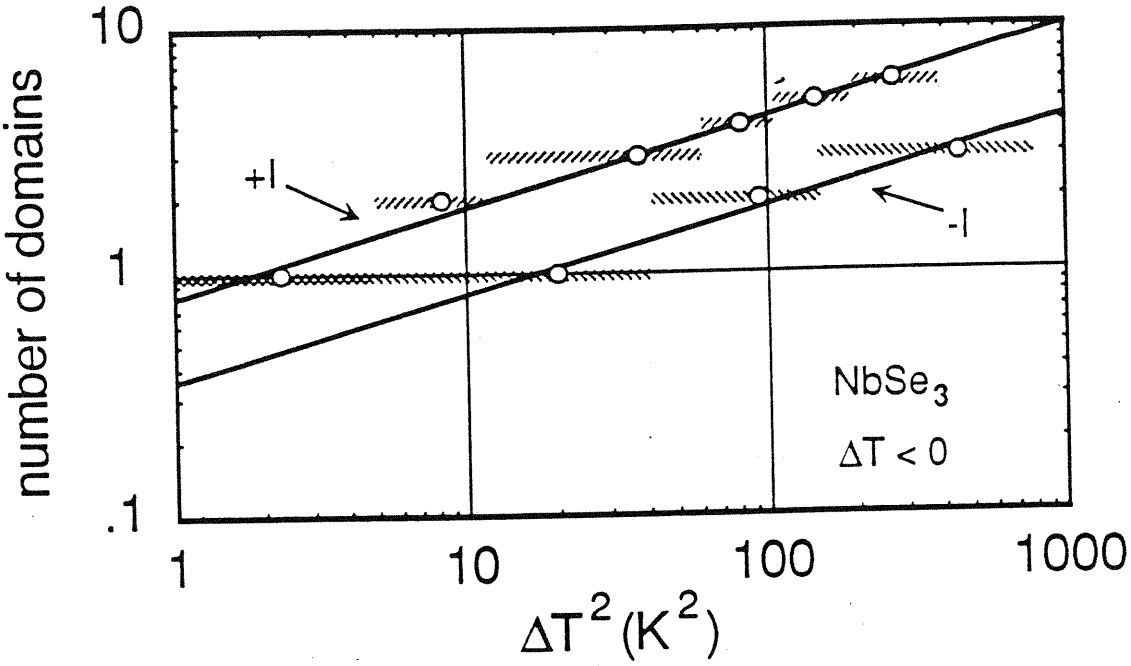

Fig. 5-6 The scaling behavior of the number of sub-domains N with temperature difference ΔT across the sample is demonstrated in these log-log plots. The hatched lines show the range of ΔT over which the sample has a fixed N, the circles show the center of the step, and the solid lines are the least-squares fit to the data (see text). Note that reversing the bias direction only causes a shift in the scaling proportionality constant.

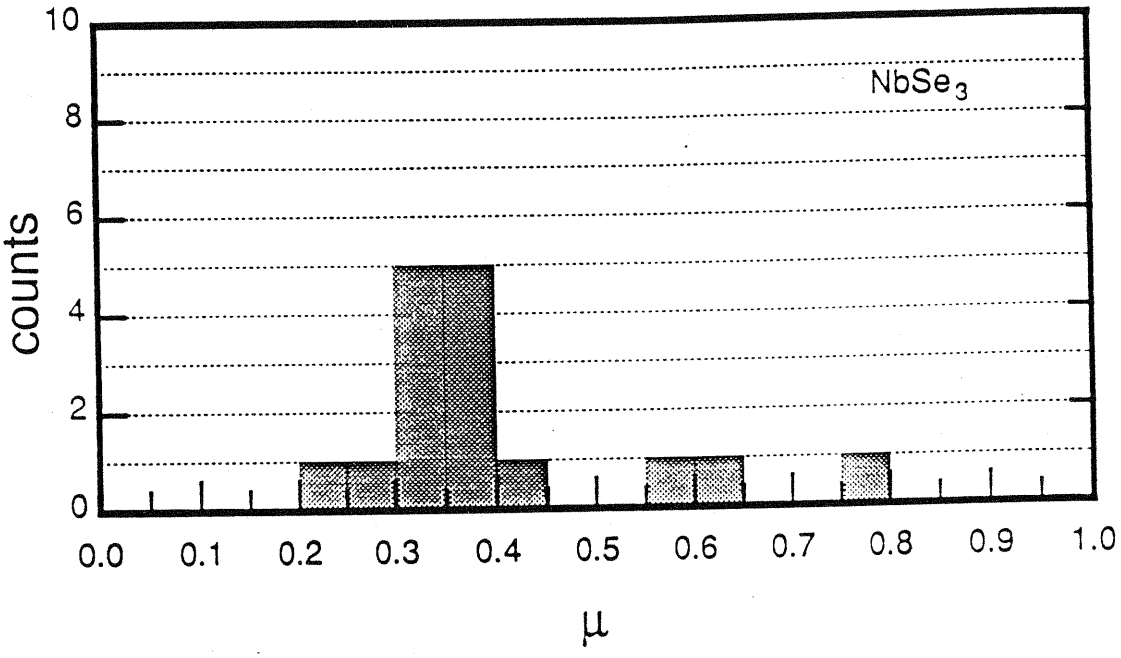

Fig. 5-7a Histogram of the scaling exponent μ for data fit to Eqn. (5-1a). The data are from three $NbSe_3$ samples with various directions of the temperature gradient and electric field. The median of the data is ~ 0.35.

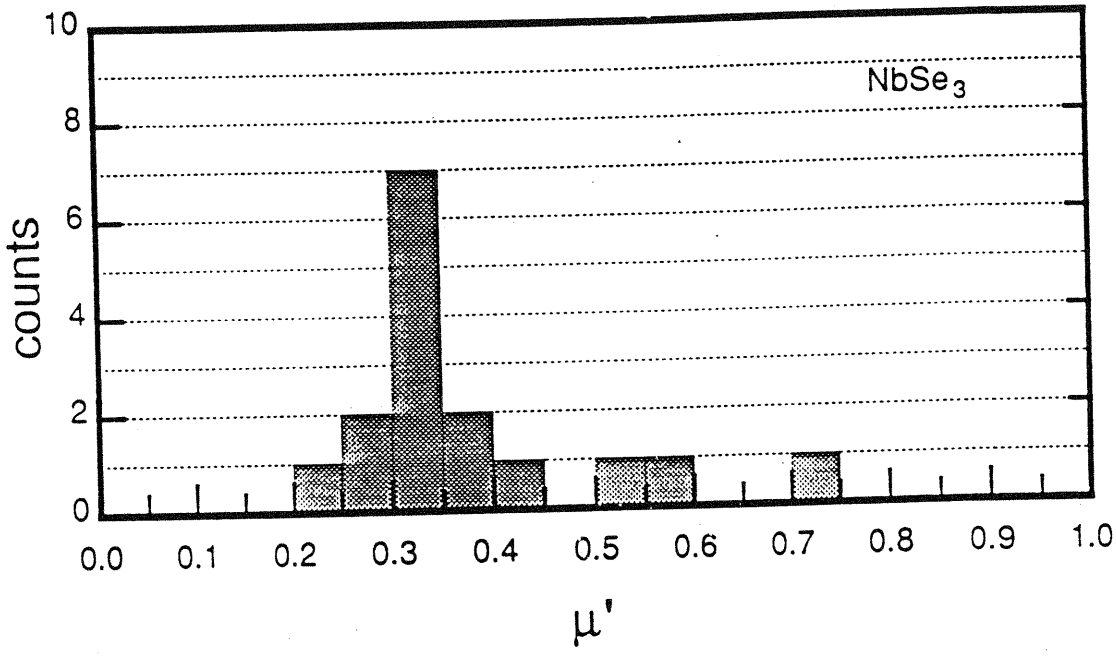

Fig. 5-7b The same data of Fig. 5-7a were fit using Eqn. (5-1b) and yields this histogram for μ'. For small N, the theory predicts that fits to Eqn. (5-1a) will produce a slightly biased estimate for the scaling coefficient; Eqn. (5-1b) removes this bias. The median of the data is ~ 0.33.

- **CDW Velocity**

For a given magnitude of the bias current |I| and the temperature difference $|\Delta T|$ across the sample, the CDW velocity depends on whether the sample is in the parallel or anti-parallel configuration. This can be easily seen by just reversing the sign of the current in a sample with an applied temperature gradient and observing the change in the NBN spectrum. In a sample with a small $|\Delta T|$, this just results in the single NBN peak shifting slightly in frequency. With larger $|\Delta T|$, the NBN might show splitting in one direction and not in the other (this is caused by the dependence of Ω on the experimental configuration as discussed above). In this latter case, the average NBN frequency shifts; the average is defined in the usual manner:

$$\langle f_{NBN} \rangle = \frac{\sum_{i=1}^{N} f_{NBNi}}{N} \qquad (5\text{-}2)$$

where N is the total number of sub-domains.

Figs. 5-8 plot the average NBN frequency as a function of ΔT for the four experimental configurations. The data were taken without any bias reversals during each of the experimental runs in keeping with the desire to minimize any metastable effects. There are a number of interesting points to notice. First, the parallel configuration velocities are greater than the anti-parallel configuration velocities.

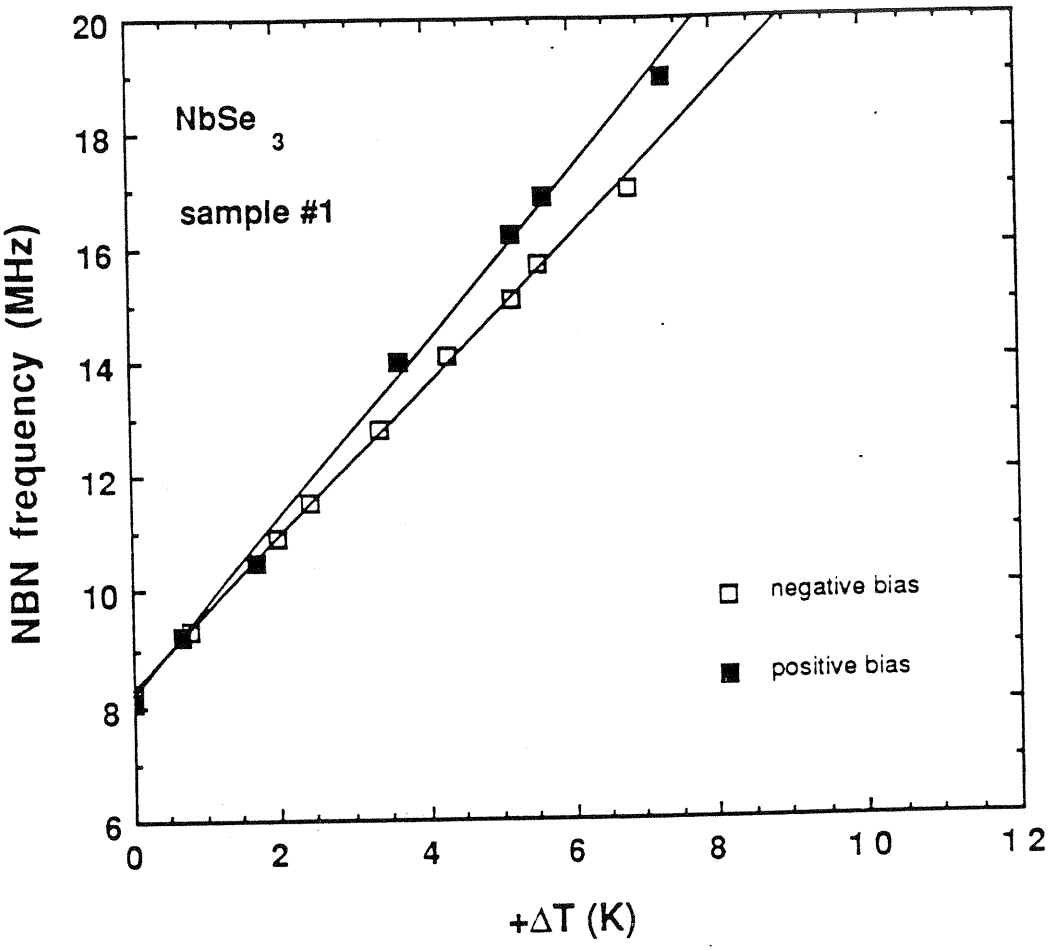

Fig. 5-8a Average narrow-band-noise frequency versus temperature difference ΔT across sample #1 for different bias and temperature gradient directions. Figs. 5-8 a) and b) show the data with positive and negative ΔT respectively. The solid lines are least-square fits to the data.

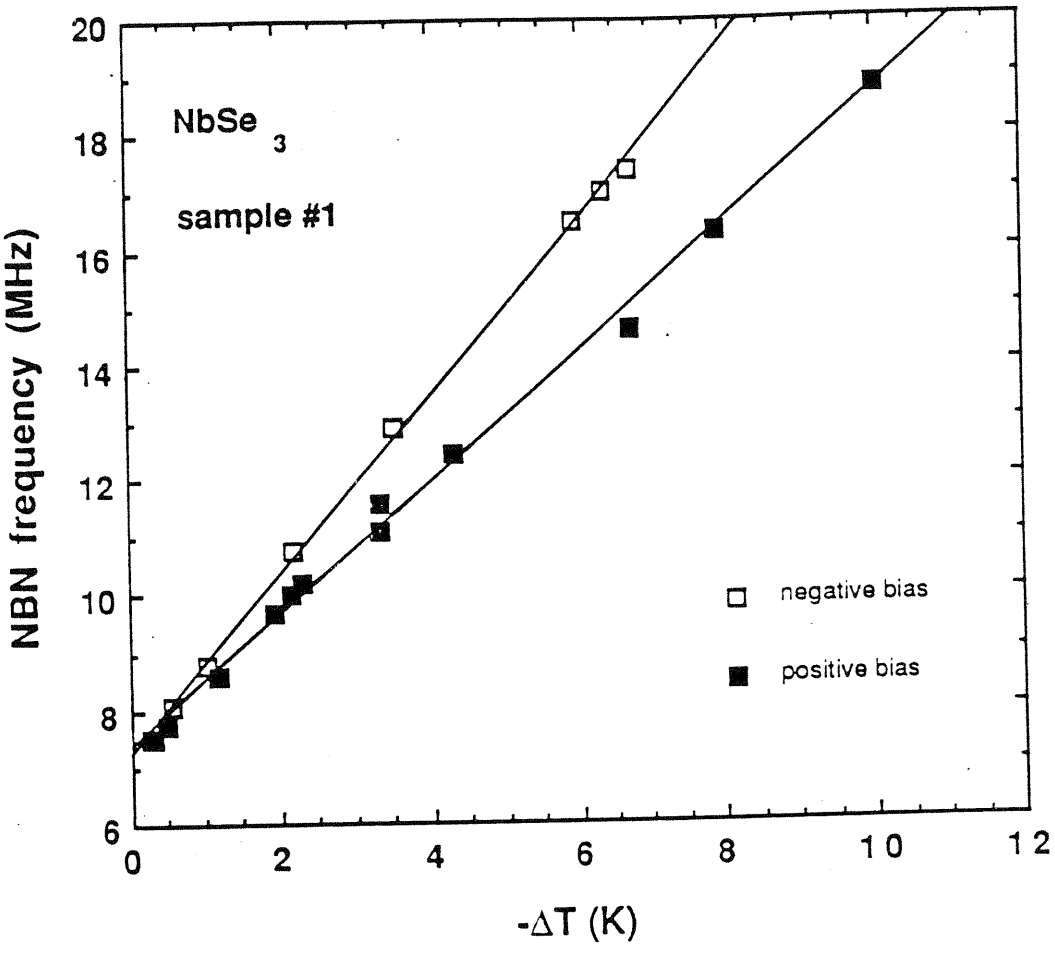

Fig. 5-8b Average narrow-band-noise frequency versus temperature difference ΔT across sample #1 for different bias and temperature gradient directions. Figs. 5-8 a) and b) show the data with positive and negative ΔT respectively. The solid lines are least-square fits to the data.

Second, the data are well described by a linear fit in ΔT (the lines in the figures are the linear least-squares fits to the data). This fit is independent of the number of sub-domains; for example, the anti-parallel data in Fig. 5-8b contain points with the sample having from one to five sub-domains. The main effect on going between the parallel and anti-parallel configurations is to modify the slope of the line. The average of the slopes is not zero because the experiment is performed with the temperature of one of the ends held constant; applying a temperature gradient across the sample causes the average temperature of the sample to rise. And third, the data do show a slight discrepancy in the EEC.

The magnitude of the relative change in the CDW velocity when going between the parallel and anti-parallel configurations depends on the sample. Since the number of examined samples was so low, it is not clear what factors influence this effect. Further work is needed to resolve this issue.

- **Hysteresis in the Differential Resistance Curves**

The differential resistance (dV/dI) of the samples as a function of bias current is examined to determine what effect a temperature gradient has on the low-electric-field properties of the samples. The dV/dI curves are recorded for a given ΔT across the sample by ramping the bias current symmetrically around zero bias with a maximum current far

above threshold. The current is cycled many times before any data are recorded to eliminate any spurious initial metastable states.

With $\Delta T = 0$, the curves show behavior consistent with previous studies and can be roughly divided into two regions. Below the threshold current, the differential resistance is constant; while above threshold, it decreases monotonically. An additional feature seen is a hysteresis loop below the threshold current. The size of the hysteresis loop is sample dependent with some samples having a very small loop observable only with increased resolution or no detectable loop at all. Such hysteresis has been observed many times before and is attributed to the internal polarization of the CDW.[14] There are many possible pinning configurations available to the CDW and this results in a large number of metastable states which are close in energy.[15] The CDW is polarized by applying a large enough electric field to the crystal so that significant portions of the CDW overcome the pinning from defects and impurities. At $T = 0$, the polarization persists until a sufficiently strong electric field can rearrange the CDW. At finite temperatures, thermal activation can also cause the CDW to relax to lower energy configurations. This is consistent with the temperature dependence of the hysteresis which tends to vanish with increasing temperature.[16] The hysteresis loops in the differential resistance record the polarization history of

the sample as a function of bias. We will discuss this process in greater detail in chapter 6.

A non-zero ΔT directly affects the hysteresis loop. In samples which show no loop at $\Delta T = 0$, increasing $|\Delta T|$ causes a loop to form. The dV/dI curves are asymmetric with respect to the current direction and this asymmetry reverses when the temperature gradient reverses. In samples with a hysteresis loop under isothermal conditions, a similar effect is seen except that the initial isothermal loop "offsets" the effect. The loop will either close up or expand depending on the direction of ΔT. If the symmetry of the isothermally-produced loop is opposite that of the ΔT-induced loop, they tend to "cancel" and the hysteresis loop closes. If the symmetries are the same then the size of the loop increases with ΔT. With the loop closing, a value of ΔT can be found where the loop vanishes. If $|\Delta T|$ is then further increased, a loop reappears but with the opposite symmetry of the isothermally-produced loop. In this respect, it is as though the physically isothermal sample has an effective internal "temperature gradient" and that applying an external temperature gradient simply adds to the internal "gradient" as so far as the hysteresis loops are concerned. This description should <u>not</u> be taken too literally because some of the data are inconsistent with this interpretation. For example, sample #2 displayed a hysteresis loop under isothermal conditions; this loop vanished when the external $\Delta T \approx +0.34$ K which implies that the internal effective ΔT is

≈ -0.34 K. However, the shift seen in the N vs ΔT scaling data (for an example of this type of shift, see Fig. 5-5b) implies that the effective internal ΔT is ≈ +0.5 K and has the opposite sign from the hysteresis estimate.

Fig. 5-9a gives an example of the hysteretic dV/dI by showing the curves for negative and positive ΔT from sample #1. Note that the dV/dI curves are asymmetric around I = 0 and that the asymmetry reverses with the reversal of ΔT. For most of the region inside the hysteresis loop, the differential resistance is constant and indicates that the CDW is pinned. Towards the ends of the loop are the transition regions where the sample changes from the low resistance state to the high resistance state or vice versa. On the low resistance side of the curve, the dV/dI decreases immediately outside the hysteresis loop and suggests that, at least, a portion of the CDW has depinned. On the high-resistance side, however, the dV/dI remains relatively flat for a short distance before decreasing and would tend to imply that the CDW is still pinned. If this is the case, then the threshold current is significantly different for positive and negative biasing when a temperature gradient is applied.

It is not entirely clear what the threshold currents are because, for some samples, the dV/dI *increases* slightly at first immediately outside the hysteresis loop (on the high resistance side) before gradually peaking and then decreasing steadily in the usual fashion to indicate CDW conduction.

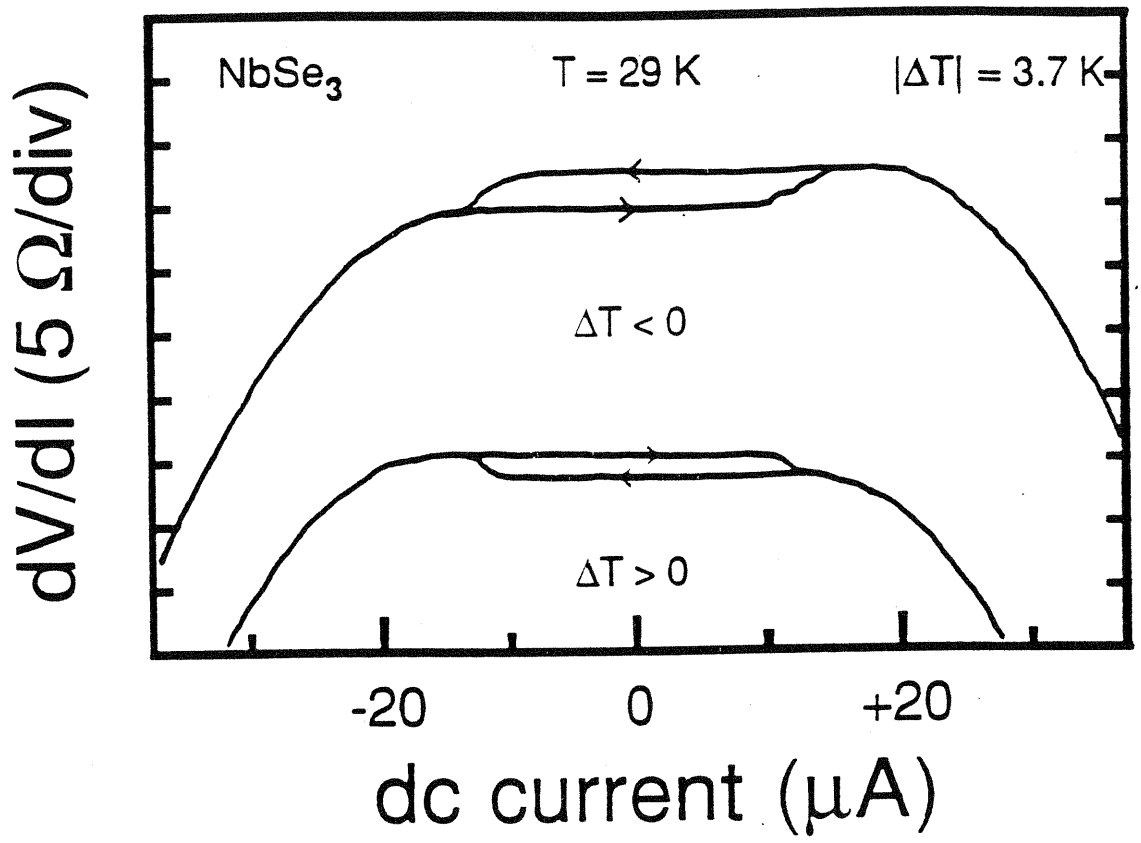

Fig. 5-9a Differential resistance curves for sample #1 with $|\Delta T| = 3.7$ K. The top trace corresponds to negative ΔT and the bottom trace corresponds to positive ΔT. Note that the features of the curves are reversed with respect to each other. The curves have been offset arbitrarily for clarity.

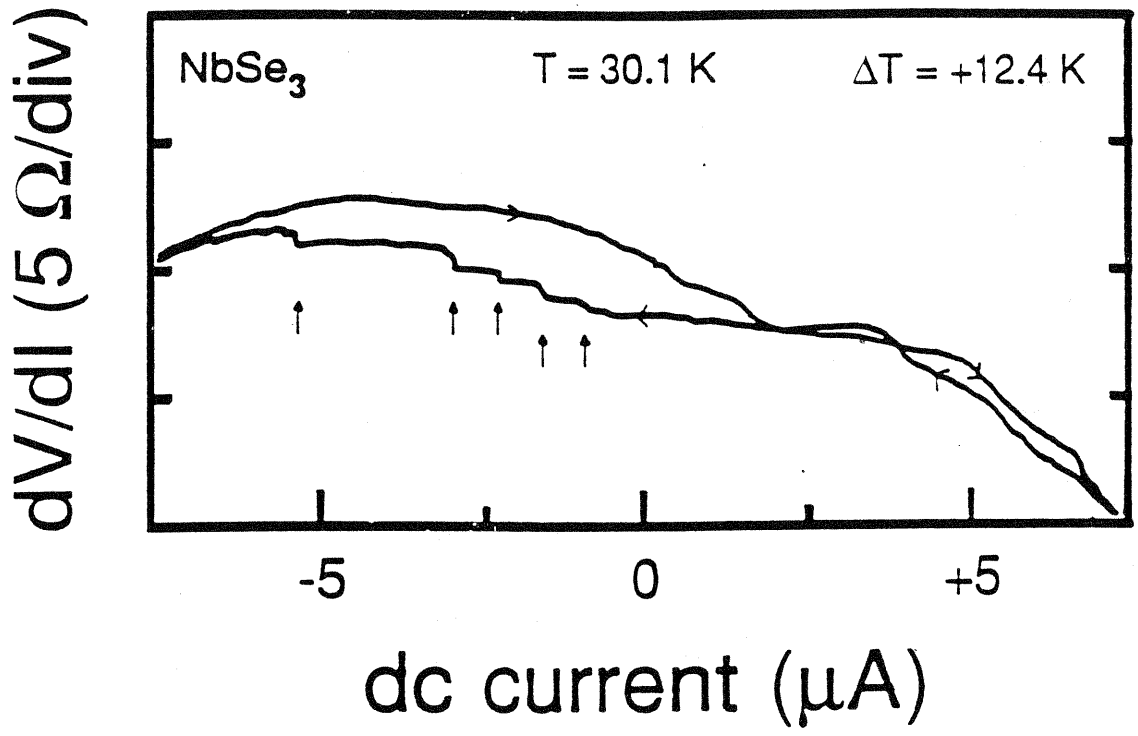

Fig. 5-9b A typical differential resistance curve for large $|\Delta T|$. The arrows mark the locations of the steps which appear in the lower section of the hysteresis loop. Although the steps are commonly seen with large $|\Delta T|$, the number and location of the steps vary from sweep to sweep of the bias.

This could suggest, for instance, that some mechanism which causes the dV/dI to increase is competing against the onset of CDW motion which causes the dV/dI to decrease. With this scenario, using the differential resistance curves to determine the threshold field or current with high accuracy may no longer be valid. Asymmetric dV/dI curves with unequal threshold currents and hysteretic loops have previously been reported in TaS_3.[14] In this instance, the high resistance side was associated with a *lower* threshold field; clearly, further investigation is needed to understand this phenomenon.

The height of the loop changing with ΔT is shown in Fig. 5-10 which plots $\Delta R \equiv R_- - R_+$ versus ΔT for sample #2, where R_- (R_+) is the low-field resistance state arrived at by going to large negative (positive) biases. The data are described well by a linear fit which is also shown in the figure. Note that this sample has a non-zero hysteresis loop under isothermal conditions and this just results in the line being offset from the origin.

For large ΔT, the hysteresis loops become qualitatively different. Distinct step-like features appear in the lower-resistance section within the hysteresis loop and the overall flatness of the curve is greatly diminished; it is not entirely clear if there are any step-like features in the upper part of the loop (see Fig. 5-9b). With small ΔT, the polarization reversal occurs in a very narrow region near the ends of the loop. As $|\Delta T|$ is increased, the reversal region

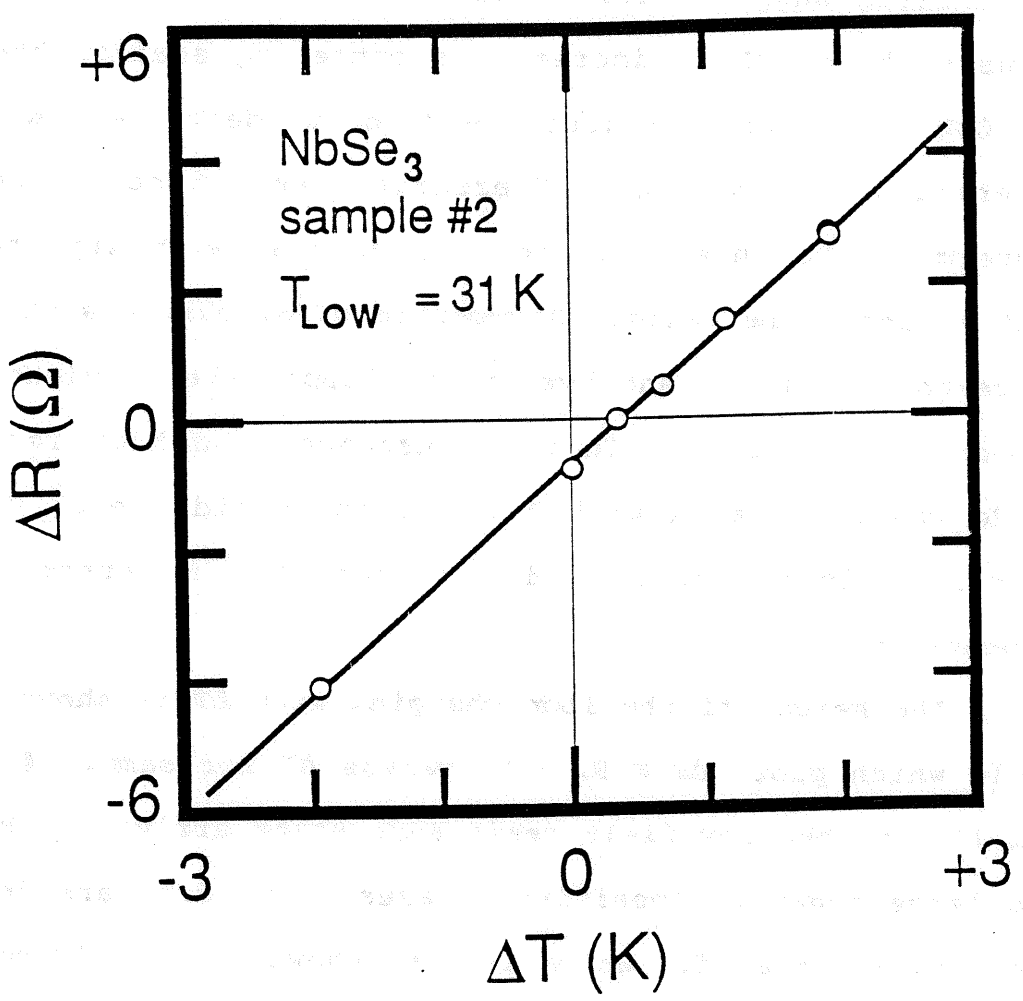

Fig. 5-10 The height of the hysteresis loop ΔR as a function of ΔT show a linear relationship. This sample has a non-zero hysteresis loop under isothermal conditions which causes the line to be offset from the origin.

spreads out and small steps become distinguishable. Two such steps are already observable in the $\Delta T < 0$ hysteresis loop of Fig. 5-9a. Further increasing $|\Delta T|$ spreads the region even more and makes still more steps observable. The data suggest that the CDW reverses its polarization in limited sections corresponding to the local temperature of the section. Each step in the dV/dI corresponds to a distinct section of the crystal reversing its polarization. Repeat measurements of the curves show that the number and location of the steps is not always constant although the step features do consistently appear in the curves.

Conclusion

This concludes the present experimental investigation into the effect of a temperature gradient on CDW systems. We will defer the discussion of this until after a model is presented in the next chapter.

[1]N.P. Ong, G. Verma, and K. Maki, *Phys. Rev. Lett.* **52**, 663 (1984);
G. Verma and N.P. Ong, *Phys. Rev.* B **30**, 2928 (1984);
X.J. Zhang and N.P. Ong, *Phys. Rev.* B **30**, 7343 (1984);
S.E. Brown, A. Janossy, and G. Grüner, *Phys. Rev.* B **31**, 6869 (1985);
J.W. Lyding, J.S. Hubacek, G. Gammie, and R.F. Thorne, *Phys. Rev.* B **33**, 4341 (1986).

[2]M.F. Hundley and A. Zettl, *Phys. Rev.* B **33**, 2883 (1986).

[3]P. Monceau, J. Richard, and M. Renard, *Phys. Rev. Lett.* **45**, 43 (1980).

[4]S. E. Brown and L, Mihaly, *Phys. Rev. Lett.* **55**, 742 (1985);
M.F. Hundley and A. Zettl, Proceedings of the International Conference on Science and Technology of Synthetic Metals (ICSM '88), Santa Fe, NM (*Synthetic Metals* **29**, F463 (1989).

[5]Chapter 8 of this thesis.

[6]J. S. Bendat and A. G. Piersol, Random Data, 2nd ed. (John Wiley and Sons, New York, 1986).

[7]G. Lee Link and G. Mozurkewich, *Solid State Commun.* **65**, 15 (1988).

[8]R. J. Cava, R. M. Fleming, P. Littlewood, E. A. Rietman, L. F. Schneemeyer, and R. G. Dunn, *Phys. Rev.* B **30**, 3228 (1984).

[9]See Appendix B.

[10]At higher biases and increasing temperature gradient, once the NBN had split, the highest NBN frequencies quickly surpassed the harmonics of the lower NBN frequencies and made tracking of the fundamentals exceedingly difficult; furthermore, the higher frequencies were more apt to disappear into the increased background noise from the commercial FM radio spectrum. With each splitting of the NBN, the NBN amplitude is reduced, and so a very low background noise is desirable to ensure detection of all the splittings. By choosing a lower bias, the increased noise region could be avoided. The chosen bias represents the highest bias which allows manageable tracking of the fundamental frequencies and the largest number of *observable* NBN splittings.

[11]The spectrum analyzer was operated in analog mode with 1 or 2 MHz/div. Another time scale affecting the time resolution of the experiment is the amount of time any given frequency is sampled by the analyzer. This depends on the sweep rate and the bandwidth and was on the order of 75 μS for the settings used.

[12]S. Bhattacharya, J.P. Stokes, M.J. Higgins, and R.A. Klemm, *Phys. Rev. Lett.* **59**, 1849 (1987).

[13]Eqn. (5-1b) is only valid in the large-ν limit of the model. The rough fit obtained from Eqn. (5-1a) is consistent with the CDW system being in the large-ν limit. See Chapter 6.

[14]S. E. Brown, L. Mihály, and G. Grüner, *Solid State Commun.* **58**, 231 (1986).

[15]P. B. Littlewood, *Phys. Rev.* B **33**, 6694 (1986).

[16]R. P. Hall, M. F. Hundley, and A. Zettl, *Phys. Rev.* B **38**, 13002 (1988);

B. Burk, P. A. Parilla, and A. Zettl, unpublished.

Chapter 6

Model of a Sliding CDW in a Temperature Gradient

Introduction

One of the common themes found in the study of charge-density-wave (CDW) materials is the concept of the CDW as a deformable medium.[1,2,3,4] There have been numerous investigations into the CDW properties arising from the ability of the CDW to deform; these include polarization and metastable effects.[5] There has also been wide acceptance that a deformation of the CDW will produce a local change in the CDW wave vector and thereby affect the nesting of the Fermi surface and the energy gap of the CDW.[6]

In this chapter, a model of a sliding CDW in a temperature gradient is developed based on the following ideas:

1) The dynamical and elastic properties of a CDW are temperature dependent. In particular, for a given bias current, the velocity of the CDW is temperature dependent.

2) Except across phase-slip centers, the CDW can be viewed as a <u>continuous</u> elastic medium.

3) Given points 1) and 2), a sliding CDW in a crystal with an applied temperature gradient will have an

internal elastic strain. For example, in the temperature range of the experiments in chapter 5, the CDW has a higher effective mobility[7] at higher temperatures (see Fig. 5-2). Therefore, the CDW at the hot end will tend to move faster than the CDW at the cold end; this will continue until the internal physical properties of the CDW (i.e. the elasticity and the processes mentioned in point #4 below) compensate for the disparity in the spatially non-uniform mobility and the entire CDW is moving at a compromise steady-state velocity.

4) A strain in the CDW changes the local wave vector which then can change the local properties of the CDW. In particular, we will consider the CDW charge density and the CDW damping.

5) It takes energy to break the continuity of the CDW elasticity (For a moving CDW, this results in phase-slip processes).

6) If the internal strain becomes sufficiently large, it will be energetically favorable to break the sliding CDW into multiple velocity sub-domains separated by phase-slip centers [PSC].[8]

We propose that the concepts presented above are the principles behind the sub-domain formation actually seen in real CDW materials. When a theory is developed from the above outline, not only does it predict the scaling behavior between the number of sub-domains and the temperature gradient; but it also predicts the asymmetry seen in the CDW velocity and the asymmetry in the scaling behavior (The asymmetry is with respect to the relative directions of the electrical current versus heat current.). Furthermore, the above model also suggests an explanation to the hysteresis seen in the dV/dI curves at low electric field and has direct implications in explaining many of the hysteretic phenomena seen in these materials.

This chapter can be roughly divided into 4 parts. In the first part, a model of the CDW is introduced which possesses the essential characteristics needed to describe the temperature gradient phenomena; the postulates, assumptions, and approximations are explicitly given. The second part gives the calculation of the internal strain and strain energy induced by a temperature gradient in the sliding CDW. The results of the calculations are then examined for their properties. The third part continues with the minimization of the strain and PSC energies which results in scaling behavior between the number of CDW velocity sub-domains and the applied temperature gradient. A comparison to the experiments is made and the results are discussed in the fourth and final part.

I. Model Preliminaries

Since we are constructing a model to compare with the results of experiment, the first assumption is the hypothesis: Materials with a sliding CDW and an applied temperature gradient will break into velocity sub-domains in order to minimize the combined energies of internal strain and PSC formation. We are now left with the task of calculating the strain and PSC energies.

PSC model

In one model of phase slippage, the CDW collapses at the interface along a line of phase vortices which move transverse to the CDW chain axis.[9] The energy of a single phase vortex is approximately

$$U_{pv} \approx N(E_F)\ \Delta^2\ \xi_{\|}\ \xi_{\perp}^2\ , \qquad (6\text{-}1)$$

where $N(E_F)$ is the density of states at the Fermi surface, Δ is the CDW energy gap and $\xi_{\|}$ ($\xi_{\perp}$) is the CDW amplitude correlation length parallel (perpendicular) to the chain axis. Except for temperatures close to the CDW transition temperature, the parameters in the above equation are relatively independent of temperature and so there is no variation in the PSC energy with position in the crystal in the presence of a temperature gradient. However, due to the small size of the phase vortex (it has a volume of $\xi_{\|}\ \xi_{\perp}^2$), large variations in the phase-slip energy may exist if the

phase slip were to occur on or near an impurity site where the relevant parameters [Δ and $N(E_F)$] may be far below the clean, bulk value. Implementing this into the model will greatly complicate it because the exact effect of impurities on the phase-slip process is unknown. As a first approximation, we ignore this possibility of PSC energy variation with the impurity configuration. Instead, so far as the model is concerned, the PSC is characterized by three properties:

1) The energy needed to form a PSC is a constant U_{PS} independent of location and temperature.

2) The PSC acts as a sink or as a source of CDW phase and, as such, forms the boundary for the sub-domain.

3) The boundary condition associated with the PSC is specified by a strain which may depend on a number of parameters (temperature, CDW velocity, etc.). Intuitively, we might expect that you have to 'push' the CDW into a PSC in order to have it act as a sink and 'pull' it out of the PSC in order to have it act like a source. For the time being, we let this strain be zero, a constant. In this case, the PSC acts as an 'effortless' sink or source of the CDW.

The total phase-slip energy is just U_{PS} multiplied by the number of PSC's:

$$U_{TPS} = (N - 1) U_{PS} \qquad (6\text{-}2)$$

where U_{TPS} is the total PSC energy and N is the number of CDW velocity sub-domains. The two PSC's at the electrical contacts are not counted because they need to be present for any and all CDW sliding to occur (even with $\Delta T = 0$).

CDW model

The electronic charge density $\rho(x)$ that makes up a CDW can be represented by

$$\rho(x) = \rho_m + \rho_c \cos [Qx + \Phi(x,t)] \qquad (6\text{-}3)$$

where ρ_m is the mean CDW charge density, ρ_c is the density wave amplitude, $Q = 2k_F$ is the CDW wave vector, and $\Phi(x,t)$ is the position- and time-dependent CDW phase. Both CDW motion and distortion are accounted for by the phase variable $\Phi(x,t)$. In the presence of a bias current I_B which exceeds the depinning threshold current I_T, the CDW slides relative to the lattice with a velocity v_o which is related to the time derivative of the phase $d\Phi/dt$. The (time-averaged) CDW phase velocity is independent of the position coordinate x within a CDW domain due to the phase distortion term in the CDW Hamiltonian[2,3]

$$H_{elastic} = \frac{1}{2} K \int \left|\nabla\Phi\right|^2 d^3x \qquad (6\text{-}4)$$

where K is the CDW phase elasticity. If the CDW velocity were strictly position-dependent, this elastic strain energy would increase in time, and eventually destroy a moving CDW. In actuality, what happens is that the strain builds up in a way which compensates for any spatial inhomogeneities in the forces and the condensate moves at a uniform velocity (on the average).

With the above picture in mind, we look for solutions of $\Phi(x,t)$ of the form

$$\Phi(x,t) = Q v_o t + \phi(x) \ , \qquad (6\text{-}5)$$

i.e. the CDW is moving at a uniform velocity v_o and has a time-independent distortion $\phi(x)$. It might be naive to expect the solution to be of so simple a form in these complex systems; more realistically however, one could expect the time-averaged solution or ensemble-averaged solution to approach the form of Eqn. (6-5).

We follow the approach of Feinberg and Friedel[10] and consider the CDW as a classical elastic medium. However, Feinberg and Friedel only considered the case where the CDW was pinned, while in this model the CDW is sliding at a

uniform velocity. Experimental studies[11] suggest that the CDW behaves as an overdamped system; accordingly, a phenomenological damping term is added. Furthermore, we only consider the saturated electric field limit ($E >> E_T$) where the effects from the impurity potential are relatively reduced[3,12] and therefore as a simplification, the model does not explicitly treat impurities or contain a threshold field E_T. The importance of impurities in the temperature gradient effects will be discussed for the low-field limit. The CDW couples to an electric field through its average charge density ρ; the effect of the CDW distortion on the local charge density is explicitly handled. There is also experimental evidence which indicates that the damping of the CDW depends on the low-field resistivity.[13] At first, we will ignore this possibility for the initial calculations and we call this model 'A'; later, this feature will be included to form a modified model referred to as model 'B'. For simplicity, we assume a one-dimensional system.

II. Strain and Strain Energy Calculation

Consider a one-dimensional sample of length L, with a constant temperature gradient $\frac{\Delta T}{L}$. Further consider that the sample is biased far above threshold with a current I_B and that the sliding CDW has divided into velocity sub-domains one of which is of length L_D. The sub-domain contains a CDW traveling with velocity v_o and is bounded by the two PSC's at either end. Fig. 6-1 illustrates this sub-domain and

introduces the x coordinate system used in the calculations. ΔT is positive if $T(x=-L_D/2) < T(x=+L_D/2)$. At this time, it is useful to introduce the variable s defined by

$$s = s(x) \equiv \frac{1}{Q} \frac{d\phi(x)}{dx} = \frac{\Delta Q}{Q} \tag{6-6}$$

Note that s gives the relative change of the CDW wave vector.

The appropriate differential equation is[3]

$$\frac{\gamma(x)}{Q} \frac{d\Phi}{dt} - \frac{1}{Q} \frac{d}{dx}\left(\kappa(x) \frac{d\Phi}{dx} \right) = \rho_m(x) E(x) \tag{6-7}$$

where γ is the damping parameter, κ the elasticity of the CDW, ρ_m the average CDW charge density, and E the electric field. The assumption will be made that the position dependence of the parameters γ, κ, and E is strictly due to the variation in temperature and that the position dependence of ρ_m is strictly caused by the strain. As an approximation, a Taylor expansion is taken of the temperature-dependent terms.

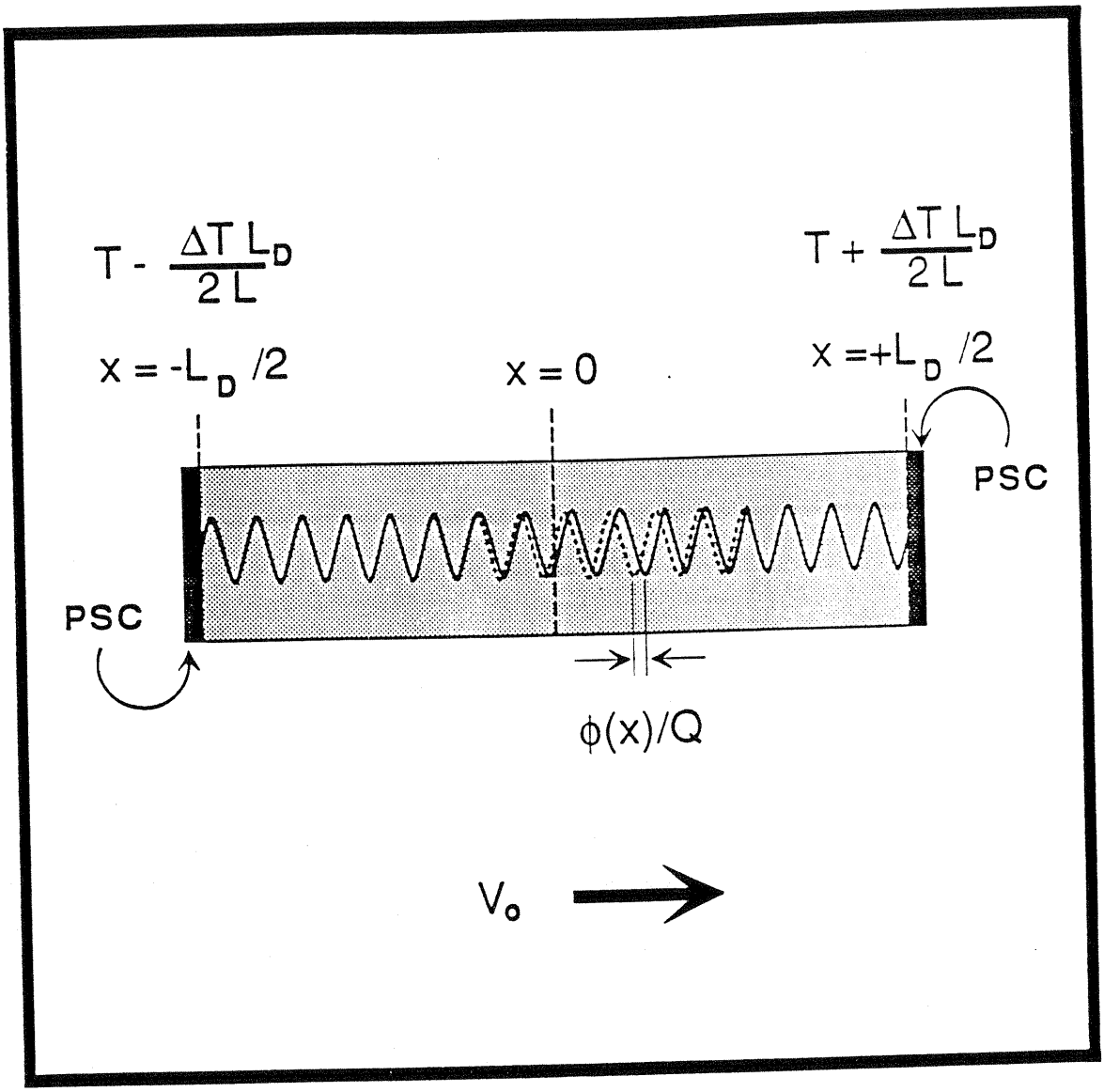

Fig. 6-1 A typical sub-domain as pictured by this one-dimensional model. The CDW is moving with steady-state velocity v_o. The sub-domain is bounded by the PSC's which also act as sinks and sources of the CDW. A 'snapshot' of the phase of the CDW is shown in a slightly distorted condition (solid line) as compared to the undistorted CDW (broken line).[14]

$$\gamma(x) = \gamma(T(x)) \approx \gamma + \gamma' \frac{\Delta T}{L} x \; ; \quad \gamma' = \frac{d\gamma}{dT} \tag{6-8a}$$

$$\kappa(x) = \kappa(T(x)) \approx \kappa + \kappa' \frac{\Delta T}{L} x \; ; \quad \kappa' = \frac{d\kappa}{dT} \tag{6-8b}$$

$$E(x) = E(T(x)) \approx E + E' \frac{\Delta T}{L} x \; ; \quad E' = \frac{dE}{dT} \tag{6-8c}$$

$$\rho_m(x) = \rho_m(s(x)) \approx \bar{\rho} - \rho_s \, s \tag{6-9}$$

Equation (6-9) can also be considered the first-order Taylor expansion around $s = 0$. In general, ρ_s can be negative or positive; however for later convenience, an explicit minus sign has been introduced. The parameter ρ_s describes how the CDW charge density changes with a modification of the CDW wave vector. We will not attempt to estimate its value *ab initio* since this would require a detailed calculation based on the microscopic principles of the CDW and the idiosyncrasies of the specific material. Three processes are expected to contribute to this parameter:

1) A change in the CDW wave vector can directly effect the CDW charge density through the requirement that the energy gap remain at the Fermi surface.[2]

2) A modification of the CDW wave vector might significantly change the *percentage* of Fermi surface area nested, in effect, directly converting one carrier type to the other. This could be particularly important in materials which show incomplete nesting such as $NbSe_3$.

3) A change in the magnitude of the energy gap will effect the number of thermally activated carriers.[6]

If the model were strictly classical with the CDW charge 'imbedded' uniformly into the elastic material, then ρ_s would equal $\bar{\rho}$ (accurate to first order). For now, we will just consider ρ_s as another parameter and expect that the solution to the differential equation be accurate for small (ρ_s s). After inserting Eqns. (6-5), (6-8), and (6-9) into Eqn. (6-7) and utilizing Eqn.(6-6), the differential equation becomes

$$\frac{ds}{dx} + \frac{\left(\kappa' \frac{\Delta T}{L} - \rho_s E - \rho_s E' \frac{\Delta T}{L} x \right)}{\left(\kappa + \kappa' \frac{\Delta T}{L} x \right)} s = \frac{\left(f_o + f_o' \frac{\Delta T}{L} x \right)}{\left(\kappa + \kappa' \frac{\Delta T}{L} x \right)} \qquad (6\text{-}10)$$

where f_o and f_o' are defined by

$$f_o \equiv \gamma\, v_o - \bar{\rho}\, E \tag{6-11a}$$

$$f_o' \equiv \gamma'\, v_o - \bar{\rho}\, E'. \tag{6-11b}$$

The naught subscript serves as a reminder that these parameters depend on v_o, the velocity of the CDW.

The solution to Eqn. (6-10) is

$$s(x) = \frac{1}{\kappa}\left(1 + \frac{\kappa'\,\Delta T}{\kappa\, L}\, x \right)^{-\beta} \exp\left(\frac{\rho_s\, E'}{\kappa'}\, x \right) \times \tag{6-12a}$$

$$\int_{-\frac{L_D}{2}}^{x} \left(1 + \frac{\kappa'\,\Delta T}{\kappa\, L}\, z \right)^{\beta-1} \exp\left(-\frac{\rho_s\, E'}{\kappa'}\, z \right) \left(f_o + f_o' \frac{\Delta T}{L}\, z \right) dz$$

$$\beta = 1 - \frac{\rho_s\, (\kappa' E - \kappa\, E')}{\kappa'^2\, \frac{\Delta T}{L}}\ . \tag{6-12b}$$

The integral in Eqn. (6-12a) can be solved in terms of sums and differences of the partial gamma function; however, the entire equation becomes much simpler if we consider the limit where $\frac{\kappa'\Delta T}{\kappa} << 1$; i.e., the limit where the relative change in the elasticity due to the temperature gradient is small. In this limit Eqns. (6-12) become

$$s(x) = \frac{\exp\left(\alpha\ z - \frac{\kappa'\ \Delta T}{\kappa\ L}\ x \right)}{\kappa} \times$$

(6-13a)

$$\int_{-\frac{L_D}{2}}^{x} \exp(-\alpha\ z) \left(f_o + f_o'\ \frac{\Delta T}{L}\ z \right) dz$$

$$\alpha = \frac{\rho_s\ E}{\kappa} \ . \qquad (6\text{-}13b)$$

Integration is now simple and the resulting s(x) is:

$$s(x) = \frac{\exp\left(-\frac{\kappa'\ \Delta T}{\kappa\ L}\ x \right)}{\kappa\ \alpha} \left[f_o \left\{ \exp\left(\alpha\ x + \frac{\alpha\ L_D}{2} \right) - 1 \right\} \right.$$

(6-14)

$$\left. - f_o'\ \frac{\Delta T}{L} \left\{ x + \frac{1}{\alpha} + \left(\frac{L_D}{2} - \frac{1}{\alpha} \right) \exp\left(\alpha\ x + \frac{\alpha\ L_D}{2} \right) \right\} \right]$$

Eqns. (6-12), (6-13), and (6-14) were constructed to be consistent with the boundary condition $s\left(x = -\frac{L_D}{2}\right) = 0$. Ensuring that the other boundary condition is satisfied ($s = 0$ at $x = +\frac{L_D}{2}$) determines the CDW velocity v_o which can be solved for from Eqn. (6-14):

$$v_o = \frac{\bar{\rho}\ E}{\gamma}\left[\frac{1 - \frac{L_D\ E'\ \Delta T}{2\ E\ L}\ \xi\left(\frac{E}{\varepsilon}\right)}{1 - \frac{L_D\ \gamma'\ \Delta T}{2\ \gamma\ L}\ \xi\left(\frac{E}{\varepsilon}\right)}\right] \equiv \frac{\bar{\rho}\ E}{\gamma}\ \eta(\Delta T, E) \quad (6\text{-}15a)$$

$$\xi(\nu) = \coth(\nu) - \frac{1}{\nu} \quad (6\text{-}15b)$$

$$\nu \equiv \frac{E}{\varepsilon} \equiv \alpha\frac{L_D}{2} = \frac{\rho_s\ E\ L_D}{2\ \kappa} \quad (6\text{-}15c)$$

$$\varepsilon \equiv \frac{2\ \kappa}{\rho_s\ L_D}\ . \quad (6\text{-}15d)$$

Eqns. (6-15) constitute the first significant result from the theory. They describe how the velocity of the CDW is affected by the electric field and temperature gradient. The prefactor $\frac{\bar{\rho}E}{\gamma}$ is the velocity of the CDW in the absence of any temperature gradient. One of the most interesting aspects of these equations is its symmetry with respect to ΔT and E. $\xi(\nu)$ is an odd function and so changes sign with E. This makes $\eta(\Delta T, E)$ invariant if <u>both</u> ΔT and E change signs:

$$\eta(+\Delta T, +E) = \eta(-\Delta T, -E) \quad (6\text{-}16a)$$

$$\eta(+\Delta T, -E) = \eta(-\Delta T, +E)\ . \quad (6\text{-}16b)$$

However, if only one changes sign, they are not equal; i.e.

$$\eta(+\Delta T,+E) \neq \eta(+\Delta T,-E)\,. \qquad (6\text{-}16c)$$

Therefore, the theory predicts a shift in the CDW velocity if only one of the ΔT, E pair has a sign reversal and there should be no change if both change sign. The underlying physics behind this effect will be discussed in more detail in part IV.

The model has produced three natural parameters which are all interrelated as is demonstrated in Eqn. (6-15c). ν is a dimensionless parameter whose magnitude will determine which one of three regimes the solution s(x) lies, ε represents a 'yardstick' to measure the electric field in relation to ν, and $\frac{1}{\alpha}$ reflects a length scale which measures the sub-domain size in relation to ν and a 'decay' length for s(x) to change within the sub-domain. Before discussing these further, we will complete the calculation. The next step is to substitute the expression v_o back into Eqn. (6-14):

$$s(x) = \frac{\left(\frac{\bar{\rho}}{\rho_s}\right)\left(\frac{E'}{E} - \frac{\gamma'}{\gamma}\right)\frac{\Delta T}{L}\exp\left(-\frac{\kappa'\,\Delta T}{\kappa\, L}\,x\right)}{1 - \frac{L_D\,\gamma'\,\Delta T}{2\,\gamma\, L}\,\xi\left(\frac{E}{\varepsilon}\right)} \times \qquad (6\text{-}17)$$

$$\left[\, x + \frac{L_D}{2}\coth(\nu) - L_D\,\frac{\exp(\alpha x)}{\exp(\nu) - \exp(-\nu)}\,\right]$$

It is then straightforward to calculate the strain energy U_s,

$$U_s = \frac{1}{2} \int \kappa(x) \; |s(x)|^2 \, dx \tag{6-18}$$

The leading order term of Eqn. (6-18) is (again in the limit $\frac{\kappa' \Delta T}{\kappa} << 1$)

$$U_s \approx \frac{\frac{\kappa}{2}\left(\frac{\bar{\rho}}{\rho_s}\right)^2 \left(\frac{E'}{E} - \frac{\gamma'}{\gamma}\right)^2 \left(\frac{\Delta T}{L}\right)^2}{\left\{1 - \frac{L_D \gamma' \Delta T}{2 \gamma L} \xi\left(\frac{E}{\varepsilon}\right)\right\}^2} \times \tag{6-19}$$

$$\left[\frac{L_D^3}{3} + \frac{L_D^3}{4} \operatorname{csch}^2(\nu) - \frac{3 L_D^2}{2 \alpha} \coth(\nu) + \frac{2 L_D}{\alpha^2}\right].$$

The behavior of Eqns. (6-17) and (6-19) depend crucially on the magnitude of the parameter ν (and its cousin α; $\nu = \alpha \frac{L_D}{2}$) and can be divided into three regimes defined by $|\nu| << 1$, $|\nu| \sim 1$, and $|\nu| >> 1$. The properties of the equations for $|\nu|$ large and small are best shown by looking at these equations in the appropriate limits. For $|\nu| << 1$,

$$s(x) \sim \frac{\alpha}{2}\left[\frac{L_D^2}{4} - x^2\right] + \vartheta(\nu^2) \qquad (6\text{-}20a)$$

$$U_s \sim \frac{\alpha^2 L_D^5}{120} + \vartheta(\nu^4 L_D^3) \qquad (6\text{-}20b)$$

and for $|\nu| >> 1$ (and positive),

$$s(x) \sim x + \frac{L_D}{2} - L_D \exp\left[\alpha\left(x-\frac{L_D}{2}\right)\right] + \vartheta(L_D e^{-2\nu}) \qquad (6\text{-}21a)$$

$$U_s \sim \frac{L_D^3}{3} + \vartheta\left(\frac{L_D^3}{\nu}\right) \qquad (6\text{-}21b)$$

Eqns. (6-20) and (6-21) are the expansions of the terms in the square brackets in Eqns. (6-17) and (6-19); the prefactors, which depend only weakly on ν, have been omitted.

The expansions show that for small $|\nu|$ the variable s has a quadratic profile as a function of x and scales with α. Accordingly, U_s will vary as L_D^5 and scale with α^2. The behavior for large $|\nu|$ is quite different. First of all, $s(x)$ and U_s are approximately independent of α. Also, for most of the sample, s is linear in x except for a region of length $\sim L_D \frac{\ln(2\nu)}{2\nu}$ next to one of the PSC's. In this region, $s(x)$ ceases to be linear and instead exponentially decreases

to zero as required by the boundary condition. Which PSC is associated with this fast decrease depends on the sign of ν. For $\nu > 0$, the exponential decrease occurs near $x = +\frac{L_D}{2}$; while for $\nu < 0$, the decrease is at $x = -\frac{L_D}{2}$. Fig. 6-2 shows $s(x)$ for a range of values of ν in a hypothetical sub-domain of length .1 cm. The small-$|\nu|$ curves have been normalized so that they equal the large-$|\nu|$ curves at $x = 0$. The curves have also been arbitrarily offset for clarity. The arrows mark the maxima of $s(x)$ and in the large-$|\nu|$ limit can be looked upon as approximately dividing the sample into linear and exponential regions. The linear dependence of $s(x)$ on x in the large-$|\nu|$ limit implies that U_s will vary as L_D^3. The scaling of U_s with L_D is directly demonstrated in Fig. 6-3 which plots the term in square brackets in Eqn. (6-19) at various values of α. Each curve shows the three regimes corresponding to $|\nu| << 1$ where $\frac{d[\log(U_s)]}{d[\log(L_D)]} = 5$, $|\nu| \sim 1$ which is a transition region spanning approximately a decade in L_D, and $|\nu| >> 1$ where $\frac{d[\log(U_s)]}{d[\log(L_D)]} = 3$. How U_s varies with sub-domain length has important consequences in the minimization of strain and phase-slip energies which will be discussed in part III.

As was mentioned earlier, experimental evidence[13] strongly suggests that the CDW damping γ depends on the low-field resistivity. We now incorporate this feature into the equations to form model 'B'. If the assumption is made that this dependence is through the carrier concentration (and not mobility effects), then Eqn. (6-8a) becomes

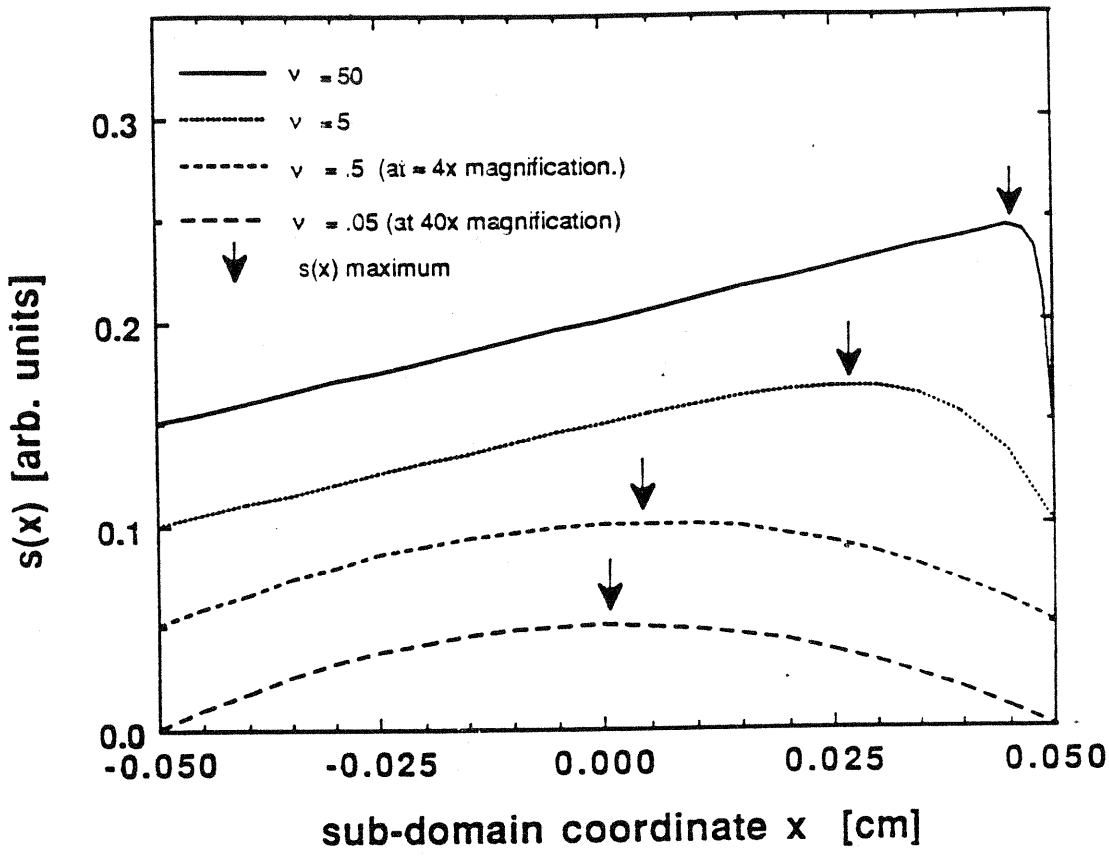

Fig. 6-2 shows s(x) at various values of v. For v small, s(x) shows a parabolic profile, while for large v, s(x) is predominantly linear except near one of the PSC's where it decreases exponentially fast. The curves have been arbitrarily offset for clarity and the small-|v| curves have been normalized so that they equal the large-|v| curves at x = 0.

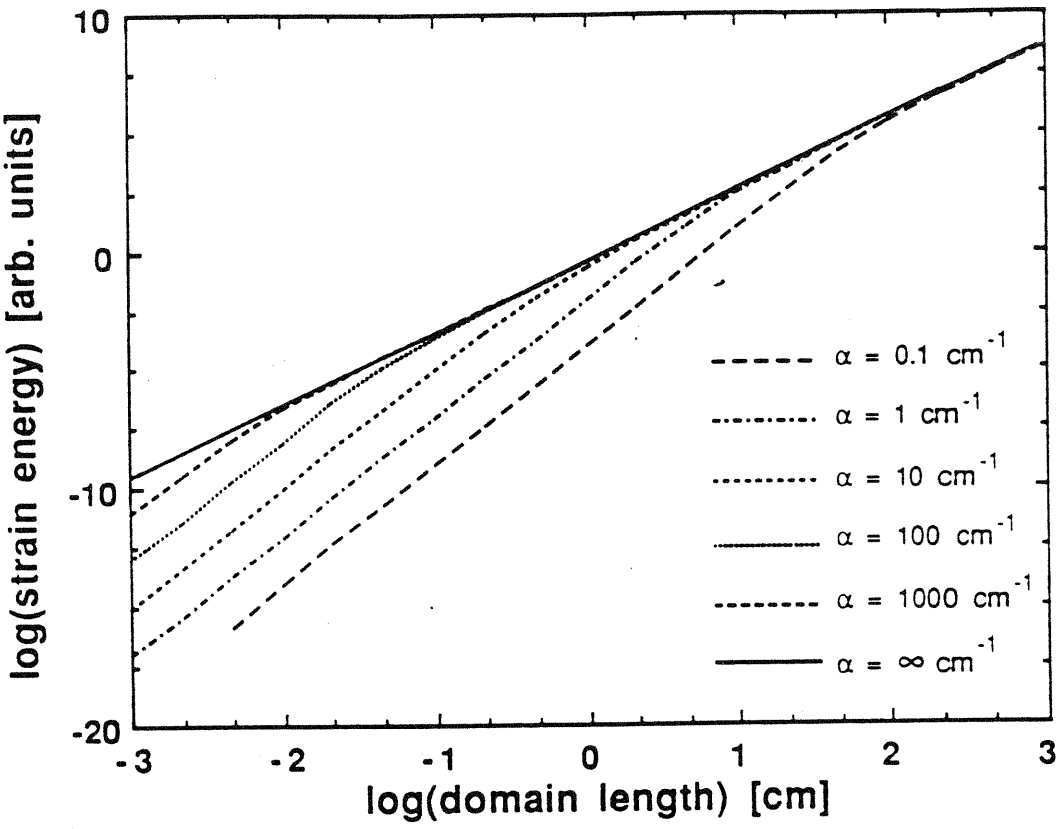

Fig. 6-3 These log-log plots show how the strain energy in a sub-domain scale with the size of the sub-domain with α as a parameter. Two regimes are clearly evident. The first has $U_s \sim L_D^5$ and scales with α; the second has $U_s \sim L_D^3$ and is independent of α. The transition between the two occur at a length scale $\sim \frac{1}{\alpha}$.

$$\gamma(x) = \gamma(T,s) \approx \gamma + \gamma' \frac{\Delta T}{L} x - \gamma_s s. \qquad (6\text{-}22a)$$

It will be convenient to define γ_s in terms of other parameters in the model and a free parameter r.

$$\gamma_s = \gamma \frac{\rho_s}{\bar{\rho}} r \qquad (6\text{-}22b)$$

Eqn. (6-22a) can be considered as the first order Taylor expansion for a bivariate function; the assumption has also been made that the local <u>total</u> carrier density is constant, and so, any decrease in CDW carrier concentration is accompanied by an increase in normal carrier concentration and vice versa. The constant γ_s is expected to be positive in order to be consistent with the experimental results. Incorporation of the above equation into the theory is straightforward and leads to nearly identical results except that Eqn. (6-13b) becomes modified to

$$\alpha'' = \frac{\rho_s E}{\kappa} (1 - r \eta_o) = \alpha (1 - r \eta_o) \qquad (6\text{-}23a)$$

$$\eta_o \equiv \frac{v_o \gamma}{\bar{\rho} E} . \qquad (6\text{-}23b)$$

The equation for v_o (Eqn. (6-15a)) then becomes a transcendental equation with a parameter ν'' in $\xi(\nu)$ analogous to α''. In the limit of small temperature gradient (i.e. $\frac{E'\Delta T}{E} << 1$ and $\frac{\gamma'\Delta T}{\gamma} << 1$), a good estimate for v_o can be obtained by setting $\eta_o = 1$ in ν''.[15] By making this approximation, one can proceed as before with the results

$$s''(x) = \frac{s(x)}{(1 - r)} \tag{6-24}$$

where $s(x)$ is the expression (6-17) with all the ν, α, and ε replaced with their double-primed counterparts.[16] Similarly, the strain energy (Eqn. (6-19)) becomes

$$U_s'' = \frac{U_s}{(1 - r)^2} \tag{6-25}$$

again with the substitution of the double-primed parameters for the unprimed ones. The net result of model 'B' is to scale ν and α directly and ε, $s(x)$, and $\sqrt{U_s}$ inversely with $(1 - r)$. There are other important consequences of the carrier-concentration-dependent damping which will be discussed in part IV.

III. Minimization of Energy

Having obtained expressions for the phase-slip and strain energies, the aim is now to minimize the sum of these energies:

$$U_{tot} = U_{TPS} + U_{ts} \tag{6-26}$$

where U_{TPS} is the total phase-slip energy which is given by Eqn. (6-2) and U_{ts} is the total strain energy given by

$$U_{ts} = \sum_{i=1}^{N} U_{si} \,. \tag{6-27}$$

The sum in Eqn. (6-27) is over the number of sub-domains and U_{si} is the strain energy of the $i^{\underline{th}}$ sub-domain which is of the form of Eqn. (6-19). The procedure to find the minimum energy sub-domain configuration is as follows:

1) For a fixed temperature gradient and bias current I_B, minimize U_{ts} by optimizing the locations of the PSC's. Do this for N = 1, 2, 3,.... This results in a series of minimum $U_{ts}(\Delta T, I_B, N)$ sequenced by N.

2) By inspection, find the N which minimizes the total energy U_{tot}.

In general, the difficulty lies in the calculation of 1). We will first set up the problem. Define a coordinate system p in a sample of length L with the origin at the center $(-\frac{L}{2} \leq p \leq +\frac{L}{2})$. Let the position of the $i^{\underline{th}}$ PSC be denoted by p_i with $0 \leq i \leq N$, $p_{i-1} < p_i$, $p_0 = -\frac{L}{2}$, and $p_N = +\frac{L}{2}$; the $i^{\underline{th}}$ sub-domain then lies between p_{i-1} and p_i and the PSC's fixed at $\pm\frac{L}{2}$ are the ones needed to interface

to the external current source. Inspection of Eqn. (6-19) reveals that the strain energy of the i^{th} sub-domain will depend on p_{i-1} and p_i in two ways. First, they will enter in the length dependence of the sub-domain $(p_i - p_{i-1}) \equiv L_{Di}$; and second, they will enter in the temperature dependence of the parameters E and γ which are defined to be the values of the electric field and the damping at the center of the sub-domain $p = \frac{1}{2}(p_i + p_{i-1}) \equiv \bar{p}_i$, i.e.

$$E_i = E_o + E' \frac{\Delta T}{L} \bar{p}_i \qquad (6\text{-}28a)$$

$$\gamma_i = \gamma_o + \gamma' \frac{\Delta T}{L} \bar{p}_i \qquad (6\text{-}28b)$$

where E_o and γ_o are the values of the electric field and damping at $p = 0$. The strain energy of the i^{th} sub-domain can then be considered a function of L_{Di} and $\bar{p}_i$,

$$U_{si} = U_s(L_{Di}, \bar{p}_i) \qquad (6\text{-}29)$$

where the function U_s is taken from Eqn. (6-19) with the substitutions $L_D \rightarrow L_{Di}$, $E \rightarrow E_i$, and $\gamma \rightarrow \gamma_i$. The total strain energy is

$$U_{ts} = \sum_{i=1}^{N} U_s(L_{Di}, \bar{p}_i) \quad . \qquad (6\text{-}30)$$

In principle, Eqn. (6-30) can be minimized by taking the partial derivatives with respect to the p_i; this yields N-1 equations for the N-1 unknowns. For a general function U_s, there is no guarantee of a unique solution; nor is there a guarantee that the solutions can be easily found. Only with certain restrictions on the function U_s can these difficulties be overcome.

A class of functions which overcome both difficulties is the class U_s which is only dependent on the variable L_D and whose first derivative $\frac{dU_s}{dL_D}$ has one-to-one mapping on the interval $0 \leq L_D \leq L$. Minimization of U_{ts} then yields the equations

$$\frac{\partial U_{ts}}{\partial p_i} = \frac{dU_s}{dL_D}(L_{Di}) - \frac{dU_s}{dL_D}(L_{Di+1}) = 0; \quad 1 \leq i \leq N-1. \qquad (6\text{-}31)$$

The obvious solution for Eqns. (6-31) are

$$L_{Di} = \frac{L}{N}; \qquad 1 \leq i \leq N, \qquad (6\text{-}32)$$

i.e. all the sub-domains are of equal size.

Examination of Eqn.(6-19) shows that $U_s(L_D, \bar{p})$ is only weakly dependent on $\bar{p}$; thus, it is reasonable to expect that the system will behave similarly to the $\bar{p}$-independent system. The weak dependence on $\bar{p}$ results from the fact that the variation of the strain energy with sub-domain position in the crystal is a first-order effect. Since the L_{Di} and the $\bar{p}_i$

are not independent variables, any change in the $\bar{p}_i$ to minimize the strain energy will be severely constrained by the much stronger dependence of the strain energy on the L_{Di}; therefore, the sub-domains should be of approximately equal sizes. The weak $\bar{p}$-dependence is confirmed by noticing that the <u>total</u> strain energy is only affected to second order in the variation of the $\bar{p}_i$ because the first order terms cancel in the summation in Eqn. (6-30). We will henceforth make the approximation that all the sub-domains are equal in size and that $E_i \approx E_o$ and $\gamma_i \approx \gamma_o$. Strictly speaking, however, the degree to which the $\bar{p}$-dependence is weak depends on the magnitude of the temperature gradient and that at sufficiently large temperature gradients the $\bar{p}$-dependence could become significant.

Calculation on the total strain energy U_{ts} is then straightforward especially in the limits of small or large $|v|$. The derivation will follow the large-$|v|$ limit; the derivation for the small-$|v|$ limit is similar and the results will just be listed. The strain energy of a single domain can be put in the form (in the limit $|v| >> 1$)

$$U_s = B(E_o, \Delta T, L_D) \left(\frac{\Delta T}{L}\right)^2 L_D^3 \qquad (6\text{-}33a)$$

$$B(E_o, \Delta T, L_D) = \frac{\frac{\kappa}{6}\left(\frac{\bar{\rho}}{\rho_s}\right)^2 \left(\frac{E'}{E_o} - \frac{\gamma'}{\gamma_o}\right)^2}{\left[1 - \frac{L_D\, \gamma'\, \Delta T}{2\, \gamma_o\, L}\, \xi\left(\frac{E_o}{\varepsilon}\right)\right]^2} \equiv B \qquad (6\text{-}33b)$$

where B is a function of E_o, ΔT, and L_D. The E_o dependence occurs in ξ and possibly in $\frac{E'}{E_o}$ if the sample is non-Ohmic. Besides the obvious presence of L_D and ΔT in the denominator, there is also a L_D dependence in ε. As a convenience, the naught subscript on E_o and γ_o will now be dropped. Finally, using Eqn. (6-32), B can be viewed as a function of N instead of L_D.

This last observation brings up the point that ν is also a function of N;

$$\nu = \frac{E}{\varepsilon} = \alpha \frac{L_D}{2} = \frac{\rho_s\, E\, L_D}{2\, \kappa} = \frac{\rho_s\, E\, L}{2\, \kappa\, N} \,. \qquad (6\text{-}34)$$

As N increases, ν decreases and so, for the large-$|\nu|$ limit to remain a valid approximation, it is necessary that $|\nu(N=N_{MAX})| >> 1$. Typically, for the ΔT experiments discussed in chapter 5, $N_{MAX} \sim 10$ and so $|\nu| >> 10$ for a single-domain sample would satisfy the requirements.

It can be argued that B is a weak function of its arguments. As long as the large-$|V|$ limit is valid, ξ depends only on the sign of its argument,

$$\xi\left(\frac{E}{\varepsilon}\right) \approx \text{sign}\left(\frac{E}{\varepsilon}\right).$$

In this case, ξ is independent of the magnitude of E; furthermore, ξ no longer has any N (or L_D) dependence. The ΔT and L_D dependences in B are relatively weak compared to these same factors multiplying B which will dominate the overall behavior; furthermore, these two factors work against each other because as ΔT increases, the number of sub-domains increase and L_D decreases. This leaves only the ratio $\frac{E'}{E}$. Since the total current density is a constant throughout the sample,

$$\frac{E'}{E} = -\frac{\sigma'}{\sigma},$$

where σ is the (possibly non-linear) conductivity with both CDW and normal carrier contributions; σ' is its temperature derivative. For an Ohmic sample, this ratio is independent of E. CDW materials, on the other hand, have intrinsically non-linear conductivities which depend on the E-field. At large electric fields, the conductivity saturates[17] and the ratio becomes only weakly dependent on E. This is the case here since it was originally assumed that the model applied

to the large electric field limit. Thus B can be considered a weak function.

If B is a sufficiently weak function, then it can be approximated by a constant. The total strain energy is then

$$U_{ts} = B \frac{(\Delta T)^2 L}{N^2} \equiv \frac{U_{s1}}{N^2} \tag{6-35}$$

where U_{s1} is the strain energy in a single-domain sample and is proportional to both ΔT^2 and L. By employing Eqns. (6-2) and (6-35), Eqn. (6-27) becomes

$$U_{tot} = (N-1)\ U_{PS} + \frac{U_{s1}}{N^2} \equiv U_N \ . \tag{6-36}$$

Eqn. (6-36) is the result that we were looking for. In (U_{tot}, U_{s1}) space, it describes a series of lines with decreasing slopes and increasing y-intercepts as N increases. Each line has a limited span on the domain U_{s1} where it has the lowest energy. By setting $U_N = U_{N+1}$, the transition from N domains to N+1 sub-domains is found to be

$$\frac{U_{s1}}{U_{PS}} = \frac{N^2\ (N+1)^2}{2N + 1} \equiv u_{N,N+1} \ . \tag{6-37}$$

In the limit of large N, this becomes

$$\lim_{N\to\infty} N = \left(\frac{2\ U_{s1}}{U_{PS}} \right)^{\frac{1}{3}} = \left(\frac{2\ B\ [\Delta T]^2\ L}{U_{PS}} \right)^{\frac{1}{3}} \ . \tag{6-38}$$

Fig. 6-4 shows the predicted number of sub-domains as determined by Eqn. (6-37) versus the normalized strain energy, U_{S1}/U_{PS}; the large N limit, Eqn. (6-38), is plotted also for comparison. Substituting Eqn. (6-38) for N in the expression for U_N (Eqn. (6-36)) yields an excellent approximation for the total energy as a function of U_{S1}:

$$\frac{U_N}{U_{PS}} \approx \frac{3}{2}\left(\frac{2\ U_{S1}}{U_{PS}}\right)^{\frac{1}{3}} - 1 \ . \qquad (6\text{-}39)$$

Fig. 6-5 shows that Eqn. (6-39) closely follows the exact result (obtained from Eqns. (6-36) and (6-37)) for $N > 3$.

Before proceeding to a discussion on the above model and a comparison with the experimental data, we list the results of a similar calculation in the limit of small $|v|$. The equations listed below are the analogs to Eqns. (6-36), (6-37), (6-38), and (6-33b) respectively. The corresponding variables and parameters are underlined to distinguish them from their large $|v|$ counterparts.

$$\underline{U}_{tot} = (N-1)\ U_{PS} + \frac{\underline{U}_{s1}}{N^4} \equiv \underline{U}_N \qquad (6\text{-}40)$$

$$\frac{\underline{U}_{s1}}{U_{PS}} = \frac{N^4\ (N+1)^4}{4N^3 + 6N^2 + 4N + 1} \equiv \underline{u}_{N,N+1} \qquad (6\text{-}41)$$

$$\lim_{N\to\infty} N = \left(\frac{4\ \underline{U}_{s1}}{U_{PS}} \right)^{\frac{1}{5}} = \left(\frac{4\ \underline{B}\ E^2\ [\Delta T]^2\ L^3}{U_{PS}} \right)^{\frac{1}{5}} \qquad (6\text{-}42a)$$

$$\underline{B} = \frac{\frac{\bar{\rho}^2}{240\ \kappa} \left(\frac{E'}{E} - \frac{\gamma'}{\gamma} \right)^2}{\left[1 - \frac{L\ \gamma'\ \Delta T\ \rho_s\ E}{12\ \gamma\ N^2\ \kappa} \right]^2} \qquad (6\text{-}42b)$$

In the equation for $\underline{B}$, the function $\xi(\nu)$ has been approximated by its small-$|\nu|$ limiting value. In this limit, the denominator will be very nearly equal to one due to the smallness of $\xi(\nu \to 0)$.

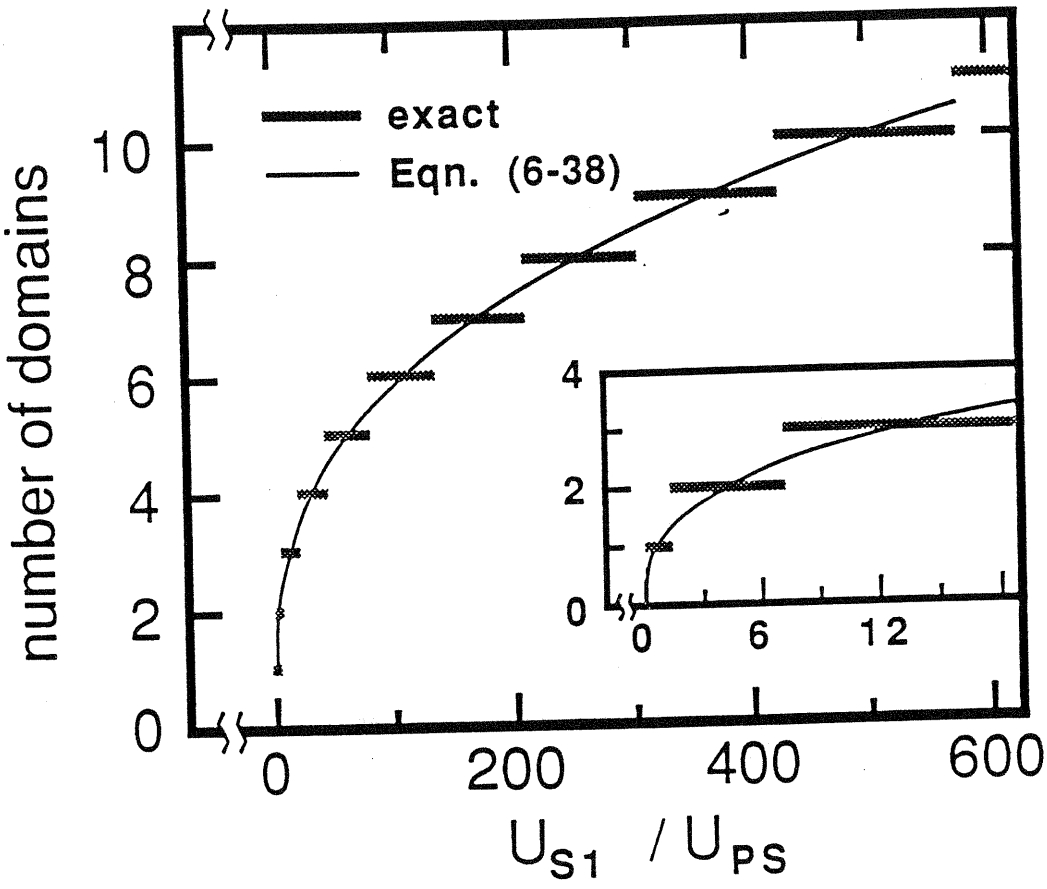

Fig. 6-4 Number of sub-domains N as a function of the normalized strain energy calculated for the model in the large-|v| regime (gray steps). Note that the step width increases as N increases. The approximate expression for N (Eqn. (6-38)) is also plotted for comparison (solid line). The inset shows the region near the origin.

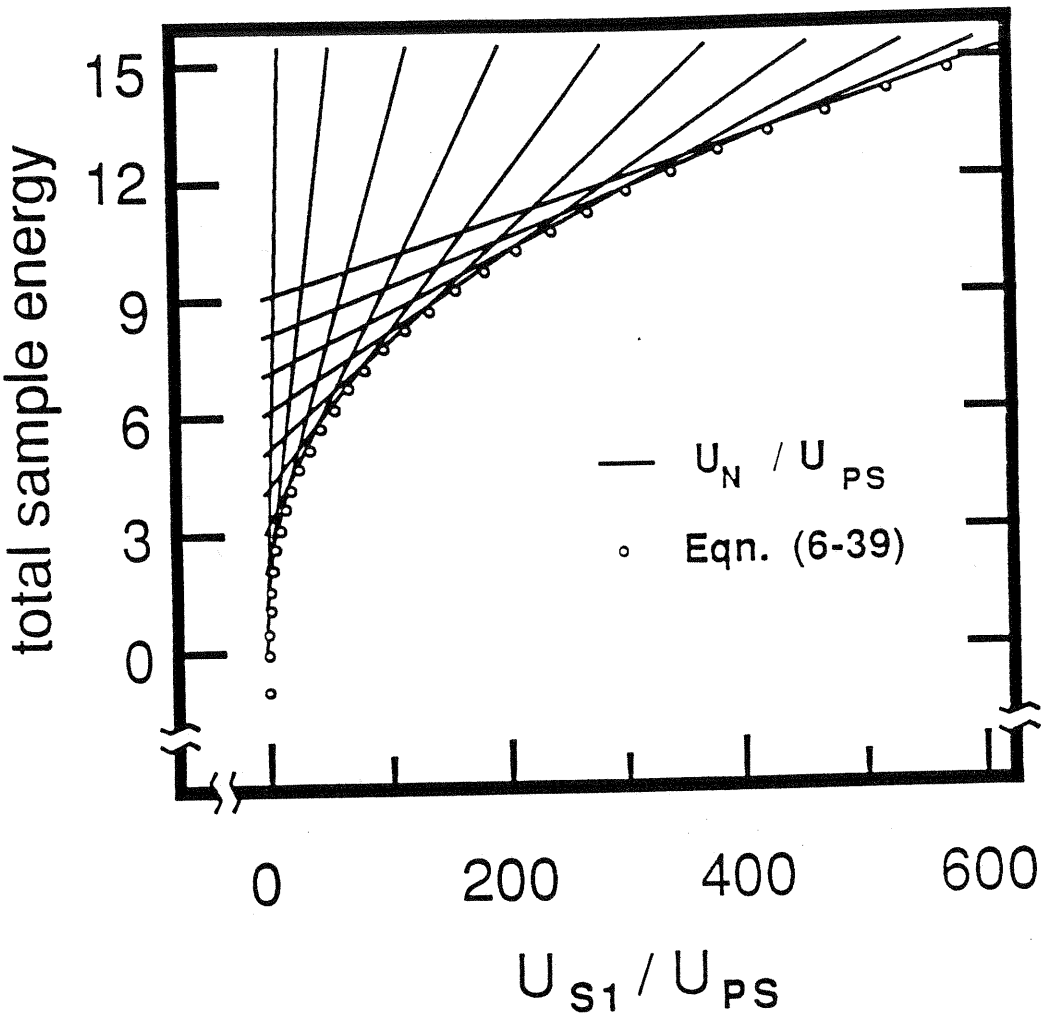

Fig. 6-5 Total (normalized) energy of the sample versus U_{S1}/U_{PS} for the model in the large-|V| regime. The total energy can be described be a series of lines whose slopes and y-intercepts depend on the number of sub-domains N. The line which gives the minimum energy determines how many sub-domains the CDW divides into. For N > 3, this energy is closely approximated by Eqn. (6-39) which is also plotted (hollow circles).

IV. Discussion

In this discussion, we will compare the predictions of the model to the experimental evidence, point out the consistencies and discrepancies, and provide insight into the physical processes which are thought to occur in this system. The main motivation for this experimental investigation and development of the model was the splitting of the CDW into a number of sub-domains with increasing temperature gradient; accordingly, this will be the first topic of the discussion.

Scaling of Sub-domains

The theoretical framework described here shows that N is an increasing function of ΔT because large applied temperature differences cause a considerable phase strain to build up within a moving CDW; splitting the CDW into velocity sub-domains reduces this strain at the cost of creating PSC's. The overall energy is reduced below the system energy if no PSC's had formed. The scaling behavior emerges quite naturally from the theory and depends critically on the sub-domain length dependence of the strain energy. As we have seen, the strain properties of the model have two regimes categorized by the parameter $|v|$. In the large-$|v|$ limit, the length dependence is $\sim L_D^3$, while in the small-$|v|$ limit, there is an approximate L_D^5 dependence. These length dependences propagate directly through to the scaling behavior and result in the large-$|v|$ regime having $N \sim \Delta T^{2/3}$, while the small-$|v|$

limit has $N \sim \Delta T^{2/5}$ (see Eqns. (6-38) and (6-42a) respectively).

There are some practical concerns in analyzing the scaling of sub-domain number with temperature gradient. The scaling quoted above is for the large N behavior; however, the experiments are always performed in the low N regime. It is probable then that there will be a bias present in a straightforward measurement of the scaling behavior. Furthermore, in analyzing the data from the experiments, it is convenient and useful to be able to use standard fitting procedures (such as least-squares) to determine the best estimate for the scaling coefficient. The scaling data, however, are in the form of a series of discrete step functions which are not a proper form for utilizing such procedures. The solution to these problems is discovered by noticing that the large-N limit approximation (Eqn. (6-38)) very nearly intersects the middle of each level of the step functions as seen in Fig. 6-4. The middle of these steps is

$$u_{mN} \equiv \frac{1}{2}\,(u_{N-1,N} + u_{N,N+1}) \tag{6-43a}$$

$$= \frac{2\,N^5}{4\,N^2 - 1} = \frac{\frac{N^3}{2}}{1 - \frac{1}{4N^2}} \tag{6-43b}$$

$$= \frac{B\;L\;\langle \Delta T_N^2 \rangle}{U_{PS}} \tag{6-43c}$$

$$\langle \Delta T_N^2 \rangle \equiv \frac{1}{2}\,\left[(\Delta T_{N-1,N})^2 + (\Delta T_{N,N+1})^2 \right] \tag{6-43d}$$

where $\Delta T_{N,N+1}$ is the temperature difference applied across the sample at which the number of sub-domains goes from N to N+1. The relation (6-43c) makes use of Eqn. (6-35) and assumes B is a constant. Notice in Eqn. (6-43b) that as $N \rightarrow \infty$, the middle of the step rapidly converges to a pure N^3 scaling behavior. Eqns. (6-43) suggest that the data can be fit to the equation

$$N = \Omega\,\langle \Delta T_N^2 \rangle^{\mu} \tag{6-44a}$$

or the equation

$$N' \equiv N\left(1 - \frac{1}{4N^2}\right)^{-\frac{1}{3}} = \Omega' \langle \Delta T_N^2 \rangle^{\mu'}. \qquad (6\text{-}44b)$$

A fit using Eqn. (6-44a) will give a good estimate of the scaling coefficient μ independent of the parameters in the model; however, a fit to this equation will have a bias associated with it if the data consist of values of N which are small; Eqn. (6-44b) removes this small-N bias (for large-$|\nu|$ limit only).

As described in chapter 5, the data from the experiments were fit to Eqns. (6-44) and resulted in values for the median of 0.35 for μ and 0.33 for μ'. (See Figs. 5-7 a and b.) These values are in excellent agreement with the system being in the large-$|\nu|$ regime and thus for the scaling to be $N \sim \Delta T^{2/3}$. In order for large-$|\nu|$ scaling to occur for a sample of ~.1 cm and for $1 \leq N \leq 7$, the minimum α needed is in the range between $500 \rightarrow 1000$ cm^{-1} (see Fig. 6-3). In the context of model 'A', a lower estimate of the magnitude of ρ_s can be made by using measurements of the parameters from these and other experiments: $\kappa \sim 10^9$ dynes/cm^2[18], $E \sim 4 \times 10^{-4}$ statV/cm, and $\bar{\rho} \sim 10^{12}$ esu/cm^3[19], yield $|\rho_s/\bar{\rho}| \sim 10^3$.

The estimate for the magnitude of ρ_s changes if model 'B' is considered. When s-dependent damping is included, the parameter α is multiplied by the factor (1 - r). Without a detailed knowledge of the CDW damping mechanism, little can

be said concerning the magnitude of the ratio r. Calculations by Littlewood[20] yield a damping term of the form

$$\gamma(s) \sim \frac{\bar{\rho}^2}{\sigma_n} \qquad (6\text{-}45a)$$

where σ_n is the contribution of the normal carriers to the conductivity. This suggests that the ratio $\frac{\gamma_s}{\gamma}$ is

$$\frac{\gamma_s}{\gamma} = \left[2 + \frac{\bar{n}}{n_n}\right] \frac{\rho_s}{\bar{\rho}} \qquad (6\text{-}45b)$$

or r is

$$r = \left[2 + \frac{\bar{n}}{n_n}\right] \qquad (6\text{-}45c)$$

where $\bar{n}$ is the CDW carrier concentration and n_n is the normal carrier concentration. In the lower CDW state of $NbSe_3$, the ratio $\frac{\bar{n}}{n_n}$ has been estimated to be ~ 1.5[21] and puts the multiplicative factor (1 - r) at -2.5. Although this does not substantially change the magnitude of ρ_s, it does yield a slight decrease in the estimate of $|\rho_s/\bar{\rho}|$ to ~ 400.

$NbSe_3$ is unique, however, in that it remains metallic at all temperatures, in contrast to the semiconducting-like CDW materials on which the original damping studies were performed.[13] Band structure studies on $NbSe_3$ calculate that the Fermi surface consists of five surfaces: 2 pairs of

plane-like surfaces which are responsible for the high and low temperature CDW transitions, and a partially closed surface presumably giving the material its non-vanishing metallic behavior.[22] This brings into question whether the n_n in Eqn. (6-45) should include all the normal charge carriers or only those carriers on the Fermi surface responsible for the CDW transition which remain due to thermal activation or imperfect nesting. If the latter possibility is correct, then there could be a substantial increase in the effective ratio $\frac{\bar{n}}{n_n}$. However, in the proposal by Littlewood, the CDW is damped through the screening effects of the normal carriers on the CDW and so any available normal carrier would be expected to contribute to the damping. Further investigation is needed to resolve this issue.

An important feature seen in the scaling of N with ΔT is the dependence of the scaling on the relative directions of the electric field and the temperature gradient (it exhibits the same symmetry as Eqns. (6-16)). Fig. 5-6 of chapter 5 indicates that this effect mainly causes a change in the parameter Ω (or Ω'). The predicted relation between this fitting parameter and the model is

$$\Omega \text{ (or } \Omega') = \left(\frac{2\ B\ L}{U_{PS}} \right)^{\frac{1}{3}}. \qquad (6\text{-}46)$$

In the denominator of the expression for B (see Eqn. (6-33b)), there is a factor which has the desired symmetry with respect to ΔT and E. It influences Ω as

$$\Omega \propto \left(1 - \frac{\Delta T \, \gamma'}{2 \, N \, \gamma} \xi(E) \right)^{-\frac{2}{3}}. \qquad (6\text{-}47)$$

It is this term which effectively changes Ω according to the relative direction of the temperature gradient and the electric field. In this respect, there is good qualitative agreement with experiment. The factors needed to explain the experimental data are rather large, however, and are out of the range of validity for the model. (For example, the experimental data show that Ω can change up to a factor of ~ 2 just by changing the direction of the electric field; see Fig. 5-6). An improved model would need to have an expression analogous to Eqn. (6-47) which saturated quickly; otherwise, the ΔT-dependence of this term would influence the scaling coefficient μ. Numerical simulations using Eqns. (6-33) show that although the scaling is still approximately $N \sim \Delta T^{2/3}$, there is a detectable change in μ comparable to the change in Ω. In contrast, the experimental data show that Ω can change appreciably while there is no detectable change in μ.

Eqn. (6-38) indicates that the number of CDW domains should increase with sample length as $L^{1/3}$ ($\nu >> 1$). This is in qualitative agreement with the results of experiments

on $NbSe_3$ where very short samples are not split by large gradients[23] while long samples are easily split by relatively small gradients.[23,24] Similarly, no change in the NBN spectrum of $NbSe_3$ crystals is observed when the length over which the temperature difference is applied is small.[25] In the small-|v| limit, the number of sub-domains should scale as $L^{3/5}$ (Eqn. (6-42a)). At present, there has been no direct measurement of the length dependence on the scaling of sub-domain number with ΔT; one could repeatedly measure the scaling behavior for a single sample successively shortening the sample each time.

Eqns. (6-33) shows that the expression for the strain energy is to first order independent of the electric field (in the large-|v| limit). As a result, changing E will not change the strain energy; and thus, the number of sub-domains is <u>not</u> dependent on the bias. Any change in E will be compensated by a change in the velocity, v_o, for the sub-domains. This is in contrast to the small-|v| limit which has $U_s \sim E^2$ and there should be a strong bias dependence on the number of sub-domains in the crystal. As reported in chapter 5, both types of behavior have been observed. Further investigation is needed to ascertain under what conditions will each of the respective behaviors be expressed and what role do impurities play in this process.

Finally, an important feature of the phase strain energy model is the ability to further resist splitting as the

number of sub-domains grows. This feature is apparent in the model by the step width of the sub-domain number:

$$\Delta u_N \equiv u_{N,N+1} - u_{N-1,N} = 2N^2 \frac{3N^2 - 1}{4N^2 - 1} \qquad (6\text{-}48a)$$

$$\lim_{N\to\infty} \Delta u_N = \frac{3}{2} N^2 , \qquad (6\text{-}48b)$$

i.e. as N increases, the step width increases as N^2. As the number of sub-domains grow, the sub-domain velocity can more closely match the velocity dictated by the local conditions. Further increases in the temperature gradient cause the velocity differences among the sub-domains to increase rather than causing a rapid increase in the strain energy. This provides an insight into why depinned CDW samples which appear to be split into multiple domains with no applied thermal gradient are not further split by the application of a gradient.[26] In these samples, the sizes of the zero gradient domains are relatively small, and, as a result, thermal strain energy sufficient to split them cannot develop. Effectively, an internal impurity gradient, analogous to a thermal gradient, already exists in the sample and as a result moderate thermal gradients cannot split apart the already divided domains.

Effect on the CDW Velocity

As we have seen both in the model and the observations of sliding CDW's in $NbSe_3$, the velocity of the CDW depends on the relative directions of E and ΔT. The reason behind this effect is quite simple: The total charge attributable to the CDW is not constant and depends on the relative direction of the temperature gradient with respect to the electric field. In model 'A', this has the single effect of changing the coupling to the electric field through $\rho_m(x)$ and therefore changes the total force on the CDW. As expected, when the average charge of the CDW is greater (less) than normal, the CDW moves faster (slower). This supposition is easily confirmed by calculating the spatial average of the charge in a single sub-domain (model 'A'):

$$\langle \rho_m(x) \rangle = \frac{1}{L_D} \int_D (\bar{\rho} - \rho_s \, s) \, dx = \bar{\rho} \, \eta(\Delta T, E) \qquad (6\text{-}49)$$

where η is the function which modifies the CDW velocity (Eqn. (6-15a)). In other words, the change in the CDW velocity can be attributed solely to the change in the average CDW charge density in model 'A'.

In model 'B', the situation is slightly more complicated because the damping is s-dependent also. Part of the velocity change Δv_c can be linked to the average change in

the coupling to the electric field and part to the change in the average damping,

$$\frac{\Delta v_c}{v_c(\Delta T=0)} = \frac{\langle \Delta\rho \rangle}{\bar{\rho}} - \frac{\langle \Delta\gamma \rangle}{\gamma} . \qquad (6\text{-}50)$$

It is easy to show that

$$\frac{\Delta v_c}{v_c(\Delta T=0)} \equiv \frac{v_o\, \gamma}{\bar{\rho}\, E} - 1 = \eta - 1 \qquad (6\text{-}51a)$$

$$\frac{\langle \Delta\rho \rangle}{\bar{\rho}} \equiv \frac{\langle \rho_m(x) \rangle}{\bar{\rho}} - 1 = \frac{1}{1-r}(\eta - 1) \qquad (6\text{-}51b)$$

$$\frac{\langle \Delta\gamma \rangle}{\gamma} \equiv \frac{\langle \gamma(x) \rangle}{\gamma} - 1 = \frac{r}{1-r}(\eta - 1) . \qquad (6\text{-}51c)$$

If $r > 1$, the change in the damping will dominate the change to the CDW velocity, i.e. the sign of the change in velocity will be opposite the sign of the change of the CDW charge density,

$$\frac{\Delta v_c / v_c}{\Delta\rho / \bar{\rho}} = 1 - r < 0 \quad ; \text{ if } r > 1. \qquad (6\text{-}52)$$

This shows that for model 'B', having less charge associated with the CDW does not necessarily imply that the CDW will

move at a slower velocity. Model 'A', on the other hand, predicts the two track each other exactly and is easily seen by setting r = 0 in Eqn. (6-52).

The crucial concept behind the above processes is that the total charge associated with the CDW can vary which then effects the dynamical properties. As previously discussed, the total charge varies through processes such as changes in the thermal activation and nesting of the Fermi surface. Variation in the relative amount of normal and CDW carriers can also explain the hysteresis seen in the dV/dI curves.

Hysteresis in the dV/dI curves.

Since the total charge density is assumed to remain a constant, any net decrease (increase) in CDW charge density will result in an increase (decrease) in normal-carrier charge density. Any property of the CDW material which is dependent on the concentration of CDW or normal electrons should be affected by these changes. In particular, the low-field resistivity will depend on the concentration of normal carriers. The model developed in this chapter does not apply in the low-field limit; however, it is certainly reasonable to expect that the system behaves in a qualitatively similar manner. For instance, consider a sample containing an undistorted CDW, with zero bias, and with an applied temperature gradient. As the electric field is increased, there will come a point where one end of the sample (the hot end in these experiments) will be at the threshold field

while the other end will be below threshold. Thus, the CDW will start to slide at one end, yet remained pinned at the other. Depending on whether the CDW at the sliding end is entering or leaving the sub-domain, the average strain of the CDW will either increase or decrease. Accompanying this will be a corresponding change in the relative number of normal and CDW carriers. This one-sided sliding will continue until the elastic forces build and cause either the pinned side to break free or the sliding side to come to a stop.

The hysteretic differential resistance curves are explained by making one additional assumption: Below the threshold electric field, the impurities present in the sample prevent the distortions of the CDW from relaxing. With this assumption, the change in the respective carrier densities is frozen into place until an electric field directed in the opposite direction with a magnitude on the order of the minimum threshold field in the sample is applied. At that time, the sign of the strain will be reversed resulting in the carriers with a surplus decreasing in number and the depleted carriers increasing. The hysteresis observed in the dV/dI curves records this process by monitoring the total number of normal carriers through their effect on the low-field resistance.

If we continue with the assertion that the model qualitatively applies to the low-field regime, the effect on the CDW velocity is tentatively linked to the hysteretic dV/dI curves in the sense that they are both caused by the

relative changes in the number of normal and CDW carriers. If the model were rigorously valid in the low-field regime, the relationship would be

$$\frac{\Delta v_c}{v_c(\Delta T=0)} = (1 - r) \frac{\Delta R_o}{R_o(\Delta T=0)} \qquad (6\text{-}53)$$

where R_o is the low-field (Ohmic) resistance. Looking at the data (Figs. 5-8 and 5-9 are from the same sample.) reveals that model 'B' is consistent with the data provided that $r > 1$, while model 'A' ($r = 0$) is not. Note that the increased (Ohmic) differential resistance is associated with the conditions producing the slow CDW velocity. The increased value of dV/dI implies depleted normal carriers which in turn implies surplus CDW carriers and, in the context of model 'A', this implies a fast CDW which disagrees with the data. Only model 'B' can account for the data; with $r > 1$, the relative changes of v and R_o can be negative with respect to each other as indicated by Eqn. (6-53). The data can also yield an estimate for the magnitude of r by comparing the magnitude of the relative changes. This yields an estimate of $r \sim 51$ which should be compared to the theoretical estimate of 3.5 given earlier.

There are additional indications that these two effects are related. The dV/dI data (Fig. 5-9a) show an asymmetry between positive and negative temperature gradients in the size of the hysteresis loops. There is also an asymmetry in

the NBN data with respect to the direction of the temperature gradient (Figs. 5-8). Notice that the height of the hysteresis loop and the difference of the two f_{NBN} vs ΔT slopes are larger when the temperature gradient is negative compared to when it is positive. Both model 'A' and 'B' predict there should be no asymmetry; however, as discussed below, defects or impurities could cause such an effect. What is interesting is that the relative change in going from positive to negative temperature gradients on both sets of data is approximately the same (about a factor of 2); this is perhaps an indication of a relationship between the two. Further experiments need to be done in order to test the degree of correlation between these two effects.

There are other interesting implications and interpretations concerning CDW's. For instance, any inhomogeneity in the sample which causes a spatially non-uniform CDW mobility (such as inhomogeneous threshold field, damping, electric field, etc.) could also produce a hysteretic dV/dI. In the above model, the temperature gradient produced the inhomogeneity via the temperature-dependent damping and E-field; other possible conditions where the hysteresis could be observed are non-uniform doping or irradiation, asymmetric electrical contacts, and inhomogeneously distributed defects and impurities. Such hysteretic dV/dI curves are in fact commonly seen[27] and, in one case for a 'switching' sample, the sample was shown to be inhomogeneous with the hysteretic dV/dI curve originating

from a non-switching segment of the crystal.[28] In such samples, one would expect that the CDW velocity would also be affected, i.e. a shift in the NBN frequency with a reversal of the bias direction ($\Delta T = 0$) or the symmetry represented by Eqns. (6-16 a) and b) is broken such as was seen above. As of yet, this has not been tested in detail.

Another implication is that this effect allows the determination of whether a CDW is hole-like or electron-like in the sense that it determines which direction the CDW moves in response to an electric field. The basic premise is that if the velocity of the CDW is directed parallel to the hot-to-cold (fast-to-slow) direction, then the CDW will tend to be compressed. On the other hand, if the CDW is traveling in the cold-to-hot (slow-to-fast) direction, the CDW will be extended. These respective strains imply corresponding CDW and normal carrier concentrations; the latter can be detected through the low-field resistance. In the context of model 'B', the data imply that the low-temperature CDW in $NbSe_3$ is <u>hole-like</u>. The evidence is compiled as follows. The sign of the change of the low-field resistance is determined by a number of factors,

$$\text{sign}\left(\Delta R_o\right) = - \text{sign}\left[\Delta T \bullet E \bullet e^* \bullet n_s \bullet \left(\frac{E'}{E} - \frac{\gamma'}{\gamma} \right)\right] \qquad (6\text{-}54a)$$

$$\rho_s = e^* \, n_s \qquad (6\text{-}54b)$$

$$\bar{\rho} = e^* \, \bar{n} \qquad (6\text{-}54c)$$

$$n_s \equiv - \frac{d\bar{n}}{ds} \qquad (6\text{-}54d)$$

where e^* is the effective charge of the CDW and n is the concentration of CDW carriers. For the temperature range considered here, the quantity $\left(\frac{E'}{E} - \frac{\gamma'}{\gamma} \right)$ equals the temperature derivative of $\log(v_c)$ and is positive. n_s is positive as determined through the relationship (6-22b) and the fact that γ, γ_s, $\bar{n}$, and r are all positive. The signs of ΔT and E are laboratory-controlled parameters. Eqn. (6-54a) can be rearranged to yield

$$\text{sign}(e^*) = - \text{sign}\left[\Delta T \bullet E \bullet \Delta R_o \bullet n_s \bullet \left(\frac{E'}{E} - \frac{\gamma'}{\gamma} \right)\right]. \qquad (6\text{-}55)$$

Plugging in the results from the experiments shows that $\text{sign}(e^*) = +1$. (For example, with $\Delta T < 0$ and $E > 0$, the data show $\Delta R_o > 0$; see Fig. 5-9a.)

At very large temperature gradients, the hysteresis of the dV/dI curves qualitatively changes. Distinct step-like features appear in the lower-resistance section of the hysteresis loop and the overall flatness of the curve is greatly diminished; it is not entirely clear if there are step-like features in the upper part of the loop (see Fig. 5-9b). The data suggest that the CDW reverses its strain in finite sections. Each step in the dV/dI corresponds to a distinct section of the crystal reversing its relative proportion of CDW and normal carriers. A possible explanation for this behavior is that the crystal 'remembers' the sub-domain configuration at the time of pinning. A sample with a large temperature gradient will divide into multiple sub-domains. As the bias is lowered, a point will be reached where the CDW at the cold end of the coldest sub-domain will repin. The unpinned CDW at the end of this sub-domain will momentarily slide until the strain quickly builds and forces it to stop. The adjacent sub-domain continues to slide. Eventually, when the bias is reduced further, the cold end of the next sub-domain repins. At that time, the strain profile of the first sub-domain is locked in by the impurities. The process continues until all the sub-domains are repinned. The end result is a sequence of "strain sub-domains" along the crystal. As the bias is increased in the opposite direction, the warm end of the warmest strain sub-domain depins and reverses the strain profile. The depinning

process then continues in a analogous manner to the repinning process.

There is no reason to expect that the sub-domain configuration in the depinning or repinning processes are stable or exactly reproducible in these highly complex systems as is evident in the dV/dI curves which consistently show step-like features but not at identical locations nor are they identical in number. One aspect of the data worth noting is that after the steps, the dV/dI curves are relatively flat and indicate that the CDW is still pinned. This suggests that even after the strain has reversed, there is another blocking mechanism preventing the CDW from sliding. The apparent lack of step features in the upper part of the hysteresis loop could indicate an inconsistency in the above scenario or perhaps they are present but too numerous and small to be detected (The upper loop is associated with the conditions where the CDW tends to divide into many sub-domains). At present, there is insufficient data to completely explain the process behind the large-ΔT differential resistance curves.

Estimation of parameters.

We will now compare the model's predictions regarding the magnitude of the effects with the experimental data. Some of the parameters can be estimated from measurements on isothermal samples, while the others are estimated from the ΔT experiments themselves. One of the conditions assumed to

be valid was that $\frac{\kappa' \Delta T}{\kappa} << 1$. This ratio can be estimated by assuming that $\kappa \sim Y_o - Y_\infty \equiv \Delta Y$, where Y_o and Y_∞ are the Young's moduli in the limit of small and large electric fields respectively ($Y_o = Y(E \rightarrow 0)$; $Y_\infty = Y(E \rightarrow \infty)$). This estimate for κ results from experiments which measure the change in the Young's modulus of the CDW material as a function of electric field.[18,29,30] At a sufficiently large dc electric field, the CDW begins to slide with respect to the lattice; accompanied with this onset of CDW motion is a reduction in the Young's modulus. The CDW possesses a very non-linear conductivity as a function of E. The differential resistivity and the E-field-dependent Young's modulus track each other closely with both saturating at large electric fields. The conventional wisdom regarding this phenomenon is that the CDW has an elasticity which contributes to the lattice elasticity when the CDW is pinned to the lattice. As the CDW velocity increases, the coupling of the CDW elasticity to the lattice decreases. Thus, by measuring the change in the Young's modulus, one can estimate the pinned CDW's contribution to the total elasticity of the lattice. One can then interpret this contribution to be an estimate for the magnitude of the CDW's elasticity. The ratio $\frac{\Delta Y}{Y}$ has been measured as a function of temperature for $TaSe_3$[18] and yields $\frac{\kappa'}{\kappa} \approx -8 \times 10^{-3}\ K^{-1}$. For moderate ΔT, the relation $\frac{\kappa' \Delta T}{\kappa} << 1$ will hold.

In the temperature range of the experiments, the quantity $\left(\frac{E'}{E} - \frac{\gamma'}{\gamma} \right)$ equals the temperature derivative of

$\log(v_c)$ ($\frac{\partial \bar{\rho}}{\partial T} \approx 0$ in this temperature range) and can be measured directly from a NBN frequency versus temperature curve (recall that f_{NBN} is directly proportional to v_c). The estimate for this quantity is ~ 0.05 K^{-1} (Fig. 5-2; I_B = 80 μA). As previously estimated r ~ 51 which implies a minimum estimate for $\frac{\rho_s}{\bar{\rho}}$ ~ 20. Other quantities of interest are L = .1 cm and $\kappa \sim 10^9$ dynes/cm^2[18]. In order to calculate the energy U_{s1} to compare with the PSC energy U_{PS}, two additional pieces of information are required. The first is the temperature difference where the sample first divides into two sub-domains and is ΔT ~ 2 K; the second is an averaging factor which allows comparison between the strain energy and the PSC energy.

This factor is needed because theories on the nature of phase slip often consider the PSC as a dynamic object which either moves within the sample or only exists for a short period of time. Estimates of the PSC energy, however, often consider the PSC as static. For example, in the theory of phase vortices, the phase vortex is considered a defect in the CDW 'lattice' and associated with this defect is an energy. In response to an advancing CDW, the phase vortex moves perpendicular to the CDW, sinking or sourcing CDW phase as it travels. In the time period where the CDW advances by 2π (T_{NBN}[31]), the phase vortex will have swept out an area A_{pv}. Hence, it is the strain energy in the volume L x A_{pv} which should be compared to the phase slip energy.

In another example, the numerical simulations of Batistic´ et al.[32], which are based on the microscopic CDW equations in one dimension, show that phase slip occurs by having the order parameter periodically vanish. Compared to the overall period where the CDW advances by 2π, the time scale of the actual phase slip is quite short. The appropriate phase-slip energy for comparison to the strain energy is the time-averaged energy associated with the CDW amplitude collapse.

Independent of the phase-slip model, one can account for the average energy of the above phase-slip processes by introducing an averaging factor ϖ:

$$U_{ps} = \varpi\, U_{pv} = \varpi\, N(E_F)\, \Delta^2\, \xi_{\parallel}\, \xi_{\perp}^2 \ . \qquad (6\text{-}56)$$

This average energy should be compared to the strain energy in the volume $\xi_{\perp}^2$ x L. For the first example given above, ϖ can be associated with ratio $\xi_{\perp}^2 / A_{pv}$, while for the second example, ϖ represents the 'duty-cycle' of the phase-slip process. Using $\xi_{\perp} \approx 10$ Å, the strain energy in the volume $\xi_{\perp}^2$ x L is $\sim 10^{-2}$ meV. The estimate for U_{pv} is of the order of 100 meV; hence, $\varpi \sim 10^{-4}$. In relation to the above phase-slip examples, this value of ϖ implies that the phase vortex covers an area $10^4\ \xi_{\perp}^2$ during the NBN period or that the phase-slip occurs on a time scale of $\sim 10^{-4}\ T_{NBN}$. Given the large uncertainties associated with the parameters of the model, it

is perhaps more appropriate to specify a range for ϖ: $10^{-2} \leq \varpi \leq 10^{-6}$. Furthermore, the reader is reminded that the above analysis is based on the lower-bound estimate of $\rho_s/\bar{\rho}$; larger values of this ratio will reduce the strain energy estimate and consequently reduce the estimate for ϖ.

Table 6-1 compares the relative changes of various parameters between the predictions of the model and the measurements of experiments. The relative changes in the CDW velocity and low-field resistance are related through r and so the theoretical estimates disagree with the experimental ones by the same factor of ~ 4. The model predicts that the average charge associated with the CDW changes $\left(\frac{\langle\Delta\rho\rangle}{\bar{\rho}}\right)$; assuming that $\frac{\langle\Delta\rho\rangle}{\bar{\rho}} \sim \frac{\langle\Delta\rho_c\rangle}{\rho_c}$, (see Eqn. (6-3))this should, in principle, be detectable through a change in the intensity of CDW superlattice spots in an x-ray scattering experiment. The relative change, however, is rather small and a long signal integration time would be needed to detect the changes. No scattering experiments have been performed on non-isothermal samples; there have been experiments on isothermal ones to detect changes in the CDW wave vector.[33]

In these isothermal experiments, there is the possibility of detecting a change through the internal polarization of the sample. dV/dI studies suggest that the total charge associated with the CDW does <u>not</u> change; the charge <u>is</u> redistributed in the sample though.[34] In this case, any attempt to detect this redistribution by x-rays would require judicious choices for the beam size and location in

addition to having the necessary resolution. None of the experiments have detected any change in the CDW wave vector *along the chain direction* whether it be the intensity, position, or width of the superlattice spots.[33] The lack of detecting any relative change in the CDW wave vector (which corresponds to the position of the superlattice spots in reciprocal space) can be explained by the model's prediction of a very small relative change in $\frac{\langle \Delta Q \rangle}{Q}$. The magnitude of this change is even smaller than the relative change in the average CDW charge. A minimum of an order of magnitude improvement in the resolution is needed to detect a shift in Q. Assuming the necessary resolution can be achieved, it would be useful to perform x-ray scattering experiments on non-isothermal crystals to detect a shift in Q and $\bar{\rho}$.

A change has been detected for the wave vector *transverse to the chain direction* in $K_{0.3}MoO_3$; this is related to the shearing of the CDW and the evidence suggests that it is primarily caused by inhomogeneity in the electric field or caused by defects and impurities.[35] Due to the strong anisotropic nature of these materials, shearing of the CDW is expected to be much easier than the longitudinal compression or dilation.[10] The reader is reminded again that the estimates of Table 6-1 are based on the lower-bound estimate of the ratio $\rho_s/\bar{\rho}$.

Parameter	Theory	Experiment
$\left\lvert \frac{\Delta v_c}{v_c} \right\rvert \sim \left\lvert \frac{1}{2}\left(\frac{E'}{E} - \frac{\gamma'}{\gamma}\right) \right\rvert$	$0.025\ K^{-1}$	$0.11\ K^{-1}$
$\left\lvert \frac{\Delta R_o}{R_o} \right\rvert \sim \left\lvert \frac{1}{2(1-r)}\left(\frac{E'}{E} - \frac{\gamma'}{\gamma}\right) \right\rvert$	$5\times10^{-4}\ K^{-1}$	$2\times10^{-3}\ K^{-1}$
$\left\lvert \frac{\langle\Delta\rho\rangle}{\bar{\rho}} \right\rvert \sim \left\lvert \frac{1}{2(1-r)}\left(\frac{E'}{E} - \frac{\gamma'}{\gamma}\right) \right\rvert$	$5\times10^{-4}\ K^{-1}$	?
$\left\lvert \frac{\langle\Delta Q\rangle}{Q} \right\rvert \sim \left\lvert \frac{\bar{\rho}/\rho_s}{2(1-r)}\left(\frac{E'}{E} - \frac{\gamma'}{\gamma}\right) \right\rvert$	$2.5\times10^{-5}\ K^{-1}$	ref. (36) $< 3.6\times10^{-4}$

Table 6-1 Comparison of theoretical and experimental estimates of the modification of various parameters in a sample with an applied temperature gradient. The theoretical estimates are based on $\left(\frac{E'}{E} - \frac{\gamma'}{\gamma}\right) = 0.05\ K^{-1}$, $r = 51$, and $\frac{\rho_s}{\bar{\rho}} = 20$

One aspect of real CDW systems that is absent in the model is the lack of a remnant polarization or strain in the low-field limit. Although there are many experiments which demonstrate these polarization effects, there are two which directly show the spatial variation of the polarization through the measurement of the local dV/dI curve by Brown et al.[34] and the local pulsed resistance measurements of Mihály et al.[6] The experiments were performed on samples which, in addition to the normal current and voltage contacts, had been effectively divided into two segments by the introduction of a non-perturbative contact in the middle. They both show that while the total resistance of a sample does not change, the resistance of the two ends do. The dV/dI curves from the individual segments strongly resemble the hysteretic dV/dI curves seen in these ΔT experiments and showed the two segments traversing the hysteresis loops in opposite directions. Thus, while the total dV/dI curve showed no hysteresis loop, the two individual curves did. As originally proposed by Mihály et al., this can be explained if the CDW deforms in a way where the total number of CDW or normal carriers do not change, yet there is a change when looking at the carriers within the individual segments.

For the model, on the other hand, as ΔT or E goes to zero, so does the CDW deformation. There are two main reasons for this. The first is the absence of defects and impurities in the model (with the accompanying threshold field). The second is the assumed boundary conditions for

the PSC's ($s = 0$). It was originally suggested that the boundary conditions for the PSC's at $E > E_T$ (i.e. $|v_o| > 0$) correspond to whether the PSC was acting as a sink or a source. In particular, one should push the CDW into a sink and pull it out of a source. This corresponds to $s_{sink} < 0$ (compression) and $s_{source} > 0$ (extension). Since the role of the PSC's will be reversed when the E-field is reversed and this should happen in a continuous manner, a reasonable boundary condition for the PSC's to have is

$$s_{\substack{L \\ R}} = \pm S_v v_o \qquad (6\text{-}57)$$

where $S_v > 0$, s_L and s_R are the boundary conditions for the left ($x = -\frac{L_D}{2}$) and right ($x = +\frac{L_D}{2}$) PSC's respectively. With this modification, the CDW will be polarized for $E \neq 0$ and $\Delta T = 0$.

It is not clear what the boundary conditions become for $E < E_T$. One might consider that the CDW is pinned at the contacts[10] ($\phi_L = \phi(-L/2) = 0 = \phi(+L/2) = \phi_R$). Even then, the model itself breaks down in the large-$|v|$ limit with $|s| \rightarrow \frac{\bar{\rho}}{\rho_s}$, i.e. all the charge leaves the CDW (it all piles up at one of the PSC's). The reason for this breakdown is that when the CDW is moving at a velocity v_o, the damping force γv_o either exactly cancels out the force from the E-field if $\Delta T = 0$, or nearly cancels it out for $\Delta T \neq 0$. Any residual force remaining will be small and this causes the CDW to

deform. However, when $v_o = 0$, the electric field will couple to the elastic medium of the CDW fully and cause large deformations. The small-|v| limit does not suffer this fate, yet only gives results consistent with the $\Delta T = 0$ data. The reason for this stems from the boundary conditions $\phi_L = 0 = \phi_R$ which prevents any net change in the total numbers of normal and CDW carriers. The original ansatz of having the impurities 'freeze' in the strain profile as E decreases below threshold is the most consistent with the data.

Conclusion

We have developed a model which describes a sliding CDW in the presence of an applied temperature gradient. The model is based on the idea that a CDW behaves similarly to an elastic medium. We have shown that the hypothesis whereby a sliding CDW will divide into velocity sub-domains in order to minimize its energy in the presence of a temperature gradient, describes accurately the scaling behavior actually seen in $NbSe_3$ and which can be roughly stated as: the number of sub-domains scales as $\Delta T^{2/3}$. A key feature of the model is that the accumulation of strain in the CDW causes a modification in the local concentrations of CDW and normal carriers. In the laboratory, the system can be described as being in one of two states corresponding to whether, overall, the CDW is compressed or extended; or alternatively, which of the carriers (normal or CDW) is depleted and which has a surplus. If the electric field is above the threshold field,

which state the system is occupying depends solely on the relative directions of the electric field and the temperature gradient. This change in the carrier concentrations affects many of the properties of the CDW and of the material.

Two such properties are the low-field resistance and the CDW velocity. Each shows a dramatic shift in going from one state to the other. The model tentatively links these two effects in that they are both caused by the change in the carrier concentrations; experimentally, there is evidence that the two are correlated. More specifically, the change in the CDW velocity appears to be dominated by a change in the damping of the CDW, while the change in the low-field resistance is strictly dominated by the change in the normal carrier concentration. The hysteresis loop, which is present at low-fields in the differential resistance curves, most likely originates from the pinning of the CDW by impurities and defects in the crystal which cause the strain profile of the CDW is to be 'frozen' into place until an electric field of sufficient strength can overcome the pinning.

Contained in the model are a number of implications and predictions. The most interesting of which is the ability to determine the direction a CDW moves in response to an electric field. For the lower-temperature CDW in $NbSe_3$, the CDW is hole-like in that it moves in the same direction as the electric field. The model predicts that any action or circumstance which causes an inhomogeneity in the CDW mobility, will cause the dV/dI to become hysteretic and the

CDW velocity to shift in magnitude upon reversal of the electric field. If the inhomogeneity is severe enough the sample will most likely divide into velocity sub-domains.

Although the model explains many facets surrounding the phenomena of a moving CDW in a temperature gradient, there are issues left unresolved. Most of these involve the understanding of the microscopic processes behind this macroscopic model. Questions remain concerning the exact nature of phase-slip and what boundary conditions do they impose on the CDW. Furthermore, while there has been significant effort in understanding the CDW damping mechanism, there has been very little concerning the effect of modifying the CDW wave vector has on the nesting properties of the Fermi surface and; more particularly, on its effect on the CDW carrier concentration. At present, directly measuring this effect through scattering experiments is beyond modern resolution capabilities. In conclusion, however, it is apparent that the model presented here describes in detail the basic physical processes occurring in these systems. It has united a number of phenomena under a single theory. While, the theory might be lacking in some of the finer details of these phenomena, we strongly believe that the basic physical processes have been identified.

[1]P. A. Lee, T. M. Rice, and P. W. Anderson, *Solid State Commun.* **14**, 703 (1974).

[2]H. Fukuyama and P.A. Lee, *Phys. Rev. B* **17**, 535 (1978);
P. A. Lee and H. Fukuyama, *Phys. Rev.* B **17**, 542 (1978);
P.A. Lee and T.M. Rice, *Phys. Rev.* B **19**, 3970 (1979).

[3]L. Sneddon, M.C. Cross, and D.S. Fisher, *Phys. Rev. Lett.* **49**, 292 (1982).

[4]Also see the review articles, G. Grüner and A. Zettl, *Phys. Rep.* **119**, 117 (1985);
P. Monceau in *Electronic Properties of Quasi-One-Dimensional Materials*, Vol. II, P. Monceau, ed. (Reidel, Dordrecht, The Netherlands 1985), p. 139.

[5]See *Charge Density Waves in Solids*, Gy. Hutiray and J. Sólyom eds. (Springer-Verlag, New York, 1985) pages 367-458.

[6]L. Mihály, G. Mihály, and A. Janossy, *Charge Density Waves in Solids*, Gy. Hutiray and J. Sólyom eds. (Springer-Verlag, New York, 1985) page 404.

[7]This is primarily caused by the change of threshold field with temperature.

[8]M. F. Hundley, thesis, University of California, Berkeley, CA (1988).

[9]N.P. Ong, G. Verma, and K. Maki, *Phys. Rev. Lett.* **52**, 663 (1984);
G. Verma and N.P. Ong, *Phys. Rev.* B **30**, 2928 (1984).

[10]D. Feinberg and J. Friedel, *J. de Physique* **49**, 485 (1988).

[11]A. Zettl and G. Grüner, *Phys. Rev.* B **29**, 755 (1984).

[12]L. Sneddon, *Phys. Rev.* B **29**, 719 (1984).

[13]R. M. Fleming, R. J. Cava, L. F. Schneemeyer, E. A. Rietman, and R. G. Dunn, *Phys. Rev.* B **33**, 5450 (1986).

[14]The sinusoid in the figure does <u>not</u> represent the CDW charge density, i.e., Eqn. (6-3). Rather it figuratively represents the CDW as an elastic medium, in this case, a spring. The physical displacement of the spring from equilibrium is proportional to $\phi(x)/Q$.

[15]This has been verified numerically.

[16]With $\eta_o = 1$, i.e. ν, α, and $\frac{1}{\varepsilon}$ all are multiplied by the factor (1 - r).

[17]P. Monceau, N. P. Ong, A. M. Portis, A. Meerschaut, and J. Rouxel, *Phys. Rev. Lett.* **37**, 602 (1976).

[18]G. Mozurkewich, P. M. Chaikin, W. G. Clark, and G. Grüner, *Solid State Commun.* **56**, 421 (1985).

[19]i.e. $n \sim 2 \times 10^{21}$ cm^{-3}; G. X. Tessema and N. P. Ong, *Phys. Rev.* B **23**, 5607 (1981).

[20]P. B. Littlewood, *Phys. Rev.* B **36**, 3108 (1987)

[21]N. P. Ong and P. Monceau, *Phys. Rev.* B **16**, 3443 (1977)

[22]N. Shima, *J. Phys. Soc. Japan* **51**, 11 (1982);
N. Shima, *J. Phys. Soc. Japan* **52**, 578 (1982);
also see Appendix B.

[23]X.J. Zhang and N.P. Ong, *Phys. Rev.* B **30**, 7343 (1984).

[24]M.F. Hundley and A. Zettl, *Phys. Rev.* B **33**, 2883 (1986);
S.E. Brown, A. Janossy, and G. Grüner, *Phys. Rev.* B **31**, 6869 (1985);
J.W. Lyding, J.S. Hubacek, G. Gammie, and R.F. Thorne, *Phys. Rev.* B **33**, 4341 (1986);
The experiments of Chapter 5 also confirm this.

[25]P. Monceau, M. Renard, J. Richard, M.C. Saint-Lager, and Z.Z. Wang, *Charge Density Waves in Solids*, Gy. Hutiray and J. Sólyom eds. (Springer-Verlag, New York, 1985) page 279.

[26]M.F. Hundley and P. Parilla (unpublished).

[27]N. P. Ong, D. D. Duggan, C. B. Kalem, and T. W. Jing, *Charge Density Waves in Solids*, Gy. Hutiray and J. Sólyom eds. (Springer-Verlag, New York, 1985) page 279;
J. Dumas and C. Schlenker, *ibid.* page 439;
S. Bouffard, M. Sanquer, H. Mutka, J. Dumas and C. Schlenker, *ibid.* page 449;
L Mihály, Ting Chen, B. Alavi, and G Grüner, *ibid.* page 455.

[28]R. P. Hall, M. F. Hundley, and A. Zettl, *Phys. Rev.* B **38**, 13002 (1988).

[29]J. W. Brill and W. Roark, *Phys. Rev. Lett.* **53**, 846 (1984).

[30]G. Mozurkewich, P. M. Chaikin, W. G. Clark, and G. Grüner, in *Lecture notes in Physics*, Vol. 217, Gy. Hutiray and J. Solyom, eds. (Springer-Verlag, New York, 1985) p. 353.

[31]For the sake of argument, it is assumed that the pinning periodicity is equal to the CDW wavelength and thus the CDW advances by 2π in one NBN period.

[32]I. Batistic, A. Bjelis, and L. P. Gor'kov, *J. Physique* **45**, 1049 (1984).

[33]R. M. Fleming, D. E. Moncton, J. D. Axe, and G. S. Brown, *Phys. Rev.* B **30**, 1877 (1984).

[34]S. E. Brown, L. Mihály, and G. Grüner, *Solid State Commun.* **58**, 231 (1986).

[35]T. Tamegai, K. Tsutsumi, S. Kagoshima, M. Sato, K. Tsuji, J. Harada, M. Sakata, and T. Nakajima, *Solid State Commun.* **51**, 585 (1984);

R. M. Fleming, R. G. Dunn, and L. F. Schneemeyer, *Phys. Rev.* B **31**, 4099 (1985);

T. Tamegai, K. Tsutsumi, S. Kagoshima, Y. Kanai, and M. Sato, *Solid State Commun.* **56**, 13 (1985).

[36]Resolution limited measurement on isothermal samples which would only detect a shift in Q (parallel to chain axis) from the internal polarization of the CDW. Based on dV/dI curves for $NbSe_3$, the magnitude of this polarization is approximately what one would expect in the model for $\Delta T = 1$ K. R. M. Fleming, R. G. Dunn, and L. F. Schneemeyer, *Phys. Rev.* B **31**, 4099 (1985) and references within.

Pulsed Electric Field Effects

Chapter 7

Pulsed Electric Field Experiments on Isothermal Samples

Introduction

Over the past decade, there has been considerable interest in the unusual charge-density-wave (CDW) transport properties of $NbSe_3$ and related conductors.[1] A variety of recent experiments[2,3] have demonstrated that the macroscopic CDW condensate is not always well described by only a single-phase coordinate, and thus multiple degrees of freedom, corresponding to internal CDW deformations or macroscopic domain structure, must be included in a complete theoretical description.

One method of probing CDW dynamics and internal CDW phase structure is through investigations of transient electrical response. Gill[4] has used transient response to demonstrate long-time memory effects resulting from metastable states (i.e., particular configurations of local CDW phase) in $NbSe_3$. Related experiments by Fleming[5] have revealed that the coherent voltage oscillations or "narrow-band-noise" in $NbSe_3$ can be "synchronized" to the current pulses, and thus observed directly on an oscilloscope (One interpretation of these oscillations is that they represent modulations in the CDW velocity.). Transient oscillations in

$NbSe_3$ with a frequency corresponding to the internal (narrow-band noise) frequency were first reported by Zettl,[6] and subsequent work[7] has demonstrated similar "ringing" in the blue bronze $K_{0.3}MoO_3$.

In this chapter, we report measurements of transient voltage response resulting from relatively short (nsec to μsec) current pulses in the CDW state of $NbSe_3$. For current pulse amplitudes exceeding the threshold value for CDW conduction, we observe dramatic ringing during the pulse, associated with initial CDW motion. We identify the transient ringing behavior as reflecting a spatial dephasing in the modulations of the CDW velocity within a short time immediately after the pulse edge. In a different experiment, we use the ringing phenomenon as a probe to explore the time scale for the CDW to become fully pinned once the applied electric field is removed (i.e., the time for the CDW to adjust to the impurity and defect sites in the lattice).

Experimental Setup

Our experiments employed single $NbSe_3$ crystals in two-probe sample mounting configurations with silver paint contacts.[8] The biasing consisted of unipolar rectangular current pulses superposed on a variable dc bias current. The minimum pulse rise and fall times obtainable were limited by pulse generator characteristics to approximately 7 nsec. The voltage across the sample was first amplified with a low-noise high-frequency preamplifier (bandwidth ~ 100 MHz) and

subsequently recorded with a high-speed digitizer. The digitizing system (Tektronix 7912AD) allowed single-shot events to be recorded with an exceptionally fast real-time digitizing rate of 100 GHz (10 psec per address), and no interpolation or fill techniques were necessary. Signal averaging of successive single-shot events was used on occasion to either improve signal to noise or, more importantly, to compare the average of multiple traces (each triggered by the pulse generator) to a single-shot trace.

Results and Discussion

Figure 7-1(a) shows the voltage response of $NbSe_3$ at T = 48 K for three different values of current pulse amplitude, all with zero dc bias. Each trace represents the average of 64 identical traces. For the two traces where the average voltage V_f during the pulse exceeds the threshold voltage V_T for CDW conduction, transient oscillation behavior, or ringing, is clearly observed. The frequency of the oscillations corresponds directly to the steady-state narrow-band noise frequency, as determined by the spectrum analyzer observation of the noise with an applied sample voltage $\langle V \rangle = V_f$.

From the data of Fig. 7-1(a) alone it is difficult to determine if the ringing represents true transient behavior or is simply a manifestation of the signal-averaging process.

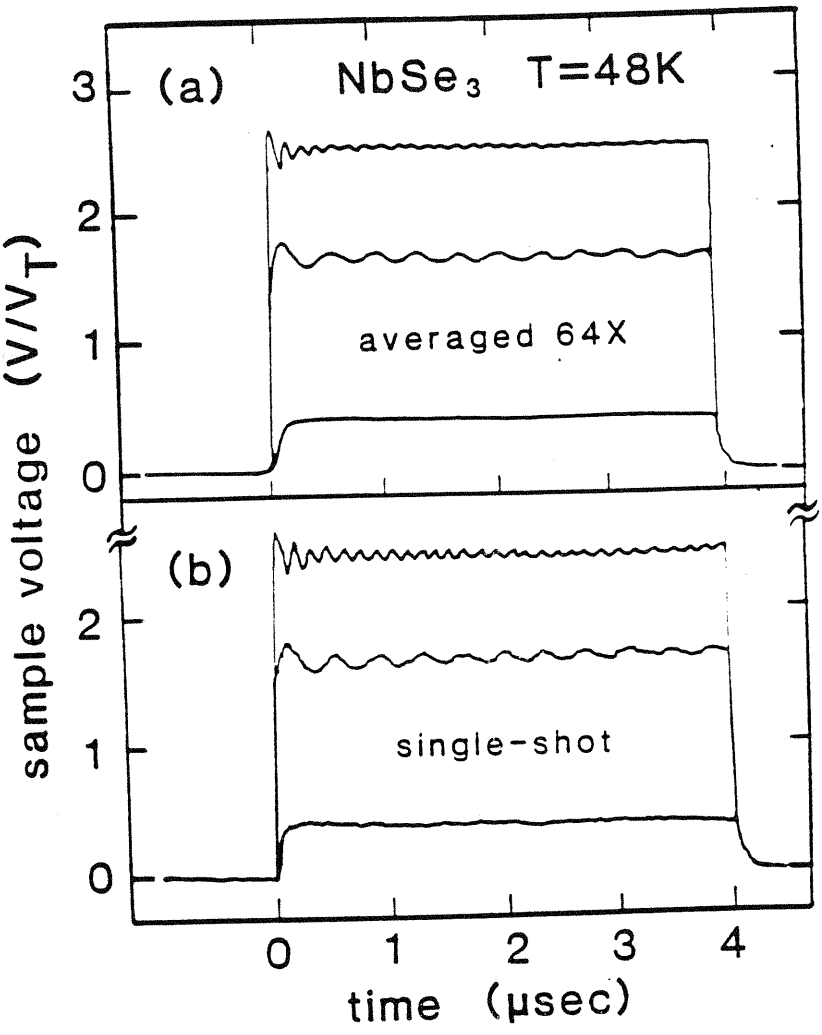

Fig. 7-1 Voltage response waveforms resulting from rectangular current pulses of various magnitude in $NbSe_3$. (a) Signal-averaged traces, (b) single-shot traces.

For example, if different waveforms used in the averaging all had uniform amplitudes and the same phases at the start of the pulse, but slightly different phases near the end of the pulse, then the normalized sum of the waveforms would erroneously resemble ringing.[9] To rule out such a possibility, single-shot recordings were performed of the voltage response due to single isolated current pulses, again with zero dc bias. The results, displayed in Fig. 7-1(b), confirm that in $NbSe_3$ transient ringing is indeed a real effect. A careful comparison of the data of Figs. 7-1(a) and 7-1(b) shows a nearly identical amplitude of the transient oscillations near the start of the pulse for signal-averaged and single-shot traces, indicating that the oscillations always start with a unique phase. The decay of the oscillations is, however, more severe in the signal-averaged representation where the oscillations eventually die out completely. In the single-shot cases, the oscillation amplitude never falls completely to zero, but rather approaches a steady-state value, equivalent to the narrow-band noise amplitude. Comparing the decay of the signal-averaged traces to that of the single-shot traces allows a determination of the phase correlation time for the steady-state oscillations.

For the moment, we consider only the ringing characteristics of single-shot traces. h_1 is defined as the amplitude of the first transient oscillation (i.e., the maximum height of the first overshoot above the time-averaged

steady-state voltage V_f during the pulse) and V_i is the dc current bias level just prior to and after the pulse. We find that, for $V_i = 0$, h_1 is independent of the pulse amplitude (and hence ringing frequency), as long as V_f exceeds V_T. This independence was verified up to $V_f/V_T = 5$; for higher amplitude pulses we were not able to accurately determine the amplitude of the oscillations due to bandwidth limitations. We find, however, the oscillation amplitude h_1 to be extremely sensitive to dc bias V_i, *even for* $V_i < V_T$. Fig. 7-2 shows the results of an experiment where V_f was *fixed* at $2V_T$, and V_i was varied from $-3\ V_T$ to over $20\ V_T$. Results from two different $NbSe_3$ crystals are shown, and all voltages have been normalized to V_T. The frequency of the ringing was found to be determined strictly by V_f and independent of V_i. However, as Fig. 7-2 shows, the amplitude of the transient oscillations is strongest if the CDW is "started" from the pinned regime, i.e., if $-V_T < V_i < V_T$. As V_i approaches V_T from below or $-V_T$ from above, h_1 decreases rapidly. Of particular interest in Fig. 7-2 is the position of the maximum value of h_1, which occurs not at $V_i = 0$, but at a slightly positive current bias value, where $V_i/V_T = 0.25\ V_T$. Thus ringing is somewhat enhanced if the CDW is pulsed from a slightly polarized configuration. Careful tests were performed to insure that the "shift" of the h_1 peak from $V_i = 0$ was not due to spurious thermal emf offsets or a "built-in" directionality in the sample or the contacts. For example, the entire experiment was repeated with all applied

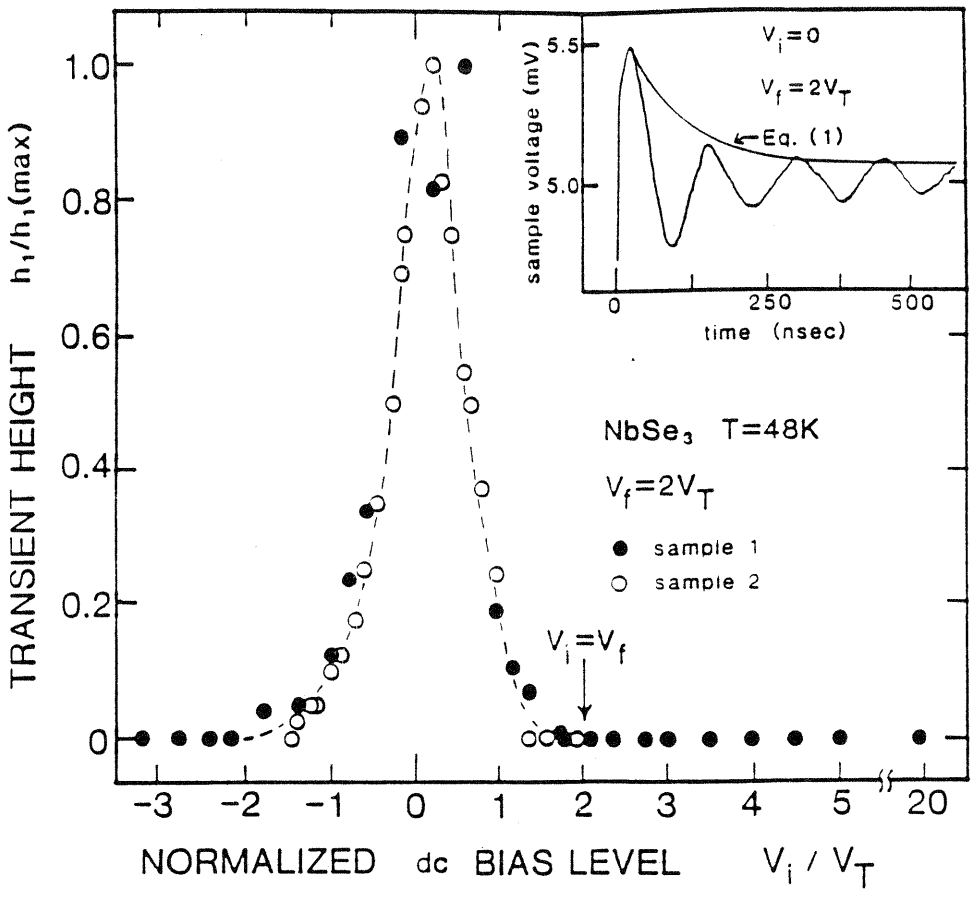

Fig. 7-2 Transient height h_1 vs dc bias current level V_i in $NbSe_3$. The current magnitude during the pulse is fixed at $V_f = 2\ V_T$. The arrow indicates the position of zero relative amplitude for the current pulse. The inset shows Eqn. (7-1) fit to a typical ringing waveform, with fitting parameters given in the text.

currents reversed in sign; for this case the peak in h_1 was found to be $V_i = -0.25\ V_T$.

In the range $V_T < V_i < V_f$, no ringing or transient "overshoot" was observed in single-shot voltage recordings. Upon signal averaging, however, transient oscillations of small magnitude were resolved, and h_1 corresponding to these oscillations has been plotted in Fig. 7-2 for the range $V_T < |V_i| < V_f$. For $V_i > V_f$, *no* transient oscillations or overshoot effects were observed, in either single-shot recordings or signal-averaged responses.

The transient ringing behavior displayed in Fig. 7-1 is reminiscent of inductive response in simple electronic circuits, and one might associate with the ringing an "inertial" CDW response. This is, however, in apparent disagreement with the overdamped response observed in low-field ac conductivity studies,[10] and with the lack of observed ringing following the end of the current pulse. On the other hand, in a study where the CDW is modeled as a purely dissipative incommensurate chain, Coppersmith[11] was able to qualitatively reproduce many of the effects seen in these experiments including the sensitivity of the transient height to the initial biasing level.

The model is based on the view that the CDW is elastic and interacts with impurities and defects as well as an electric field. At sufficiently large electric fields, the CDW can depin and slide relative to the lattice. Scattering of the CDW with impurities/defects and phonons is contained

in a phenomenological damping term. If the pinning from the defects and impurities is relatively strong, then at zero electric field (E = 0), the CDW will adjust itself to minimize the interaction at each impurity. In this respect, the CDW is organized around each of the impurities in that locally the CDW is at the bottom of the individual impurity potential "wells". In this classical model, it is this same pinning from the impurities that causes the modulation in the CDW velocity and is responsible for the generation of the narrow-band noise. At the onset of the biasing pulse, the modulation of the CDW velocity is in phase throughout the sample due to the organizing effect of the pinning. Once the CDW is depinned, the impurities no longer have any organizing effect because the electric field interaction is now the dominant[12] one and this initial coherence is quickly destroyed.

This entire process can be elucidated through an example. Fig. 7-3 shows the mechanical equivalent of the model. The CDW is represented by a series of massless balls connected together by springs with the balls lying in a periodic potential. Corresponding to each ball is an impurity site and the position of the ball in the well describes the position of the CDW with respect to that impurity site. In addition to these two forces acting on the balls, there is also a viscous drag when the ball is moving and the ball carries a charge so it couples to an electric field. For a given ball, any long-term uniform motion will

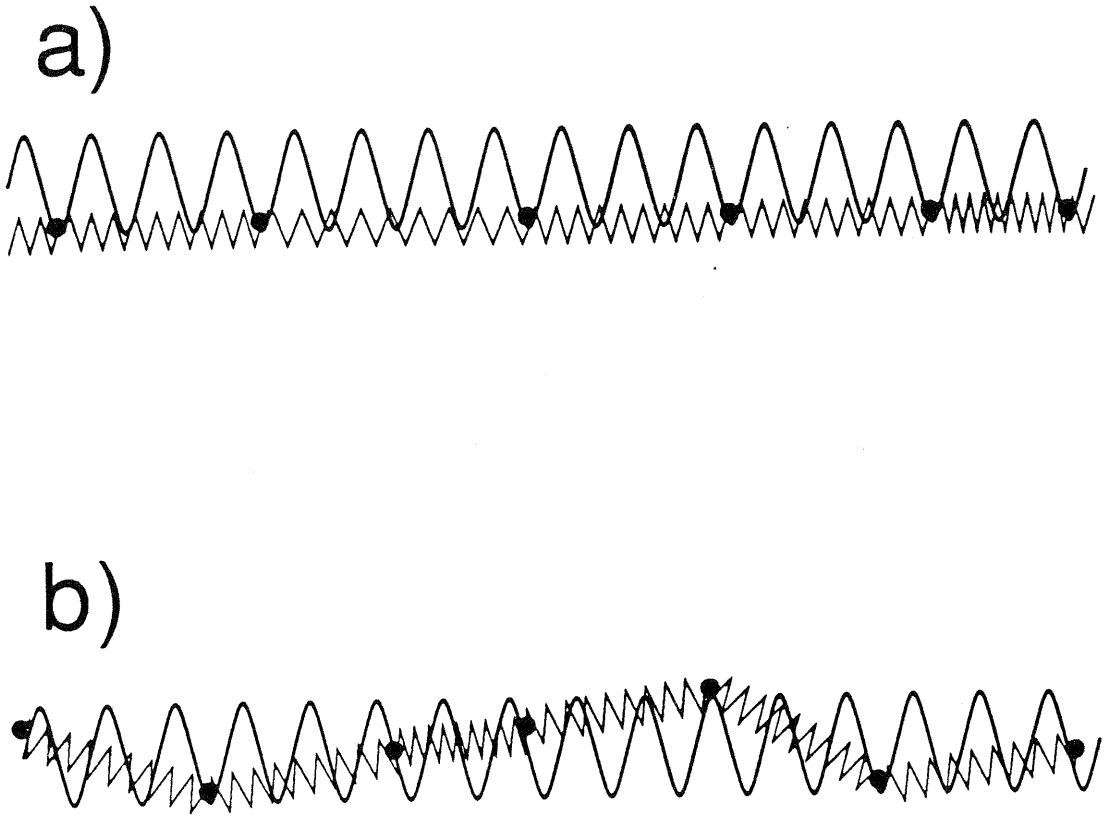

Fig. 7-3 shows a mechanical model used to illustrate how a purely dissipative system can generate "ringing". a) at E = 0, all the balls lie at the bottom of the potential. Because of this common position, the balls will all move with the same velocity right after the pulse is applied. b) as time progresses with $E > E_T$, the balls can lose their synchronization.

be accompanied by a periodic modulation of its velocity as the ball travels over the peaks and valleys of the potential. Because of this periodicity, one can define a "velocity modulation phase" (velocity phase for short) which describes both the position of the ball (modulo 2π) in the potential and the position in its velocity modulation cycle. At E = 0 and for sufficiently weak springs, all the balls will lie at the bottom of the wells (Fig. 7-3a). With the sudden application of an electric field greater than threshold, all the balls start out at the same velocity because of their common relative starting position; as time progresses, the balls no longer travel over the potential in unison; i. e., the coherence in the velocity phase has diminished (Fig. 7-3b).

The large transient seen at the beginning of the pulse reflects the temporal evolution of this velocity-phase coherence. The decay of the oscillations, as displayed in Fig.7-1(b), corresponds to the dephasing over time of the velocity modulation coherence among the impurity sites. The dephasing process does not continue indefinitely, but rather approaches a limiting value, dictated by the intrinsic velocity phase coherence of the crystal. We note that for large sample volumes, the limiting amplitude value of the oscillations may be so small that narrow-band noise is no longer observable, as is often the case in $K_{0.3}MoO_3$.[7] The CDW velocity dephasing process is entirely consistent with no transient response being observed when the $NbSe_3$ sample is

pulsed from a relatively high dc bias level to a lower (conducting) state. In this case, the CDW velocity is, just prior to the pulse, already fully dephased, and no improvement in phase correlation is possible by a simple change in electric field.[13] The (very small) ringing observed in the range $V_T < V_i < V_f$ in Fig. 7-2 suggests there exists a portion of the sample where the CDW is still pinned (even though other portions are sliding). Another possible explanation is that at these low biases, the CDW at each of the impurities spends more time in a narrow range of values in "CDW-velocity-modulation phase space". In this case, a randomly occurring pulse would still find a sufficiently organized velocity phase to produce a transient.

An important feature of the study by Coppersmith and of another study by Coppersmith and Littlewood[14] is that there should be a transient associated with any sudden bias change, positive or negative. As was discussed previously, and is apparent from Fig. 7-2, *no ringing is observed* in $NbSe_3$ if $V_i > V_f$. However, this lack of detecting any transients in the $V_i > V_f$ range could be caused by capacitive smoothing either from the polarization effects of the sample or from the experimental electronics and cabling.

As a first approximation to the dephasing mechanism, we write for the voltage oscillation amplitude during the current pulse

$$h = A + B \exp(-v_d t/\Gamma) \ , \qquad (7\text{-}1)$$

where A is the steady-state narrow-band noise amplitude, v_d is the CDW drift velocity, and B and Γ are adjustable parameters. We associate with the dephasing process a relaxation time $t_D = \Gamma/v_d = \Gamma'/f$, with f_{NBN} the narrow-band noise frequency. The inset of Fig. 7-2 shows Eqn. (7-1) fit to a typical transient oscillation in $NbSe_3$ with the fitting parameters A = 0.06 mV, B = 0.44 mV, Γ' = 0.65, and f_{NBN} = 7 MHz. Similar fits indicate that Γ' is relatively independent of current pulse amplitude (or dc bias level), as long as f_{NBN} exceeds approximately 3 MHz. This was verified up to f_{NBN} = 20 MHz. For lower f_{NBN}, Eqn. (7-1) still yields excellent fits to the transient oscillations, but Γ' increases with decreasing f_{NBN}. The strong current bias dependence (V_i versus V_f) of the ringing amplitude is contained in the parameter B.

In a second experiment, we have used the ringing phenomenon as a probe to directly determine the time dependence of relaxation to the equilibrium configuration of a CDW condensate rapidly quenched from the sliding state to the zero-field state. As shown schematically in the inset of Fig. 7-4, the experiment consists of setting the dc bias level to $V_i > V_T$, and then applying a (negative polarity) current pulse of width W. During the pulse, $V_f = 0$. Of interest is the transient response which occurs immediately following the end of the pulse, as the sample voltage returns to V_i. For sufficiently long pulse widths, the transient response following the end of the pulse is found to be

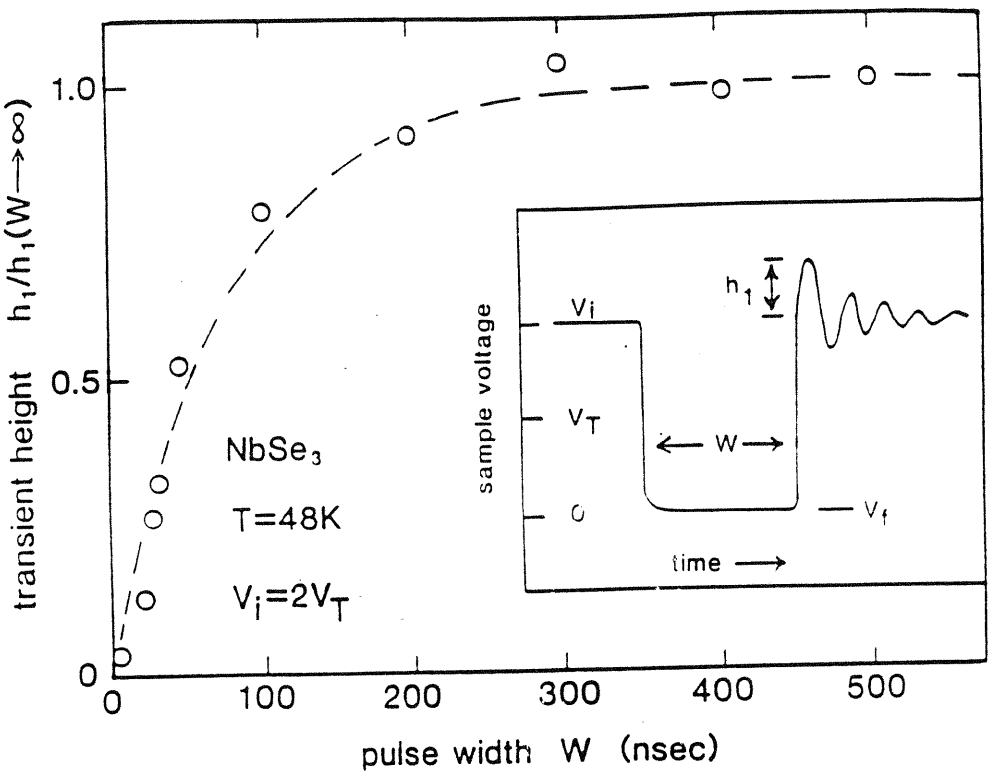

Fig. 7-4 Transient height h_1 versus pulse width W for $NbSe_3$, using the pulse configuration shown in the inset. The dashed line is Eqn. (7-2), with fitting parameters given in the text.

identical to that observed at the beginning of pulses such as described in Fig. 7-1, with zero dc bias and a similar pulse amplitude. As the pulse width W is shortened, the transient oscillation amplitude h_1 decreases markedly, although the decay time t_D and frequency of the ringing remain unchanged. Fig. 7-4 shows h_1 as a function of W for $NbSe_3$ at T = 48 K, with V_i/V_T fixed at 2. The data fit well an exponential time dependence of the form

$$h = B\ [1 - \exp(-W/t_r)]\ , \qquad (7\text{-}2)$$

with a characteristic relaxation time t_r = 77 nsec. This relaxation time corresponds closely to that determined from the classical "crossover" frequency 45 MHz = $(22\ \text{nsec})^{-1}$ for $NbSe_3$ at the slightly lower temperature 45 K, in low-field ac conductivity studies.[10] We associate t_r with the relaxation of internal phase deformations. In the present experiments, these deformations set in as the external electric field is removed from the sliding CDW state, and the CDW phase adjusts to the impurity sites. We note that the fast CDW relaxation observed here is clearly distinct from that previously determined for $NbSe_3$ and TaS_3 from pulsed memory[4] or thermal quenching[2] experiments. In effect, those experiments probe only the very slow relaxation processes associated with phase deformations, with characteristic time scales orders of magnitude larger than t_r evaluated here.

Conclusion

In conclusion, we have demonstrated transient ringing in $NbSe_3$, which we identify with dephasing of the CDW velocity modulations which are originally synchronized through the impurity potential. We have also determined explicitly the time constant for fast relaxation of the CDW from the sliding to the pinned regime. It appears that a significant enhancement in the velocity coherence , induced through the application of individual current pulses, is possible only if the CDW condensate is initially in a pinned configuration.

[1]For a review, see G. Grüner and A. Zettl, *Phys. Rep.* **119**, 117 (1985);
see also P. Monceau in *Electronic Properties of Quasi-One-Dimensional Materials*, Vol. II, P. Monceau, ed. (Reidel, Dordrecht, The Netherlands 1985), p. 139.

[2]G. Mihály and L. Mihály, *Phys. Rev. Lett.* **52**, 149 (1984).

[3]R. P. Hall, M. Sherwin, and A. Zettl, *Phys. Rev. Lett.* **52**, 2293 (1984);
S. Bhattacharya, J. P. Stokes, M. O. Robins, and R. A. Klemm, *Phys. Rev. Lett.* **54**, 2453 (1985);
Charge Density Waves in Solids, Gy. Hutiray and J. Sólyom eds. (Springer-Verlag, New York, 1985) pages 367-458.

[4]J. C. Gill, *Solid State Commun.* **39**, 1203 (1981).

[5]R. M. Fleming, *Solid State Commun.* **43**, 167 (1982).

[6]A. Zettl, Proceedings of International Symposium on Nonlinear Transport and Related Phenomena in Inorganic Quasi-One-Dimensional Conductors, Sapporo, 1983, p. 41.

[7]R. M. Fleming, L. F. Schneemeyer, and R. J. Cava, *Phys. Rev.* B **31**, 1181 (1985).

[8]See Appendix B for more detail on making contacts to samples.

[9]See, for example, R. M. Fleming, in Physics in One Dimension, edited by J. Bernasconi and T Schneider, Springer Series in Solid State Sciences, Vol. 23 (Springer, New York, 1981), p. 253;

P. Parilla and A. Zettl unpublished.

[10]A. Zettl and G. Grüner, *Phys. Rev.* B **29**, 755 (1984).

[11]S. N Coppersmith, *Phys. Rev.* B **34**, 2073 (1986).

[12]Numerical studies on models similar to the one presented here show that as the electric field increases, the effect of the impurity potential decreases and the CDW becomes less distorted. In effect, the fast-moving CDW sees a smoothed out effective potential due to averaging. S. N. Coppersmith and P. B. Littlewood, *Phys. Rev. Lett.* **57**, 1927 (1986).

[13]On the other hand, it seems rather surprising (independent of model) that no transient response of any kind is observed for very large magnitude "downward" current pulses (e,g,. for $V_i = 20\ V_T$ and $V_f = 2\ V_T$), since the associated current states then correspond to significant differences in conductivity.

[14]S. N. Coppersmith and P. B. Littlewood, *Phys. Rev.* B **31**, 4049 (1985).

Chapter 8

Sub-domain Formation Time

Introduction

A detailed discussion of the effect of a temperature gradient on a sliding CDW was presented in chapters 5 and 6 and focused on how the sliding CDW breaks into multiple velocity sub-domains. Although that discussion centered on the steady-state behavior of the CDW, some mention was made of the dynamics of this process as observed during the experiments ("snapping" versus smooth splitting of the NBN peaks and the stability of the NBN spectrum were discussed in chapter 5). In order to study the dynamics of sub-domains in more detail, an appropriate question to ask is "What types of dynamical processes are associated with sub-domains?" A simpler question with direct relevance to sub-domain formation is "How does a phase-slip center form?" At the heart of this last question lie many basic questions whose answers are as of yet unknown and deal with the very nature of a phase-slip center [PSC] and how the phase and amplitude modes of the CDW interact.

The experiments of this chapter investigate the formation of a PSC and sub-domains by observing how the CDW evolves from the pinned state where there are no phase-slip processes occurring to the sliding state where phase slip is necessary in the steady state. A rapid transition from the

pinned state to the sliding state is accomplished by applying a pulsed electric field across the sample. A temperature gradient is used to introduce a single PSC located near the middle of the sample and thereby induce the formation of two sub-domains. Immediately at the pulse edge, the signal is analyzed for its spectral content in order to infer the sub-domain configuration. This signal is compared to the spectrum obtained under steady-state but otherwise identical conditions.

Experimental Setup

Our experiments employed single $NbSe_3$ crystals grown by traditional vapor transport methods. Typical sample dimensions range from .5 mm to 1 mm in length and were on the order of a few microns squared in cross section. Only samples displaying a single clean NBN peak (and its harmonics) under isothermal conditions and split NBN peaks in a temperature gradient were used for temperature gradient experiments; others were rejected.[1] For comparison, a few samples with multiple NBN peaks were investigated under isothermal conditions only. Samples were mounted with silver paint in a two-probe configuration between two copper blocks which served as both electrical contacts and thermal anchors. The copper blocks were thermally isolated from the coldfinger and each had a heater to vary its temperature. The sample chamber was evacuated and the probe was cooled using a He gas-flow system. All measurements were made on the lower CDW

state ($T < 60$ K). Differential thermocouples measured the temperature gradient across the sample as well as the temperature difference between the copper blocks and the cold finger. The temperature of the cold finger was measured using a diode temperature sensor.

One type of sample bias configuration (which we call "bias type 1") consisted of a superposition of a current pulse on a dc current. As shown in Fig. 8-1a, initially the sample is biased above threshold using a dc current source, then the bias is rapidly reduced to zero during the pulse, and finally after the pulse, the bias rapidly returns to its original level. The duration of the pulse is long enough ($\approx$ 4 μsec) to allow the CDW to repin and a normal transient effect is observed at the end of the pulse[2]. With low repetition rates for the current pulse, this biasing profile offers the advantage of being able to simultaneously observe and capture the steady-state NBN spectrum with a conventional spectrum analyzer (Hewlett Packard 8558B) for comparison with the transient spectrum. Also, by removing the current pulse altogether, it was trivial to check that the pulse did not interfere with the measurement of the steady-state spectrum and that the measurement of the steady-state spectrum by conventional and transient methods were consistent.

Another biasing profile (which we call "bias type 2") used had a single unipolar current pulse with no DC bias and is shown in Fig. 8-1c. This more traditional pulse biasing scheme is useful to investigate the dependence of the NBN

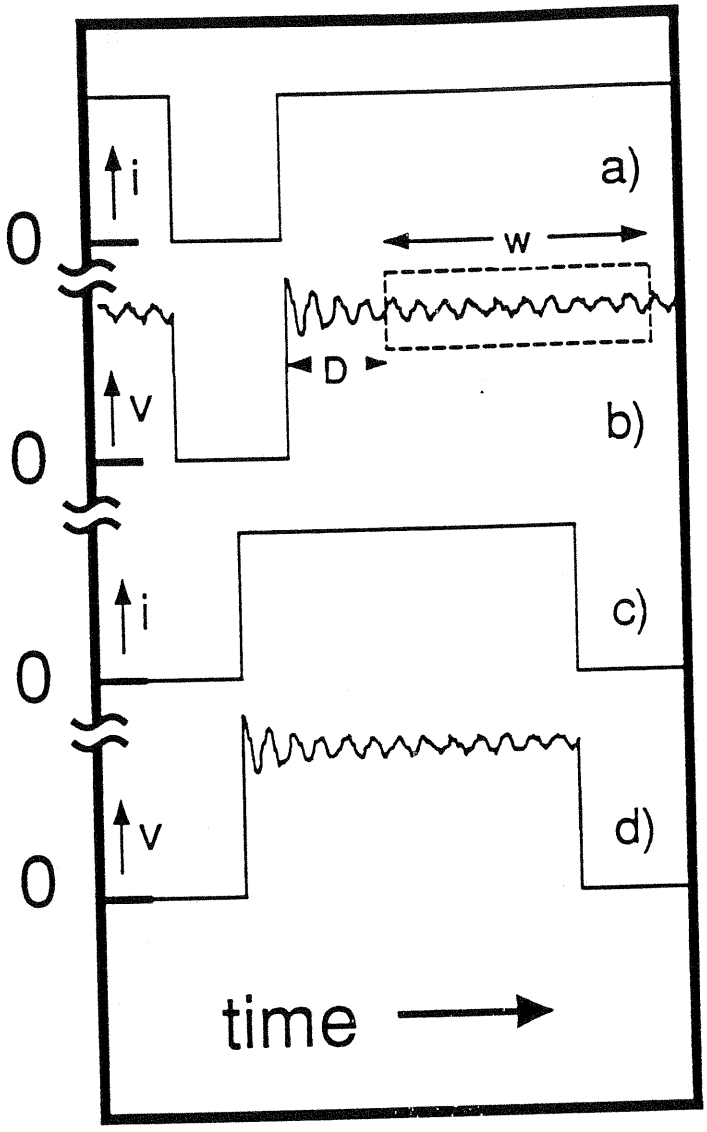

Fig. 8-1 The samples were current biased above threshold using either pulse profile a) or c). The voltage response of the samples are diagrammed in b) and d). Fig. 8-1b additionally shows the placement of the data "window" used in Fourier transforming the data.

response on the pulse width especially in the regime where the width is short compared to the NBN period (pulse width $\leq 10\ T_{NBN}$; $T_{NBN}=1/f_{NBN}$) and strong pulse synchronization effects occur. Since all of the biasing profiles used were unipolar, the CDW was in a polarized state; furthermore, before any data were recorded, the sample was repeatedly pulsed so that the response recorded was the "trained" response.

The voltage response of the sample was first amplified with a 100 MHz bandwidth low-noise preamplifier and then recorded with a Tektronix 7912AD high-speed digitizer. The sampling frequency was varied from 1024 MHz when studying transient phenomenon in the time domain to 51.2 MHz when studying the NBN spectrum in the frequency domain. For the frequency domain studies, a contiguous subset of the time domain data was windowed and the data in the window were transformed to the frequency domain via fast Fourier transform [FFT] techniques. By windowing the data, the pulse edge could be excluded from the spectrum; furthermore, the window could be moved within the data record to determine how the spectrum depended on the distance from the pulse edge (i.e. the time evolution of the NBN spectrum). The window placement within a data record is demonstrated in Fig. 8-1b; the window is of width W and is a distance D from the rising pulse edge.

Definition of Terms

This study examines the role of the PSC in CDW's overall motion and in particular the development of the sub-domain configuration. As first defined in chapter 5, we use the term *sub-domain configuration* to refer to the CDW velocity profile of the entire sample especially with respect to CDW velocity discontinuities. The characteristics of primary concern are the number of sub-domains and the values of the velocities of the sub-domains; for a more complete description, their location and size need to be known also. These characteristics can all be time-dependent. The concept of a sub-domain configuration is illustrated in Fig. 8-2.

A similar concept is the *NBN configuration* which is defined here to be the total NBN spectrum at a given instant in time. The concept of a spectrum varying with time is not compatible with a strict Fourier representation of the signal. Instead, one must use the concept of instantaneous frequency and instantaneous amplitude of an oscillator[3]. During an experiment, this instantaneous spectrum is approximated by taking a truncated Fourier transform (by analog or digital means). The sample consists of a small number of sub-domains, each of which is viewed as being an oscillator with instantaneous frequency and amplitude. The NBN configuration is expected to parallel the sub-domain configuration closely but the two concepts are <u>not</u> equivalent.

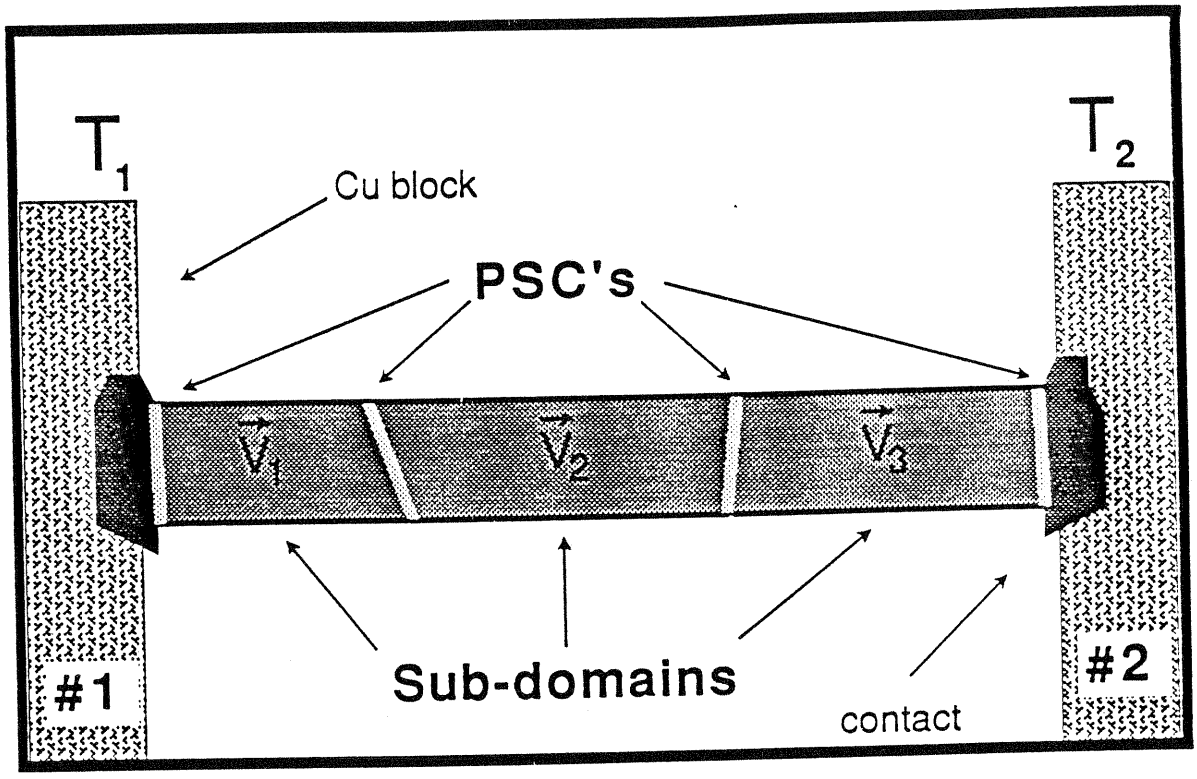

Fig. 8-2 illustrates an idealized sample with a sliding CDW whose sub-domain configuration consists of four phase slip centers PSC. Two PSC's occur at the contacts while two occur within the sample and divide the CDW into three sub-domains. The CDW in each of the sub-domains moves at unique velocities.

As was also mentioned in chapter 5, there are practical considerations in detecting the NBN configuration which can lead to misinterpreting the sub-domain configuration. Two examples of misinterpretation are as follows. The first is the case where the NBN amplitude of a sub-domain falls below the background noise; the sub-domain is then not detectable even though it exists. The second concerns the case where two sub-domains have a frequency difference smaller than the frequency resolution of the experimental apparatus; the two domains are then misinterpreted as one. Both of these cases are of prime concern here due to the focus on short time scales and consequently its inherently coarse frequency resolution and large amplitude variation. The variations are seen on a trace-to-trace basis and can be compensated for by averaging the traces together. These fluctuations are further discussed in chapter 9. We have attempted to compensate for the coarse frequency resolution by applying larger temperature gradients across the sample which produce larger frequency differences in the two NBN frequencies.

Observations

In the first experiment, we looked for indications of PSC formation by examining the NBN spectrum near the pulse edge and comparing it to the steady-state spectrum. Since bias type 1 allowed the simultaneous capture of the transient and steady-state spectra, it was used exclusively for this comparison between the two. By using low repetition rates (≈

8 Hz) and having the time spent above threshold long (≈ 125 msec), the results obtained were free from any apparent synchronization effects[4] and accurately represent the transition from transient to steady-state conditions. Data were taken both with and without a temperature gradient applied to the sample. With no temperature gradient, the time domain data showed the single-shot traces with the normal transient ringing typically seen. From trace to trace there was noticeable variation in the amplitude of the NBN. The degree of variation seen for any given sample was highly sample dependent. With application of a temperature gradient, the NBN showed beating behavior due to the presence of two velocity domains producing two NBN frequencies. The beating behavior appears to start immediately at the pulse edge and is approximately consistent with both domains starting in synchronization (i.e. a beat maximum); the transient decay is still present and is superimposed onto the beats. The variation of the NBN amplitude was still obvious and at times made it difficult to observe the beating signature. Subjectively, the degree of variation appeared to increase when $\Delta T \neq 0$, but one needs to take into account that now there are two NBN frequencies with a correspondingly reduced amplitude (as compared to one NBN frequency).

Three types of spectra were taken. The first, obtained with the conventional spectrum analyzer (HP8558B), consisted of the average of a large number of scans. This is referred to as the "steady-state spectrum". The other two were

obtained with the digitizer with and without the pulse present. The one without the pulse was used to check the consistency between the spectra from the conventional analyzer and that from the digitizer; they always agreed. The spectrum obtained with the pulse present was used to probe the spectrum near the pulse edge and is referred to as the "transient spectrum".

The data used in computing the transient spectrum consisted of the first 2.5, 5.0, or 10.0 μsec of the signal immediately following the positive pulse edge ($D \approx 0$). This data were transformed to the frequency domain and the magnitude spectrum calculated. A number of magnitude spectra were then averaged together for comparison with the steady-state spectrum. Occasionally, the NBN frequency varied among the single-shot traces (observed in the frequency domain). In these experiments, observations of frequency fluctuations were relatively rare compared to those of amplitude fluctuations; this is not surprising because the threshold to observe frequency fluctuations was high due to the inherently coarse frequency resolution (see next paragraph). It should be emphasized that the transient and steady-state spectra were taken under identical experimental conditions.

Fig. 8-3 shows the transient and steady-state spectra with and without a temperature gradient. The two peaks in Figs. 8-3b and 8-3d ($\Delta T \neq 0$) correspond to the splitting of the fundamental peak in Figs. 8-3a and 8-3c ($\Delta T = 0$). Note that the traces show that the averaged transient spectrum is

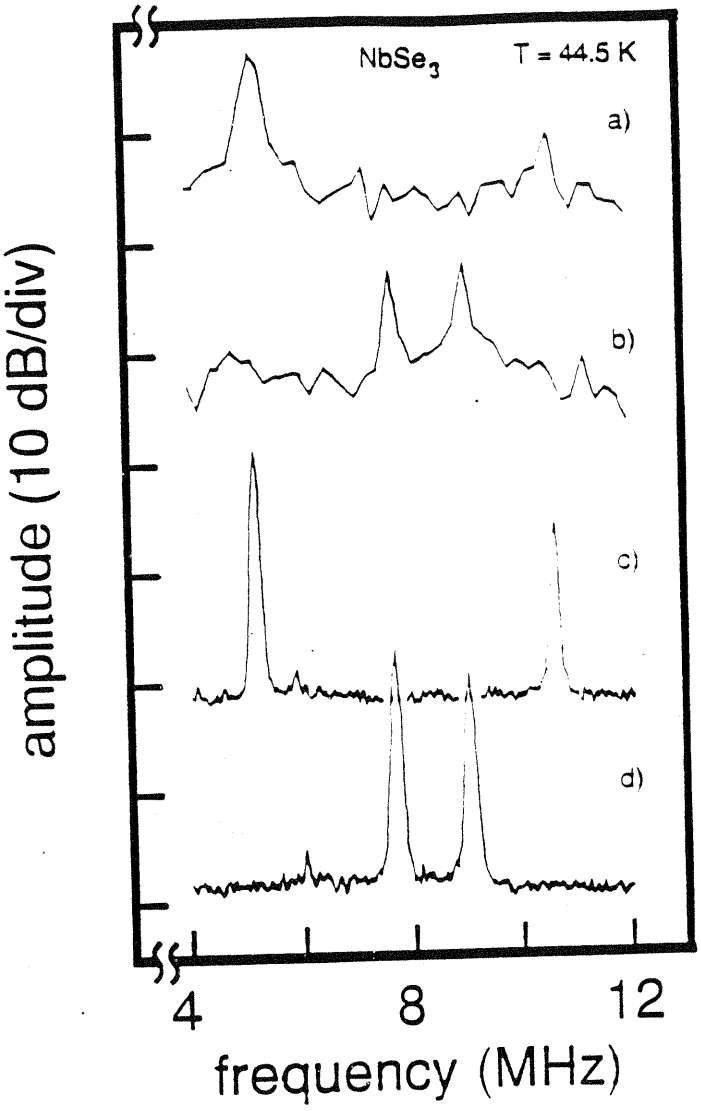

Fig. 8-3 a) The average of 10 transient spectra with ΔT = 0 K; the first and second harmonics are present. b) The average of 10 transient spectra with ΔT = 6.5 K; the first harmonic has split into two. c) The time-averaged steady-state spectrum with ΔT = 0 K. d) The time-averaged steady-state spectrum with ΔT = 6.5 K. See text for discussion.

identical to the averaged steady-state spectrum. This was done with a window length of 5 μsec for the transient spectra; window lengths down to 2.5 μsec show similar results. Window lengths on shorter time scales are inconclusive because they lack the necessary frequency resolution to accurately locate and resolve the NBN peaks, i.e. the time resolution (Δt) is limited because of the frequency resolution requirements and the relationship between the frequency resolution and the time resolution: $\Delta t = 1/\Delta f$. The main conclusion from this analysis gives an upper limit of 2.5 μsec for the time needed for the NBN spectrum to reach its steady-state value. This conclusion applies to the "typical" response of the "average" sample; occasionally exceptions were found.

The exceptions showed effects that were significantly larger. These exceptions were not just random occurrences since they were semi-reproducible, and yet, their scarcity proved them to be atypical. Fig. 8-4 shows a single-shot event from a $NbSe_3$ sample at 46.5 K. This sample displayed multiple (3 or 4) NBN peaks on the spectrum analyzer even with no applied temperature gradient. The trace shows the transient voltage response of the sample to a current pulse (bias type 2). This particular trace clearly shows that the NBN configuration (as reflected in the beat pattern) changes drastically within the duration of the pulse. At first glance it appears that near the beginning of the pulse the beat period is long, while towards the end of the pulse, the

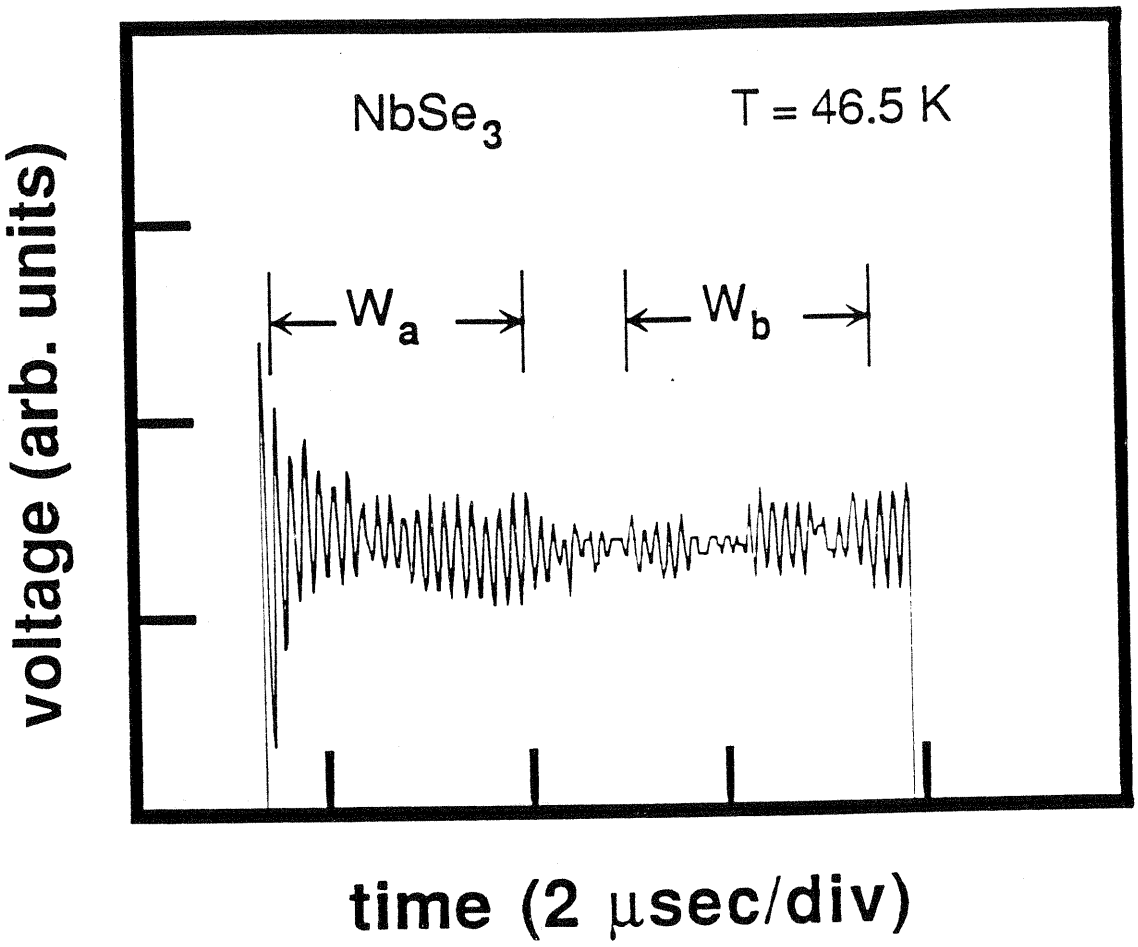

Fig. 8-4 The voltage response of a $NbSe_3$ sample showing an anomalous beating pattern. Superimposed above the voltage response are the windows used for the Fourier analysis.

beat period is short. The transition region between the two is very close to the center of the pulse and appears to be very short. The sample did consistently show this effect for a period of time; however, after cycling to other biases and temperatures, this particular beat pattern changed.

The long time scale for the frequency splitting to change allowed direct Fourier analysis of the different sections of the pulse. The windows used to calculate the spectra are shown in Fig. 8-4 and correspond to the beginning of the pulse and the end of the pulse (Figs. 8-5a and 8-5b respectively). The spectra reveal the presence of multiple sub-domains in the sample with two of the sub-domains having relatively large amplitudes which then dominate the NBN oscillations. The exact evolution of the sub-domain configuration can not be determined with absolute certainty because of the ambiguity in inferring the configuration from the NBN spectrum that we mentioned earlier; however, there is clearly a significant change in the configuration within the pulse width and a detailed examination of this particular event reveals the major features of this transformation process.

In Fig. 8-5a), a large broad peak dominates the spectrum and the total spectrum consists of multiple peaks. Two of these peaks can be seen near the base at 5.6 and 8.8 MHz (vertical arrows). Strictly speaking, the central peak has only one resolvable peak; however, in the time domain window for this data, there is a clear indication of a long-period

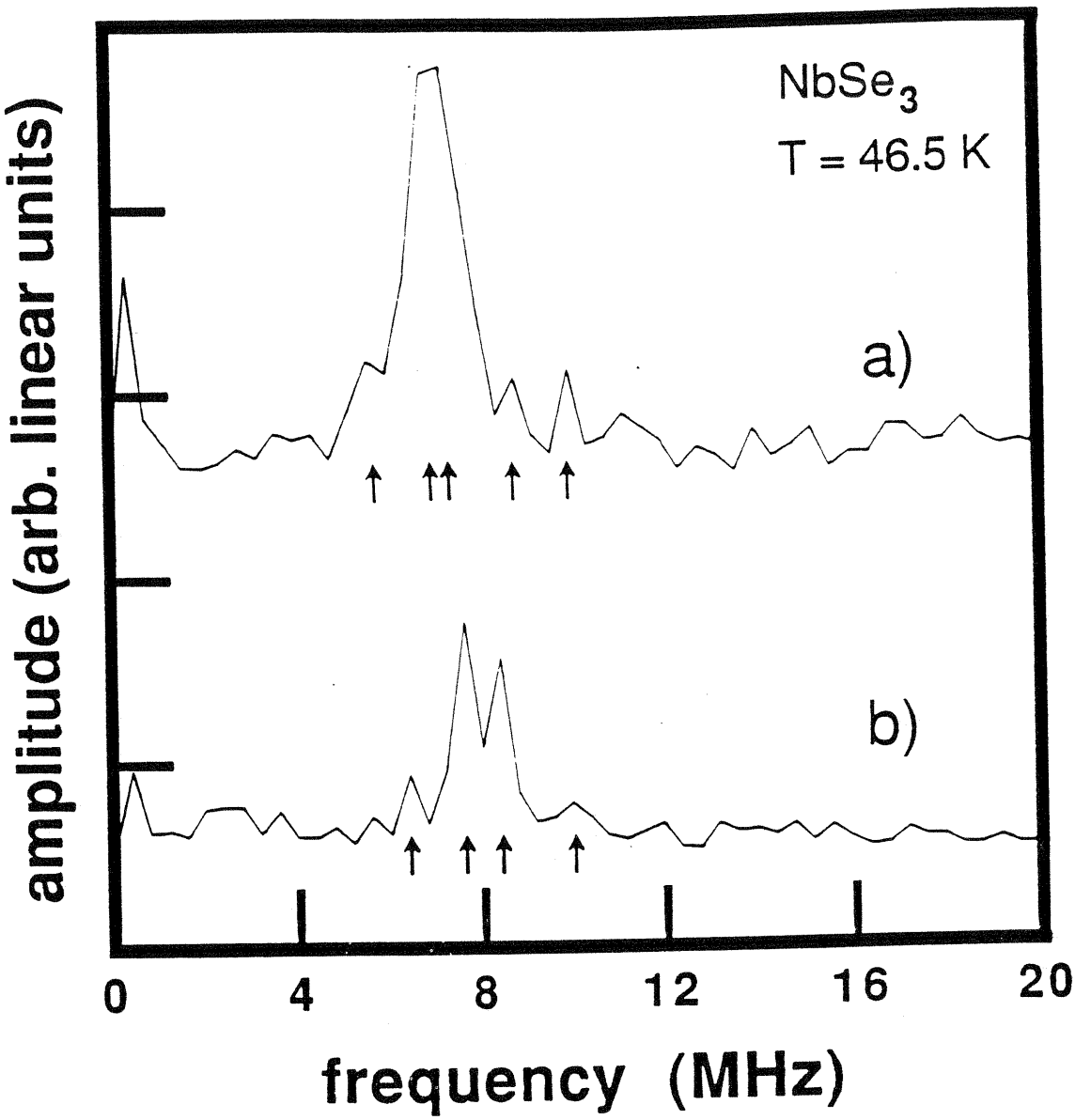

Fig. 8-5 The Fourier analysis of the data of Fig. 8-4 reveals that the sample consists of multiple sub-domains and that the NBN configuration changes drastically during the pulse width. The two spectra correspond to the data in the two windows labeled a) and b) in Fig. 8-4. See text for discussion.

beating and this is consistent with the presence of two peaks within this large central peak[5]. Except for the sub-domain producing a NBN peak at 10 MHz, there is no strong evidence for the existence of any other sub-domains; therefore, the best estimate for the number of sub-domains during the first data window is five.

Fig. 8-5b shows that the two peaks at 7.6 and 8.4 MHz are the dominant NBN sources for the data window at the end of the pulse. The peak which was located at 10 MHz in Fig. 8-5a has shifted down to 9.6 MHz and there is a peak located at 6.4 MHz making the estimate for the total number of sub-domains four. The amplitude of the NBN peaks is decreased markedly relative to the first data window; this is due to the transient ringing effect close to the pulse edge.

The data suggest that this anomalous beating pattern is due to metastability in the sub-domain configuration (as reflected in the NBN configuration). Metastability and instability of the NBN spectrum has been seen previously on longer time scales with a spectrum analyzer[6] in samples with multiple sub-domains. The fact that this effect repeatedly occurred suggests that upon application of the pulse, the sub-domain configuration settles briefly into a metastable state before it proceeds to a more stable one.

The existence of these exceptions shows that there is not necessarily a unique and intrinsic time associated with sub-domain formation, or indicates that there exist effects which prevent an accurate measurement of this formation time.

However, since the exceptions are relatively rare, it is possible that they represent non-intrinsic behavior and this behavior is absent in "normal" samples. In any case, further investigation requires finer time resolution in order to probe closer to the pulse edge. To accomplish this, one must remain in the time domain.

The idea for this second experiment is based on the anomalous beating behavior as seen in Fig. 8-4. Samples which are divided into two velocity domains have two NBN peaks corresponding to the two different CDW velocities. The superposition of the two frequencies will produce beats and the period of the beats will be inversely proportional to the beat frequency $\Delta f(t)$. Looking at the beat period as a function of time will give $\Delta f(t)$ and in particular, looking at $\Delta f(t)$ near the pulse edge might give indications of sub-domain formation. Fig. 8-6 gives NBN simulations and shows how the sub-domain formation process might be reflected in the location of the first beat minimum. The beat envelope can be used to measure $\Delta f(t)$ accurately by finding the minima and maxima of the beat envelope and the time from one minimum to the nearest maxima (or one maximum to the nearest minima) can be considered one half of a beat period (see Appendix A for details of the simulations and some comments on the data analysis).

After applying a temperature gradient sufficient to split the sample into two velocity domains, a set of 64 traces were recorded and (time) averaged together. By taking

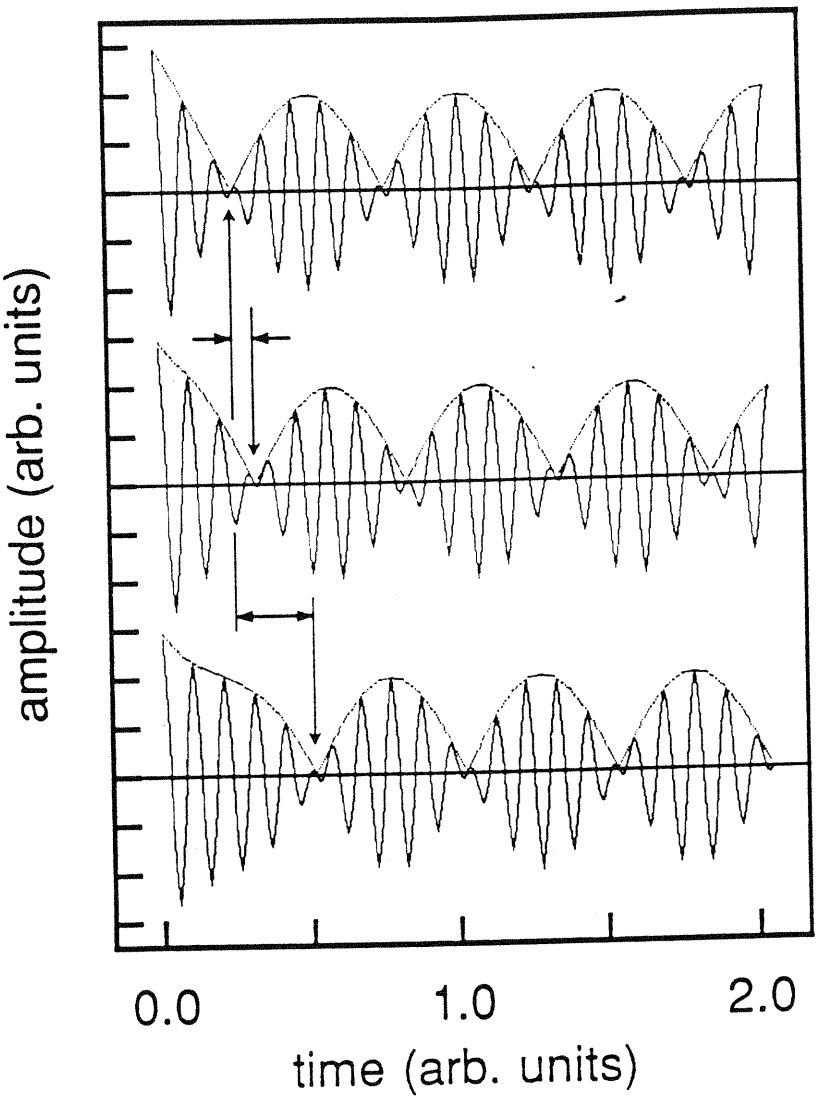

Fig. 8-6 The figure shows simulations on CDW velocity sub-domain formation and demonstrate how there might be a delay in the first beat minimum position (see Appendix A). The top trace shows the beat pattern in the case when there is no delay ($\tau_{PSC} = 0$, $\Delta\tau = 0$) while the lower two traces show the delay for $\tau_{PSC} = 0$ but non-zero $\Delta\tau$ (= 0.125 and 0.5 for the middle and bottom traces respectively).

signal-averaged data, fluctuations in the NBN spectrum were smoothed out to give the average response; additionally, it yielded an improvement in the signal-to-noise ratio. In order to check that the signal averaging was not artificially creating the beats, a number of single-shot events were captured and examined in both the time and frequency domains. They showed that the beats were indeed present and that fluctuations occurred mainly in the amplitude of the NBN peaks. A major difference was found between using bias type 1 and bias type 2. With a temperature gradient applied and using bias type 1, we found that the NBN oscillations often were not stable from trace to trace and as a result individual traces in the time average tended to cancel each other out. We attribute this to increased NBN frequency fluctuations when a temperature gradient is applied across the sample (see chapters 5 and 9). The oscillations were relatively stable when using bias type 2; the shorter pulse width allowed pulse synchronization effects to occur which in turn stabilized the NBN. The width of the pulse was adjusted to give the largest and the most stable NBN oscillations. It is interesting to note that even with the sample split into two domains by the temperature gradient, pulse synchronization effects still occur. This is analogous to mode-locking effects seen in multi-sub-domain samples[7]. The data were examined in the frequency domain where digital filtering could be applied. The data were passed through a digital bandpass filter around the NBN fundamental peaks.

The beat envelope was taken to be the amplitude function of the analytic signal calculated by the Hilbert transform of the filtered data[3] and was used to locate the beat extrema.

Fig. 8-7 gives the record of the first 400 nsec of a typical voltage response. The trace is the average of 64 traces and was acquired in approximately 8 seconds. The beating is clearly visible in the amplitude of the oscillations. The variation of the beat frequency is shown in Fig. 8-8 for a number of data records. Each individual record gives Δf estimated during each of the half-periods while comparison among the records gives the variation of the beat frequency from trace to trace. In addition, the legend has the time that the signal average was initiated. The data record from Fig. 8-7 is represented in record #4. Examination of an individual record shows that there is a large variation in the beat frequency as a function of time and that $\Delta f(t)$ can change rapidly. Examination among the records reveals that very close to the pulse edge, Δf is constant throughout the series, while further away, it can be different. There are some indications that $\Delta f(t)$ does show an additional delay near the pulse edge and therefore might represent the formation of sub-domains; however, this is sample dependent and might reflect on the stability of the sub-domain configuration rather than an intrinsic delay associated with sub-domain formation. The fact that Δf is lower at the pulse edge can not be given much significance

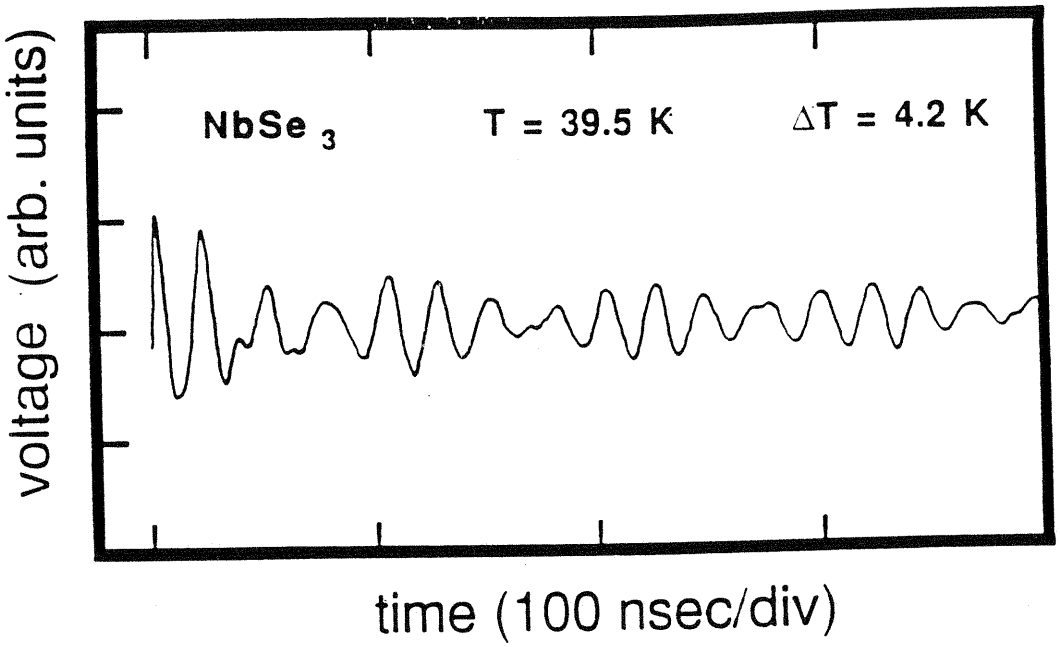

Fig. 8-7 This data record is an average of 64 traces. The beats due to the presence of two NBN sub-domains are clearly visible. Note also that the initial transient is approximately consistent with the superposition of transients from the two CDW velocity domains.

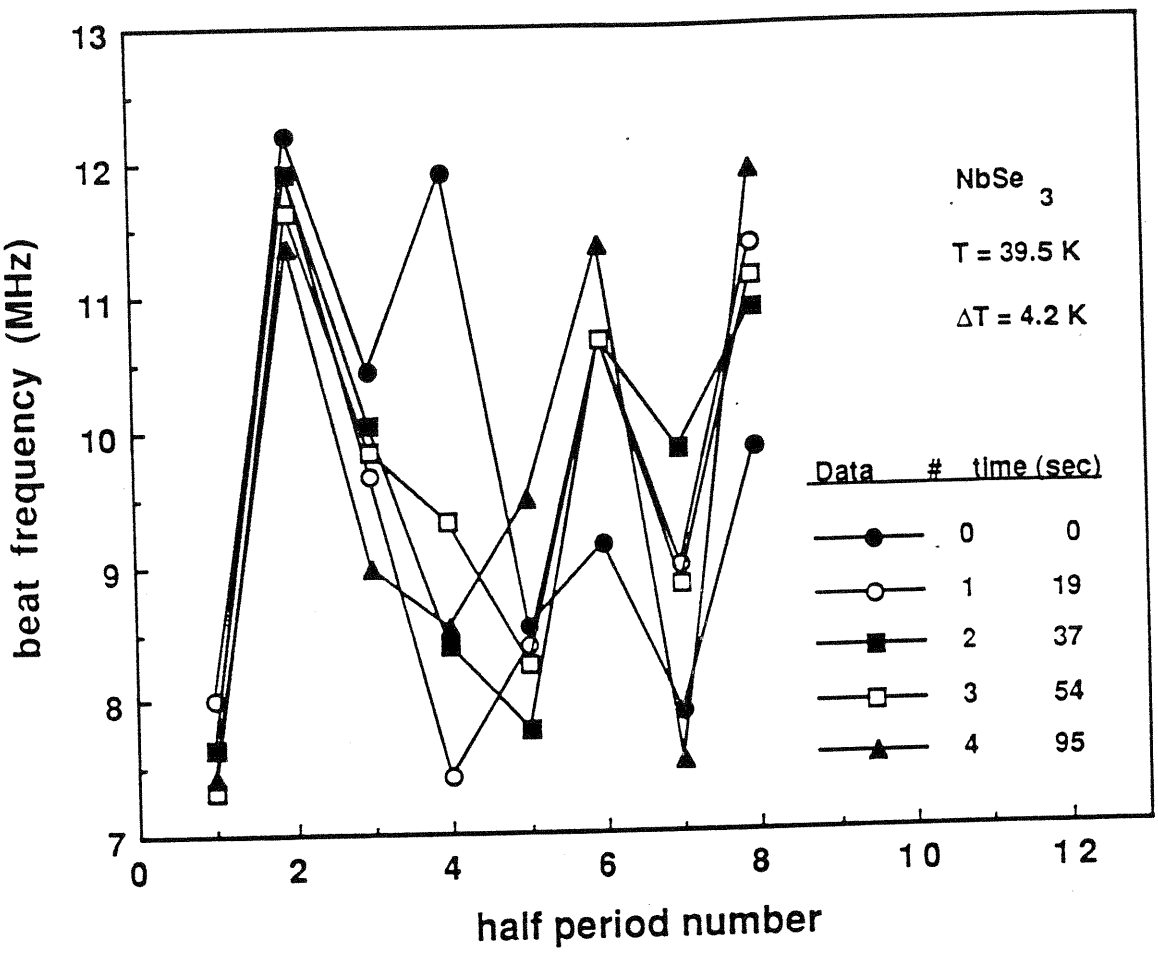

Fig. 8-8 shows the beat frequency versus the half period number for a sequence of data records. The legend is labeled with the time that the signal average was initiated. The data record from Fig. 8-7 is represented in record #4.

since it also reaches reduced levels elsewhere in the pulse; although it is interesting that the Δf variation is synchronized at the pulse edge.

A measure of the degree of variation can be made by using

$$\Delta f\% \equiv \frac{|\Delta f_{max}| - |\Delta f_{min}|}{\frac{1}{2}\left(|\Delta f_{max}| + |\Delta f_{min}|\right)} \qquad (8\text{-}1)$$

for any given data set. For the data of Fig. 8-8, this yields $\Delta f\% \sim 50\ \%$. The variations in the beat frequency are so large that they are suspect. For instance, if the signal is not the sum of two pure sinusoids, then there is the possibility that the maxima of the beat envelope are skewed with respect to the minima and this would lead to an "up-down-up-down" pattern in the data points. There are some indications of this pattern in the data. One can eliminate this particular error by taking two adjacent minima or two adjacent maxima in the beat envelope to estimate Δf and this does reduce the overall magnitude of the beat frequency variation ($\Delta f\% \sim 35\ \%$); however, the overall conclusion remains the same: there is still significant variation in $\Delta f(t)$.

Even though the data can not be strictly interpreted according to the simple model represented in Fig. 8-6, it still provides an improvement in the upper bound for the onset of phase-slip processes. If we assume that the initial

beat frequency is given by the first datum point of Fig. 8-8 (~ 7 MHz) and use 10 MHz for the value of the steady-state beat frequency (taken from the FFT of the data), then the new upper bound for sub-domain formation is ~ 20 nsec or, in the natural units for this data record, a single NBN oscillation.

Discussion

The bulk of the data shows clearly that the sub-domains (and hence the PSC) form very quickly, certainly within the first few NBN periods. The transient spectrum analysis reveals with certainty that the PSC forms within 2.5 μS of the pulse edge and the analysis of the beat periods is consistent with the PSC forming at or very near the pulse edge. This fast sub-domain formation can be understood by examining the time scales of the various CDW modes.

From the theory of Lee, Rice, and Anderson[8], the frequency of the amplitude mode is expected to be high ($\approx 10^{12}$ Hz[9]); however, in the scheme presented by Gor'kov[10] and also by Hall and Inui[11], the amplitude mode is directly driven by the phase mode and so the time scale should be dominated by this much slower phase mode. The time scales of the phase mode cover an extremely broad range depending on the circumstances. At one extreme is the time scale of the "pure" phase mode and has a characteristic frequency on the order of 10^{10} Hz[12]; at the other extreme is the cumulative motion of the phase mode as is seen in the polarization of

the CDW which has a characteristic frequency as low as 10^3 Hz[13].

The experiments discussed in this paper were performed using unipolar pulses on "trained" samples and so the polarization time scale is the minimum possible. The relevant time scale then is the one for the depinning process in a trained sample (i.e. transient ringing) and is on the order of a few NBN periods. The configuration of the polarization at zero bias is very close to the dynamic configuration: the CDW only relaxes slightly when the bias is removed[14]. *Under this scheme, if the training has occurred with a PSC present in the sample, then the polarization will have been programed to be consistent with the formation of PSC's.* In the experiments discussed here, the PSC was introduced via a temperature gradient. The introduction of the PSC and the subsequent configuration of the polarization through training allows for the quick reformation of the PSC; in a sense the PSC might be thought of as "existing" in the sample even with no applied bias.

An example is given in Fig. 8-9. Fig. 8-9a represents an unpolarized CDW and the contacts (rectangles) act like very strong impurities. Also present but not shown are many weak impurities which provide the mechanism for retaining the polarization of the CDW below the threshold field. When an electric field is applied, the CDW polarizes. With no temperature gradient applied, phase-slip processes only occur at the contacts (represented by ovals); Fig. 8-9b shows this

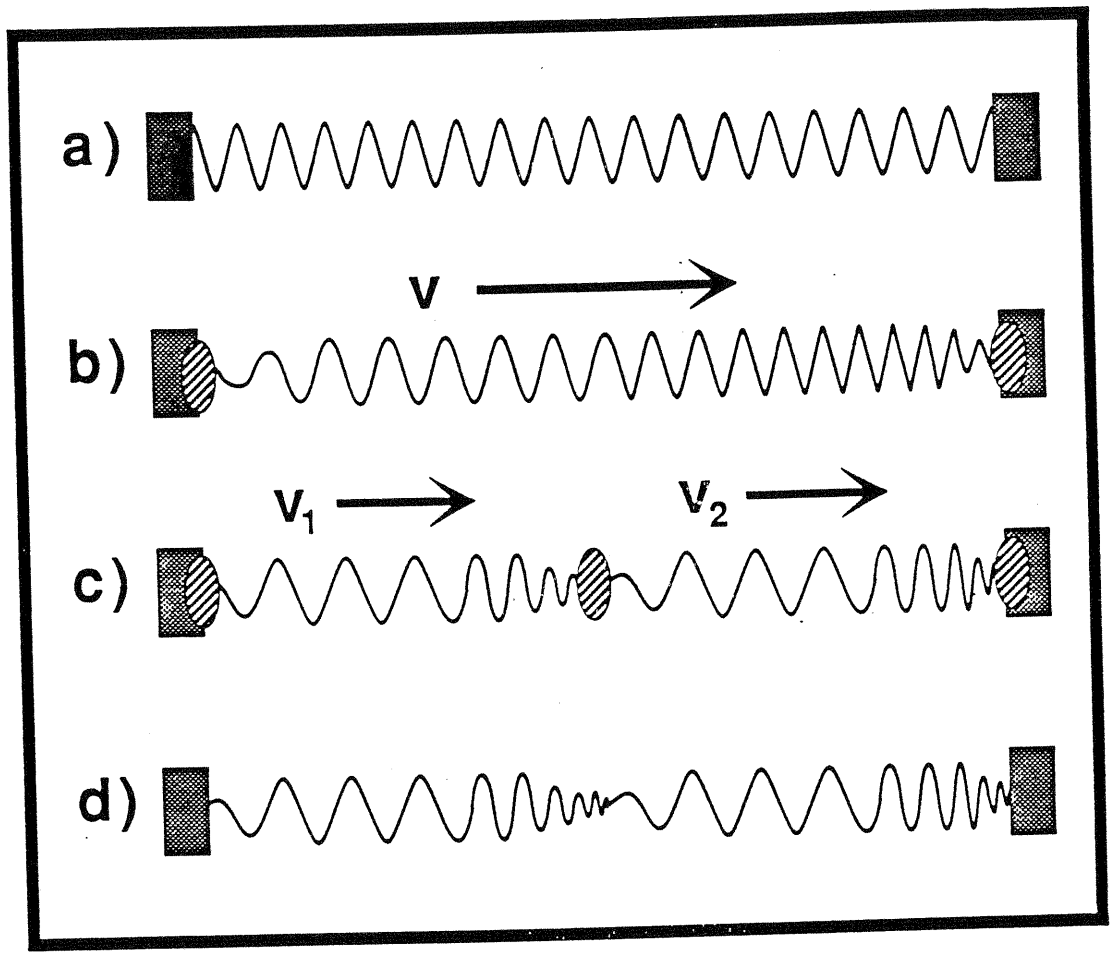

Fig. 8-9 a) Unpolarized CDW between two electrical contacts (rectangles). b) Slightly polarized CDW moving with velocity v; PSC's only occur at the contacts (ovals). c) Additional strain causes a third PSC and CDW divides into two parts with unique velocities. d) CDW after turning off the bias in c); strain profile "remembers" that a third PSC existed and allows fast PSC formation when bias is reapplied.[15]

situation for a moving CDW. Additional strain caused by a temperature gradient is sufficient to cause a PSC to form under the scheme presented in chapter 6 (Fig. 8-9c). With the temperature gradient still on but with the bias off and the CDW pinned, the polarization still reflects the "presence" of the PSC via "strain sub-domains" (Fig. 8-9d); because of this, the formation of the PSC can occur immediately once the bias is reapplied. This picture is similar to the one developed in chapter 5 to explain steps which appear in the dV/dI curves under temperature gradients and further supports the existence of strain sub-domains.

The data based on the beating of the two NBN signals show a number of features. First, that the magnitude of the variation in the beat frequency is large and this variation continues throughout the pulse. Second, near the initial pulse edge, the variation in Δf has a consistent pattern while away from this edge, the pattern varies. Finally, it is also observed that there are instances where $\Delta f(t)$ shows variation over unusually long time scales. These features show that the system is much more complicated than was originally modeled in the NBN simulations of Fig. 8-6 and suggest that additional factors need to be understood before one can ascertain if there is any delay associated with sub-domain formation.

Conclusion

We have demonstrated that the NBN spectrum is capable of reaching its steady-state configuration within 2.5 μS of applying bias to "trained" samples. Further analysis in the time domain shows that phase slip processes occur within the time scale of the first NBN oscillation. We have associated with this fast onset of phase-slip processes, the concept of CDW phase strain memory or "strain sub-domains" which is consistent with previous experiments. This investigation has also raised additional questions which need to be investigated before a thorough understanding of sub-domain formation can be achieved.

---

[1]See Appendix B.

[2]P. Parilla and A. Zettl, *Phys. Rev.* B **32**, 8427 (1985).

[3]J. S. Bendat and A. G. Piersol, Random Data, 2nd ed. (John Wiley and Sons, New York, 1986).

[4]A sample shows synchronization effects when the NBN oscillations are influenced by the pulse width (i.e. time spent above threshold). When synchronization occurs, the NBN amplitude, shape, and frequency can be affected by the pulse width and the phase of the NBN oscillations tend to be fixed relative to both the beginning and the end of the pulse(R. M. Fleming, *Solid State Commun.* **43**, 167 (1982); M. Ido, Y. Okajima, and M. Oda, *J. Phys. Soc. Jpn.* **55** 2106 (1986)) this phenomenon is closely related to modelocking. For such effects to occur, the sample must be in a trained state in that it has learned to anticipate the end of the pulse. Training is accomplished by subjecting the sample to a large number of identical unipolar pulses. For this particular measurement, the sample was in the "trained" state in that the sample was repeatedly pulsed before the data was captured; however, due to the long time above threshold and the resulting large number of NBN oscillations ($10^5 \rightarrow 10^6$), no synchronization effects were observed.

[5]This situation can be clarified by contrasting two examples: The first is a spectrum consisting of two frequencies separated by a frequency difference equal to the frequency resolution Δf_R (400 kHz in Fig. 8-5). In the second case, the spectrum has only a single frequency located halfway between the Fourier frequencies ($\equiv n \Delta f_R$; $0 \leq n \leq N/2$; n an integer, N = number of data points in the time domain window). In both cases, the main peak would consist of two adjacent Fourier frequencies; however, in the former case the time domain would show a beat period equal to the length of the data window while the latter case would show a constant amplitude sinusoid. The difference in the frequency domain between the two cases is the amount of signal strength contained in the other Fourier frequencies around the main peak.

[6]see chapter 5 and P. Parilla, unpublished.

[7]M. F. Hundley and A. Zettl, *Phys. Rev.* B **33**, 2883 (1986).

[8]P. A. Lee, T. M. Rice, and P. W. Anderson, *Solid State Commun.* **14**, 703 (1974).

[9]A. Fournel, B. Oujia, and J. P. Sorbier, *Mol. Liquid Cryst.* **121**, 83 (1985);

A. Fournel, J. P. Sorbier, M. Konczykowski, P. Monceau, and F. Levy, *Physica* **143B**, 177 (1986).

[10]L. P. Gor'kov, *Sov. Phys. JETP* **59** 1057 (1984).

[11]R. P. Hall, M. F. Hundley, and A. Zettl, *Phys. Rev.* B **38**, 13002 (1988);
M. Inui, R. P. Hall, S. Doniach and A. Zettl, *Phys. Rev.* B **38**, 13047 (1988).

[12]S. Sridhar, D. Reagor, and G. Grüner, *Phys. Rev. Lett.* **55**, 1196 (1985).

[13]The polarization time scale considered here is <u>not</u> the one associated with the very slow relaxation (10^3 years!) under zero bias conditions, but rather the transient one associated with the pulse sign memory effect that was first seen by Gill (J. C. Gill, *Solid State Commun.* **39**, 1203 (1981)); this occurs when the bias is reversed and thus the polarization shifts from one direction to the other.

[14]P. B. Littlewood, *Phys. Rev.* B **33**, 6694 (1986).

[15]The sinusoid in the figure does <u>not</u> represent the CDW charge density, i.e., $\rho(x) = \rho_m + \rho_c \cos [Qx + \Phi(x,t)]$; (Eqn. (6-3)). Rather it figuratively represents the CDW as an elastic medium, in this case, a spring. The physical height of the spring as a function of position figuratively represents the CDW's amplitude.

Chapter 9

Fast NBN Fluctuations

Introduction

Although frequency and amplitude fluctuations in the narrow-band noise (NBN) have been reported in the literature previously,[1] only recently have detailed quantitative studies been undertaken to determine their nature and to investigate their role in NBN effects and interactions: a statistical study of the NBN in $NbSe_3$ has shown that the NBN amplitude obeys statistics similar to Gaussian random noise,[2] and Bhattacharya et al.[3,4] have investigated frequency and amplitude fluctuations and their relationship to broad-band noise and mode-locking. At present, the origin of the NBN fluctuations is unknown; more information is required for a better understanding of the phenomenon. One important aspect of the fluctuations is the time scale over which they occur; knowledge of the time scales involved helps in understanding the underlying processes that are occurring. Initial observations suggest that the fluctuations can occur over a range of time scales. Indeed, we have observed that the time scale of the amplitude fluctuations varies widely from sample to sample; this observation is consistent with that reported by Link et al.[2]

In this chapter, we report observations of frequency and amplitude fluctuations on extremely fast time scales. With

the exception of Link et. al. who reported NBN amplitude correlations times on the order of 10 μS, previous studies have looked at fluctuations of relatively long time scales (milliseconds → minutes). In the course of the investigations discussed in chapters 7 and 8, we have recorded numerous traces captured at high digitizing rates which show that large fluctuations can occur sometimes over very short time intervals. During those experiments, it was very obvious that the NBN amplitude varied from trace to trace and, on occasion, the NBN signal was not even detectable. An example of this is shown in Fig. 9-1 which shows two single-shot NBN recordings of the first 10 μsec after the pulse edge. Fig. 9-1a has a strong NBN signal while Fig. 9-1b does not. This is confirmed in the Fourier analysis for the two traces shown in Fig. 9-2. The traces were taken under identical conditions on the same sample with the only difference being that trace b) was taken 32 seconds after trace a).

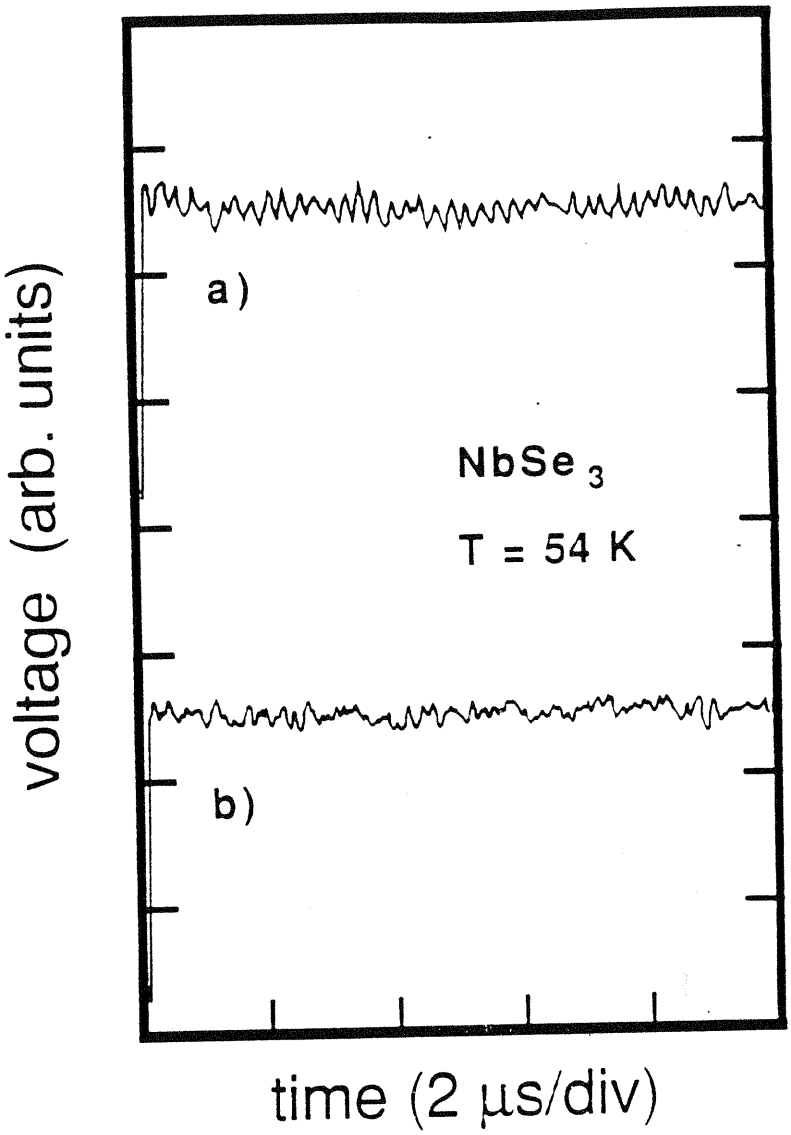

Fig. 9-1 shows an example of how the NBN amplitude can fluctuate. a) shows a single-shot voltage response with a strong NBN signal while in b), the NBN seems absent. Both traces were taken under identical experimental conditions with a) captured 32 seconds before b).

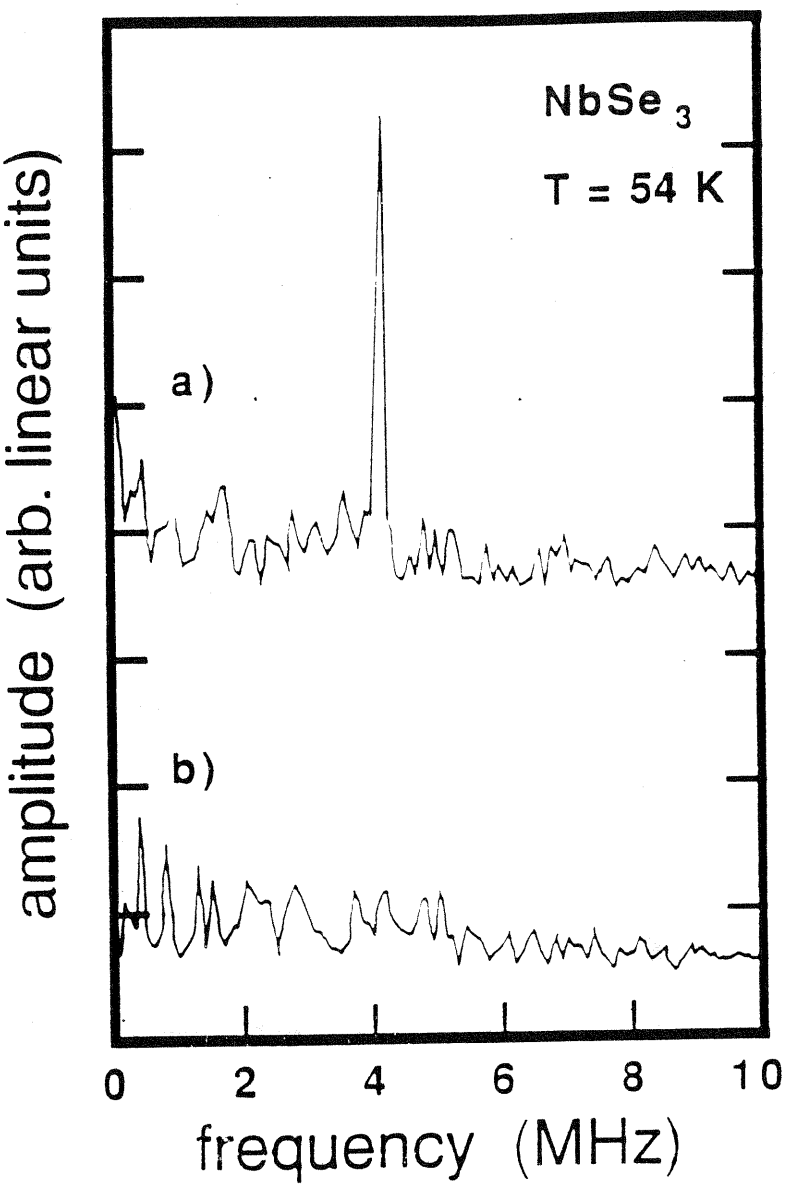

Fig. 9-2 The FFT spectra of the data in Fig. 9-1 confirm that trace a) has a strong NBN signal and b) has no clear signal.

Fast Amplitude Fluctuations

The time scale for the amplitude variation to occur can be extremely fast and this is demonstrated in Fig. 9-3. The data were obtained from a $NbSe_3$ sample under isothermal conditions and showing a single fundamental NBN peak. In the figure, between the arrows labeled #1 and #2, there is a train of 7 NBN oscillations. Outside of this area, the NBN is greatly reduced. The transition region between the two is very short especially at arrow #2. Here the transition appears to be near instantaneous; however, a conservative estimate for the decay is $\approx$ 100 nsec which, in this instance, is ~ 40 % of the NBN period. The superposed spurious random noise level also changes drastically: When the NBN amplitude is large, the random noise amplitude is small and vice versa. Close examination of the figure reveals how smooth the NBN oscillations between the arrows are as compared to those outside the arrows. If the random noise were just a time-independent background noise, then it should be superimposed on top of the NBN oscillations independent of the NBN amplitude. This is not the case; the "random" noise is directly correlated with the NBN amplitude.

The waveform in Fig. 9-3 was divided into sections for Fourier analysis; the three windows are shown in the figure and are each 1.25 μS in length. The spectra for these windows are shown in Fig. 9-4. The amplitude variation among the spectra is clearly seen in the NBN peak which is located

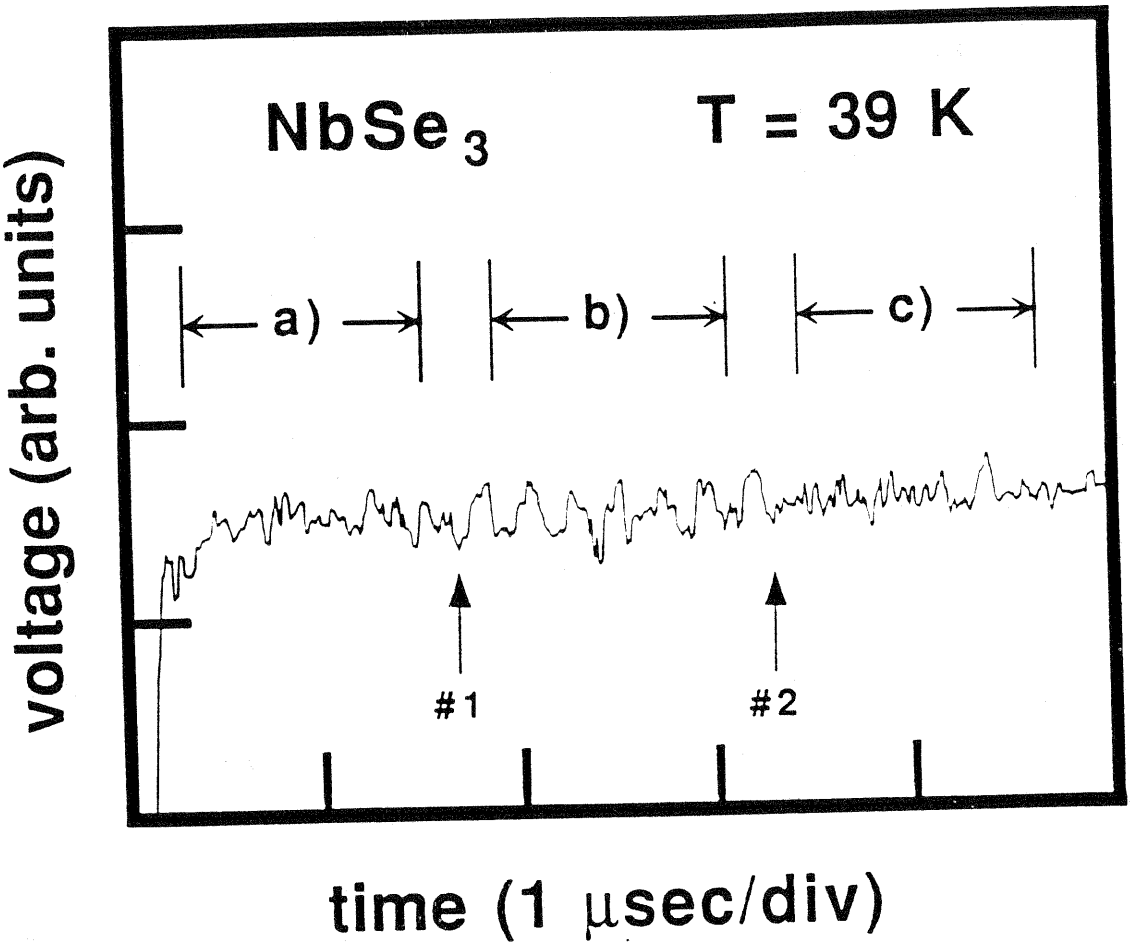

Fig. 9-3 shows an example of variation of the NBN amplitude within an extremely short time scale. Between arrows #1 and #2, seven NBN oscillations are clearly seen; outside of this interval, the oscillations are significantly reduced. The transition between the regions seems near instantaneous especially at arrow #2. a), b), and c) mark the three FFT windows.

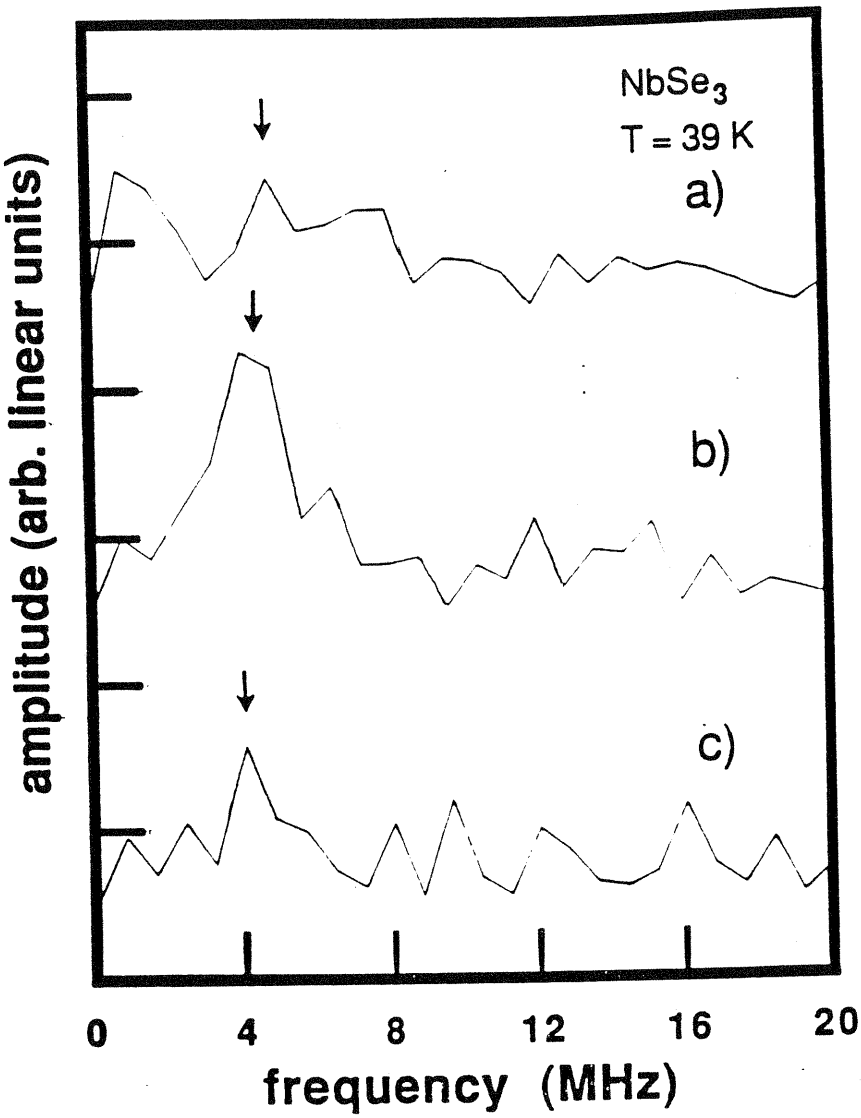

Fig. 9-4 The three Fourier transforms of the a) beginning, b) middle , and c) end of the data in Fig. 9-3 show the variation of the NBN amplitude within this data record. The windows for the three transforms are shown in Fig. 9-3 and are all 1.25 μsec long.

near 4.4 MHz (arrows). The magnitude of the peak in the middle window is twice the magnitude of the others[5]. There is also a small frequency variation present in the spectra. The increased random noise is somewhat difficult to perceive in the spectra but it is there nonetheless. A measure of the random noise can be made by summing the power in a chosen bandwidth in each of the spectra. The bandwidth was taken from 13.6 MHz to 50.2 MHz inclusive (chosen as to avoid any contribution from the power of the NBN). The random noise power increases by approximately 50% in the sections with small NBN amplitude as compared to the one with large amplitude.

The characteristics shown by this sample are highly suggestive of a process which synchronizes the NBN; furthermore, this process allows loss and re-establishment of the synchronization within very short times. As a final observation on the data in Fig. 9-3, we point out the interesting solitary voltage peak which occurs towards the end of the last FFT window. This may or may not represent a single NBN "oscillation".

Fast Frequency Fluctuations

Variations in the frequency of the NBN also can occur within short time scales. Fig. 9-5 shows a series of spectra obtained from a single-shot trace of a strictly dc biased sample. A spectrum in this series was generated by taking a 2.5 μS window in the time-domain trace and fast-Fourier

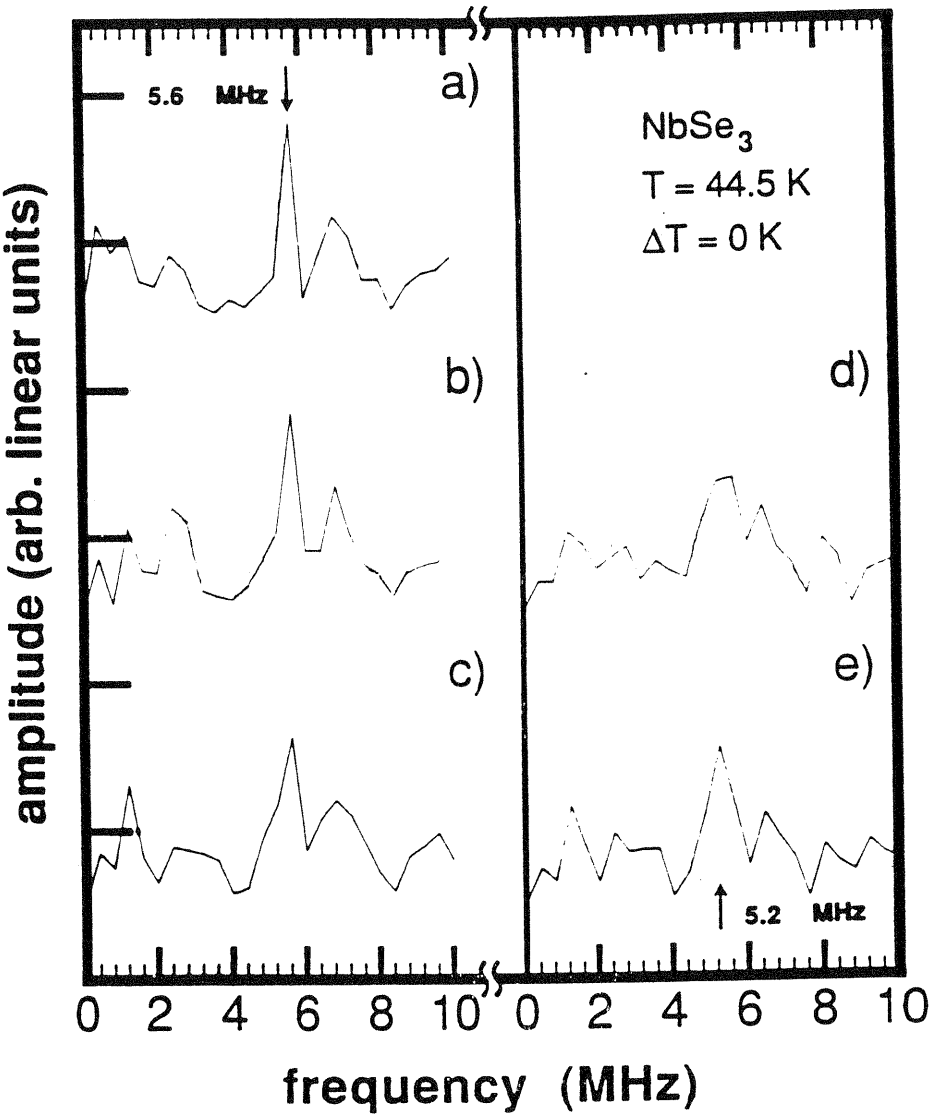

Fig. 9-5 This sequence of spectra captures the fluctuation of the NBN frequency occurring on a short time scale. The NBN peak (arrow) changes by ~400 kHz as the FFT window moves a total of 1.25 μs.

transforming it. A spectrum differs from the one preceding it by having its window translated in the time domain by $\Delta D = 0.3125\ \mu S$. In this way a sequence is generated which shows the evolution of the NBN spectrum. The sequence clearly shows the NBN peak, which is located at 5.6 MHz in Fig. 9-5a, evolve into a peak at 5.2 MHz in Fig. 9-5e. The window advances a total of 1.25 μS during this process and the window is 2.5 μS long; this gives an estimate for the rate at which the NBN frequency changes: 107 GHz/S. This remarkably fast rate represents a change of ≈ 20 kHz per NBN oscillation (assuming a value of 5.4 MHz for the average NBN frequency).

We have found that these fast frequency fluctuations are common: Three of the ten single-shot traces examined had fast frequency fluctuations. For this sample, this puts the probability of a fast fluctuation occurring at approximately 30% [6]. The traces were obtained from an isothermal sample which showed a single strong coherent NBN peak with its nine harmonics.

Sub-domain Fluctuations

In samples that tend to show multiple NBN peaks, there is strong evidence of fluctuations in the CDW velocity sub-domain configuration. The evidence suggests that the sub-domain number is not constant under otherwise steady-state conditions and that fluctuations in this number affect the frequency and/or amplitude of the NBN. For instance, under

conditions where the "average" spectrum shows two NBN peaks, the occasional disappearance and subsequent reappearance of the PSC separating the two CDW velocity sub-domains would be reflected directly in the NBN spectrum. For the case where the PSC disappears, the two NBN peaks would merge into one and the amplitude of the single peak tends to be larger in comparison to the amplitude of the split peaks. This process would be reversed for the reappearance of the PSC.

Fluctuation of the sub-domain number occurs in samples which tend to show multiple NBN peaks, i.e. in samples with an applied temperature gradient or in samples which intrinsically show multiple peaks due to impurities; furthermore, the frequency of occurrence for these fluctuations seems to increase as the CDW velocity difference between the sub-domains decreases. If the frequency of occurrence of the merging process is high enough, the effect can be seen with a spectrum analyzer. In contrast, high-quality isothermal samples which do not show any tendency of having multiple velocity domains do not show evidence of fluctuations in the sub-domain number, i.e. the fluctuations, if they occur, are rare or are below the detection threshold of the instrumentation.

A spectrum analyzer provides "snapshots" of the NBN spectrum at a fixed rate and thus shows the evolution of the spectrum in time. By reducing the temperature gradient in a sample having temperature-gradient-induced sub-domains, the distance between NBN peaks decreases. In most samples at

small NBN splitting, there is an apparent increase in the magnitude of the "frequency fluctuations" of the peaks (see chapter 5). In some samples, the magnitude of the fluctuations is large enough and the peaks can merge for long periods of time. The amplitude of the single merged peak is often larger than the amplitudes of the split peaks. Depending on the metastability exhibited by the sample, the merging can last for several scans of the spectrum analyzer; this is a clear indication that the PSC has disappeared and the two velocity domains have merged into one. While this complete merging behavior is not displayed by all samples, most samples do show increased frequency fluctuations at small splitting. We believe that these increased fluctuations are indicative of a general merging tendency. In some samples, the merging process may be incomplete or occur on a time scale too fast to be detected by the spectrum analyzer. Indeed, in some cases, data captured with a digitizer shows sub-domain number fluctuation while the spectrum analyzer display monitoring the sample simultaneously does not.

An example of digitized data demonstrating sub-domain fluctuation is shown in Fig. 9-6. The data were taken from a $NbSe_3$ sample which had an applied temperature gradient. Traces a) and b) are the magnitude spectra of two single-shot records. The three NBN peaks found in trace a) correspond to the three CDW velocity sub-domains typically seen in the spectra for this sample under these experimental conditions.

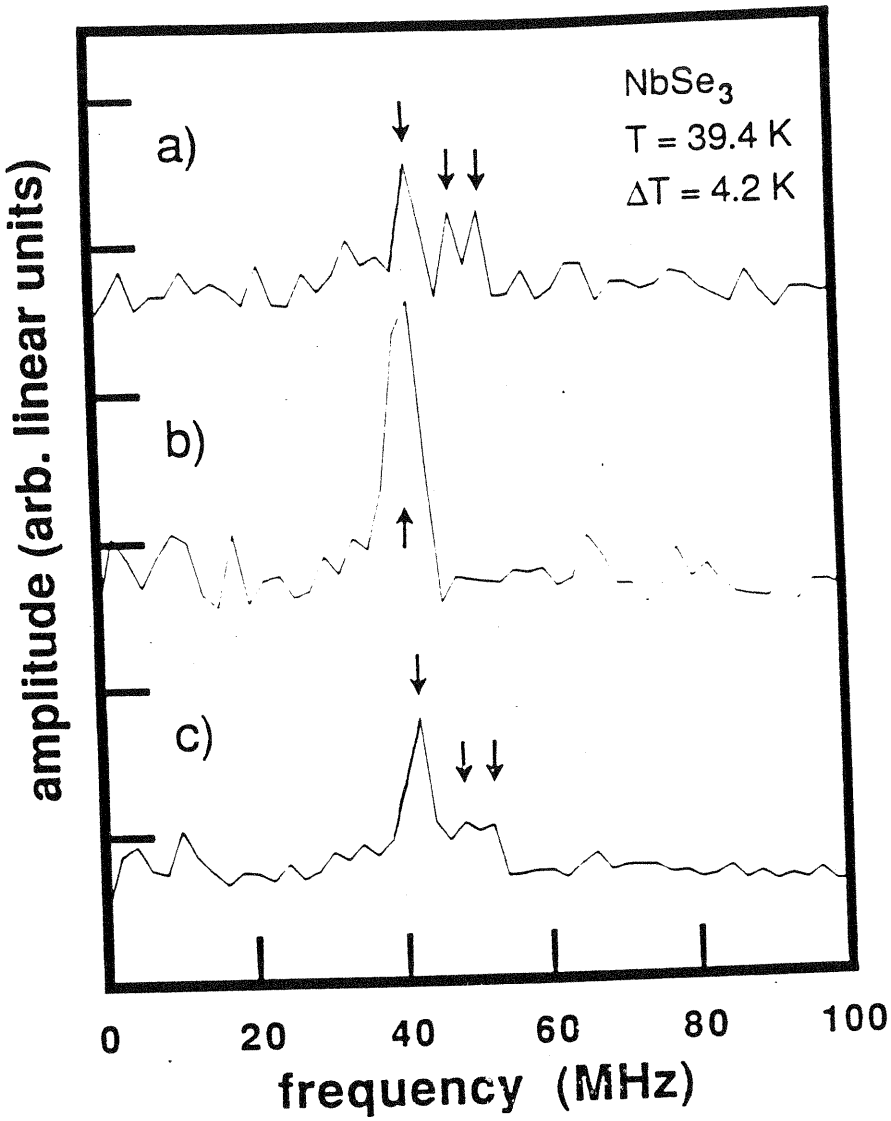

Fig. 9-6 Example of sub-domain fluctuation in non-isothermal samples. a) Typical single-shot trace shows three sub-domains for this sample. b) On occasion the peaks merged together to form a single sub-domain CDW. The elapsed time between a) and b) was 86 seconds under identical experimental conditions. c) average of ten single-shot traces.

Trace b) with its single peak of large amplitude presents strong evidence that the three domains have merged together. Trace c) is the average of ten magnitude spectra captured under identical experimental conditions; included in the average are traces a) and b). In the averaged trace, the two peaks at higher frequency are smeared out because they were constantly fluctuating in frequency and amplitude due to their small frequency splitting. Thus the number of CDW velocity sub-domains can fluctuate and associated with this are corresponding changes in the frequency and amplitude of the NBN. This correlated behavior between the amplitude and the frequency offers the strongest evidence for sub-domain configuration fluctuations.

Discussion

A discussion about the nature of fluctuations in the NBN is made difficult by the fact that the exact nature of the NBN itself is unknown. What is clear is the empirical evidence that the NBN frequency is proportional to the average CDW velocity:[7]

$$v_o = \lambda f_{NBN} \qquad (9\text{-}1)$$

where v_o is the average CDW velocity, f_{NBN} is the NBN frequency, and λ is a constant equal to the distance that the CDW travels in one period $T_{NBN} = 1/f_{NBN}$. It is therefore

reasonable to assume that fluctuations in the NBN frequency correspond to fluctuations in the average CDW velocity.

There is also evidence that the NBN represents periodic modulations in the (instantaneous) CDW velocity $v_c(t)$,[8] i.e.

$$v_c(t) = P(t) \tag{9-2a}$$

$$v_c(t) \approx v_o + v_1 \cos(2\pi f_{NBN} t + \theta_1) \tag{9-2b}$$

where $P(t)$ is a periodic function with period T_{NBN}; Eqn. (9-2b) can be considered the first two terms of the Fourier expansion of $P(t)$. These periodic modulations in the CDW velocity are not to be confused with the fluctuations in the CDW velocity. The former are periodic in time while the latter appear random in nature.

Eqn. (9-1) will be trivially satisfied for any CDW velocity profile $v_c(t)$ which displaces the CDW by exactly λ each NBN period. This is consistent with the idea that the periodic velocity modulations are caused by the interaction of the CDW with the lattice defects and $\lambda = \lambda_{CDW}$, the CDW's wavelength. (Translating the CDW by one wavelength results in an equivalent position; thus, a sliding CDW's interaction with the lattice defects will be periodic in nature.[9]) The periodic CDW velocity is equivalent to a periodic change in the resistivity of the sample and can be detected as voltage oscillations in a current-biased sample.

The characteristics associated with the lattice defects (strength, type, concentration, etc.) can vary locally and it should be expected that the instantaneous velocity will be position dependent,

$$v_c(t) = v_c(t,x,y,z). \tag{9-3}$$

The phase and frequency of the accompanying (local) voltage oscillations will also be position dependent and the total NBN voltage signal across the entire sample will consist of the superposition of the local signals. We can conceptualize this process by imagining that NBN generation can be described in terms of a collection of oscillators and that the total NBN signal $A_T(t)$ is just the sum of the signals from all the individual oscillators:

$$A_T(t) = \mathrm{Re}\left(\sum_{j=1}^{N_o} A\, e^{i\phi_j(t)} \right) \tag{9-4}$$

where $\phi_j(t)$ is the instantaneous phase of the $j^{\underline{th}}$ oscillator, $\frac{1}{2\pi}\frac{d\phi_j(t)}{dt}$ is the instantaneous NBN frequency, and N_o is the number of oscillators. For simplicity, it is assumed that the oscillators all have equal time-independent amplitudes. By considering various coupling schemes between oscillators and various restrictions on $\phi_j(t)$, a broad range of NBN models can be investigated.

Associated with each oscillator is a physical location in the crystal and each oscillator has a set of adjacent "nearest-neighbor" oscillators with which it couples. The nature of the coupling between the "oscillators" lies in the elastic properties of the CDW. The elastic nature of the CDW requires that the average CDW velocities throughout a macroscopic volume V_M be equal, i.e.

$$\frac{1}{2\pi}\left\langle \frac{d\phi_j(t)}{dt} \right\rangle = f_{NBN,M} \; ; \; \text{all } j \in V_M \qquad (9\text{-}5)$$

where the angled brackets signify the time average and the volume V_M is defined by the boundaries of the crystal walls or phase-slip processes. Due to the highly anisotropic nature of these systems, the coupling is strongest along the chain direction (the direction of CDW motion) and much weaker in the directions perpendicular to the chain. (This corresponds to the Young's and shear moduli of the CDW for the parallel and perpendicular directions respectfully.) The anisotropy can be incorporated into the oscillator model by requiring

$$\left| \phi_j(t) - \phi_k(t) \right| < B_{\|} \qquad (9\text{-}6a)$$

$$\left| \phi_j(t) - \phi_k(t) \right| < B_{\perp} \qquad (9\text{-}6b)$$

where Eqns. (9-6 a and b) refer to adjacent oscillators j and k in V_M which are on the same chain and adjacent chains respectively. $B_\perp$ and $B_\parallel$ give the maximum amount of phase that the oscillators can differ by and thus, they are a measure of how well the oscillators track each other. For the anisotropy seen in CDW systems, it is expected that $B_\perp > B_\parallel$.

In the limit that the shear modulus is zero ($B_\perp \rightarrow \infty$), we can consider the sample as composed of many chains in parallel with each chain divided into serially-arranged oscillators. The oscillators in series still must satisfy Eqns. (9-5) and (9-6a) but there is no restriction from chain to chain due to the zero shear modulus and each chain can have its own average NBN frequency. However, since the chains are expected to be similar, the average NBN frequencies of the chains will have roughly the same value. (In real systems, the shear modulus is non-zero but ripping of the CDW is possible. This is similar to the standard phase-slip process that we have considered before but shear ripping is parallel to the chain direction and is thought to occur much more easily.[10])

•Amplitude Fluctuations

One of the simplest models is to consider $\phi_j(t)$ of the form

$$\phi_j(t) = 2\pi f_{NBN} t + \phi_{oj} \qquad (9\text{-}7)$$

i.e. the NBN frequency is fixed among all the "oscillators" in the sample but each can have a unique phase. If the phases are uniformly distributed in the interval $[0,2\pi)$, then Eqns. (9-4) and (9-7) are equivalent to a two-dimensional random walk and the ensemble-averaged amplitude of the NBN is proportional to $A\sqrt{N_o}$. The model represented by Eqn. (9-7) contains no amplitude fluctuations because the ϕ_{oj} are fixed with respect to time. If we allow the ϕ_{oj} to vary with time,

$$\phi_{oj} = \phi_{oj}(t), \tag{9-8}$$

and assume this process is ergodic, then amplitude fluctuations do occur and the standard deviation in the amplitude is proportional to $A\sqrt{N_o}$.

The time scale over which $\phi_{oj}(t)$ changes determines the amplitude-amplitude correlation time. Measurements of this correlation time were performed by Link et al.[2] and showed that they were very sample dependent and ranged from ~ 10 μsec to longer than the measurement time of the instrument (> 1.3 msec). The very fast amplitude fluctuation presented in this chapter suggests that the correlation time can be very short indeed. However, the data itself suggest more than what is contained in this simple model. If the correlation time were a fixed quantity for a given sample, then the amplitude of the NBN signal in the data of Fig. 9-3 would be continuously changing on a very short time scale. Instead, this and similar data traces for this sample show

that there are relatively long periods of time where the NBN signal is strong and fairly constant separated by intervals where the NBN signal is weak or absent. This "on again/off again" pattern is reminiscent of an internal synchronization process which occasionally goes awry.

At present, there is insufficient evidence to ascertain what exactly this synchronization process is. One clue lies in the data of Ross et al.[8] which shows the CDW's velocity to be highly modulated and that during a single velocity cycle the CDW advances by λ_{CDW}. The experiments by Ross et al. detected the NMR motional narrowing caused by the sliding CDW. The motional narrowing did not occur until the CDW was biased far above threshold and suggests that the velocity cycle of the CDW consists of a very quick advancement of the CDW followed by a long interval where the CDW is stationary. This is diagrammed in Fig. (9-7). Under this scheme, the main effect of increasing the bias is to shorten the total cycle period T_{NBN} relative to the advancement interval τ_v (i.e. T_{NBN} decreases and τ_v/T_{NBN} increases) and motional narrowing occurs only when this interval of advancement is comparable to T_{NBN}.

If this velocity cycle accurately describes CDW motion, then it supports the idea that the motion of the CDW is greatly influenced by CDW amplitude collapse processes which predict such "jerky" motion.[11] (The CDW can be described by an order parameter $\Delta\, e^{i\phi}$ with Δ the CDW amplitude and ϕ the CDW phase. The dynamics of a sliding CDW in the weak pinning

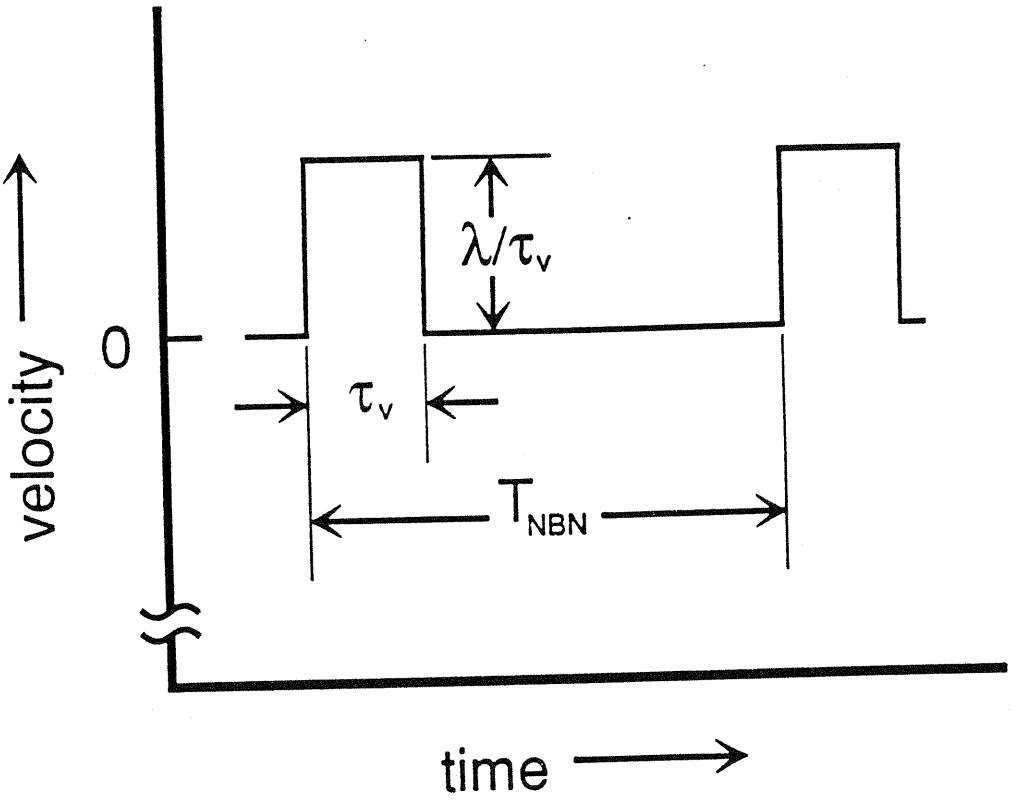

Fig. 9-7 This is a diagram of the CDW velocity cycle as suggested by Ross where the CDW moves in rapid jumps followed by relatively long stationary intervals.

regime is described by ϕ while with strong pinning, the dynamics include Δ as well. In strong pinning, it is expected that Δ must occasionally collapse for CDW motion to occur.) Although there are theories which claim that these processes occur throughout the bulk of the material,[12] it is only necessary to have them occur at isolated areas in the sample. These areas, of course, are the PSC's which in high-quality isothermal samples only occur at the contacts.

There are many imaginable schemes of how the PSC's could affect the CDW motion and they range from dominating the overall CDW motion to just providing a means to synchronize the already inherently jerky CDW motion. An example of the former is to consider the PSC's as gates which only open for a short period of time allowing a single wavelength of CDW through. This is analogous to the motion a long line of cars experience as they approach a stop sign; the stop sign acts like the PSC and allows only a single car through at a time. The overall motion of the cars is very jerky because of the effect of the stop sign.

An example of the latter is to consider how the PSC might synchronize the motion of the CDW throughout the sample by coordinating the motion on the parallel chains. The PSC can again be considered as a gate, but this time opening simultaneously across many parallel chains and therefore synchronizing them. This is analogous to the starter's pistol used to synchronize runners at the start of a race. One might consider more sophisticated schemes such as having

phase slip "nucleating" on a single chain which would start a phase-slip "ripple" propagating across the cross section of the sample. There would then be a fixed relationship among the CDW motion on the parallel chains. Loosing synchronization in the NBN signal might be as simple as having the timing of the PSC's at the two contacts become uncoordinated or by going from a single nucleating chain that regulates the entire cross sectional area of the sample to many uncoordinated nucleating chains each regulating only a fraction of the cross sectional area. Further investigation is needed to understand the spatial and temporal coherence of the NBN signal and to discover what synchronization processes might be occurring.

•Frequency Fluctuations

Allowing the phases ϕ_{oj} to vary with time in the model represented by Eqns. (9-4), (9-7), and (9-8) also cause frequency fluctuations to occur. There are two possible consequences from this. One is that there could be a distribution of frequencies throughout the oscillators at a given instant in time. This corresponds to a spatial distribution of CDW velocities in the sample. However, this distribution depends critically on the constraints given by Eqns. (9-5) and (9-6). If $B_{\perp}$ or $B_{||}$ are small then the distribution is very sharp, i.e. all the oscillators have the same frequency.

The second consequence is that even if all the oscillators have the same frequency, this frequency can drift in time. Experiments by Bhattacharya et al.[3] show that the temporal drift of the NBN frequency is the dominant effect in real systems and any spatial distribution of velocities is small. In terms of the above oscillator model, this implies that the elasticity of the CDW severely limits any spatial variation of the CDW velocity.

Bhattacharya et al. measured the NBN spectrum using a conventional swept-spectrum analyzer. A number of single sweeps were captured and the location of the frequency peak maximum was taken to be the NBN frequency for that sweep. Compiling all these frequencies into a histogram and comparing this to a time-averaged NBN peak shows that the width of the NBN peak can be accounted for by the temporal NBN frequency fluctuations. However, in a single spectrum analyzer sweep, the captured NBN spectrum actually showed a number of peaks. Because the spectrum analyzer is relatively slow in acquiring data, it is not known whether these peaks are caused by spatial variation of the NBN frequency within the sample or whether fast fluctuations during the sweep are responsible for the multiple peaks. The capture of fast frequency fluctuations as detailed in this chapter supports the idea that the variation of the NBN frequency in CDW materials is dominated by temporal fluctuations.

•Sub-domain Fluctuations

In samples which tend to show multiple sub-domain structure, there is a tendency for the number of sub-domains to fluctuate. Sub-domain fluctuations indicate that there is a rich and complicated behavior associated with the dynamic properties of phase slip centers about which very little is known. Associated with these fluctuations are large NBN amplitude and frequency fluctuations. This shows the importance that phase slip processes can have in effecting the NBN signal and also raises the question of what effect the PSC's at the contacts have on the NBN amplitude and frequency fluctuations in single sub-domain samples.

Conclusion

The data clearly show that both amplitude and frequency fluctuations can occur on very short time scales and these both have implications on theories on NBN generation and the cause of the fluctuations. In particular, it points to the importance that phase-slip processes at the contacts have on the overall motion of the CDW. The data also show that in samples which tend to form multiple sub-domains, the number of sub-domains can fluctuate. This again points to the drastic effects that phase-slip processes have on determining the motion of the CDW and the complicated dynamics associated with these processes.

[1]N. P. Ong, G. Verma, and K. Maki, *Phys. Rev. Lett.* **52**, 663 (1984);
T. W. Jing, and N. P. Ong, *Phys. Rev.* B **33**, 5841 (1986);
S. E. Brown, G Mozurkewich, and G. Grüner, Springer Lecture Notes in Physics **217**, 318 (1984);
R. E. Thorne, W. G. Lyons, J. W. Lyding, J. R. Tucker, and J. Bardeen, *Phys. Rev.* B **35**, 6348 (1987).

[2]G. L. Link and G. Mozurkewich, *Solid State Commun.* **65**, 15 (1988).

[3]S. Bhattacharya, J. P. Stokes, M. J. Higgins, and R. A. Klemm, *Phys. Rev. Lett.* **59**, 1849 (1987).

[4]S. Bhattacharya, M. J. Higgins, J. P. Stokes, and R. A. Klemm, preprint.

[5] The magnitude was calculated assuming that the NBN signal of the middle spectra was divided between the two frequency bins located at 4.2 and 4.6 MHz.

[6]More accurately, the probability is between .12 and .55 for the lower and upper 90% confidence levels respectively. "Fast frequency fluctuation" is defined as having a fluctuation occurring within the 5 μS trace.

[7]P. Monceau, J. Richard, and M. Renard, *Phys. Rev. Lett.* **45**, 43 (1980).

[8]J. H. Ross, Jr., Z. Wang, and C. P. Slichter, *Phys. Rev. Lett.* **56**, 663 (1986);

J. H. Ross, Jr., Ph.D. thesis, University of Illinois at Urbana-Champaign, 1986;

see also J. R. Tucker, *Phys. Rev. Lett.* **60**, 1574 (1988).

[9]There is also a theory which predicts that $\lambda = \lambda_{CDW}/2$. P. F. Tua, A. Zawadowski, and J. Ruvalds, *Phys. Rev.* B **29**, 6525 (1984).

[10]D. Feinberg and J. Friedel, *J. de Physique* **49**, 485 (1988).

[11]L. P. Gor'kov, *Sov. Phys. JETP* **59** 1057 (1984).

[12]J. R. Tucker, *Phys. Rev.* B **40**, 5447 (1989);

J. R. Tucker, *Phys. Rev. Lett.* **60**, 1574 (1988);

J. R. Tucker, W. G. Lyons, and G. Gammie, *Phys. Rev.* B **38**, 1148 (1988).

Appendix A

"Beats" Simulation and Analysis

Simulation

Fig. A-1 shows a series of transient ringing simulations based on the following model (this figure duplicates Fig. 8-6 of chapter 8). Assume that at the immediate leading edge of the current-drive pulse at t = 0, the PSC has not yet formed and that it takes a time τ_{PSC} to form. Immediately hereafter, the velocities of the two sub-domains begin to diverge until they reach their steady-state separation represented by their difference frequency Δf. The question then is how does the above process affect the location of the first beat minimum? Assuming a linear progression for the diverging velocities over a time $\Delta\tau$ (as shown in Fig. A-2) yields that the first beat minimum occurs at time:

$$t_{min} = \tau_{PSC} + \frac{\Delta\tau}{2} + \frac{1}{2\ \Delta f} . \qquad (A-1)$$

The first two terms on the right hand side represent the additional delay caused by the sub-domain formation process and the third term is the normal delay expected from two sinusoids starting together in synchronization. Eqn. A-1 shows that the delay caused by the formation of sub-domains can be measured by the location of the first minimum and

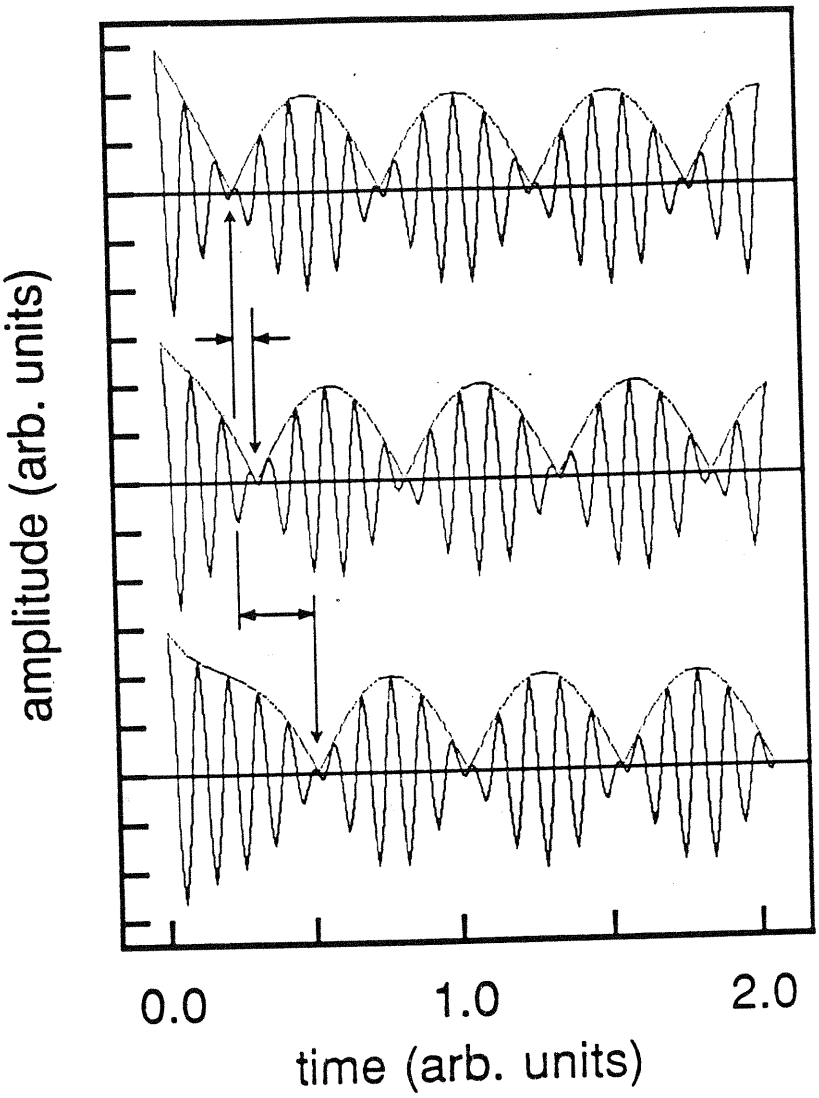

Fig. A-1 The figure shows simulations on CDW velocity sub-domain formation and demonstrate how there might be a delay in the first beat minimum position. The top trace shows the beat pattern in the case when there is no delay ($\tau_{PSC} = 0$, $\Delta\tau = 0$) while the lower two traces show the delay for non-zero $\Delta\tau$ (= 0.125 and 0.5 for the middle and bottom traces respectively).

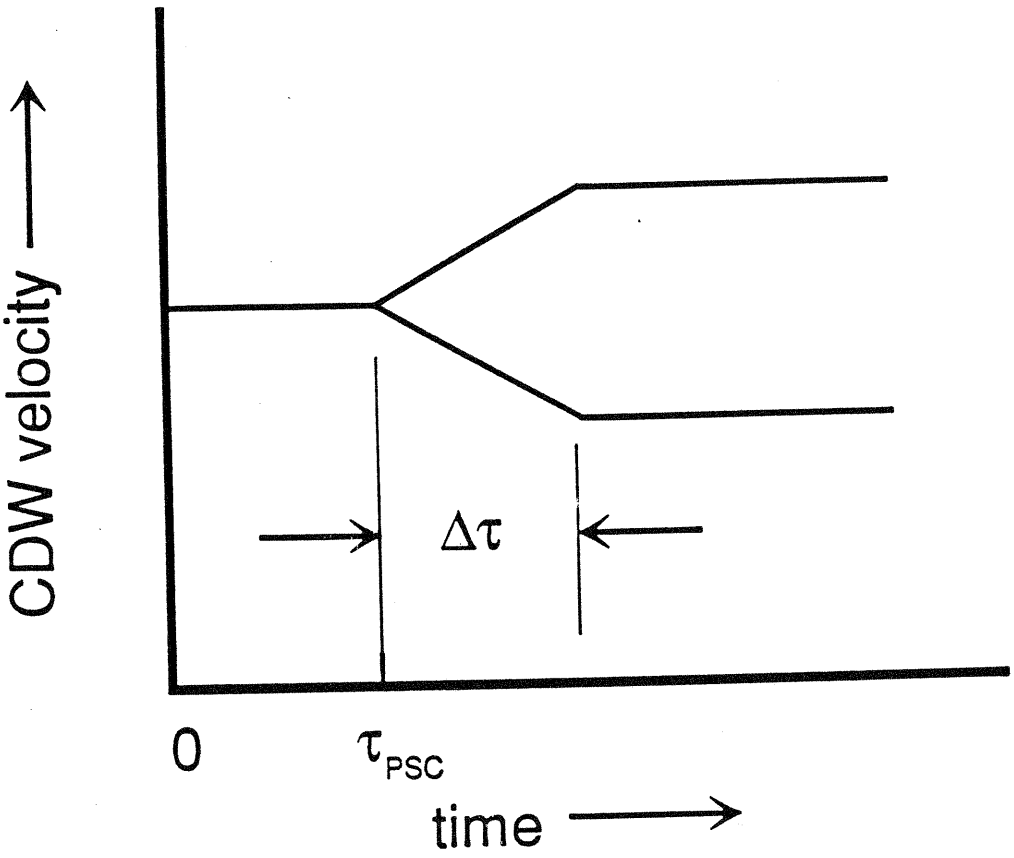

Fig. A-2 The figure shows how the model assumes the CDW velocities progress in time. At time t = 0, current bias is applied to the sample. At t = τ_{PSC}, the PSC forms and the velocities begin to diverge; the divergence continues for a time interval $\Delta\tau$ at which point it stops. The CDW velocities then remain constant thereafter.

subtracting off the normal (half) beat period $\frac{1}{2\Delta f}$. This equation assumes that the sub-domain formation process reaches steady-state conditions before the first minimum; one can find similar equations for the locations of any minima in the case of longer delays.

Fig. A-1 shows the results of simulations with $\tau_{PSC} = 0$ and values for $\Delta\tau$ of 0.0, 0.125, and 0.5 for the top, middle, and bottom traces respectively. Superposed on the simulated NBN is the beat envelope which helps pinpoint the locations of the beat extrema. For this particular model and with $\Delta\tau = 0$, the first beat minimum occurs in the shortest period of time (top trace); this trace can then be used to calibrate relative delays caused by the assumed sub-domain formation process. This additional delay is shown in the figure by the horizontal arrows.

Analysis

The beat envelope can be used to measure $\Delta f(t)$ accurately by finding the minima and maxima of the beat envelope and the time from one minimum to the nearest maximum (or one maximum to the nearest minimum) can be considered one half of a beat period. The estimate for $\Delta f(t)$ is actually an average:

$$\langle \Delta f \rangle (t_1, t_2) = \frac{1}{2\pi(t_2 - t_1)} \int_{t_1}^{t_2} \frac{d(\Delta\phi)}{dt}\, dt \qquad \text{(A-2a)}$$

$$\langle \Delta f \rangle (t_1, t_2) = \frac{\Delta\phi(t_2) - \Delta\phi(t_1)}{2\pi(t_2 - t_1)} \qquad \text{(A-2b)}$$

where $\Delta\phi(t) = \phi_1(t) - \phi_2(t)$ and the NBN voltage signal is $V(t) = V_1\cos[\phi_1(t)] + V_2\cos[\phi_2(t)]$. (For simplicity, the transient decay has been ignored. For the NBN frequency a constant, ω, $\phi(t) = \omega t$.) When t_1 and t_2 are the times of two successive beat extrema (minimum/maximum or maximum/minimum), then $\Delta\phi(t_2) - \Delta\phi(t_1) = \pi$ and thus

$$\langle \Delta f \rangle (t_1, t_2) = \frac{1}{2(t_2 - t_1)} \; . \qquad \text{(A-2c)}$$

In the case of the first beat half-period, $t_1 = 0$ ($t = 0$ is defined as the maximum of the first NBN oscillation) and t_2 is the time at which the first minimum occurs. Without loss of generality, $\Delta\phi(t_2) \equiv \pi$; however, $\Delta\phi(0)$ is unknown. Thus there is an uncertainty in the estimate of the first beat period:

$$\langle \Delta f \rangle (0, t_2) = \frac{1 - \dfrac{\Delta\phi(0)}{\pi}}{2t_2} \; . \qquad \text{(A-3)}$$

It is tempting to assign $\Delta\phi(0) = 0$ since $t=0$ is a local maximum in the beat envelope; however, this could be solely due to the transient at the pulse edge. For convenience in displaying the data, we assume $\Delta\phi(0) = 0$ even though it is

not strictly determined and thus the first half period has the combined influence of $\Delta f(t)$ and $\Delta\phi(0)$.

Appendix B

Structure and Preparation of $NbSe_3$

Structure

The crystal structure of $NbSe_3$ is illustrated in Fig. B-1. Three selenium atoms form the base of a tetrahedron with the niobium atom at the apex.[1,2] This basic building block stacks vertically to form an infinite prismatic chain: the selenium atoms delineate the surface of the "prism" while the niobium atoms are located in the prism's interior. This chain corresponds to the b axis in the crystal. Inter-chain niobium-selenium bonds join the chains together along the crystalline c axis to form a ribbon. Weaker Van-der-Waals forces are responsible for connecting the ribbons along the a axis direction.

The crystal structure perpendicular to the b axis is depicted in Fig. B-2 which shows the projection of the atomic positions onto the a-c plane. The ribbon structure is readily apparent and the packing of the chains within the ribbon is fairly complex. All of the chains in the crystal are not equivalent to each other. Rather, there are three types of chains referred to as types I, II, and III which are distinguished by the bond lengths between the selenium pairs in the tetrahedron's base. The unit cell contains six chains consisting of one pair of each of the different chain types.

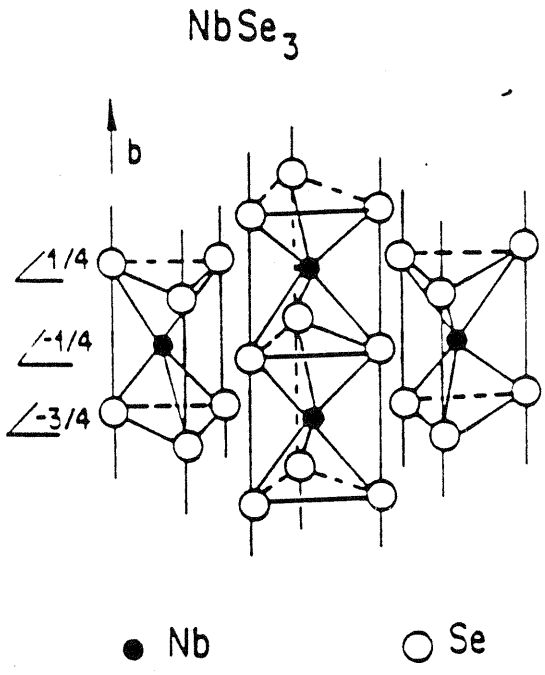

Fig. B-1 This representation of the crystal structure of $NbSe_3$ shows the tetrahedral arrangement among the three selenium and one niobium atoms. Also apparent is the prismatic chain structure formed by the stacking of the tetrahedral units. The b axis is parallel to the chains. (Ref. 1)

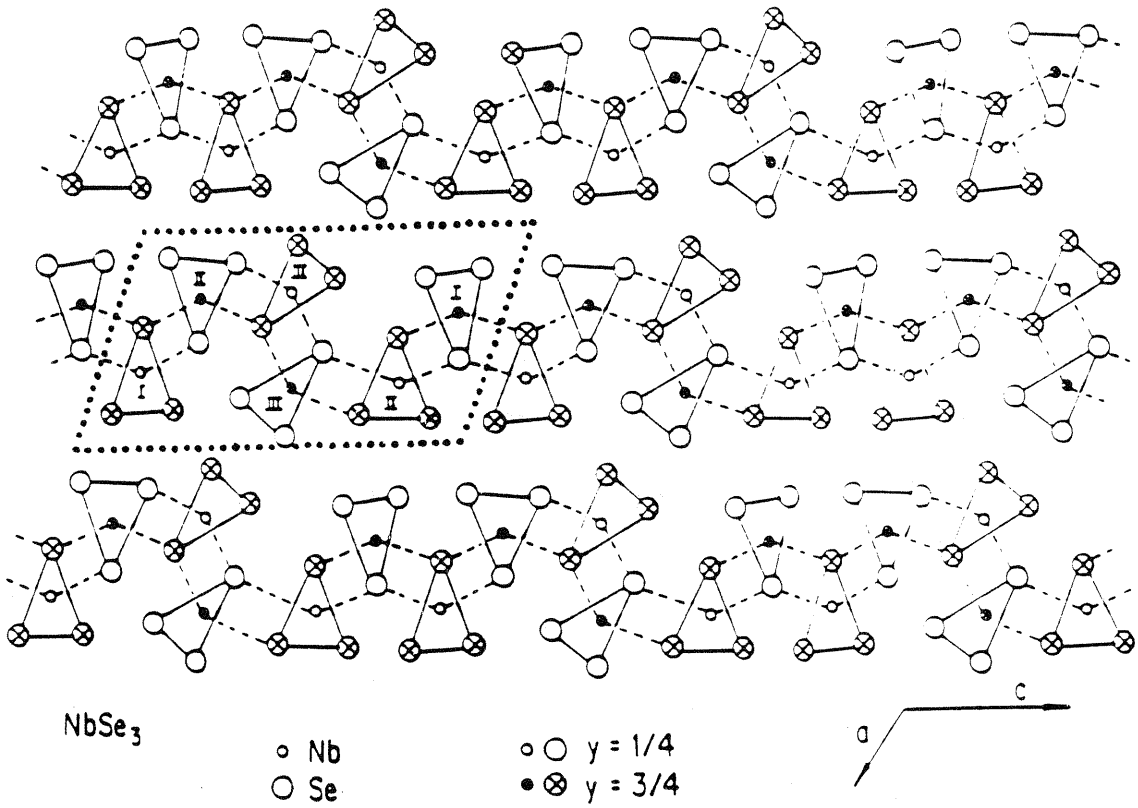

Fig. B-2 Projection of the $NbSe_3$ crystal structure in the a-c plane. The b axis is perpendicular to the a-c plane. The unit cell is outlined by the dotted lines and contains one pair each of the different chain types (labeled I, II, and III). (Ref. 2)

An example of the unit cell is shown in Fig. B-2 by a dotted outline and the different chain types are labeled.

$NbSe_3$ undergoes two Peierls transitions upon cooling: one occurs at T_{P1} =144 K, the other occurs at T_{P2} =59 K.[3] Both transitions produce a charge density wave (CDW) with wave vectors Q_1 = (0, 0.24117, 0) and Q_2 = (0.5, 0.26038, 0.5) respectively.[4] The formation of these two independent CDW's influence the material's resistivity and accounts for the two resistive anomalies seen as a function of temperature (see Fig. B-3). A unique feature of $NbSe_3$ among all the CDW compounds is that it remains metallic at all temperatures while the others have metal-to-semiconductor transitions as they undergo the Peierls transition.[5] At room temperature, the carrier concentration has the estimated value of $\sim 10^{21}$ cm^{-3}.[6]

Band structure calculations[7] suggest that five pairs of independent Fermi surfaces (FS) are created by the electronic dispersion of the three types of chains. (The FS are produced in pairs because of the quasi-one-dimensionality of the system and hence are plane-like and <u>open</u>.) The highly one-dimensional type III chain is responsible for two FS pairs which nest and cause the formation of the upper CDW (T_{P1} = 144 K). Chain types I and II together generate three pairs of FS, two of which nest and produce the lower CDW (T_{P2} = 59 K). The remaining "pair" is actually partially closed and roughly ellipsoidal in shape. Apparently, its nesting characteristics are not sufficient to produce or

contribute to any Peierls transitions and presumably accounts for $NbSe_3$ remaining metallic at temperatures below T_{P2}.

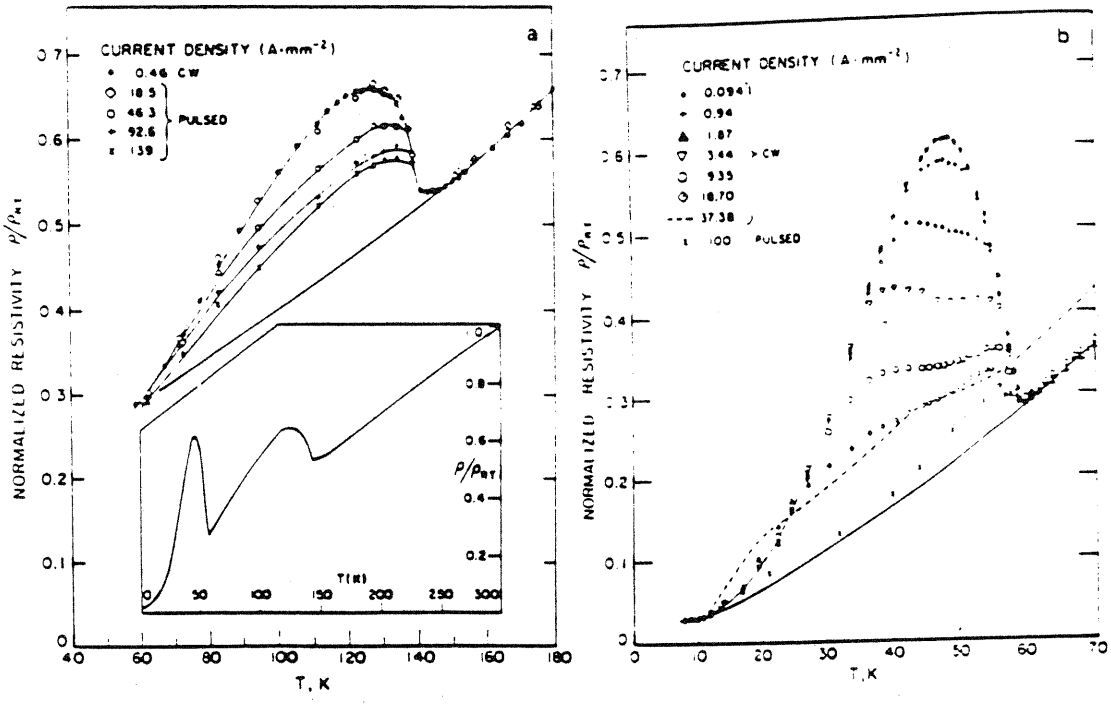

Fig. B-3 Resistivity versus temperature at various dc current biases around the two resistive anomalies in $NbSe_3$. The inset shows the low-electric-field resistivity for a broad range of temperatures (from ref. 8).

Preparation

$NbSe_3$ is prepared by mixing stoichiometric amounts of niobium and selenium in a sealed quartz tube in which the air has been evacuated. The tube, with all the starting material at one end, is place in an oven. The temperature profile of the oven is ~ 700 C at the end with the starting material and ~ 600 C at the other end. The mixture is allowed to react for two to three weeks; during this time, the material vaporizes and is transported to the cold end of tube where it can crystallize into $NbSe_3$. After satisfactory crystal growth has occurred, the tube is removed from the oven and quickly thermally quenched in order to prevent any remaining niobium vapor from condensing on the crystals. Crystals of $NbSe_3$ are long ribbon-like fibers with lengths of 1 $\rightarrow$ 5 cm and widths of 0.01 $\rightarrow$ 0.1 mm. In the quartz tube, the crystals en masse resemble fine grade steel wool. (Further information can be found in Ref. 9.)

A suitable sample is chosen for experiments by examining the crystals under an optical microscope and rejecting those with visible defects or niobium condensation. Care must be taken in handling the crystal since damaging the crystal affects the quality of the narrow-band noise (NBN) signal drastically. If the batch of $NbSe_3$ has been exposed to air for an extended period of time (~ 1 or 2 weeks), a surface oxide barrier forms and prevents establishment of a good electrical connection to the crystal. Since $NbSe_3$ cleaves

easily (parallel to the b axis), a fresh surface can be produced to circumvent this problem. Cleaving also produces smaller volume samples which tend to generate higher-quality NBN signals.

In experiments which investigate the properties of the NBN, a crystal will often be rejected because of a low-quality NBN signal, i.e., low signal-to-noise ratio, broad NBN spectral peak, unstable NBN frequency, or multiple NBN fundamental frequencies. These characteristics reflect a lack of coherence in the CDW's motion and are presumably caused by gross defects, impurities, or damage in the crystal. These gross imperfections can cause effects in the NBN signal which mask the intrinsic behavior seen in a nominally pure crystal and, therefore, are undesirable. (The metastable NBN configuration discussed in chapter 8 is an example of an anomalous effect; see Figs. 8-4 and 8-5.) As a result, finding a sample for an experiment sometimes involves screening many samples in order to find a suitable specimen (some batches have a success rate lower than 10 %). It is therefore advantageous to use techniques which allow samples to be prepared easily and quickly; this includes the attachment of electrical contacts to the crystal.

The most common method of making electrical contact from a wire to a sample is to arrange the crystal so that it touches the wire and apply silver paint (DuPont 4922) at the sample-wire junction to provide for electrical connection and to secure the sample mechanically. After the contacts have

been applied, the two-probe resistance of the sample is monitored to gauge the curing of the silver paint contacts. Once the contacts are dry, the sample is immediately put into an inert environment (either an evacuated or He-filled chamber). This is done because the contacts degrade over time if left in air; this degradation is due perhaps to the presence of oxygen or water vapor in the air. Low temperatures also reduce contact degradation and a sample may be kept intact at low temperatures for several weeks which permits long-term experimental observations.

This procedure results in a moderately good electrical connection with contact resistances on the order of 0.1 to 10 ohms. This should be compared to a typical value for the room-temperature resistance of a $NbSe_3$ crystal which ranges from 50 to 1000 ohms depending on the dimensions of the sample. Because the resistivity of $NbSe_3$ decreases as the temperature decreases, the contact resistance can not necessarily be ignored when measuring the electrical properties of samples; therefore, measurements are performed with the standard four-probe technique if possible (i.e., two outer current-injection contacts and two inner voltage-sensing contacts).

The four-probe technique however severely perturbs the coherence of the NBN signal, often causing multiple fundamental NBN frequencies to appear.[10,11] Thus, when the quality of the NBN signal is important, one must rely on the two-probe contact method and strive for good-quality contacts

to minimize any contact resistance effects. Another example where the four-probe technique must be abandoned is the measurement of the high-frequency conductivity (10 MHz → 10 GHz) where the sample is mounted directly on the coax and becomes the terminating load for the coax.

The influence of inner contacts on the NBN is indisputable evidence of the effect of contacts on the CDW. One interpretation is that any contact, which has a finite width along the chain direction of the crystal, shorts out the electric field in the material below the contact. Thus the electric field in that region is lower than the threshold field necessary for the CDW to slide and the CDW is pinned. Away from the contact, however, the electric field is above threshold and the CDW depins. This induces sufficient strain in the CDW to cause phase slip processes to occur.[12] Within this scenario, painting voltage contacts on the crystal forces the sliding CDW to break into multiple sub-domains with the location of the PSC's determined by the location of the contacts.

A figurative example is given in Fig. B-4. Fig. B-4a shows a sliding CDW in a two contact sample (two-probe). Current conversion processes (i.e., phase slip processes) occur at the contacts. The contacts are represented by the rectangles and the phase slip processes by the ovals. When two inner voltage contacts are added, the CDW configuration is severely perturbed because the contacts "short" the electric field. This causes additional phase slip processes

to occur at these contacts and the CDW divides into three regions (Fig. B-4b). The situation might be remedied by using non-perturbative contacts which are high resistance contacts that only touch the sample in a very limited region. These contacts are represented by the triangles in Fig. B-4c.

A non-perturbative contact is produced by taking a thin conducting "wire" and touching it lightly against the sample. The contact resistance can be controlled to some degree by adjusting the force of the wire against the sample. A number of experiments have been performed using this non-perturbative approach. The "wire" used in one set of experiments was another piece of $NbSe_3$[13], while in another set of experiments it was 2.54 μm Wollaston (Rh-Pt) wire.[14,15] In general, these experiments have had success with producing non-perturbative contacts, although some perturbations can still be detected.[15] Furthermore, this non-perturbative approach allows the investigation on new areas of research where the conventional methods fail. It is very possible that with time, this method will become increasingly invaluable to the research of CDW dynamics.

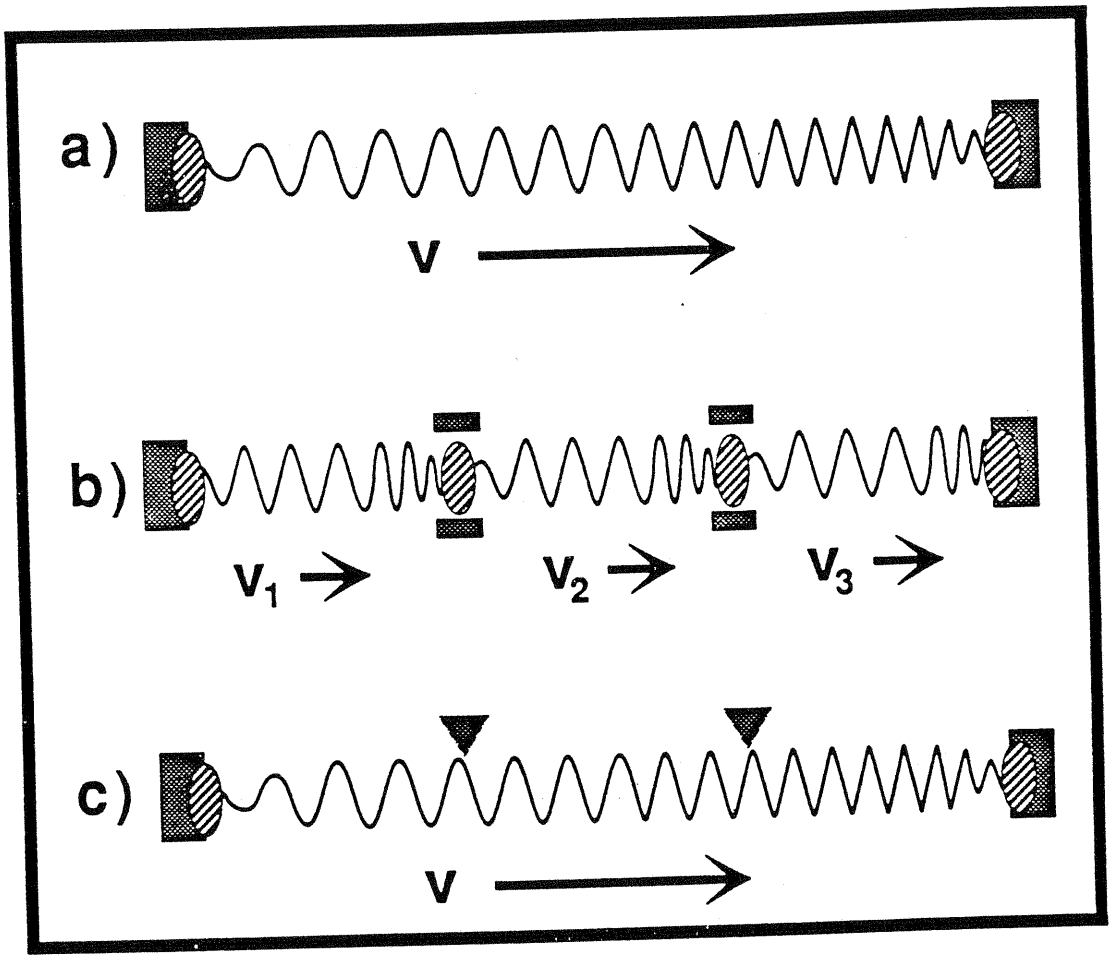

Fig. B-4 a) Diagram of a sliding CDW in a 2-probe sample. b) Diagram of a sliding CDW in a 4-probe sample. The inner voltage contacts severely perturb the CDW configuration. c) The inner perturbing contacts have been replaced with high-resistance "non-perturbing" contacts.[16] See text for discussion.

[1]A. Meerschaut and J. Rouxel, *J. Less Common Metals* **39**, 197 (1975).

[2]J. L. Hodeau, M. Marezio, C. Roucau, R. Ayroles, A. Meerschaut, J. Rouxel, and P. Monceau, *Phys. Stat. Sol.* (a) **62**, 483 (1980).

[3]R. M. Fleming, D. E. Moncton, and D. B. McWhan, *Phys. Rev. B* **18**, 5560 (1978);

P. Haen, P. Monceau, B. Tisser, G. Waysand, A. Meerschaut, P. Molinine, and J. Rouxel, in *Low Temperature Physics Lt-4*, M. Krasius and M. Vuorio, eds. (American Elsevier, New York, 1975).

[4]R. M. Fleming, C. H. Chen, and D. E. Moncton, *J. de Physique* **44**, C3-1651 (1983).

[5]For a review, see G. Grüner and A. Zettl, *Phys. Rep.* **119**, 117 (1985); see also P. Monceau in *Electronic Properties of Quasi-One-Dimensional Materials*, Vol. II, P. Monceau, ed. (Reidel, Dordrecht, The Netherlands 1985), p. 139.

[6]G. X. Tessema and N. P. Ong, *Phys. Rev.* B **23**, 5607 (1981).

[7]N. Shima, *J. Phys. Soc. Japan* **51**, 11 (1982);

N. Shima, *J. Phys. Soc. Japan* **52**, 578 (1983);

N. Shima and H. Kamimura, in *Theoretical Aspects of Band Structures and Electronic Properties of Pseudo-One-Dimensional Solids*, H. Kamimura ed. (D. Reidel Publishing Co. 1985) p. 231.

[8]P. Monceau, N. P. Ong, A. M. Portis, A. Meerschaut, and J. Rouxel, *Phys. Rev. Lett.* **37**, 602 (1976).

[9]A. Meerschaut, P. Gressier, and J. Rouxel, in *Crystal Chemistry and Properties of Materials with Quasi-One-Dimensional Structures: A Chemical and Physical Synthetic Approach*, J. Rouxel, ed. (D. Reidel Pub. Co., Dordrecht, 1986).

[10]T. M. Tritt, D. J. Gillespie, A. C. Ehrlich, and G. X. Tessema, *Phys. Rev. Lett.* **61**, 1776 (1988).

[11]N. P. Ong and G. Verma, *Phys. Rev.* B **27**, 4495 (1983).

[12]N.P. Ong, G. Verma, and K. Maki, *Phys. Rev. Lett.* **52**, 663 (1984);

G. Verma and N.P. Ong, *Phys. Rev.* B **30**, 2928 (1984);

L. P. Gor'kov, *Sov. Phys. JETP* **59** 1057 (1984).

[13]S. E. Brown and L. Mihály, *Phys. Rev. Lett.* **55**, 742 (1985);

S. E. Brown, L. Mihály, and G. Grüner, *Solid State Commun.* **58**, 231 (1986).

[14]R. P. Hall, M. F. Hundley, and A. Zettl, *Phys. Rev.* B **38**, 13002 (1988).

[15]M. F. Hundley and A. Zettl, *Phys. Rev.* B **37**, 8817 (1988).

[16]The sinusoid in the figure does <u>not</u> represent the CDW charge density, i.e., $\rho(x) = \rho_m + \rho_c \cos [Qx + \Phi(x,t)]$; (Eqn. (6-3)). Rather it figuratively represents the CDW as an elastic medium, in this case, a spring. The physical

height of the spring as a function of position figuratively represents the CDW's amplitude.